BEHRUZ KARDAN

COLLECTIVE FLOW MEASUREMENTS IN GOLD-GOLD COLLISIONS AT 1.23 AGEV WITH HADES

GOETHE UNIVERSITÄT

Collective flow measurements in Gold-Gold collisions at 1.23 *A*GeV with HADES

Dissertation
zur Erlangung des Doktorgrades
der Naturwissenschaften

vorgelegt beim Fachbereich Physik
der Johann Wolfgang Goethe-Universität
in Frankfurt am Main

von
Behruz Kardan
aus Tabriz

Frankfurt 2022
(D30)

Collective flow measurements in Gold-Gold collisions
at 1.23 *A*GeV with HADES

Behruz Kardan, *18. November 2022*

Vom Fachbereich Physik der
Johann Wolfgang Goethe - Universität als Dissertation angenommen.

Dekan:
Prof. Dr. Roger Erb

Gutachter:
Prof. Dr. Christoph Blume
Prof. Dr. Joachim Stroth

Datum der Disputation:
26. Mai 2023

Die vorliegende Druckfassung enthält geringfügige, inhaltlich nicht relevante Änderungen gegenüber der beim Promotionsbüro eingereichten Fassung.

To Jana, for her unwavering support.

Abstract

Heavy-ion collisions allow to investigate the properties of strongly interacting matter under extreme conditions in laboratory experiments. There is a large scope of experimental measurements of different nuclei in their ground state and in excited states which try to infer the properties of nuclear matter. But only relativistic heavy-ion collisions can compress matter to densities comparable to dense stellar objects. The unique advantage of a laboratory-controlled environment is that, depending on the beam energy, the choice of target and bombarding nuclei and the varying reaction violence due to the centrality of each individual collision, very different conditions can be explored. The achieved energy densities are high enough to excite nuclear matter in such a way to transform it to new states of matter with different properties, like hadronic or quark-gluon matter. The phases of strongly interacting matter and the transitions to each other is one of the most important and still open topics in nuclear and particle physics. The accurate formulation of the equation of state of dense matter is crucial for the understanding of the evolution of the Universe shortly after the Big Bang, the features of core-collapse supernovae explosions, the structure and stability of neutron stars and the process of their merger. The main goal of relativistic nuclear research is to extract information about this hot and dense phase, either by direct signal observables from rare and penetrating probes or by rewinding the dynamical evolution of the system from the final state measurements backwards up to this moment in model calculations. The properties of the hot expanding matter, the details of its geometrical initial source, its dynamical interaction with the cold spectator matter and the intensities due to the thermal and collective motion results in complicated emission pattern and should be encoded over the various flow moments. It is common to quantify the azimuthal anisotropy in the particle emission via a Fourier decomposition yielding to the flow coefficients v_n of several orders. One expects that including specific flow coefficients adds the sensitivity required for a detailed theoretical description of flow phenomena.

In this thesis, the flow coefficients v_n of the orders $n = 1 - 6$ are studied for protons and light nuclei in Au+Au collisions at $E_{\text{beam}} = 1.23\ A$GeV, equivalent to a center-of-mass energy in the nucleon-nucleon system of $\sqrt{s_{\text{NN}}} = 2.4$ GeV. The detailed multi-differential measurement is performed with the HADES experiment at SIS18/GSI. HADES, with its large acceptance, covering almost full azimuth angle, combined with its high mass-resolution and good particle-identification capability, is well equipped to study the azimuthal flow pattern not only for protons, deuterons, and tritons but also for charged pions, kaons, the ϕ-mesons, electrons/positrons, as well as light nuclei like helions and alphas. The high statistics of more than seven billion Au-Au collisions recorded in April/May 2012 with HADES enables for the first time the measurement of higher order flow coefficients up to the 6^{th} harmonic. Since the Fourier coefficient of 7^{th} and 8^{th} order are beyond the statistical significance only an upper bound is given. The Au+Au collision system is the largest reaction system with the highest particle multiplicities, which was measured so far with HADES. A dedicated correction method for the flow measurement had to be developed to cope with the reconstruction in-efficiencies due to occupancies of the detector system. The systematical bias of the flow measurement is studied and several sources of uncertainties identified, which mainly arise from the quality selection criteria applied to the analyzed tracks, the correction procedure for reconstruction inefficiencies, the procedures for particle identification (PID) and the effects of an azimuthally non-uniform detector acceptance. The systematic point-to-point uncertainties are determined separately for each particle type (proton, deuteron and triton), the order of the flow harmonics v_n, and the centrality class. Further, the validity of the results is inspected in the range of their evaluated systematic uncertainties with several consistency checks. In order to enable meaningful comparisons between experimental observations and predictions of theoretical models, the classification of events should be well defined and in sufficiently narrow intervals of impact parameter. Part of this work included the implementation of the procedure to determine the centrality and orientation of the reaction.

In the conclusion the experimental results are discussed, including various scaling properties of the flow harmonics. It is found that the ratio v_4/v_2^2 for protons and light nuclei (deuterons and tritons) at mid-rapidity for all centrality classes approaches values close to 0.5 at high transverse momenta, which was suggested to be indicative for an ideal hydrodynamic behaviour. A remarkable scaling is observed in the p_{t} dependence of v_2 (v_4) at mid-rapidity of the three hydrogen isotopes, when dividing by their nuclear mass number A (A^2) and p_{t} by A. This is consistent with naive expectations from nucleon coalescence, but raises the question whether this mass ordering can also be explained by a hydrodynamical-inspired approach, like the blast-wave model. The relation of v_2 and v_4 to the shape of the initial eccentricity of the collision system is studied. It is found that v_2 is independent of centrality for all three particle species after dividing it by the averaged second order participant eccentricity $v_2/\langle\varepsilon_2\rangle$. A similar scaling is shown for v_4 after division by $\langle\varepsilon_2\rangle^2$.

In view of the new multi-differential high-precision data, including higher harmonics, it would be an ideal opportunity to revisit transport model calculations, including mean field potentials and studying their sensitivity to the nuclear equation of state. The goal in the future is to extend our *a priori knowledge* of elementary particle physics and low-density nuclear experiments, that are incorporated in the state-of-the-art models, to unknown regions of large baryon and energy densities, and to constrain the wide space of parameters using a Bayesian inference method.

Inhaltsangabe

Schwerionenkollisionen ermöglichen die Eigenschaften von starkwechselwirkender Materie unter extremen Bedingungen im Labor zu untersuchen. Es gibt ein Fülle von experimentellen Messungen von verschiedenen Atomkerne in ihrem Grundzustand und in angeregten Zuständen, die versuchen auf die Eigenschaften der Kernmaterie zu schließen. Aber nur Relativistische Schwerionenkollisionen können Materie zu Dichten komprimieren, die vergleichbar sind mit denen von dichten stellaren Objekten. Der einzigartige Vorteil innerhalb eines Versuchsaufbau im Labor mit Hilfe eines Beschleuniger ist, dass die Schwerionenreaktionen unter sehr verschiedenen Bedingungen untersucht werden können. Das wären die Abhängigkeit von der Strahlenergie, die Auswahl der zu beschießenden und zu beschleunigenden Atomkerne und die sich ändernde Heftigkeit der Reaktion in Abhängigkeit der Zentralität jeder einzelnen Kollision. Die erreichten Energiedichten sind hoch genug, dass diese Nukleare Kernmaterie so weit anregen kann, um in eine neue Zustandsform mit anderen Eigenschaften zu wechseln, wie Hadronischer oder Quark-Gluon Materie. Die Phasen starkwechselwirkender Materie und die damit verbundenen Übergänge zueinander sind eine der wichtigsten und bislang ungelösten Fragestellung der Kern- und Teilchen Physik. Die genaue Formulierung der Zustandsgleichung von dichter Kernmaterie ist entscheidend für unser Verständnis der Entwicklung der Universums kurz nach dem Urknall, die Merkmale vom Kernkollaps-Supernovae Explosionen, die Struktur und Stabilität von Neutronensternen und den Prozess ihrer Verschmelzung. Das Hauptziel des Forschungsfeld der relativistischen Kernphysik ist es, Informationen über diese heiße und dichte Phase zu gewinnen, entweder durch direkte Messung von seltenen und durchdringenden Sonden oder mit Hilfe von Modellberechnungen, wo die dynamische Entwicklung des Systems von den Endzustandsmessungen bis zu diesem Moment rekonstruiert werden kann. Die Eigenschaften der heißen expandierenden Materie, die Details ihrer geometrischen Ursprungsform, ihrer dynamischen Wechselwirkung mit der kalten Spektatorenmaterie und die Intensitäten aufgrund der thermischen und

kollektiven Bewegung führen zu einem komplizierten Emissionsmuster. Die Information darüber sollte über die verschiedenen Flussmomente kodiert sein. Üblich ist die Quantifizierung der azimutalen Anisotropie in der Teilchenemission durch eine Fourier-Zerlegung, aus der sich die Flusskoeffizienten v_n mehrerer Ordnungen ergeben. Man erwartet, dass die Einbeziehung spezifischer Flusskoeffizienten, die erforderliche Empfindlichkeit für eine detaillierte theoretische Beschreibung von Flussphänomenen erhöht.

In dieser Arbeit werden die Flusskoeffizienten v_n der Ordnungen $n = 1 - 6$ für Protonen und leichte Kerne in Au+Au-Kollisionen untersucht. Die Messung erfolgte mit dem HADES-Experiment am SIS18/GSI bei einer Strahlenergie $E_{\text{beam}} = 1.23$ AGeV, was einer Massenschwerpunktenergie im Nukleon-Nukleon-System von $\sqrt{s_{\text{NN}}} = 2.4$ GeV entspricht. HADES, mit seiner großen Akzeptanz, die fast den gesamten Azimutwinkel abdeckt, kombiniert mit seiner hohen Massenauflösung und der guten Fähigkeit zur Teilchenidentifizierung, ist gut ausgestattet, um das azimutale Flussmuster nicht nur für Protonen, Deuteronen und Tritonen, sondern auch für geladene Pionen, Kaonen, der ϕ-Mesonen, Elektronen/Positronen, sowie leichte Kerne wie Helionen und Alphas zu studieren. Die hohe Statistik von mehr als sieben Milliarden Au-Au-Kollisionen, die im April/Mai 2012 mit HADES aufgezeichnet wurden, ermöglicht zum ersten Mal die Messung von Flusskoeffizienten bis zur sechsten Ordnung. Da die Fourier-Koeffizienten der siebten und achten Ordnung außerhalb der statistischen Signifikanz liegen, wird nur eine obere Grenze angegeben. Das Au+Au Kollisionssystem ist das größte Reaktionssystem mit den höchsten Teilchenmultiplikationen, die bisher mit HADES gemessen wurden. Eine Korrekturmethode für die Flussmessung musste entwickelt werden, um die durch die Auslastung des Detektorsystems bedingten Ineffizienzen zu bewältigen. Systematische Fehler in der Flussmessung werden untersucht und mehrere Quellen von Unsicherheiten identifiziert. Diese sind hauptsächlich die Kriterien der Qualitätsauswahl für die zu analysierenden Teilchenspuren, dem Korrekturverfahren der Ineffizienzen, dem Verfahren zur Teilchenidentifizierung und die Auswirkungen einer ungleichmäßigen azimutalen Detektorakzeptanz. Die Systematischen Punkt-zu-Punkt-Unsicherheiten werden separat für jeden Teilchentyp (Proton, Deuteron und Triton), die Ordnung der Flusskoeffizienten v_n und die Zentralitätsklasse bestimmt. Außerdem wird die Gültigkeit der Ergebnisse im Bereich ihrer abgeschätzten systematischen Unsicherheiten mit mehreren Konsistenzprüfungen überprüft. Um sinnvolle Vergleiche zwischen experimentellen Beobachtungen untereinander sowie mit Vorhersagen aus theoretischen Modellen zu ermöglichen, sollte die Klassifizierung der Ereignisse gut definiert sein und in ausreichend engen Intervallen des Impaktparameters. Ein Teil dieser Arbeit umfasst die Implementierung eines gut definierten Verfahrens zur Bestimmung der Zentralität und Ausrichtung der Reaktion.

In der Schlussfolgerung werden die experimentellen Ergebnisse diskutiert, einschließlich verschiedener Skalierungseigenschaften der Flusskoeffizienten. Es kann festgestellt werden, dass das Verhältnis v_4/v_2^2 für Protonen und leichte Kerne (Deuteronen und Tritonen) in der Schwerpunkts-Rapidität für alle Zentralitätsklassen Werte nahe 0.5 bei hohen Transversalimpulses erreicht, was als Indiz auf ein ideales hydrodynamisches Verhalten gesehen werden kann. Eine bemerkenswerte Skalierung von v_2 (v_4) in Abhängigkeit des Transversalimpulsen in der Schwerpunkts-Rapidität ist beobachtbar für alle drei Wasserstoffisotope, wenn diese jeweils durch ihrer Kernmassenzahl A (A^2) dividiert und p_t mit A. Dies steht im Einklang mit der naiven Erwartungen der Nukleonen Koaleszenz, wirft aber die Frage auf, ob diese Massenordnung auch mit einem hydrodynamisch inspirierten Ansatz, wie dem *Blast-Wave Modell* erklärbar ist. Die Beziehung von v_2 und v_4 in Relation zur initialen Form der Exzentrizität des Kollisionssystems wird untersucht. Es zeigt sich, dass v_2 für alle drei Teilchen unabhängig von der Zentralität ist, nachdem durch die gemittelte Partizipanten-Exzentrizität zweiter Ordnung $v_2/\langle\varepsilon_2\rangle$ dividiert wird. Eine ähnliche Skalierung kann auch für v_4 nach Division durch $\langle\varepsilon_2\rangle^2$ beobachtet werden.

In Anbetracht der neuen multidifferentiellen Hochpräzisions-Daten, welche die Messung von Flusskoeffizienten höherer Ordnung beinhaltet, wäre es eine ideale Gelegenheit die Berechnung von Transport-Modellen, welche *Mean Field* Potentiale beinhalten, auf ihre Sensitivität hinsichtlich der Zustandsgleichung von Nuklearer Kernmaterie zu überprüfen. Das Ziel in der Zukunft wird sein unser *apriorisches Wissen* der Elementaren Teilchenphysik sowie die Ergebnisse von kernphysikalischen Experimenten, welche Bestandteil moderner Modelle sind, in unbekannte Regionen der Baryon- und Energiedichten zu erweitern und den weiten Parameterraum mit Hilfe von *Bayes'schen Inferenzmethode* Methoden einzugrenzen.

Contents

Introduction

One of the fundamental questions is the origin and nature of matter, the substance which forms everything visible around us, including galaxies, stars, planets, and all living beings. Since matter can exist under different conditions in the universe, the natural question arises about what to expect as properties of nuclear matter under the most extreme conditions and how can we study these in the laboratory. The detailed investigation of the properties of strongly interacting matter, described by *Quantum Chromodynamics* (QCD), the underlying quantum field theory, has a direct impact on our understanding of crucial concepts on both microscopic and cosmic scale [1–5]:

- How do the emergent properties of matter at different levels develop from basic constituents and fundamental interactions?
- What is the nature of the nuclear force that binds protons and neutrons to nuclei?
- How does the strong force produce the colour-confinement of quarks leading to hadrons and what is the origin of hadron masses?
- How do the hadrons and their constituents, quarks and gluons, behave in extreme conditions, *e.g.* high density and high temperature?
- How is chiral symmetry, a fundamental symmetry in QCD, broken in nature? Can we find indications of chiral symmetry restoration in dense baryonic matter?

The main goal of relativistic nuclear research is to explore the properties of excited nuclear matter, where the achieved energy densities are sufficiently high for the transition of matter into new states with different properties, such as hadronic or quark-gluon matter. The unique advantage of laboratory-controlled settings are the ability to investigate a wide range of conditions, depending on the beam energy, choice of target and bombarding nuclei, and the varying reaction violence caused by the different centralities of each collision. The phases of strongly interacting matter and their transition is one of the most important topics in nuclear and particle physics, where the accurate formulation of the equation-of-state (EOS) of dense matter is crucial for our understanding of the evolution of the universe shortly after the Big Bang [6], the features of core-collapse supernovae explosions and the structure and stability of compact stars [7–9].

Standard Model of Particle Physics

The contrary philosophical stand-point of reductionism is that of emergent phenomenon, both highly debatable [10–12]. But it should be noted that *collective flow phenomena* is a clear example for emergent behaviour, which arise in a *macroscopic volume if the number of microscopic constituents approaches infinity* [13]. Further distinct emergent phenomena in a physical system would include features of phases of matter, such as spontaneously broken symmetries or critical phenomena.

The ancient greek materialists, Democritus and Leucippus, argued for the original *reductionists* concept, that matter is composed of indivisible and indestructible entities called *atoms* which move in the infinite *void* [14]. Since then, the quest of reductionism is to explain macroscopic properties in terms of their microscopic components. One example is the understanding of the abundance of more than 100 chemical elements, numerous additional isotopes, the variety of their excited states, explained only in terms of proton-neutron configurations. This concept of ultimate building blocks of matter had to be revised with the advent of particle accelerators powerful enough to not only break the colliding particles apart, but also to generate newly produced particles. The formulation of the quantum field theory resolved this reductionist principle, in the form of fields that create and destroy their associated particles. Therefore, the properties of quantum fields with their excitations (quanta) realise the building blocks of matter [15].

Based on a wealth of observational data collected in the past century, our best efforts to explain the world are described in two theories, known as the *Standard Model* of cosmology and particle physics [11, 16, 17]. Together with the strong force, the weak, the electromagnetic and the gravitational force all observable interactions in nature can be described. These four fundamental forces differ in two important aspects, their range and their strength. Gravitational and electromagnetic interaction vary as $1/r$ (r being the distance between two objects) and their strength will be very small at large distances, but does not vanish. The strong and weak interaction, on the other side, only have a very limited reach. In the case of the weak interaction this is due to the high mass of the exchange bosons ($W^{\pm}$, Z^0), while in case of the strong interaction it is caused by the non-abelian nature of the gluons, giving rise to the phenomenon of *confinement*. The binding energies of quarks become so strong that any energy invested to break

Interaction		Group	Dim.	Particles	Coupling	Range	Relative strength
strong	QCD	SU(3)	8	gluons	α_s	$\approx 10^{-15}$ m	1
electromagnetic	QED	U(1)	1	photon	$\alpha \approx 1/137$	∞	10^{-2}
weak	EWT	SU(2)	3	$W^+ W^- Z^0$	g_w	$< 10^{-18}$ m	10^{-7}
gravitational	GR			*graviton* (hypothetical)	G_N	∞	10^{-39}

Table 1: Fundamental interactions

them apart is used to produce new quark-antiquark pairs [18]. The answer to the diversity of newly discovered hadron species came from Gell-Mann and Ne'eman in 1961, who interpreted that hadrons are not elementary objects, but are bound states of sub-particles [19, 20], which Gell-Mann called *quarks* [21]. The experimental evidence for point-like constituents inside protons was given in 1968 at the SLAC with electron-proton deep-inelastic scattering experiments [22, 23]. The postulated idea of the *quark model* can up-to-now describe all observed mesons (quark-antiquark bound states) and baryons (three, or more, quark bound states) by six *quark flavors* (u, d, s, c, b, t). Like the six *leptons* $(e, \nu_e, \mu, \nu_\mu, \tau, \nu_\tau)$, the *quarks* are grouped into three generations, but with the difference that each *quark-flavor* has three versions, characterised by the quantum number *color* (see Fig. 1).

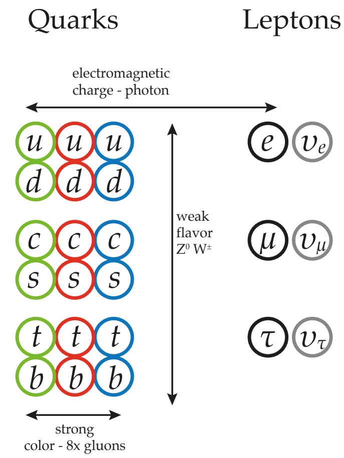

Figure 1: The six *leptons* $(e, \nu_e, \mu, \nu_\mu, \tau, \nu_\tau)$ and the six *quarks* (u, d, s, c, b, t) are grouped into three generations, their weak charge is the source of the weak interaction, which is mediated by the W^0 and $Z^\pm$ bosons. Each *quark-flavor* has three *colored* versions, where their *color-charge* is the source of the *strong force* mediated by eight *colored* gluons. Beside the *neutrinos*, all elementary particles are electrically charged and experience the *electromagnetic interaction* via the *photon*.

It took nearly ten years (1972) for the formulation of *Quantum Chromodynamics* (QCD) as the underlying quantum field theory of the strong force. By describing the coupling of *gluons* to the *color-charge* of the quarks and gluons themselves, two features of QCD became apparent. One is the *color confinement*, which manifests itself in the fact that the hadron spectrum contains only colour neutral states. The other, called the *asymptotic freedom* [25, 26], is describing the fact that the strength of the strong interaction becomes asymptotically weaker with increasing energy, thus probing smaller distances. In other words, at very small distances quarks behave as free particles up to the resolution scale of a nucleon, beyond which they are confined. While this behaviour at large momentum transfers can be treated with perturbation theory, the description of the interactions at small momentum transfers has to rely on effective models. This means that the *running coupling constant* α_s (see Fig. 2) increases logarithmically towards smaller *momentum transfer* Q:

$$\alpha_s(Q^2) = \frac{1}{\beta_0 \ln(Q^2/\Lambda^2_{\text{QCD}})} \tag{1}$$

with $\beta_0 = \frac{1}{12\pi}(33 - 2n_f)$, n_f the number of flavours and and Λ_{QCD} as the QCD scale parameter. The determinations of α_s, the coupling parameter of the strong interaction between quarks and gluons, became available since the early 1980's, based on experimental data at sufficiently large energy scales [27], in combination with theoretical QCD calculations, in next-to-leading or higher order of perturbation theory. The first estimate of $\alpha_s(M_Z^2) \approx 0.11 \pm 0.01$ was made by Altarelli (1989), with with an overall uncertainty of about 10% [28]. The latest world summary (2021) by the Particle Data Group (PDG) quotes a value of $\alpha_s(M_Z^2) = 0.1179 \pm 0.0009$, with an overall uncertainty of below 1% [24], which is a remarkable experimental validation of the non-abelian behaviour of QCD.

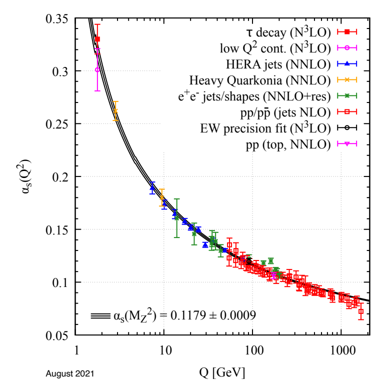

Figure 2: The coupling constant of the strong interaction as a function of momentum transfer Q. Shown is a summary of experimental measurements with the respective degree of QCD perturbation theory used in the extraction, as indicated in brackets. Taken from [24].

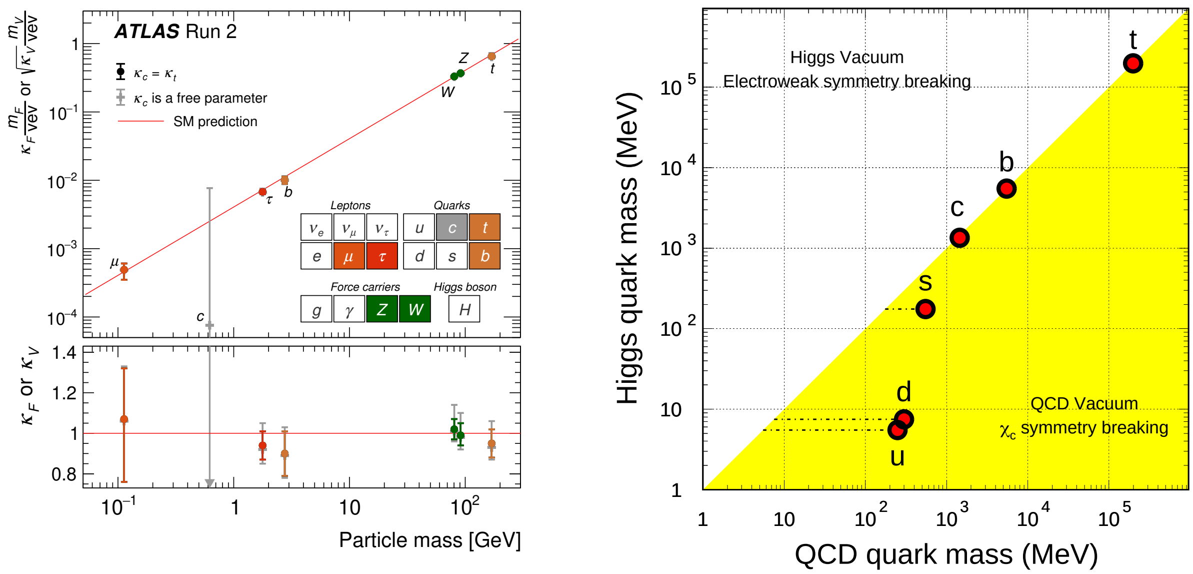

Figure 3: Left: Higgs boson coupling strength as a function of the masses for the fermions (τ, μ, τ, c, b, t) and the vector bosons ($W^{\pm}, Z^0$) derived from data on the cross section and branching ratios [29]. Right: Quark masses in the Higgs vacuum compared to the ones in the QCD vacuum. A large fraction of the light quark masses is due to the chiral symmetry breaking in the QCD vacuum [30].

In the Lagrangian of the standard model 28 free parameters appear explicitly, describing the properties of quarks, leptons and gauge bosons [17]. The parameters are: three coupling constants and the Weinberg angle (α_s, α, g_w, θ_W), CP-violating parameters (8, encoded in CKM and PMNS Matrix and the QCD vacuum phase θ_{QCD}) and the two parameters defining the Higgs-potential (λ and μ^2). Further the masses of the quarks and leptons are defined via the 12 coupling strengths to the Higgs field [29]. The left panel of Fig. 3 shows the coupling strength to the Higgs field. The mechanism of *spontaneous chiral symmetry* breaking in QCD is primarily responsible for the generation of hadron masses. The contribution of the QCD vacuum condensates to the masses of the three light quark flavours u, d and s is significantly larger than that from the coupling to the Higgs field, as shown in the right panel of Fig. 3 [30].

Strongly Interacting Matter

Very early after the development of QCD, Cabibbo and Parisi (1975) [31] formulated the idea of a phase transition between *confined* and *de-confined* matter based on the physical interpretation of the Hagedorn limiting temperature [32]. For sufficiently large energy densities the system is expected to transition in a *de-confined* phase with quarks and gluons as the relevant degrees of freedom, called the *Quark-Gluon Plasma* (QGP) [33]. Fig. 4 shows the conjectured QCD phase diagram of

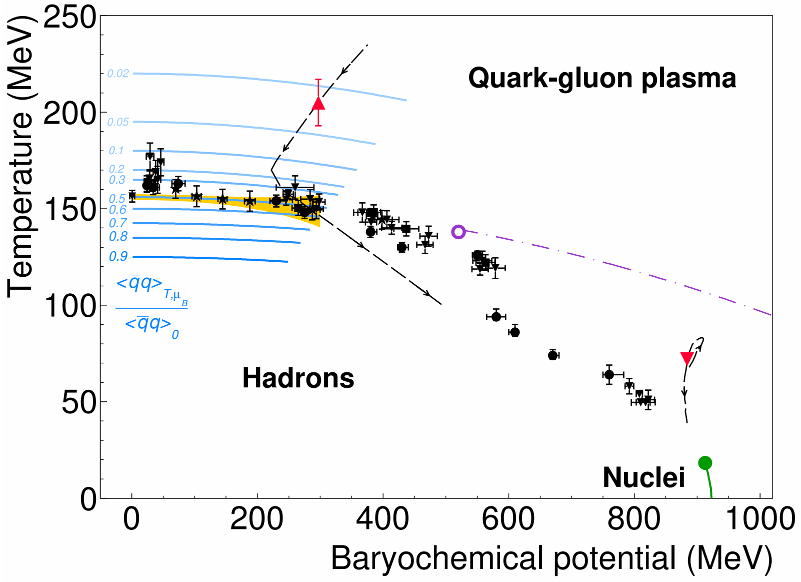

Figure 4: QCD phase diagram of strongly interacting matter. The chemical freeze-out points deduced from the experimentally measured hadron abundances in a statistical hadronization model are shown as black symbols. The relative values of the chiral condensate to those in a QCD vacuum [41] are shown as blue contour lines and the crossover region as a yellow band [40]. The red triangle displays the temperature extracted from the invariant-mass spectrum of di-muons measured by the NA60 Collaboration [42] and from di-electrons measured by the HADES Collaboration [34]. The green point and curve show the critical end-point and the first-order liquid–gas phase transition in nuclear matter [43, 44]. Figure taken from [34].

strongly interacting matter, parameterised by the temperature T and the baryo-chemical potential μ_B [34]. The results of lattice QCD calculations [35–37] predict the phase transformation between confined hadrons and de-confined quarks and gluons at vanishing baryo-chemical potentials ($\mu_B \to 0$ MeV), with a smooth *cross-over* region between the two phases, shown as a yellow band with a pseudo-critical temperature $T_{pc} = 156.5 \pm 1.5$ MeV [38–40]. The relative values of the chiral condensate to those in a QCD vacuum [41] are shown as blue contour lines. For higher baryo-chemical potentials it is expected that the parton-hadron phase boundary changes from a *cross-over* to a *first order phase transition*, with the consequence of a hypothetical *critical end-point* [45], both shown as magenta dashed line and circle. In the energy regime of relativistic heavy-ion collisions the produced energy densities are high enough to excite nucleons into baryonic resonances. This hadronic phase relies only on hadronic degrees of freedom of *color-confined* hadrons. For the description of *hadronization* at the parton-hadron phase boundary line, the measured hadron production data are used to determine the degree of chemical equilibration. The *statistical hadronization model* (SHM) [46–49], in combination with the *hadron resonance gas* (HRG) [50–52], are used for the extraction of the chemical freeze-out parameters T_{ch} and μ_B. It should be emphasised that regardless of the oversimplified description neglecting dynamics, these models are in good agreement with the experimental abundances [53]. The chemical freeze-out points thus deduced are shown as black symbols. The red triangle displays the temperature extracted from the invariant-mass spectrum of di-muons measured by the NA60 Collaboration [42] and from di-electrons measured by the HADES Collaboration [34]. The two black dashed curves indicate the corresponding predicted fireball evolution extracted by transport models. The best empirically observed region in this diagram is nuclear matter at ground state density $\rho_0 = 0.16$ fm^{-3} and zero temperature, where the the baryo-chemical potential is $\mu_0 = m_N - B/A = 923$ MeV equivalent to energy density at $\epsilon_0 \approx 0.14$ GeV fm^3. Here nuclei exist as a *quantum liquid*, a system of up to hundreds of nucleons bound by the nuclear forces. The green point and curve show the critical endpoint and the first-order liquid–gas phase transition in nuclear matter [43, 44, 54, 55].

Neutron Stars

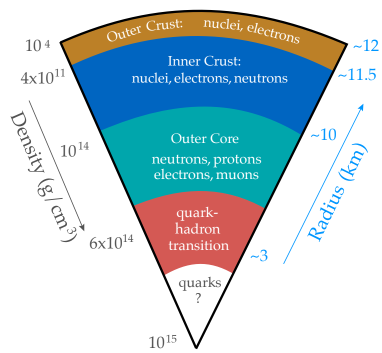

Figure 5: The radial density profile of neutron stars with its interior structure and matter composition. Adapted from [56].

The densest observable object in the universe are Neutron Stars (NS). The concept dates back to Lev D. Landau, who was one of the first arguing for the possible existence of dense stars which look like one giant nucleus [57], shortly before the discovery of the *neutron* by Chadwick in 1932 [58]. The mass of a neutron star cannot be arbitrarily large before collapsing, owing to its gravitational pull. There should be an upper limit corresponding to the pressure available to resist a collapse. The relationship between the mass and radius of compact stars can be solved by using the *Tolman-Oppenheimer-Volkoff* (TOV) equation for a known Equation-Of-State EOS [59]. A harder EOS, *i.e.* with higher pressure for a given density, should support the stability of neutron stars with larger masses. In Fig 5 the interior structure and composition of the neutron stars predicted by theory are illustrated. The density increases toward the centre of the star, reaching densities several times the nuclear saturation density $\rho = 0.16/\text{fm}^3$, and the degrees of freedom change. In the outer crust, matter consists of nuclei and electrons, but in the core of an NS, the matter transforms into a uniform liquid of neutrons, with a small contribution from other particles, including protons, electrons, and muons. In NSs with large masses, the densities encountered in the inner core could be sufficiently high for a phase transition to matter-containing de-confined quarks. Date from gravitational wave observations of binary neutron star mergers [60] and the subsequently emitted electromagnetic radiation suggest that the maximum mass limit is approximately 2.17 solar masses [61, 62]. Model calculations suggest that temperatures of $50 - 80$ MeV and densities around twice the nuclear ground-state densities might be reached, similar to what is expected in heavy-ion collisions [56, 63, 64].

Heavy-Ion Collisions

The first stage of a heavy-ion reaction, called the *initial state interaction*, is commonly depicted as two Lorentz-contracted nuclei in the ground state, where the configuration of the nucleons is approximated to be frozen. In the collision process of two nuclei, the individual nucleons decelerate owing to nuclear stopping, and their longitudinal kinetic energy is converted into thermal and compressional energy in the pre-equilibrium stage, which is then released during the thermalisation of this high-density phase in a collectively expanding system. The gradient of the buildup pressure provides the accelerating forces for the rapidly expanding matter, which exists only for a very short time.

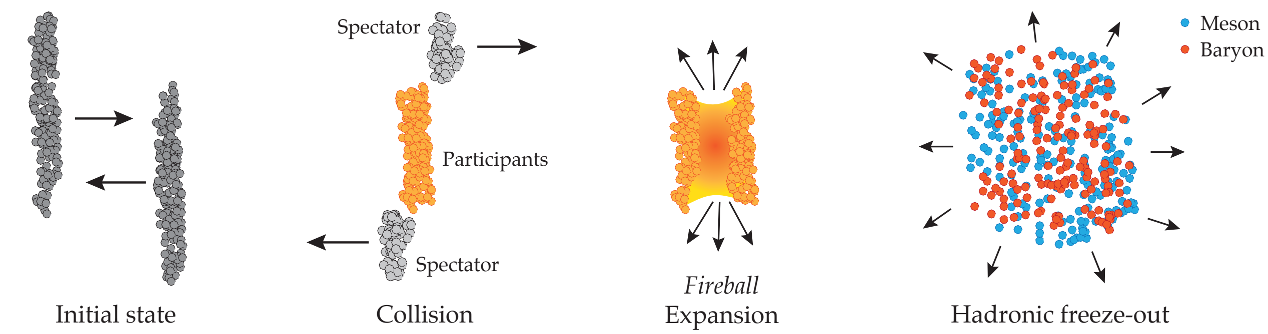

Figure 6: The subsequent stages of a heavy-ion reaction.

In perfectly central collisions the expansion should be isotropic, leading to symmetrical transversal and longitudinal flow. In more peripheral collisions, which are characterised by a reaction region which is largely non-uniformly distributed, the initially deposited energy and baryon densities decrease from the central core of the reaction to the outer perimeter and form two elongated bands up to the residual fragments, called spectators, which pass-by unstopped with the initial velocity. Due to the non-uniform size, shape, and densities in the azimuthal and longitudinal directions of the medium, the anisotropies of the expanding medium are encoded in the thermal and collective movement of the emitted particles. If the expansion is faster than the movement of the spectator residuals, the spectator matter can effectively block particle emission from the central fireball in their direction. The subsequent interaction between hot expanding matter and cold spectator matter results in a complicated emission pattern. Once the system cools down to the critical temperature, hadrons form (*hadronization*) and as soon as sequential inelastic collisions cease the *chemical freeze-out* point is reached, *i.e.* the observable particle abundances are fixed. In the further development the phase space distributions of the hadrons still change until the *kinetic freeze-out* is reached, where elastic collision cease. Observables of bulk properties, like radial, directed and elliptic flow, as well the abundances of fragments due to coalescence, remain unchanged. It is common to analyse the azimuthal anisotropy of the final particle emission via a Fourier decomposition, yielding the flow coefficients v_1, v_2 and up to higher orders v_n. This type of unfolding into specific flow moments adds to the sensitivity required for a detailed theoretical description of flow.

Collective Flow Phenomena

Since the discovery of the atomic nuclei in 1911 by Rutherford [65], systematic studies of nuclei radii and their nuclear density distributions have led to the realisation of the short-range properties of the nuclear force and of the saturation and incompressibility of nuclear matter, which suggests the analogy of a liquid-like behaviour. The term *collectivity* is rooted in the development of nuclear models describing this quasi-macroscopic properties of nuclear matter (liquid-drop models, models of nuclear rotation and vibration or giant resonances) [66–69]. In the context of nuclear dynamics, the general definition of *collectivity* is a characteristic which is observable in the emission of several particles correlated in momentum-space. *Collective flow* is an example for such a common feature and describes the movement of a large number of emitted particles within the same velocity field or into similar direction owing to their common dynamic origin [70, 71].

At the 184-inch *synchronised cyclotron* built by Ernest Lawrence in Berkeley one important experimental observation was the emission of pions from a carbon target when bombarded with 380 MeV alpha particles [72], which led to the development of the statistical thermal model for particle production [73–76]. Based on this, Belenkij and Landau [77] were the first in 1955 to use a fluid dynamical model to describe particle production evolving from a hydrodynamic expansion after the collision of nucleons and nuclei. Glassgold, Heckrotte, and Watson [78] considered in 1959 that hydrodynamic shock waves could form when a high-energy proton or pion passing through a nucleus exceeded the nuclear speed of sound. They proposed that the nuclear compressibility coefficient can be determined from the angular distribution of the nucleons emitted after the hydrodynamic shock wave passed through the nuclear surface. Their idea remained largely unnoticed until the early seventies, until it was realised that the existing proton synchrotrons can also be used to accelerate heavy-ions up to relativistic energies. The field of relativistic nuclear matter research was developing and, in contrast to elementary particle collisions, where smaller dimensions can be probed as beam energies increase, the interest in heavy-ion collisions originated from the possibility of creating

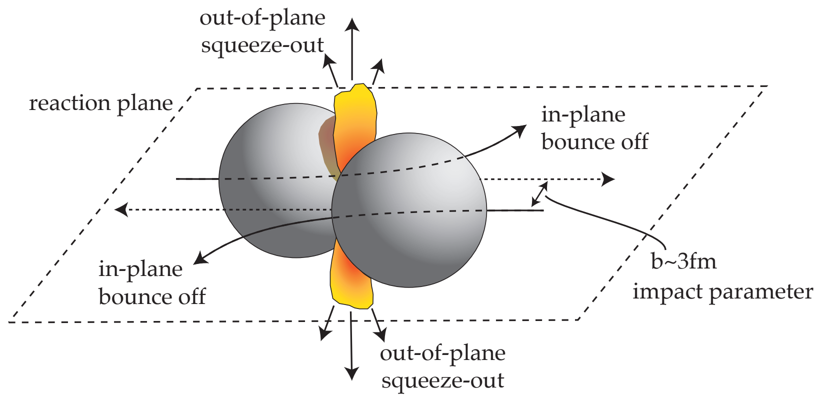

Figure 7: Illustration of a semi-central collision of two nuclei with an impact parameter of ~ 3 fm in the Bevalac/SIS energy regime, with the direction of the flow phenomena indicated with arrows into (*bounce-off* or *side-splash*) or perpendicular (*squeeze-out*) to the reaction plane. Figure adapted from [96].

high-energy densities over large volumes [79, 80]. Experimental observables were confronted with new theoretical models [81–84] and this motivated a large number of theoretical studies on the application of hydrodynamical models to heavy-ion collisions, which were mainly concerned with the incompressibility and propagation of shock waves in nuclear matter [85–91]. The pioneering work resulted in the development of computer codes by the *Los Alamos*, *Livermore* and *Frankfurt* groups with quite different realisations. The relativistic *Los Alamos* code utilised the particle-in-cell method [92], whereas the non-relativistic *Frankfurt* code, which implemented binding and potential effects, used a flux-corrected-transport algorithm. The applicability and validity of hydrodynamics in the context of nuclear matter remains a controversial issue [93], due to the assumption of local thermal equilibrium at all stages of the reaction, which should be unrealistic in the initial collision and the final *freeze-out* phases. The thermodynamic properties, needed to study the equation-of-study, are only well defined when the created system thermalises rapidly towards local thermal equilibrium [94, 95]. To address the limitations of ideal hydrodynamics in the accurate description of diffusion and non-equilibrium effects, microscopic transport approaches were developed. For a historical review of the hydrodynamic models, see Refs. [96, 97].

Flow Phenomenology Several important features have already been predicted by early ideal hydrodynamic calculations, which could be verified experimentally later. The *transverse expansion* of matter causes a push which is faster outwards, *i.e.* perpendicular to the relative motion of the two nuclei, than in the longitudinal direction [88]. A *bounce-off* of the projectile and target residues at large impact parameters, deflected by the opposite nuclei, a similar *side-splash* of compressed matter in the reaction plane [98], or the *squeeze-out* of compressed participant matter perpendicular to the reaction plane was anticipated [99]. The semi-central collision of two nuclei with an impact parameter of ~ 3 fm in

Accelerator	Facility	Year	Projectile	max. Energy	Experiments
Bevalac	LBNL, Berkeley	1974 - 1993	C, Ne, Ar	2 AGeV	
		1982 - 1984	Ca, Nb, La, Au	1 AGeV	PlasticBall, Streamer Chamber
		1984 - 1993	Ca, Nb, La, Au	1 AGeV	DLS, EOS TPC
Synchrophasotron	JINR, Dubna	1974 - 1985	d, He	5 AGeV	
Saturne	Saclay	1978 - 1997	Ne, Ar	1 AGeV	DIOGENE
ISR	CERN, Geneva	1980 - 1983	d, He	15.7 AGeV	
SPS	CERN, Geneva	1986 – today	O, S, In, Pb	200/158 AGeV	NA35, NA45, NA44, NA49, NA61 WA80, WA93, WA97, WA87, NA57 ...
AGS	BNL, Brookhaven	1986 - 1994	Si, Au	14.5/11.5 AGeV	E802, E810, E814, E859, E866, E877 E891, E895, E896, E910, E917 ...
SIS18	GSI, Darmstadt	1990 – today	Au, Bi	2 AGeV	FOPI, KaoS, HADES ALADIN, INDRA, TAPS
RHIC	BNL, Brookhaven	2000 - today	Cu, Au, U d, He, Zr, Ru	$\sqrt{s_{NN}} = 200$ GeV	Star, PHENIX, BRAHMS, Phobos
LHC	CERN, Geneva	2009 - today	Xe, Pb	$\sqrt{s_{NN}} = 5.5$ GeV	ALICE, CMS, ATLAS, LHCb
SIS100	FAIR, Darmstadt	*2027*		$11 - 14$ AGeV	HADES, CBM

Table 2: History of accelerators in heavy-ion physics [102, 112]. For SPS and AGS, only a selection of experiments is shown. The projectile nuclei shown are those primarily used in the key experiments.

the Bevalac/SIS energy regime is illustrated in Fig. 7, with the direction of the flow phenomena indicated with arrows. The first experimental confirmation of collective flow was made in 1984 at Bevalac by the Plastic Ball [100–102], followed by the Streamer Chamber [103, 104] and DIOGENE at Saturne [105, 106]. Since than over four decades a wealth of measurements on collective flow at the SIS18 (GSI), SPS (CERN), AGS (BNL), RHIC and LHC has been accumulated over several magnitudes of energies (see Tab. 2) and theoretical models on flow phenomenology developed. For a comprehensive review see [70, 107–111] and references therein. The signatures on collective flow relevant to the SIS and future FAIR energies (with overlap to AGS and RIHC BES) are described as follows.

Nuclear stopping is a necessary condition for the creation of dense and hot nuclear matter, where the expansion scenario resulting in collective flow depends on the degree of stopping [103, 108, 113–115]. The Fig. 8 shows different model scenarios that are expected in heavy-ion collisions at SIS energies with long spectator passing times. On the left, the Landau scenario with total stopping [77], in the middle, the Bjorken scenario with partial stopping and initial longitudinal flow (middle panel) [116], and on the right, the Myers-Hagedorn scenario [81, 117], where stopping depends on the nuclear density and partially stopped matter moves at different rapidities. This concept is similar to that of the *firestreak* model [118].

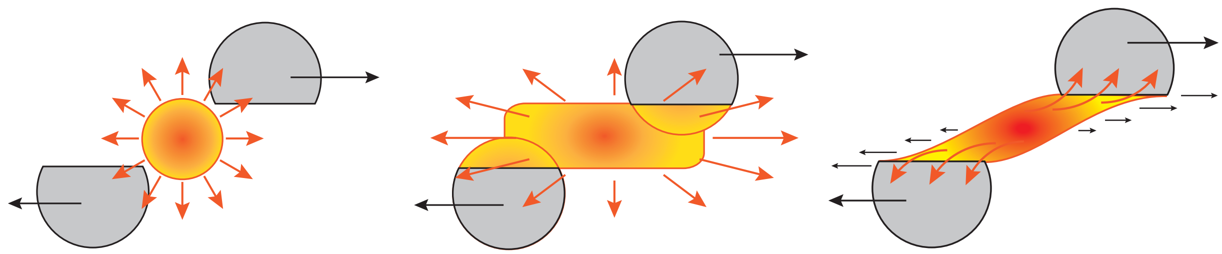

Figure 8: Illustration of a heavy-ion collision at SIS energies with long spectator passing times. Landau scenario with total stopping (left panel)[77], the Bjorken scenario with partial stopping and initial longitudinal flow (middle panel) [116], and the Myers-Hagedorn scenario [81, 117], where stopping depends on the nuclear density and partially stopped matter moves therefore with different rapidities.

Radial flow According to the fireball model, in a purely static thermal scenario, particles are emitted isotropically from an equilibrated hot source, and their kinetic spectra can be described in Maxwell–Boltzmann form:

$$E\frac{d^3N}{dp^3} \propto \exp(-E/T) \ . \tag{2}$$

In the hydrodynamic-inspired *Blast Wave model*, the expanding thermal source is characterised by a spherical symmetric velocity field which describes the collective expansion of the fireball [119–121]. The term *radial flow* describes the common velocity independent of the direction, where *transverse flow* is used whenever the velocity is found to be independent of the azimuthal angle. The *longitudinal flow* describes the collective motion of the particles in their original direction, defined by the beam axis.

Fourier decomposition The first suggestion to characterise the particle emission aligned to the reaction plane by a Fourier decomposition was made by Wong [122] (1979) as a selection criterion for most central events with perfect azimuthal symmetry, where all Fourier coefficients vanish. The same idea was outlined earlier, based on *spherical harmonic expansion* [123], where the specific coefficients are zero for perfectly symmetric collisions. To quantify the two flow phenomena of *bounce-off* in-plane and *squeeze-out* out-of-plane (see Fig. 7), the Fourier coefficients v_1 and v_2 are used and are called *directed flow* and *elliptic flow*, respectively. A positive *directed flow* v_1 is oriented in the direction of the impact parameter between the projectile and target nuclei, with an enhanced emission in this direction, rising in absolute values towards the projectile and target rapidities. The *elliptic flow* describes an emission pattern with back-to-back symmetry oriented perpendicular to the reaction plane at mid-rapidity for collisions in the SIS energy regime [124, 125]. The approach of combining Fourier coefficients to obtain the full event shape over the full phase-space was further developed [104, 126, 127]. The next goal is to resolve the triple differential invariant cross-section, not through Fourier decomposition, but fully

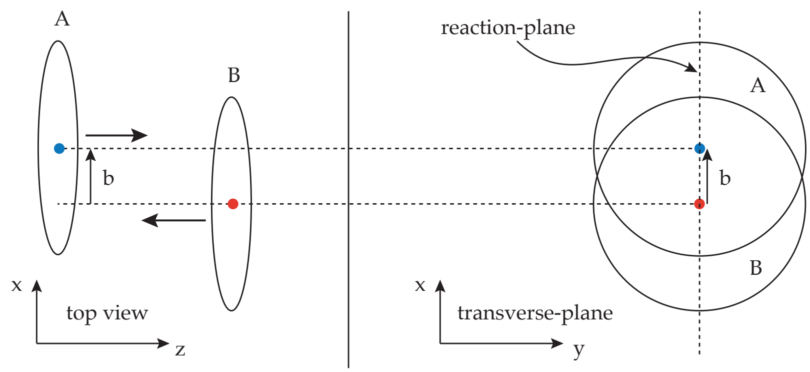

Figure 9: Schematic picture of the orientation of two nuclei in the reference frame (adapted from [135]).

corrected by unfolding and deblurring methods [128]. The goal is to extract novel information associated with the orientation of the reaction plane, which is generally averaged over the azimuthal angle. This can be a detailed measurement of the coalescence parameter B_A or the apparent temperature and velocity profile of the final particle emission beyond existing measurements at mid-rapidity [129, 130].

Higher order flow harmonics At low energies (SIS18), higher flow coefficients with respect to the reaction plane have so far not been studied. There are indications that in the FOPI data a significant v_3 and v_4 for protons and in particular for fragments (deuterons) can be observed. However, this has never been published [131]. The upper limits on the higher flow coefficients were determined by E877 at the AGS [132] with an absolute accuracy of approximately 10% consistent with zero for v_3 [133] and at most 2% for v_4 [134].

Collision Geometry

For the general interpretation of flow phenomena, an understanding of the geometrical aspects of the collisions is essential. The collision between two nuclei is characterised by the transverse distance between their centres (*impact parameter*) and their angular orientation (*reaction plane*) in the direction of the impact.

Reaction Plane The orientation of the collision system, defined by the plane spanned by the beam axis $\vec{z}$ and the direction of the impact parameter $\vec{b}$ of the colliding nuclei, is called *reaction plane* RP with its azimuthal angle Ψ_{RP} [126, 136–138]. In theoretical simulations, its orientation is per definition aligned with the reference frame, *i.e.* $\Psi_{\mathrm{RP}} = 0$, whereas in the experiment, the orientation of Ψ_{RP} with respect to the laboratory frame is distributed uniformly. However, since the orientation of the colliding nuclei is not accessible experimentally before the impact, the azimuthal angle of the *reaction plane* can not be measured directly. Early-on, in the first flow measurements [100, 103, 139] it was found that the events become *self-analysing* [111] if the orientation of the reaction system is determined by the anisotropic flow itself. Since then, it has been common practice for the analysis of the azimuthal particle distribution to use a relative orientation that maximises the event-by-event averaged values of the flow coefficients v_n, called the *event plane* EP [104]. The relative azimuthal angle of a particle is either given with respect to the orientation of the measured event plane $\phi = \phi_{lab} - \Psi_{\mathrm{EP}}$ or the reaction plane $\phi = \varphi - \Psi_{\mathrm{RP}}$. Owing to the finite multiplicity of collision products and their fluctuations, the estimated *event plane* has a dispersion in relation to the true *reaction plane*. Additionally, systematic effects such as finite granularity, occupancy, and efficiency of the detector setup further degrade the measured angular correlations and increase the internal dispersion. Depending on this dispersion, also called the *event plane resolution*, the values of the flow coefficients measured relative to this plane decrease and have to be corrected.

Centrality Experimentally, heavy-ion collisions are quantified by the measurement of their *total reaction cross section* and have been studied systematically for both theory and experiment, and several empirical parameterisations have been developed. In a geometrical picture, where two colliding nuclei are considered as black disks, one can assume that because of the short range of the strong force and neglecting electromagnetic interactions, the nuclei will interact when their sharp edges touch. This *reaction cross section* corresponds to the *geometrical cross section*:

$$\sigma_{geom} = \pi(R_{proj} + R_{targ})^2 = \pi b_c^2 \tag{3}$$

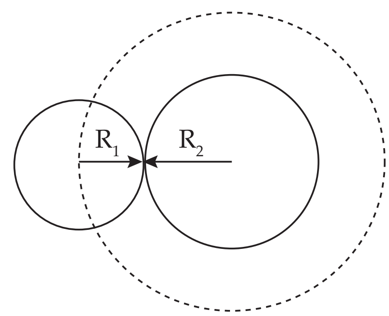

Figure 10: Definition of the geometrical cross section (adapted from [112]).

where b_c is the maximal critical impact parameter inside which nuclear reactions will occur with high probability (see fig. 10). This parameterisation is also referred to as *sharp cut* using the relation between the nuclear radius R and the mass number A, parametrised as $R = r_0 A^{1/3}$:

$$\sigma_{geom} = \pi r_0^2 (A_{proj}^{1/3} + A_{targ}^{1/3})^2 \tag{4}$$

with a radius parameter around $r_0 = 1.15 - 1.27$ fm. The centrality c is defined as the fraction of the total nucleus-nucleus cross section

$$\sigma_{AA} = \int_0^\infty \frac{d\sigma}{db'} \, db', \tag{5}$$

and is directly related to the impact parameter

$$c = \frac{1}{\sigma_{AA}} \int_0^b \frac{d\sigma}{db'} \, db', \tag{6}$$

with the differential cross section $d\sigma/db$. This requires a precise determination of σ_{AA} and a good understanding of the relation between b and the measurable observables, like the event track or hit multiplicity N, such that the events can be sorted according to the corresponding fraction of the total cross section

$$c \approx \frac{1}{\sigma_{AA}} \int_{N^{\rm thr}}^{\infty} \frac{d\sigma}{dN'}\, dN', \tag{7}$$

where $N^{\rm thr}$ is the lower multiplicity threshold of a given centrality. A crucial concept is the one of *participants* and *spectators*, first proposed to describe the fragmentation process within the *abrasion and ablation model* by Swiatecki et al. (1973) [140, 141]. It pictured nuclear collision as a sequential process. The two nuclei, which pass each other closely, cut off an overlapping volume during the *abrasion* process. The scraped-off volume is proportional to the number of participating nucleons, and the remaining spectator nucleons outside the overlap region did not experience any violent interaction. Within the Glauber model approach [135] colliding nuclei are assumed to move in straight-line trajectories, such that only their geometrically overlapping parts interact and what remains are the *spectators*. Figure 11 shows an example of the spatial configuration of two colliding nuclei obtained using the Glauber MC model approach [142, 143]. To apply the Glauber MC model to the relatively low centre-of-mass energies of the heavy-ion collisions under consideration, several adjustments had to be performed [144].

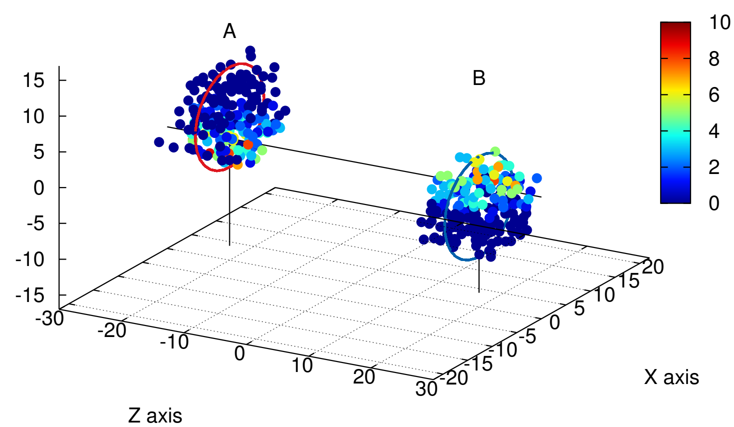

Figure 11: Spatial distribution of the nucleons before the collision of nuclei A and B as generated with the Glauber MC model with an impact parameter $b = 6$ fm. The beam direction is along the Z-axis. The color scheme encodes the number of inelastic collisions that a single nucleon experiences in this particular collision process. The size of the nucleons corresponds to the inelastic nucleon-nucleon cross section and the radii of the circles to the one of the gold nuclei.

The *total reaction cross section* can be calculated with the help of the Glauber MC model with the maximal geometrical cross section for the impact parameter range (b_{max}), corrected by the fraction of events with at least one nucleon-nucleon collision, to the total number of events:

$$\sigma_{tot} = \frac{N_{reaction}(N_{coll} \geq 1)}{N_{total}(N_{coll} \geq 0)} \times \pi b_{max}^2 \; , \tag{8}$$

The concept of *wounded-nucleon* by Bialas et al. [145] introduced the idea that the multiplicity distribution of produced particles in a nucleus-nucleus collision can be described as the incoherent superposition of the multiplicity distributions of each wounded nucleon, *i.e.* a nucleon which undergoes at least one inelastic collision. On the base of probability arguments the number of collisions (N_{coll}) and the number of wounded, or also called participating, nucleons (N_{part}) can be calculated. The correlation between the impact-parameter b, respectively N_{part}, and the obtained multiplicity distribution is used in the following to obtain centrality classes. By taking fractions of the total cross section, defined as centrality percentiles, the corresponding centrality classes with their averaged values for impact parameter $\langle b \rangle$ and $\langle N_{part} \rangle$ are determined.

In Fig. 12 the shape and orientation of the overlap region is characterised by the overlap area S, the participant eccentricity ε_{part} and plane angle ψ_{pp} using the spatial distribution of all participating nucleons. In [146] the observation of higher-order collective flow is described by the anisotropic and fluctuating shape of the overlap region. The approach to map *flow observables*, like elliptic or triangular flow, to their corresponding eccentricity of different order, calculated using Glauber MC approach, can reveal that the geometrical initial anisotropies might determine the observed flow pattern.

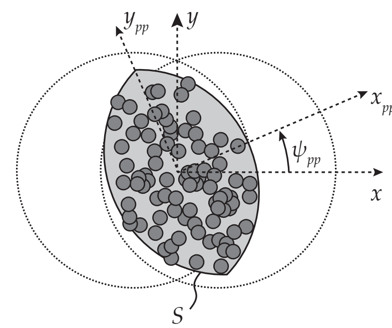

Figure 12: The overlap area S of the participating nucleons, the participant eccentricity ε_{part} and the plane angle ψ_{pp} as calculated using the Glauber MC approach.

Theoretical Models

There are two prominent theoretical model types for the description of the dynamics of heavy-ion collisions. Transport models describe the microscopic properties of nuclear matter via the free or effective in-medium cross sections and are extended to explain macroscopic properties via mean-field potentials. In hydrodynamic models the macroscopic equilibrium properties of nuclear matter are taken into account via the EOS. The microscopic dissipative and non-equilibrium effects are formulated in form of *quasi-macroscopic* transport coefficients, such as the *shear viscosity*, governing the hydrodynamic expansional evolution.

Microscopic Transport Models There are basically two different categories of kinetic transport codes, where the relativistic transport equations are solved numerically, either employing with test particles or using the molecular dynamics approach. The *Boltzmann-Uehling-Uhlenbeck*

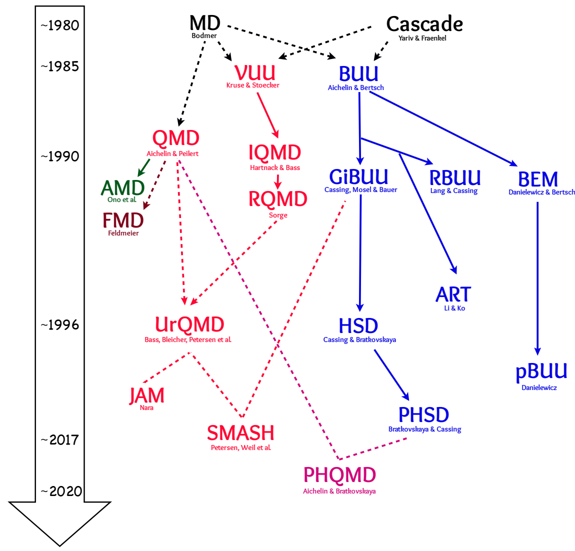

Figure 13: Development history of QMD and BUU transport models. The figure was adapted from the original by Steffen A. Bass with updates from Ref. [147].

(BUU) model is a density based approach, where the evolution of the one-body phase-space distribution follows the *Vlasov equation*, a relativistic mean-field theory of the Walecka type, in combination with a *Boltzmann collision term*, describing the dissipation effects. The *Quantum Molecular Dynamics* (QMD) model is an event based many-body approach, which simulates multi-particle collision dynamics. The QMD models incorporate directly event-by-event fluctuations, whereby BUU requires the inclusion of a stochastic part. The development history of several generation of QMD and BUU transport models is shown in Fig. 13 and for a detailed review of the different approaches used for transport simulations see [147, 148]. The systematic comparison of the measured data to different model predictions allows to constrain the parameter space of the models and to answer open questions in the model descriptions, which can not be resolved via first principles of the underling theory of strong interaction. For instance, the microscopic nucleon-nucleon collisions in the medium need to be treated in detail, where the effects of Pauli blocking, the formulation of effective particle masses, and the modifications of interaction cross-sections in a dense medium are important. In addition, the initial construction of realistic ground-state nuclei before collision must be constrained and the production and emission mechanism of hadrons, mesons and light nuclei from the expanding and thermalising medium. Various approaches are used to formulate mean-field potentials in microscopic transport simulations [149, 150], where the collision dynamics are also influenced by other ingredients that have to be accurately determined. Usually, the potentials are parameterised by the incompressibility modulus K

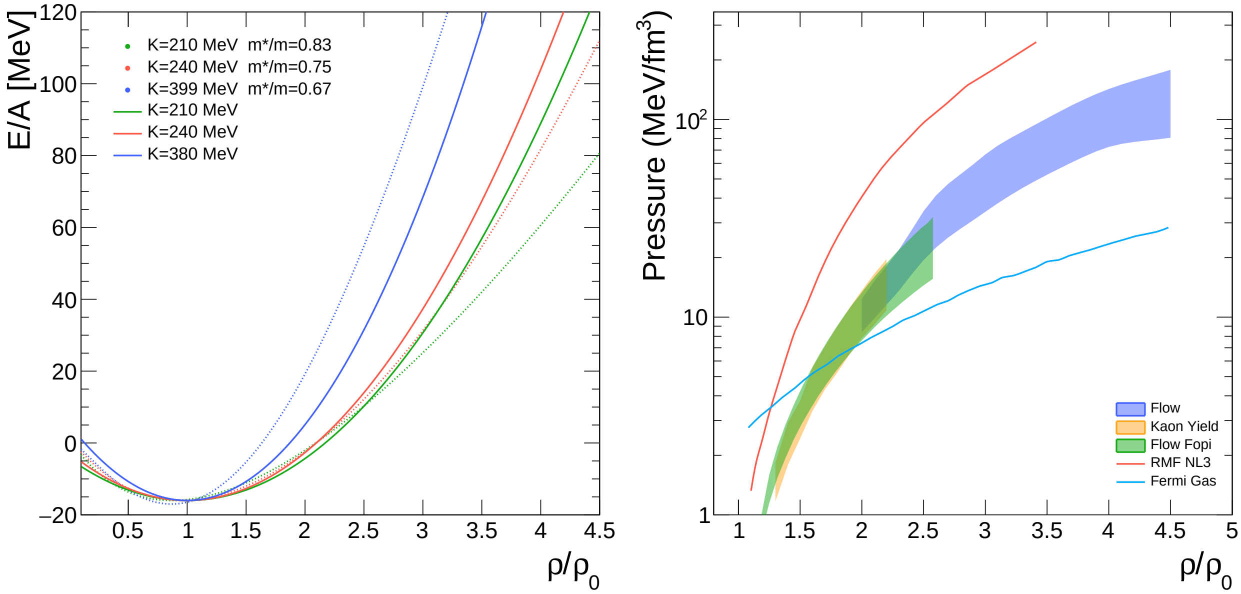

Figure 14: Left: Parameterisations of the ground state energy per nucleon are shown as function of nuclear matter density. The solid curves approximate the density dependence with a parabolic form [97, 151] and the dashed curves represent more realistic parametrizations, illustrating the effect of including the effective nucleon mass m^*/m. Right: The EOS of symmetric nuclear matter expressed as pressure versus baryon density, constraint from proton flow (blue area) [152, 153], from elliptic flow data of proton and light nuclei taken by FOPI (green area) [154], from Kaon data taken by KaoS (yellow area) [155, 156]. The EOS of a class of relativistic mean field model (red line) [157] and of a Fermi Gas (cyan line).

and the *Landau effective mass* at the Fermi surface $m^* = p_F/v_F$, both constrained at the normal nuclear matter density of $\rho_0 = 0.168$ fm^{-3} with a binding energy of $B = -16$ MeV. The left panel of Fig. 14 shows several parameterisations of the ground state energy per nucleon as a function of the nuclear matter density, where the solid curves follow a simple parabolic form [97, 151]:

$$E/A = \frac{1}{18} K \cdot (\rho/\rho_0 - 1)^2 + B \, , \tag{9}$$

with the $K(\rho_0) = 380$ MeV (hard) and 210 MeV (soft), and the dashed curvatures a more realistic parametrizations including the effective nucleon mass m^*/m. To determine the mean-field potential suitable for describing the measurements of collective flow several studies have been conducted. Mainly constraint by the integrated values of the directed and elliptic flow of proton and light nuclei as a function of beam energy [125, 152, 154, 158–162]. Although the importance of the momentum dependence of the EOS has long been known [163–169], constraints based on transverse momentum-differentiated flow data are scarce [170]. In the right panel in Fig. 14 the EOS of symmetric nuclear matter is expressed as pressure versus baryon density, with constraints based on transport model calculations in comparison to proton flow data (blue area) [152, 153], or to the elliptic flow data of proton and light nuclei taken by FOPI (green area) [154]. The estimate for the EOS from the Kaon data taken by KaoS [155, 156] is shown in yellow. In addition, two EOS, a class of relativistic mean field model RMF as a red line [157] and a Fermi Gas as a cyan line, are shown.

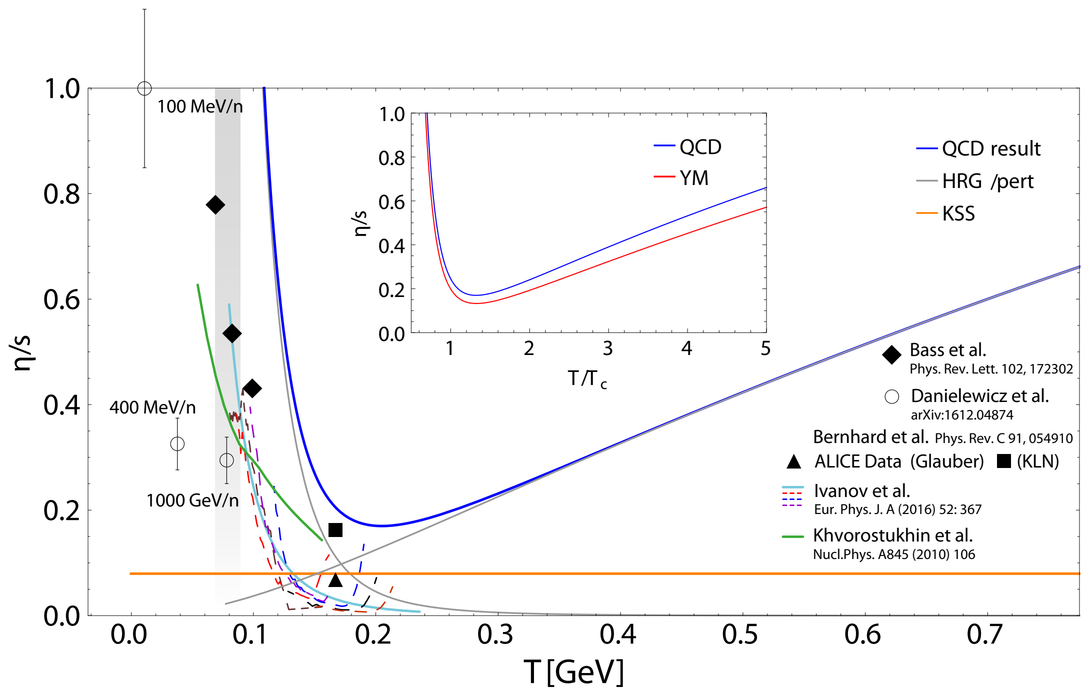

Figure 15: The estimated values for the ratio of the shear viscosity and the entropy density η/s as function of temperature is shown as predicted by several models [115, 175, 176]. The yellow line corresponds to the KSS boundary [177]. The non-perturbative FRG calculation (blue line) and Yang-Mills Theory results (red line) [178], the quasiparticle in a relativistic mean field model (green line) [179], and 3-Fluid simulation (dashed coloured lines) [180]. Figure adapted from the original in Ref. [178].

Macroscopic Description Based on the assumption of instantaneous local thermal equilibration, the dynamics of a macroscopic system can be treated based on conservation laws, leading to equations of motion for the density, local temperature, and flow velocity. In the case of *ideal fluid dynamics*, the only input is the equation of state, which results in an isentropic evolution of the system. In *viscous fluid dynamics*, local conditions away from perfect equilibrium are introduced by transport coefficients, describing the shear and bulk viscosity, as well as thermal conductivity. These can be determined by kinetic transport models [115, 171–175]. In the left panel of Fig. 15 the estimated values for the ratio of the shear viscosity and the entropy density η/s as function of temperature is shown as predicted by several models [115, 175, 176, 179, 180]. The yellow line corresponds to the conjecture from the AdS/CFT boundary of Kovtun, Son and Starinets (KSS) at $\eta/s = 1/4\pi$ [177]. The blue line shows the non-perturbative QCD calculation based on the Functional Renormalization Group (FRG), and the inset shows a comparison with the Yang-Mills theory results (red line) for temperatures normalised by the respective critical temperatures [178]. The green line represents the calculation based on quasiparticles in a relativistic mean field model [179] and the dashed coloured lines depict the trajectories from 3-Fluid simulation at different collision energies [180, 181]. The open circles are η/s values extracted by transport model calculation constrained by stopping data [115].

In *three-fluid dynamics*, the two colliding nuclei are treated as incoming fluids which stream into each other and create a third through the collision process. This requires additional coefficients to control the transport between the fluids, but has the advantage that the fluids can be treated in different equilibrium phases. All hydrodynamic approaches require a mechanism for *freeze-out*, where fluid elements are converted into individual particles, commonly with the Cooper-Frey prescription [182]. Determining whether baryon-dominated matter in the SIS energy regime exhibits hydrodynamic behaviour, or at least in its expanding phase before freeze-out, can be properly described by theoretical calculations within a hydrodynamic framework requires further investigation [183–187].

Outline of this Thesis

In the previous an overview over the topics of strongly interacting matter, the dynamics of heavy-ion collisions, and their geometrical properties, collective flow phenomena and the theoretical models are given. The HADES experiment, its detector setup, its physics program and the required design consideration are outlined in the next chapter.

In the analysis chapter the essential methods and corrections that are necessary to understand the data analysis are presented. The experimental conditions and the trigger settings during data taking are discussed in connection with the estimated trigger cross section, needed to evaluate the fraction of recorded most central reactions. The steps of event-characterisation and centrality determination used in the flow analysis are given in detail with special emphasis on the determination of the event plane and its resolution. Furthermore, the procedure of track reconstruction and particle identification is explained. The distortions due to occupancy effects in regions of high track densities and their corrections are discussed. Additionally, the bias from any non-uniformity of the detector is evaluated in combination with Toy Monte Carlo simulations. The chapter ends with a discussion of the systematic effects in the measurement of the flow coefficients and the description of the procedure used to estimate the systematic uncertainties in the context of the different bias. The experimental results of the multi-differential measurements and their discussion including various scaling properties, as well as the comparison to previous experimental data and transport model calculations are presented in following two chapters. In the final chapter, concluding remarks on the measurement of collective phenomena and an outlook are summarised.

HADES Experiment

HADES, the *High-Acceptance Dielectron Spectrometer*, is located at the SIS18 accelerator at the *GSI Helmholtzzentrum für Schwerionenforschung* facility in Darmstadt, and is currently the only experimental setup with the unique ability to measure rare and penetrating probes at the low-energy frontier of the QCD phase diagram. The main objective of the HADES experiment is to investigate the *emissivity of resonance matter* [188, 189] formed in heavy-ion collisions in the $1-2$ AGeV energy regime, the role of baryonic resonances in these reactions, and the mechanism of strangeness production. The physics program comprises experiments with elementary and heavy-ion reactions, and the combination with proton-, deuteron-, or pion-introduced reactions. The possibility of performing measurements with the same apparatus in a variety of reaction systems enables a broad and complementary way to explore the properties of strongly interacting matter in elementary exclusive channels, in cold nuclear matter, and in its dense and excited state.

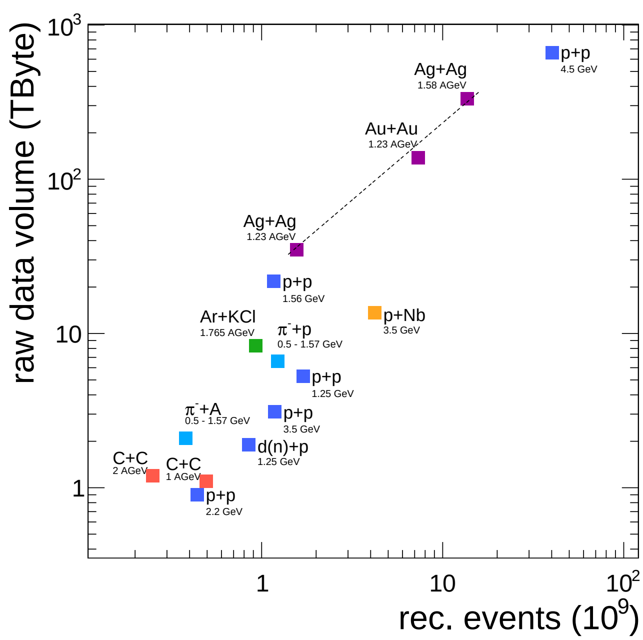

Figure 16: Compilation of all HADES production beam times. The total recorded data volume (TByte) is shown as function of the number of recorded events, with the values given in Tab. 3.

Between 2002 and 2022 various experiments with different collision systems at beam energies between $0.5 - 4.5$ GeV have been investigated by HADES. A compilation of the recorded number of events and their total data volume is shown in Fig. 16 and given in Tab. 3. The experiments until 2008 were recorded with a dedicated trigger on the di-lepton signal, reducing the data rate, to cope with the limited bandwidth of the readout. Since the overhaul of the data-acquisition system all experiments from 2012 on were recorded with a general event multiplicity trigger.

Table 3: Experiments with different collision systems and beam energies conducted with the HADES spectrometer with the number of events and the data volume recorded.

Year	System	Energy [AGeV]	rec. [10^9]	data [Tbyte]	Reference
2002	C+C	2	0.25	1.2	[190]
2004	p+p	2.2	0.44	0.9	
2004	C+C	1	0.495	1.1	[191]
2005	Ar+KCl	1.765	0.925	8.3	[192]
2006	d(n)+p	1.25	0.85	1.9	[191]
2007	p+p	1.25	1.70	5.3	
2007	p+p	3.5	1.18	3.1	[193]
2008	p+Nb	3.5	4.21	13.6	[194]
2012	Au+Au	1.23	7.31	138	[195]
2014	π^-+A	$0.5 - 1.57$	0.38	2.1	[196]
2014	π^-+p	$0.5 - 1.57$	1.23	6.6	[196]
2019	Ag+Ag	1.58	13.64	333.6	[197]
2019	Ag+Ag	1.23	1.56	34.8	[197]
2022	p+p	4.5	40.2	662	
2022	p+p	1.58	1.17	21.8	

The first runs with carbon-carbon reactions at 1 and 2 AGeV [190, 191, 198] were performed to confirm, with better acceptance and statistics, the measurements of the DLS (DiLeptonen Spektrometer) collaboration [199] at Bevalac, which showed an enhancement of low-mass dileptons in heavy-ion reactions. In 2006 and 2007 the experiments with p+p & d(n)+p collisions at 1.25 GeV were conducted, which allowed to draw conclusions on the origin of virtual photons in elementary and light collision systems, *i.e.* C+C. With the p+Nb reactions, measured in 2008, and the elementary reference p+p at 3.5 GeV measured in 2007 the properties of cold nuclear matter at saturation density could be studied [193, 194]. In 2005 the medium sized system Ar+KCl [192] was measured. After the updates of several detector systems and an overhaul of the data-acquisition system in 2012 an important milestone was achieved by the measurement of the large size system gold-gold [195] with 7.3 billion events accumulated over 5 weeks of beam time. A measurement of pion induced reactions in the momentum region $0.612 - 1.7$ GeV/c and using tungsten (^{74}W), carbon (^{12}C) and polyethylene (CH_2) as target was accomplished in 2014. The next medium sized system silver-silver was measured in 2019 at the two beam energies of 1.23 and 1.58 AGeV and in 2022 p+p collisions at 1.58 and 4.5 GeV.

The hexagonal structure of the HADES spectrometer in the 6 m high frame is sketched in Fig. 17 and a cross section through the mid-plane of one sector is shown in Fig. 18. As beam detectors two *diamond counters* are mounted directly in front of and behind the segmented target (START-Target-VETO). Together with the *Multiplicity and Trigger Array* META, consisting of two time-of-flight walls placed in the region behind the tracking system, they provide the trigger information for the *Central Trigger System* CTS. At larger polar angles, between 44° and 88°, the scintillating *time-of-flight wall* TOF is positioned and the forward region, between 18° and 45°, is instrumented with *Resistive Plate Chambers* RPC, a gaseous parallel plate avalanche detector, which replaced the TOFino detector in 2008. The particle trajectories are derived from the hit positions of the *Mini-Drift Chambers* MDC, with two chambers per sector in front of and two behind the toroidal magnetic field of the *superconducting magnet coils* ILSE. For the identification of electrons and positrons there are two dedicated detectors. One is the hadron-blind gas *Ring Imaging Cherenkov detector* RICH, operating in a region nearly

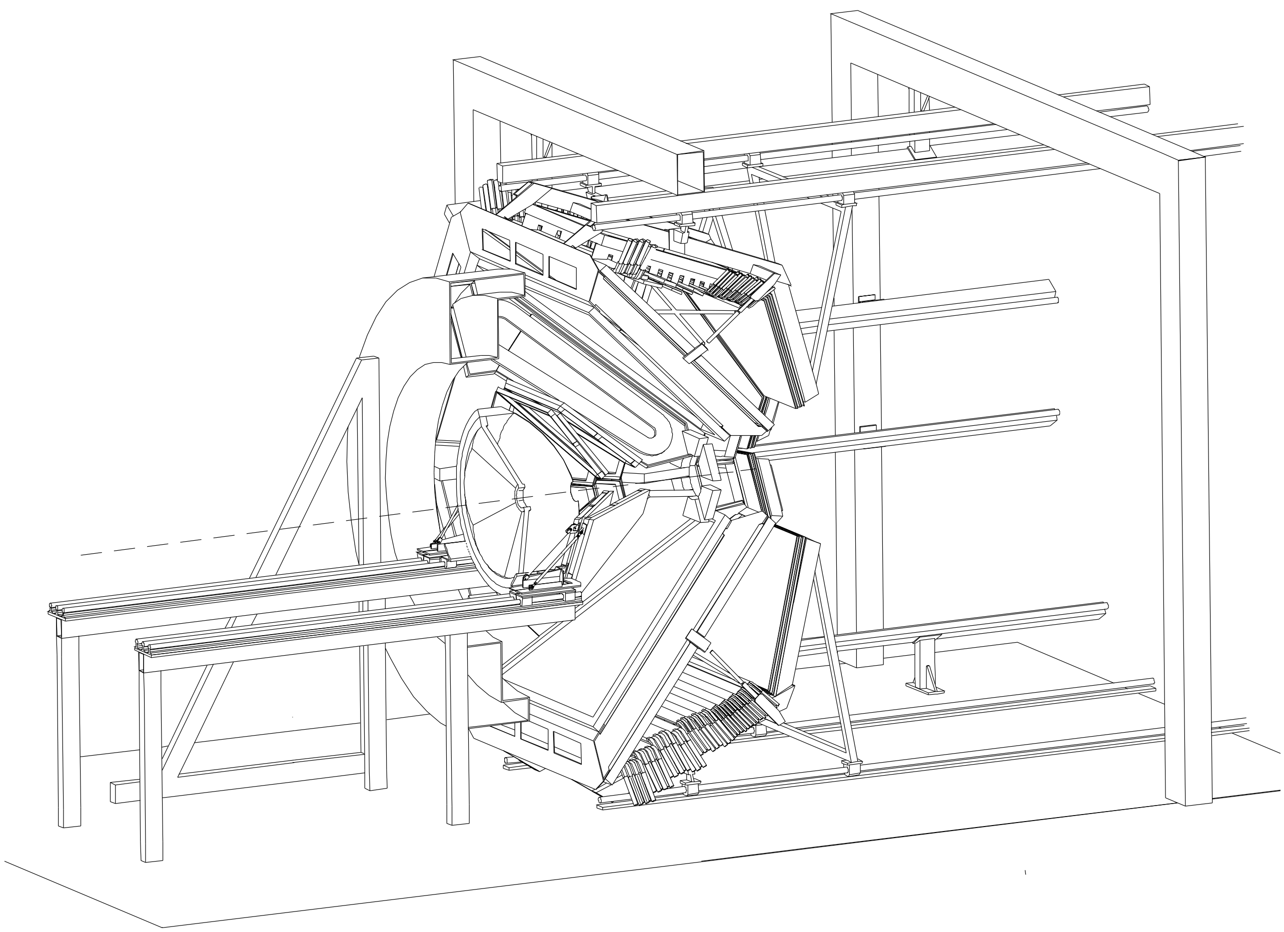

Figure 17: HADES experimental setup with the frame where individual sectors can be moved out for maintenance. The dashed line represents the axis of the incoming beam. Figure is adapted from [200].

free of the magnetic field, surrounding the segmented target, and the other, the `PreShower` detector at the end of each sector utilising the electromagnetic shower of leptons. The *Forward Wall* `FW` is placed at a distance of 6.8 m behind the target covering forward angles between 0.3° and 7°.

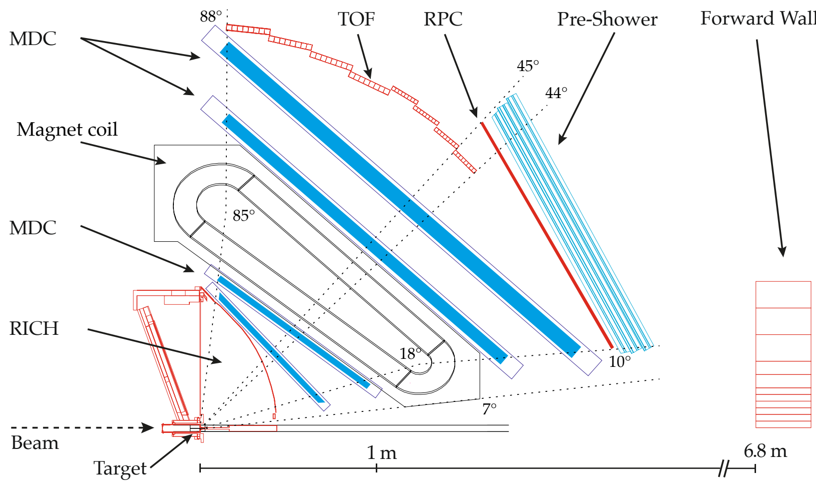

Figure 18: Cross section of one HADES sector. The segmented target irradiated by the beam, which is fully surrounded by the RICH detector. The magnet spectrometer consists of four layers of drift chambers (MDC), each two in front of and behind the toroidal magnetic field. At the end of the apparatus the *time-of-flight wall* TOF and the *Resistive Plate Chambers* RPC, followed by the electromagnetic pre-shower detector, are placed. The TOF detector covers the geometrical polar angel between 44° and 88°, the RPC 10° and 45°, with an overlap of 1°. The maximal acceptance in polar angle for charged particles corresponds to 18° − 85°.

The HADES setup is a general purpose fixed-target detector with the particular design goal of performing precise measurement of the light vector mesons ρ and ω in their leptonic decay channel. The measurement of this rare electron-positron pairs inside a huge hadronic environment, which exceeds the di-electron signal by many orders of magnitude, puts specific constraints on the apparatus [201–203]:

- *Geometrical and kinematic acceptance*: To increase the statistics of di-electron pairs the acceptance has to be as large as possible. This requirement is realised by an geometric acceptance within the polar angles of 18° and 85° and an almost full coverage in azimuthal angle. The region between the sectors, blocked by the magnet coils, is designed to be as small as possible and amounts to 17% at maximum. In the energy regime of $1-2$ GeV around $\sim 40\%$ of the di-electron with large opening angles from low mass vector mesons can be detected.

- *Momentum resolution*: A sufficient mass resolution in the invariant mass region of light vector mesons with $\Delta m/m \approx 1$ % is required. The required momentum resolution of 1% is achieved with a spatial resolution in the `MDC` of $35-50$ μm in polar direction and $85-125$ μm in azimuthal direction.

- *Material budget*: To reduce the probability of photon conversion into di-electron pairs, the components around the target region consist of low-Z materials. Furthermore, a reduction in multiple scattering is achieved with a low radiation length X/X_0 of approximately 0.5% between the first and last MDC, where 0.3% is the contribution from the air between the chambers.

- *Rate capability*: To collect large statistics the fast detectors allow the operation at beam intensities of up to 10^8 Hz in elementary reactions. All detectors can be read out with rates of $10 - 50$ kHz depending on the particle multiplicity [204].

- *High granularity*: The ability to efficiently detect individual charged particles in a high-multiplicity environment constrains the size of the detector elements in relation to the anticipated track densities.

- *Particle identification*: To provide a clean di-electron sample by rejecting the hadronic background several identification techniques and two dedicated sub-detectors (RICH and PreShower/ECAL) are used.

- *Event characterisation*: The information from fast detectors are used in the decision to trigger and record specific events and further estimate the reaction cross sections. Further general event information are used to classify different events.

Before describing in the following sections the exact experimental setup during the Au+Au beam time in 2012, we shortly summarise the various replacements and updates of detector systems since then. To further improve the capability of particle identification and to also include photon detection, the PreShower detector was replaced by an *Electromagnetic Calorimeter* ECAL, which was used for the first time in the silver-silver beam time in 2019 [205]. The total active area of the ECAL amounts to around 8.3 m^2 with a total weight of about 15 tons [206]. The calorimeter consists of 978 individual lead-glass modules, recycled from the OPAL End-Cap calorimeter at CERN [207] and equipped with a new readout. The ECAL is utilising the fast signal of the Cherenkov radiation produced by charged particles in the lead-glass, which are part of the *electromagnetic shower* produced by high-energetic electrons and photons [144]. The *RICH detector* was upgraded by the replacement of the existing photosensitive CsI cathodes and multi-wire proportional chambers MWPC, with arrays of multi-anode photo multipliers MAPMT. The new MAPMTs significantly enhance the electron-identification efficiency and will be used further for the RICH detector of the CBM experiment [208]. In preparation for future runs with higher beam intensities at the SIS18 and SIS100 accelerator the drift chambers are being upgraded. To prevent aging effects in the drift chambers the drift gas in the outer chambers was changed in 2019 from Ar/iso-Butane to Ar/CO_2 and to the counting gas of the inner chambers a fraction of 0.1% water (H_2O) was added. To improve the performance of the front-end electronics and to increase the bandwidth of data taking, an upgrade of the front-end electronics is in progress [209, 210]. For beam monitoring and reaction time T_0 measurements the diamond detectors with a thin layer of metallisation based on the chemical vapour deposition technique, were used until 2019. They are replaced with fast silicon detectors, based on the *Low Gain Avalanche Diodes* LGAD technology, which combines an excellent position measurements and a fast signal response with a high radiation hardness [205, 211].

Schwerionen-Synchrotron SIS18

The accelerator complex, consisting of the *Universal Linear Accelerator* UNILAC and the heavy ion synchrotron - *Schwerionen-Synchrotron 18* SIS18, located at the *GSI* facility (Helmholtzzentrum für Schwerionenforschung), provides the beams for the HADES experiment.

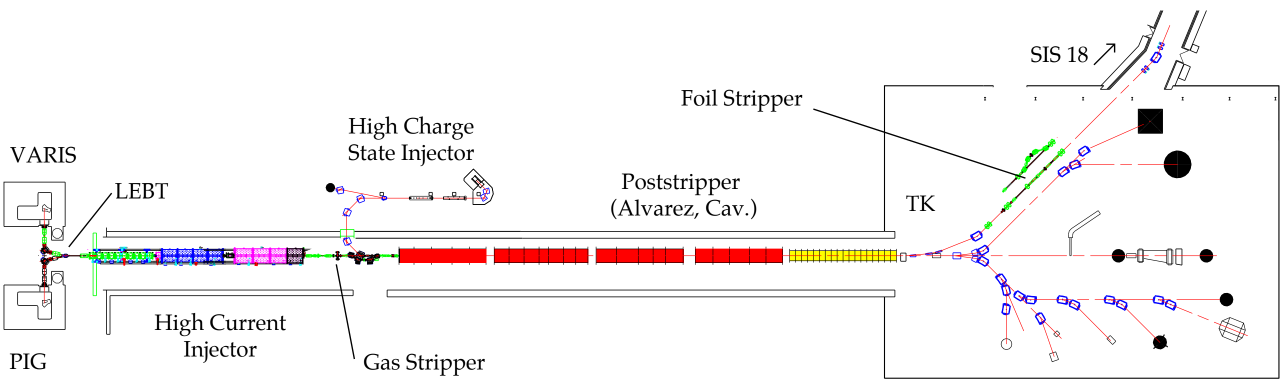

Figure 19: UNILAC: The ion source (VARIS), the Low Energy Beam Transport system (LEBT), High Current Injector with 4 Stages (RFQ, Super Lens, HI1, HI2), Gas Stripper, 4 Stages of Alvarez linear accelerators and the 150 m long Transport-Kanal (TK) to the SIS18. Image adapted from [212].

The UNILAC, with the versatility to accelerate ions over a wide range of masses and charge states from protons to Uranium, is in operation since 1975. Its purpose is to extract ions from a source and to pre-accelerate and inject them into the synchrotron. The *Vacuum ARc Ion Source* VARIS is a high intensity ion source, used for the first time in 2012, with currents up to 6 mA [213]. A vacuum arc discharge is generating a plasma from a gold-chromium alloy (mixture of ^{197}Au with 50% ^{24}Cr) [214]. The different charge states of gold and chromium ions in the plasma are separated within a mass spectrometer in the *Low Energy Beam Transport system* LEBT, and only the charge-state Au^{4+} is further transported to the *High Current Injector* with a kinetic energy of 2.2 AkeV. The ions are accelerated to an maximum energy of 1.4 AMeV and stripped from further electrons in the gas stripper by a supersonic gas jet. The kinetic energy of the ion beam can reach up to 11.4 AMeV after the Alvarez linear accelerator. The ions can be sent to the experimental hall or transported in a 150 m long *Transport-Kanal* (TK - transport channel) with a foil stripper to be injected into the SIS18. The maximum magnetic rigidity of the synchrotron is 18 Tm and the maximally reachable kinetic energy depends on the mass-to-charge ratio of the ion beam and is around 1 *A*GeV for U^{73+}, 1.25 AGeV for Au^{69+} and 4.5 GeV for protons. The SIS18, with the circumference of 216.72 m, is divided into 12 identical sections, each equipped with two 1.8 T dipoles for beam bending, one quadrupole triplet and one sextupole for beam focusing. The acceleration of the ions is realized in two ferrite cavities on opposite sides of the ring. Each ion experiences there a voltage drop of 16 kV in a frequency range of $0.8 - 5.6$ MHz. The full process of the ion acceleration in the *fast ramping* mode and the slow extraction of the beam results in 10 s long spills.

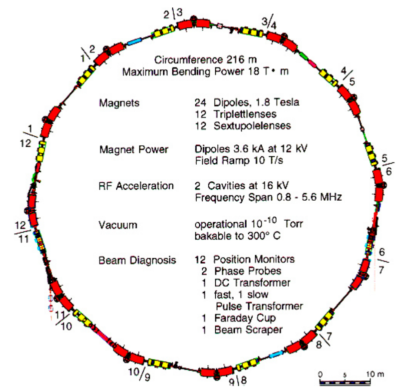

Figure 20: SIS18: 12 identical sections each with two 1.8 T dipoles (red) and one quadrupole triplet and one sextupole (yellow). Two ferrite cavities (blue) on opposite sides of the ring.

Segmented Target

The target, shown in Fig. 21, is a 15-fold segmented gold target, with each of the 25 μm thick gold plates glued on to a kapton strip with a thickness of 7 μm and a hole at the area of the target disk [216]. The kapton stripes are mounted on a 54.5 mm long carbon fibre tube with an inner diameter of 20 mm and a wall thickness of 0.5 mm. The low Z of the carbon target holder tube and the kapton stripes together with the arrangement of the segmented gold targets at distances of 4 mm ensures that the photon conversion probability in the target region is as low as possible. The total thickness of the target is 0.375 mm and corresponds to an overall interaction probability of 1.5%.

Figure 21: 15 gold foils placed on kapton strips and mounted on the target holder tube. [215]

Magnetic Spectrometer

The Magnetic Spectrometer consists of a toroidal field provided by six superconducting coils and in total 24 low-mass multi-wire chambers with mini-drift cells MDC. In each of the six sectors, there are two planes of MDC in front and two planes behind the magnetic field in order to reconstruct inner and outer *tracklets*, see Fig. 22, which are combined to reconstruct the trajectories of charged particles. The momentum reconstruction is carried out by the iterative solution of the equation-of-motion with the *Runge-Kutta* method in the known local magnetic field. The particle polarity from the bending direction relative to the magnetic field. Furthermore, a large momentum range of $p = 0.1 - 2$ GeV/c must be accepted over a large solid angle. The purpose of the magnet is to provide a transverse kick to charged particles in order to obtain their momenta with sufficiently high precision of the order of $\sigma_p/p \approx 2\%$ for 0.15 GeV/c electrons and 4% for 1 GeV/c protons.

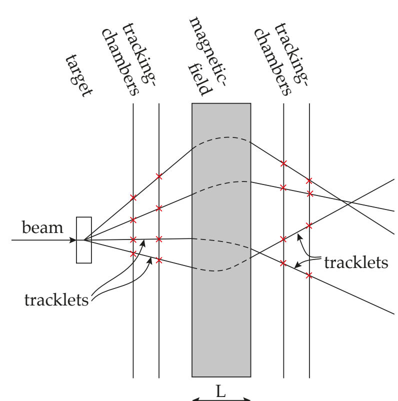

Figure 22: Principle of a magnetic spectrometer

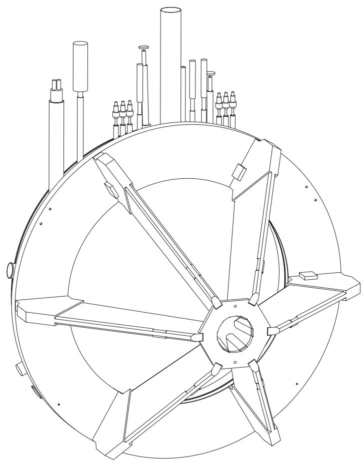

Figure 23: The superconducting magnet consisting of six coils, surrounding the beam axis, and a circular support structure. On the upper part the power and gas supplies are connected.

Superconducting magnet

The superconducting toroidal magnet ILSE [217], shown in figure 23, consists of six superconducting coils surrounding the beam axis and produces a toroidal field which bends the particles in first approximation only in the polar direction. With a maximum current of $I = 3500$ A, the magnetic field strength inside the coils corresponds to 3.5 T, falls to a maximum of 3 T at the borders of a sector and reaches values around 0.9 T in center of a sector. This field configuration results in an additional deflection in the azimuthal direction, causing a focusing effect. The superconducting material in the coils consists of a niobium-titanium alloy enclosed in a copper matrix, where the copper is needed for mechanical stability. In the case that the superconductivity is lost, a so-called *quench*, it will also drain away the large currents. The copper and niobium-titanium matrix, twisted into wires, is also inclosed again in aluminium to ensure that a sudden drop of the magnetic field will not damage the coils [217]. The coils are surrounded by a shield cooled by liquid nitrogen at 85 K and the current leads are cooled with single phase He at 2.8 bar and 4.7 K.

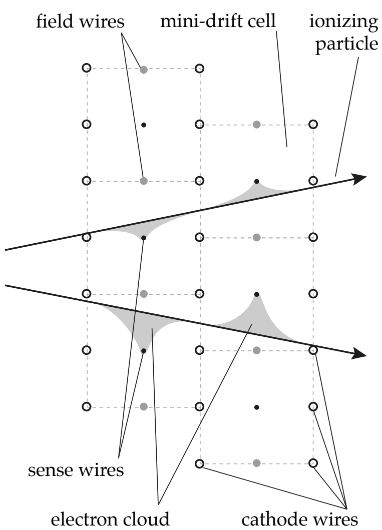

Figure 24: Sketch of a trajectory of two ionizing particles reconstructed inside the MDC drift cells via the drift time of the electron cloud collected at the sense wires.

MDC Chamber

The active area for the inner chambers is $0.35\,\mathrm{m}^2$ and for the outer chambers $3.21\,\mathrm{m}^2$. The smallest sensitive unit of the multi-wire drift chamber is the *mini-drift cell* MDC which consists of one plane with one sense wire in the center of the cell and potential wires on both sides. This plane is enclosed by planes of cathode wires, see Fig. 24. The cathode and potential wires are made from annealed aluminium with 80 and 100 μm diameter and the sense wires from gold-plated tungsten with a diameter of 20 and 30 μm. Each chamber contains about 1100 of these elongated mini-drift cells organised in six layers with five different orientation angles with respect to each other (0°, ±20°, ±40°), so-called *stereo angles*. This pattern ensures a homogeneous spatial resolution of $85 - 125$ μm with respect to the azimuthal angle and enhances the spatial resolution in polar angle direction to $35 - 50\,\mu$m, which is oriented in the direction of the momentum kick [218, 219]. The most inner chamber plane MDCI was filled with Ar/CO_2 (70 : 30) as counting gas and the three other planes with Ar/iso-Butane (84 : 16). Charged particles flying through the chamber ionize the gas and the released electrons are drifting to the sense wires, producing an avalanche around the sense wires via secondary ionisation. The collected charge pulse is amplified, shaped and discriminated by a dedicated ASIC (ASD8-B). This chip provides additionally the *time-over-threshold* (ToT) of each hit. These signals are routed to TDCs and are transmitted to the general read-out system by optical fibers [204].

Diamond START- and VETO-counter

The beam detectors `START` and `VETO` are used to monitor the beam quality and luminosity. In coincidence with the multiplicity trigger, the `START` detector provides a signal for event triggering and high-precision start time T_0. In combination with *time-of-flight walls* `TOF`, `RPC`, and `FW`, it is used for time-of-flight determination. The `VETO` detector was conceptually designed to reject non-central peripheral reactions at the event triggering level. However, its signal is used in the offline analysis to suppress pile-up events, expected from non-interacting beam ions flying through the `VETO` detector shortly before or after the triggered event. The main properties of the detector are highly efficient charge collection and short signal collection time, together with a low interaction probability with beam ions because of the narrow thickness of $\sim$ 60 μm [220]. This is achieved with radiation hard diamond detectors with a thin metallisation coating based on the chemical vapour deposition (CVD) technique [221, 222]. The metallisation layer [223] of the mono-crystalline CVD diamond `START` detector consists of a 50 nm chromium layer on a 150 nm gold layer arranged in 16 stripes with a width of 200 μm and 90 μm gaps on each side of the diamond, providing an x-y position measurement (see Fig. 25). The `VETO` detector, located 70 cm downstream of the target and aligned along the beam line axis, is divided into eight individual readout segments.

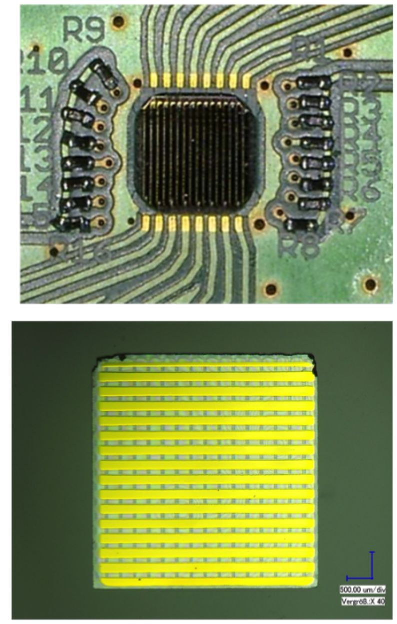

Figure 25: START diamond detector shown in the upper picture mounted on the circuit board. In the lower panel only the active area with the stripes for position measurement (4.39×4.39 mm^2) is shown [220].

Trigger system, Data acquisition and Slow control

The main goal of each trigger system is to efficiently use the available bandwidth of the data-acquisition system `DAQ` via a reduction in the read-out data size by a specific selection and enhancement of physically relevant events. The performance is mainly driven by the beam intensity and multiplicity per event, which can be very large in heavy-ion collisions compared to elementary reactions. Therefore, a multipurpose electronic device with on-board data acquisition, the *trigger and readout board* `TRB`, was developed [204]. It provides a general read-out and data transfer system, generates the trigger signal, and provides slow control access to the detectors. Communication and data transport in the network are realised using the TrbNet protocol. The *Central Trigger System* `CTS` is implemented on a dedicated AddOn board to the TRB, but can also be operated in a stand-alone mode. The accepted data packages from different sub-detectors are collected event-wise by event-builders and are written to mass storage in a binary raw event file format, *HADES List-mode Data* `HLD`. The *slow control* is based on the `EPICS`[1] control system, and includes hardware control, recording, and monitoring of all detector parameters during data collection.

[1] Experimental Physics and Industrial Control System

TOF Wall

The time of flight wall TOF [224, 225] consists in total of 384 scintillator rods, organised in each sector in eight modules with eight scintillator rods. The rods are made of polyvinyltoluene-based plastic scintillator *BC-408* from Bicron, which was chosen for its low light attenuation length, high scintillation light yield and short decay time. The rod cross section is 20×20 mm^2 for the innermost rods and 30×30 mm^2 for the outermost rods. By passing through the scintillating material a charged particle deposits energy and generates excited states in the material, which fall back to their ground state by light emission. The light travels with a specific group velocity v_g inside the rod to both ends, where it is read out by two photomultiplier tubes of type EMI 9133B and thus producing two arrival times and two signal amplitudes. From these information the hit position along the rod, the time-of-flight, after subtraction of the reaction time T_0, and the deposited energy E_{dep} can be calculated:

$$x = (t_{\mathrm{right}} - t_{\mathrm{left}})/2 \cdot v_g \,, \tag{10}$$

$$t = (t_{\mathrm{right}} + t_{\mathrm{left}})/2 - T_0 \,, \tag{11}$$

$$E_{\mathrm{dep}} = k e^{\,l/\lambda_{\mathrm{att}}} \cdot \sqrt{q_{\mathrm{right}}\, q_{\mathrm{left}}} \tag{12}$$

where t_{left}, t_{right}, q_{left} and q_{right} are the corrected times and amplitudes, λ_{att} the light attenuation length, l the rod length and k a normalization parameter, which translates the measured signal amplitudes into units of energy loss of a minimum ionizing particle (MIP). The intrinsic time resolution is 150 ps and the spacial precision of the hit position along a rod is around 25 mm.

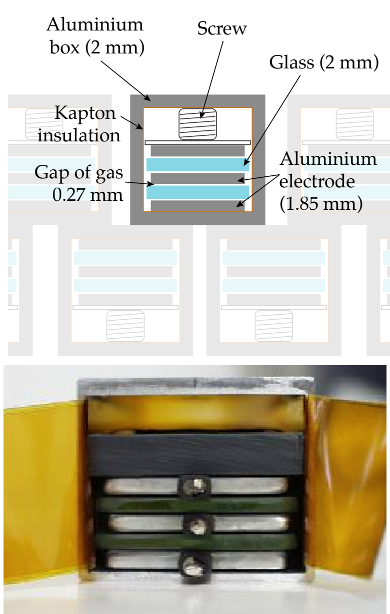

Figure 26: RPC cell with aluminum-electrodes, glass electrodes, plastic pressure plate, kapton insulation, aluminum-shielding tube. Figure taken from [228]

RPC Wall

The six *Resistive Plate Chamber* RPC detectors consist of two partially overlapping layers with three columns of 31 individually shielded RPC cells [226, 227]. Each RPC cell, shown in Fig. 26, consists of a shielding insulated with kapton, a plastic pressure screw and three stacked aluminum electrodes isolated with two glass plates in between. The cell is filled with an admixture of SF_6 and $C_2H_2F_4$ gas.

The electrodes are supplied with a high voltage of 5 kV, and in the case of a charged particle crossing the cell and ionizing the gas so that electrons are accelerated in the electric field towards the anode. This causes further ionization and creates an electron avalanche and thus a measurable electric signal, which can measured on both sides of the cell by dedicated front-end electronics. The achieved time resolution is 80 ps and the hit position has a spacial resolution of better than 8 mm.

Forward Wall

The Forward hodoscope Wall FW was installed in 2007 [229] and built from scintillators and photomultiplier tubes of the small-angle spectator hodoscope originally used in the Streamer Chamber experiment at Bevalac [230, 231] and later in the TAPS [232] and KaoS experiments [233]. It was successfully used in the d+p experiment [234] for tagging the spectator proton to select quasi-free n+p reactions at 1.25 GeV beam energy. The FW is positioned 6.8 m downstream of the target. In the area between HADES and the FW a helium-bag is installed to reduce multiple scattering of the spectators and also secondary interactions. The 288-element array covers an active area of $1.8 \times 1.8\ \mathrm{m}^2$, corresponding to an polar angular range of $0.3° < \theta < 7.3°$. The support structure of the magnet coils shadows a region from 7° upwards. To match the increasing spectator multiplicity at smaller angles the size of the detector cells varies according to the expected particle flux: a 8×8 cm beam hole in the centre, 140 small cells (4×4 cm) near the beam axis, 64 mid-size cells (8×8 cm) and 84 large cells (16×16 cm) on the border of the detector (see Fig. 27). The cells thickness is 2.54 cm (one inch) and consists of the plastic-scintillator BC408 [233]. This detector system provides information on the position, charge, and time of flight. The projectile spectators are identified by the energy deposition in the scintillator modules and by their time of flight. Protons with a velocity of $\beta = 0.9$ deposit an energy of ~ 5 MeV when they traverse the scintillator, whereby spectator fragments with larger charge Z have a Z^2-fold energy loss.

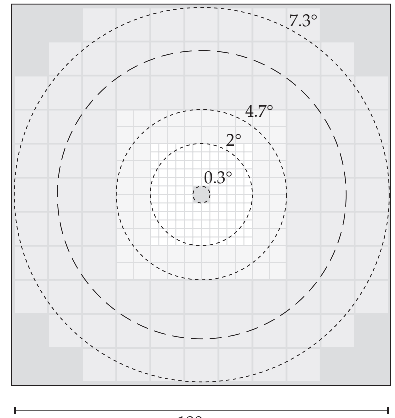

Figure 27: Forward hodoscope Wall

Electron and Hadron separation

The *Ring Imaging Cherenkov* RICH detector is a hadron-blind gas detector designed with together the second sub-detector PreShower for the identication of electrons and positrons. The RICH comprises a gas volume filled with the radiator gas perfluorobutane C_4F_{10}, where charged particles with high enough velocity emit *Cherenkov radiation*. The Cherenkov light cone is reflected by a low mass spherical mirror ($R = 872$ mm) trough a CaF_2 window of 5 mm thickness and is imaged as rings on the photon detector, shown in Fig. 28. In Fig. 29 a magnified part of one of the six multi-wire proportional chambers MWPC with photosensitive CsI cathodes is shown. The light cone has a characteristic emission angle depending on the velocity of the particle and the refractive index of the medium:

$$\cos\theta_c = 1\ /\ \beta n \tag{13}$$

with the condition $|\cos\theta_c| \leq 1$ the threshold velocity results [235]:

$$\beta_{\mathrm{th}} = 1/n\ ,\ \gamma_{\mathrm{th}} = n/\sqrt{n^2-1}\ . \tag{14}$$

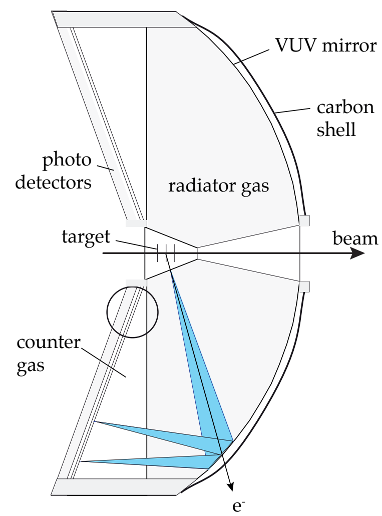

Figure 28: Schematic cross section of the RICH detector. The light cone (blue) emitted by an electron is reflected by a spherical mirror onto the photon detector at backward angles.

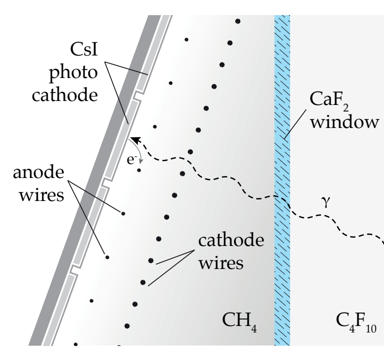

Figure 29: Magnified view of the radiator gas C_4F_{10}, the CaF_2 window, the CH_4 counting gas, the MWPC wire and the photosensitive CsI cathodes.

λ	refractive index n	γ_{th}
145 nm	1.001734	17.0
210 nm	1.001468	18.5

Table 4: The refractive index for C_4F_{10} at 145 nm (absorption threshold) and 210 nm (detection limit of the photo detector) and the corresponding Cherenkov thresholds.

The chromatic dispersion of the refractive index $n(\lambda)$, its dependence on the photon wavelength, is given by the Sellmeier approximation [236, 237]:

$$(n(\lambda)-1)\cdot\ 10^{-6} = A/1/\lambda_0^2 - 1/(\lambda/nm)^2 \tag{15}$$

with $A = 0.2375$ and $\lambda_0 = 73.63$ for perfluorobutane. The values with the corresponding Cherenkov threshold are listed in table 4. The radiator gas is chosen such to maximize the transparency for UV photons down to $\lambda \geq 145$ nm with a minimum of scintillation. The optical parameters of the different RICH detector components relevant for the photon detection are shown in Fig. 4.

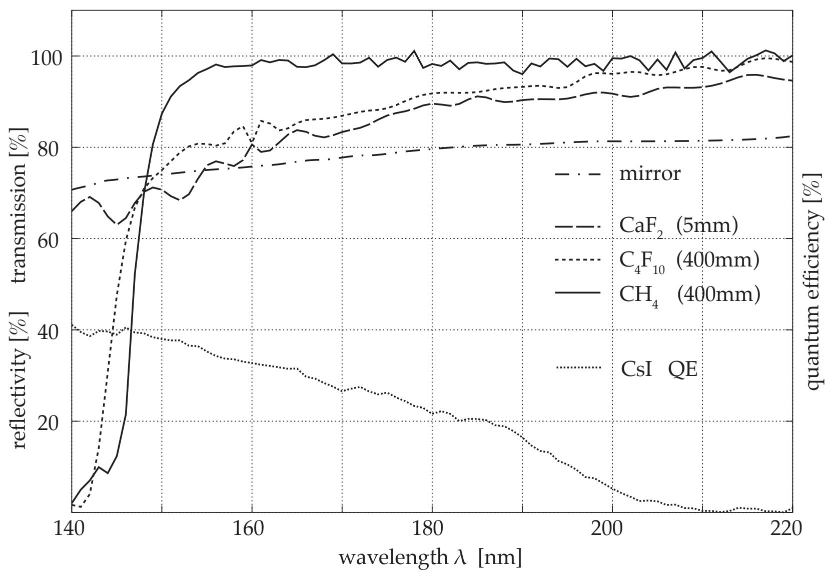

Figure 30: Optical parameters of the different RICH detector components: measured transmissions of the radiator gas C_4F_{10}, the counting gas CH_4, the CaF_2 window and the CsI photocathode quantum efficiency (Q.E.) [238] together with the mirror reflectivity as determined in 2001 [239].

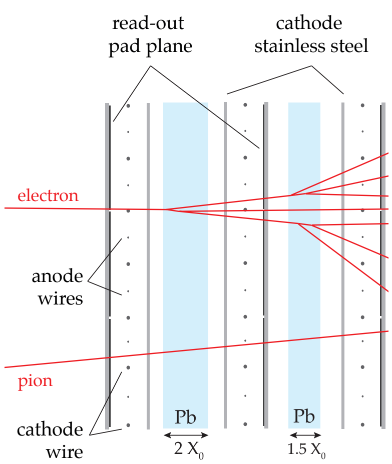

Figure 31: Cross section of a PreShower cell consisting of three wire chambers and two Pb converters. While leptons generate an electromagnetic shower, the effect is suppressed for hadrons.

The `PreShower` detector located behind the `RPC` uses the electromagnetic cascade of electrons for their detection. Each of the six sector modules consists of three trapezoidal wire chambers with 1024 readout pads. The pre-chamber and two post-chambers are separated by lead converter plates with lengths of 2 and 1.5 times the radiation length of lead ($X_0 = 0.56$ cm) [240]. A charged particle passing through the gas chambers is registered by measuring the induced charge on the cathode pads. In case that a particle develops an electromagnetic shower, the comparison of the integrated charges from the different layers would show an increase from chamber to chamber. The wire chambers are filled with an isobutane-based gas mixture and operated in the limited self-quenching streamer (SQS) mode, where the charge collection is rather proportional to the number of particles propagating throw the chamber than to their specific energy loss [241, 242].

Analysis Framework

The data analysis is realised within the HYDRA framework[2], developed for the on- and off-line processing of events recorded with the HADES setup. It is based on the ROOT class package [243] originally developed in 1995 for the NA49 heavy-ion experiment and which became a standard in high-energy experiments. The object-oriented design provides a flexible way to derive detector- or task-specific classes from a common set of base classes. The data input can be taken from several data sources, either during data-taking directly from the event builders, from recorded *HADES List-mode Data* HLD files or from processed *Data Summary Files* DST at various stages of analysis. The initialisation of geometry, the setup and calibration parameters are maintented in the HADES data base, implemented as ORACLE DB.

[2] *Hades sYstem for Data Reduction and Analysis*

Experimental and Simulated Data The are several sequential levels of the event processing chain. The binary data readout are decoded by the so-called *unpacker* and the signals are structured for each detector into corresponding HYDRA classes. After one or more calibration steps (*cal level*), the information of one or more signals are merged into individual *hit points*, when the impact of a particle in an active area could be reconstructed. The following core-process of the framework is the assembly of all relevant hit informations of the sub-detectors to reconstruct *particle candidates*. Additionally extracted physical informations are added, such as the momentum, polarity, track quality, matching quality and particle identification properties. For simulated events the output of an event-generator, either based on transport models or on statistical thermal models (PLUTO [244]), are processed by tracking the particles of each event through a simulated HADES detector using the HGeant package (based on Geant 3.21 [245]). The full geometry with material budget, the specific interaction cross sections with the material and an accurate magnetic field map are included. The detector response to the interaction of the detected particle is implemented in the *digitizers*, where a signal pattern is generated based on the detector response functions, mimicking the calibrated real detector readout. This information is filled into the *sim cal level*, corresponding to the *cal level* of the experimental data, but in addition also containing the information to retrieve the known properties from the event generator. From this stage on, the reconstruction of simulated data is treated in exactly the same way as the experimental data. The framework allows the overlay of simulated tracks onto real events for efficiency and performance investigations, a procedure which is called *embedding*.

Flow Analysis

It is the common convention [246, 247] to define the kinematics of a particle trajectory in a fixed-target experiment with its total momentum p, its inclination angle θ to the beam direction, where $\theta = 0°$ points along the beam direction, and its azimuthal angle in the transverse plane ϕ_{lab} as measured in the laboratory reference-frame. The longitudinal and transversal components of the momentum p are defined as follows:

$$p_z = p\cos\theta, \quad p_t = p\sin\theta \tag{16}$$

and the projections of the transverse momentum p_t respectively onto and perpendicular to the plane with the azimuthal angle ϕ as:

$$p_x = p_t\cos\phi, \quad p_y = p_t\sin\phi\ . \tag{17}$$

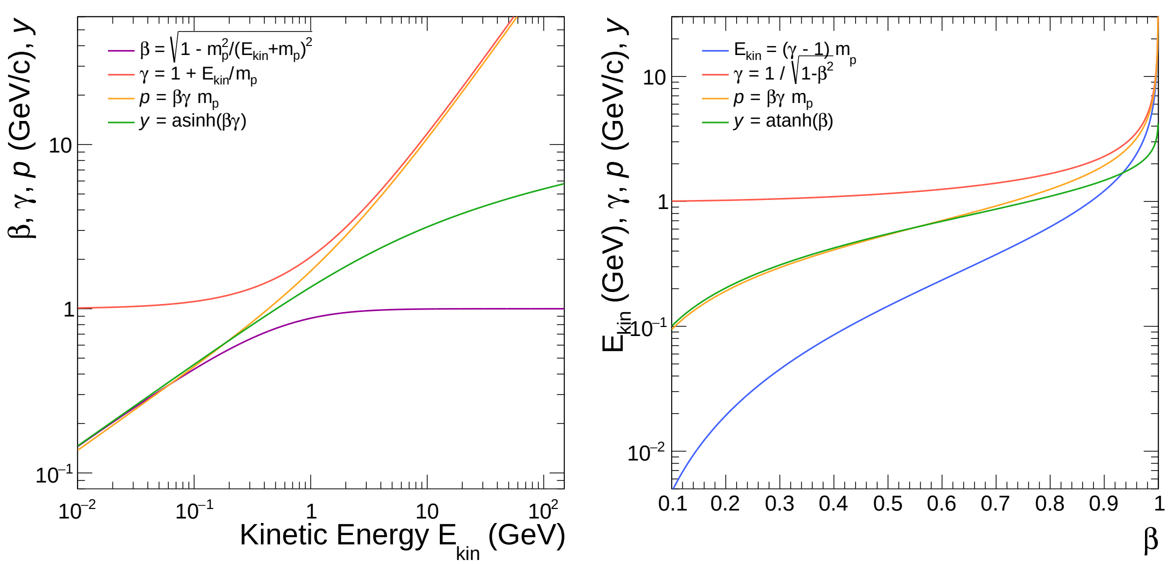

Figure 32: The relations between the kinetic energy E_{kin}, the relativistic velocity β, the Lorentz factor γ, the rapidity y and the momentum p of a particle with the proton mass m_p shown on the left as a function of its kinetic energy and on the right as a function of β.

In Fig. 32 the relationships between the relativistic velocity $\beta = v/c$, Lorentz factor γ, momentum $p = \beta\gamma m_0$, kinetic energy $E_{kin} = E - m_0$ and rapidity y of the particle are illustrated as a function of E_{kin} (left) and β (right). The total energy of the particle is $E^2 = p^2 + m_0^2$. It is convenient to use the relativistic measure of rapidity y instead of the velocity or longitudinal momentum of a particle because rapidity is an additive quantity, with the consequence that the differences in rapidity are invariant. The particle rapidity in the laboratory frame can be expressed as:

$$\begin{aligned} y &= \tanh^{-1}(p_z/E), \\ y &= \tanh^{-1}(\beta_z) = \cosh^{-1}(\gamma) = \sinh^{-1}(\gamma\beta_z)\,, \end{aligned} \tag{18}$$

and in the centre-of-mass system as $y_{\mathrm{cm}} = y - y_{\mathrm{proj}}/2$, with the projectile rapidity y_{proj}.

In the flow analysis, the collision events are characterised according to their centrality and angular orientation, with the measured event multiplicity and the *event plane* (see introduction of the geometrical aspects of the reaction). The triple differential distribution of the particle density in momentum space can be written in the form of a Fourier expansion with its dependence on the relative azimuthal angle ϕ [122, 126, 127, 136–138, 248]:

$$E\frac{d^3N}{dp^3} = \frac{1}{2\pi}\frac{d^2N}{p_{\mathrm{t}}\,dp_{\mathrm{t}}\,dy}\left(1 + 2\sum_{n=1}^{\infty} v_n(p_{\mathrm{t}},y)\cos(n\phi)\right)\,, \tag{19}$$

with $v_n(p_{\mathrm{t}},y)$ as the n^{th} cosine harmonic coefficient. The relative azimuthal angle of a particle is given with respect to the orientation of the measured event plane $\phi = \phi_{lab} - \Psi_{\mathrm{EP}}$ and owing to the finite multiplicity of collision products and their fluctuations, the estimated *event plane* has a dispersion in relation to the true *reaction plane*, which has to be corrected. By using the shorthand notations for the single-particle density

$$\begin{aligned} \varrho(p_t,y,\phi) &= E\frac{d^3N}{dp^3} = \frac{d^3N}{p_{\mathrm{t}}\,dp_{\mathrm{t}}\,dy\,d\phi} \\ \varrho(p_t,y) &= \int_0^{2\pi}\varrho(p_t,y,\phi)\,d\phi = \frac{d^2N}{p_{\mathrm{t}}\,dp_{\mathrm{t}}\,dy} \end{aligned} \tag{20}$$

it can be shown with the following expression:

$$v_n(p_t,y) = \frac{\int_0^{2\pi}\cos(n\phi)\;\varrho(p_t,y,\phi)\,d\phi}{\int_0^{2\pi}\varrho(p_t,y,\phi)\,d\phi} \tag{21}$$

and the orthogonality relations of cosine and sine functions that v_n is the expectation value of $\langle\cos(n\phi)\rangle$. The integral in the numerator yields $v_n \times \varrho(p_t,y)$ and the denominator $\varrho(p_t,y)$ [249]. The anisotropies in the azimuthal distribution can be directly quantified as the *azimuthal moments* by the flow coefficients:

$$v_n(p_{\mathrm{t}},y) = \langle\cos(n\phi)\rangle \tag{22}$$

when $\langle \cdots \rangle$ denotes the average over all particles of interest in a given p_t and y interval and all events of the same centrality class. The Fourier coefficients v_n can be expressed in terms of single-particle averages and together with Eq. (17) as their expansion:

$$v_1 = \langle \cos\phi \rangle = \langle p_x / p_t \rangle, \tag{23}$$
$$v_2 = \langle \cos(2\phi) \rangle = \langle (p_x^2 - p_y^2) / p_t^2 \rangle, \tag{24}$$
$$v_3 = \langle \cos(3\phi) \rangle = \langle (p_x^3 - 3p_x p_y^2) / p_t^3 \rangle, \tag{25}$$
$$v_4 = \langle \cos(4\phi) \rangle = \langle (p_x^4 - 6p_x^2 p_y^2 + p_y^4) / p_t^4 \rangle, \tag{26}$$
$$v_5 = \langle \cos(5\phi) \rangle = \langle (p_x^5 - 10p_x^3 p_y^2 + 5p_x p_y^4) / p_t^5 \rangle, \tag{27}$$
$$v_6 = \langle \cos(6\phi) \rangle = \langle (p_x^6 - 15p_x^4 p_y^2 + 15p_x^2 p_y^4 - p_y^6) / p_t^6 \rangle. \tag{28}$$

In general, the sine-terms of the Fourier series vanish due to the reflection symmetry with respect to the reaction plane:

$$\sin(n\phi) = -\sin(-n\phi) \quad \Rightarrow \quad \langle \sin(n\phi) \rangle = 0 \,. \tag{29}$$

Therefore, any violation likely indicates a measurement bias due to detector non-uniformity or a potential global polarisation in the particle spectra. To discuss the case that particles are not distributed symmetrically around the reaction plane, we quantify the Fourier coefficients of the sine-terms with $s_n(p_\mathrm{t}, y) = \langle \sin(n\phi) \rangle$. The following flow analysis procedure is based on the event plane method [137, 138, 248], where the flow coefficients up to the 8$^{\text{th}}$ order are measured relative to the first order event plane $\Psi_{\mathrm{EP},1}$, which is estimated from the forward-going projectile spectator fragments. Due to the limited statistical significance, only the results up to the 6$^{\text{th}}$ order are presented in the following chapter in detail and an upper limit for the absolute accuracy of the measurement of the 7$^{\text{th}}$ and 8$^{\text{th}}$ order is given.

Experimental data

Beam		
Ion		$^{197}_{79}\mathrm{Au}^{69+}$
Intensity		$1.2 - 2.2$ MHz
Energy	E_{kin}	1.23 AGeV
	$\sqrt{s_{NN}}$	2.4 GeV
Momentum	p/A	1.96 GeV/c
Rapidity	y	1.48
Beta	β	0.9
Lorentz fac.	γ	2.3

Table 5: Beam specifications.

First day	5.4.2012 – 22h
Last day	7.5.2012 – 07h
Data taking	558.3 hours
Number of days	33
Total file size	138 TByte
Number of events	7.31×10^9
Mean event rate	3.6 KHz
Nominal field	
Data taking	530.15 hours
Number of events	6.94×10^9
Reversed field	
Data taking	28.09 hours
Number of events	0.37×10^9

Table 6: Statistics of the gold-gold production beam time 2012 taken from the experiment logbook.

The gold-gold production beam time was performed from April 5$^{\text{th}}$ to May 7$^{\text{th}}$ 2012 in a fixed target configuration with a beam energy of $E_{\text{beam}} = 1.23$ AGeV, corresponding to a center-of-mass energy in the nucleon-nucleon system of $\sqrt{s_{\text{NN}}} = 2.4$ GeV and resulting in mid-rapidity being located at $y_{cm} = 0.74$. Further beam specifications are summarised in table 5. Within the 5 weeks of beam time, the heavy-ion synchrotron SIS18 delivered 684 hours of Au^{69+} ions beam to the HADES cave [250] with intensities between 1.2 and 2.2 million ions per second. The total data volume recorded on disk is 140 Tbyte, including calibration and cosmic runs. At the start of the beam time data was recorded for about 5 hours with no magnetic field, which is used for detector alignment. In addition to the 530 hours of data taking with nominal magnetic field with a current setting of 2500 A, data was taken for around 28 hours at the end of the beam time with a reversed polarity, but same magnetic field strength. The summed statistics of these two data sets, summarised in table 6, amounts to 7.31×10^9 events. The main fraction of recorded events are the central PT3-triggered events (around 80%), corresponding to 5.85×10^9 events. The remaining fractions include the peripheral PT2-events (17%) as well as pulser, calibration and `CTS` events (3%). The `CTS` events are generated every second and contain the last state of counters, called *CTS scalers*, before they are reset to zero. The scalers count the number of processed physics triggers and valid inputs signals from the `START`, `VETO` and `TOF/RPC` detectors. The upper panel in Fig. 33 the averaged beam intensities observed by the `START` detector, as extracted from the `CTS` events, are shown as black solid lines. It is calculated via a running mean of over 8000 successive non-empty bins with a width of one second and a beam particle rate of at least > 200 Hz. The gaps indicate periods where no data was taken due to beam stops or cave access. The beam intensity measured using the `START` (`VETO`) detector during data acquisition is shown in blue (red). For visibility, it is averaged over intervals of 4 min. The average intensity was between 11 and 20 million ions per spill, with a duration of 10 s and a duty cycle of approximately 65%. The latter can also be seen directly as the difference between the running mean rates during beam spills (black) and the averaged rates (blue/red), including the spill gaps. The green line shows the cumulative sum of the detected beam particles seen by the `START` detector, summing up to 1.83×10^{12} at the end of the data acquisition period with a nominal magnetic field configuration. The 8$^{\text{th}}$ generation (gen8) of the processed data is used in the final results of this thesis. Summaries with detailed description of the physics analysis of the Au+Au beam time can be found in references [251–258].

Trigger Settings

Two Physics Triggers (PT) based on hardware thresholds were activated in the Au+Au beam-time. The thresholds on the integrated analog signal of all PMTs in the `TOF` detector were adjusted in a way that only events with a multiplicity of above 5 (PT2) or 20 (PT3) hits were accepted (see table 7). The multiplicity threshold ensured that the central trigger PT3 only collected central gold-gold collisions without any contribution from reactions with the material surrounding the target. From the triggered events only those were recorded by the data

Trigger	PT1	PT2	PT3
analog threshold [mV]	80	160	670
equivalent hit multiplicity	2	5	20
downscaling factor	0	8 (4)	1
time window with start [ns]	60	50	40

Table 7: Trigger settings during the Au+Au beam time.

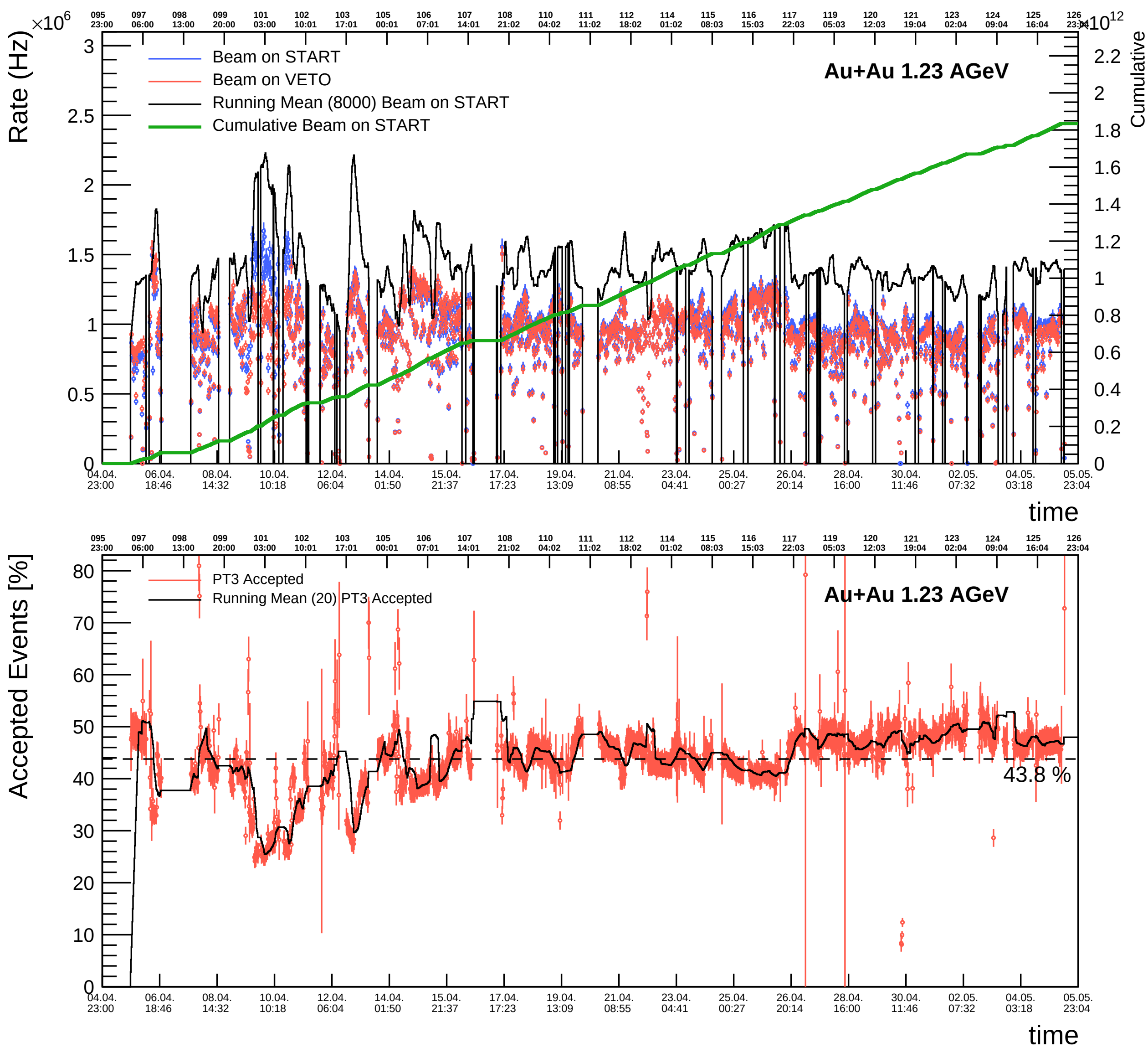

Figure 33: (Upper panel) The beam intensity seen by the START (VETO) detector is shown as blue (red) points and is averaged over intervals of around 4 minutes. In black the averaged beam intensity presented as a running mean over non-empty bins with a width of one second. The green line shows the cumulative sum of all detected beam particles measured by the START detector during the beam time. (Lower panel) The rate of accepted PT3 events in comparison to all triggered PT3 events are shown as red points and as black line the running mean over non-empty bins.

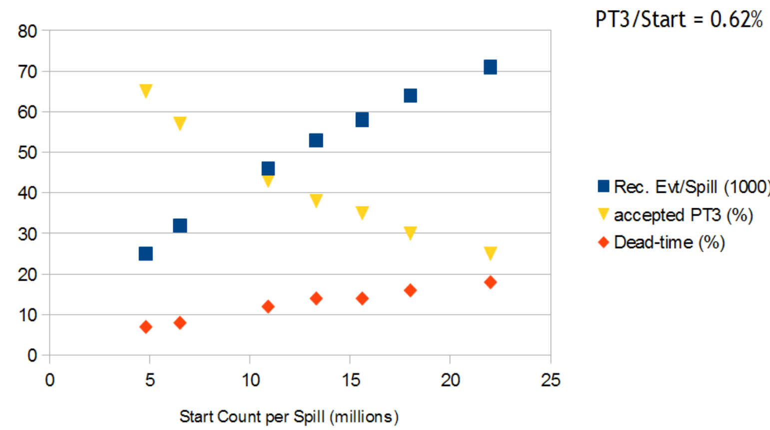

Figure 34: The performance of the data acquisition during the Au+Au beam time. The number of recorded central PT3 events (yellow) decreases with respect to the number of triggered events with rising beam intensities. The fraction of events lost due to the dead time also increases. Figure taken from [259].

acquisition, which were in coincidence with a signal from the START detector in a time window of 40 ns for PT3 events (50 ns for PT2)[3]. In the lower panel of Fig. 33 the rate of accepted PT3 events in comparison to all triggered PT3 events are shown as red points and as black line the running mean over non-empty bins.

After a physics trigger is generated by the trigger electronics CTS a signal is distributed to the front-end-boards which initiates data

[3] In the recorded data, three different trigger bits were used: the downscaled PT2 and PT3 events and the unscaled PT3 events. In the following *minimum-bias* data refers to the sample of recorded events with the downscaled PT2 and PT3 trigger bit and *central* data corresponds to the events with the un-scaled and the down-scaled PT3 trigger bit.

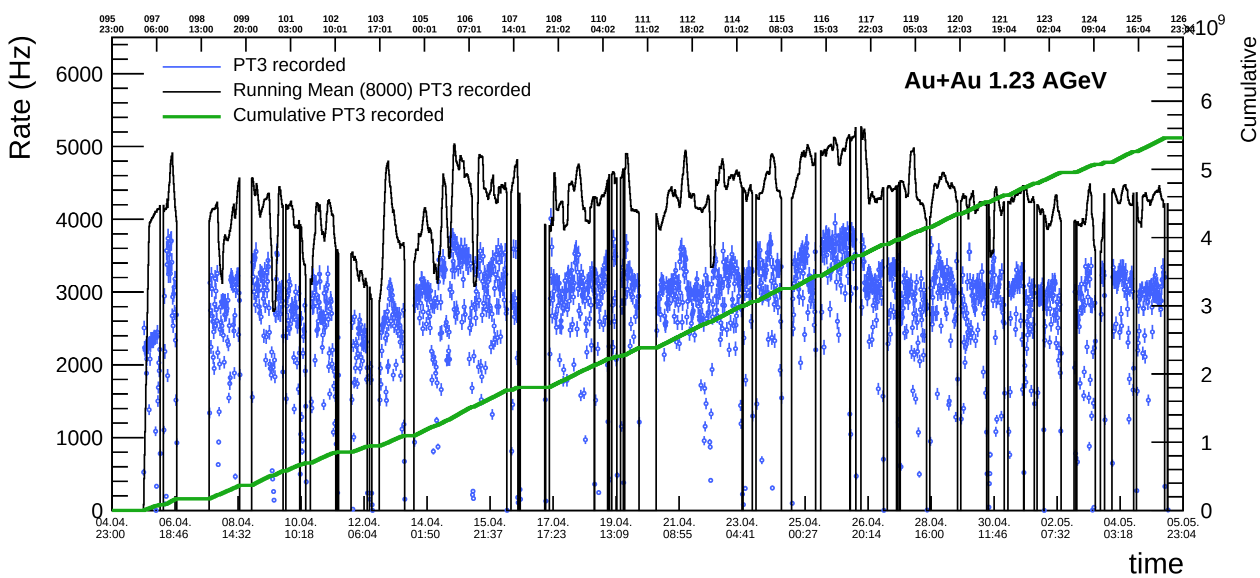

Figure 35: The rate of recorded PT3 events (blue points) averaged over intervals of 4 minutes. The black lines represent the running mean over non-empty bins with a width of one second and the green line shows the cumulative sum of all recorded PT3 events for the beam period with nominal field configuration with 5.46×10^9

readout, data processing, and transmission to the `DAQ`. As soon as the transfer is completed a busy-release signal is generated. During this process (*dead time*) no further triggers will be accepted. The average dead time per event is estimated to be around 15 μs [204]. The comparison between beam intensity in the upper panel to the rate of accepted PT3 events in the lower panel of Fig. 33 shows that the probability that events are rejected depends strongly on the beam intensity and the micro spill struture. On average around 44% of all triggered PT3 events are recorded. In Fig. 34 the dependence of accepted PT3 events as a function of beam intensity is shown. At maximal beam intensity of 2.2 million ions per second the rate of accepted events is around 25%. To increase the amount of recorded PT3 events, only a downscaled number of PT2 events is triggered and recorded. This was every 4$^{\text{th}}$ PT2 event, and beginning at April 16$^{\text{th}}$ (day107) adjusted to only every 8$^{\text{th}}$. In Fig. 35 the rate of recorded PT3 events (blue points) averaged over intervals of 4 minutes are shown as black solid lines. The gaps indicate periods where no data was taken due to beam stop or cave access and the green line shows the cumulative sum of all recorded PT3 events, summing up to 5.46×10^9 at the end of the data-taking period with the nominal magnetic field configuration.

Trigger Cross Section

The *total reaction cross section* includes the contribution from inelastic, as well as elastic and dissociation reactions, as illustrated in figure 36. For very peripheral events with large impact parameters the elastic and dissociation reactions are dominant and produce low multiplicity events in the HADES acceptance. In contrast, only the inelastic interactions are contributing generally to particle production and can be selected by a sufficiently high multiplicity threshold. A total hadronic cross section of 6.83 ± 0.43 barn is calculated for Au+Au collisions at $E_{\text{beam}} = 1.23\ A$GeV via Glauber Monte Carlo simulations [142, 144] which is in good agreement with measurements at BEVALAC and the Synchrophasotron [260–263]. The additional cross section for inclusive electromagnetic and nuclear dissociations with one-, two- and three-neutron removal is measured to be around 3.89 ± 0.23 barn for Au+Au reactions at 1 AGeV [264]. For a certain experimental trigger condition the trigger cross section can be calculated with [265, 266]:

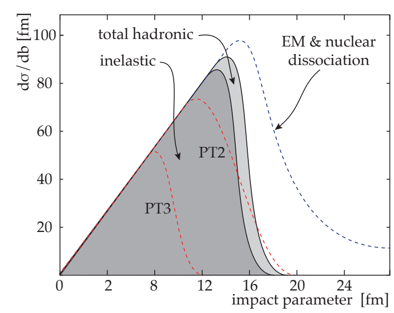

Figure 36: Schematic plot of the total cross section and its different contributions, as well as estimates for the multiplicity trigger PT2 and PT3 (red lines).

$$\sigma_{trig} = \frac{N_{trig}}{N_{beam}} \cdot \left(\rho \cdot d \cdot \frac{N_A}{M} \right)^{-1} \tag{30}$$

where N_A is the Avogadro constant, d the thickness of the target, ρ the density and M the molar mass of the target material. Using the *CTS scaler* information the interaction probability N_{trig}/N_{beam} can be

^{197}Au-Targets	
int. prob. L_0	1.51%
segments	15
tot. thickness d	375μm
density ρ	19.3 g/cm^3
^{12}C START detector	
int. prob. L_0	0.36%
thickness d	$\sim$ 50μm
density ρ	3.51 g/cm^3

Table 8: Target and START detector specifications.

	PT2	PT3
N_{trig}/N_{beam}[%]	1.694	0.692
σ_{trig}[mb]	7657.3	3125.5

Table 9: The interaction rate for the PT2 and PT3 trigger and the resulting trigger cross section averaged over the total beam time.

derived from the number of triggered N_{trig} and the number of total beam particles N_{beam} as registered by the START detector. The target setup with a total length of 54.5 mm consists of a stack of fifteen segments of gold targets, separated by a distance of 4 mm. Each target disc has a thickness of 25 μm, adding up to 0.375 mm and an overall interaction probability of 1.51% (see table 8).

The PT3 trigger cross section is estimated to be 3.13 barn averaged over the total beam time and corresponds to 45.8% of the total cross section (see table 9). In Fig. 37 the PT3 trigger cross section is shown for the full beam time. The comparison to the averaged value indicates periods, where the cross section is overestimated due to the lower efficiency of the START detector. Since the beam particles can not be delivered by the accelerator uniformly distributed in time, due to the extraction process, there is a finite probability that two or more events can occur close in time in the detector. These events are called *pile-up* events, and even if their individual multiplicity would not satisfy the trigger threshold, the combined signals can pass the trigger condition [267]. The PT2 events have the highest contribution from background-events, originating from reactions with the material of the START detector (diamond ^{12}C with a metallisation of ^{197}Au and ^{24}Cr) and the target holder (carbon fiber tube and Kapton holding strips containing light nuclei as ^{1}H, ^{12}C, ^{14}N, and ^{16}O).

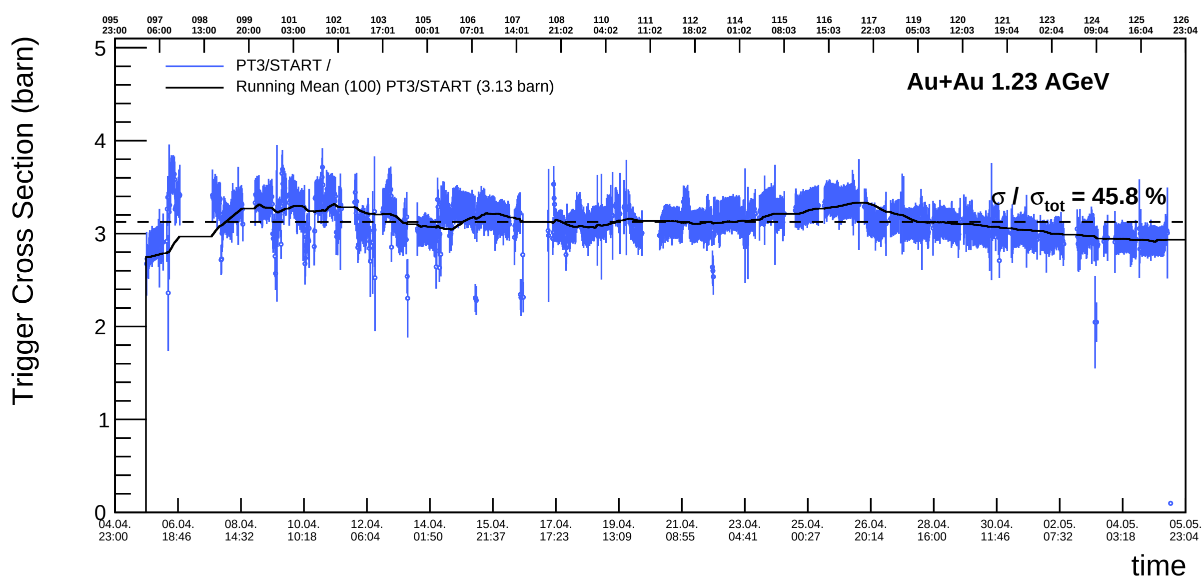

Figure 37: The PT3 trigger cross section calculated from the rate of triggered PT3 events and the rate of beam particles seen by the START detector during the full beam time. In black a running mean is shown. The averaged value is estimated as 3.13 barn, corresponding to 45.8% of the total cross section.

Event characterisation

The aim of the event characterisation in the offline analysis is to determine the properties of individual events. The most important concepts to differentiate events are:

- *position of the collision*: the global event vertex is the interaction point to which all emitted primary particles can be traced back.
- *timing of the event* T_0: is used for time-of-flight measurement and needed for the accurate determination of the velocity of the particles.
- *centrality of the collision*: the violence of the reaction can be used to categorize events in classes of similar *centrality*, corresponding to different fractions of the total cross section. These centrality classes can then be related to the averaged estimated distance of the centers of the nuclei during the collision (*impact parameter b*) and to the average number of nucleons participating in the reaction (N_{part}).
- *orientation of the collision*: the plane spanned by the beam and impact parameter of the collision is called *reaction plane*.

To ensure that only events are used in the physics analysis, where the location, timing, centrality, and orientation of the event can be determined with sufficient accuracy, selection methods are applied. The goal is to select the most central inelastic hadronic interactions as efficiently as possible and to reduce the contribution from off-target or pile-up events by excluding them if observables indicate an overlap of two or more events. The event selection flags used in the analysis are discussed in the section Event Selection. The determination of the centrality and the event-plane orientation of the Au+Au and Ag+Ag data samples are part of this study, and the corresponding procedures and parameterisations, as well as the required corrections, are implemented in the Hydra Analysis Framework used by other groups for analyses of the same data. The essential aspects used in the flow analysis are described below.

Event Vertex Reconstruction

The precise and efficient determination of the interaction point is crucial in two ways. First it is the point to which all primary particles are traced back to. The accuracy of the event vertex reconstruction influences the reconstruction of the particle trajectories and their momenta. It enables the separation of particles decaying outside of the collision zone via the reconstruction of secondary vertices. Secondly, it allows to reject reactions with the surrounding material outside of the target region or events contaminated by one or more pile-up events. There are three

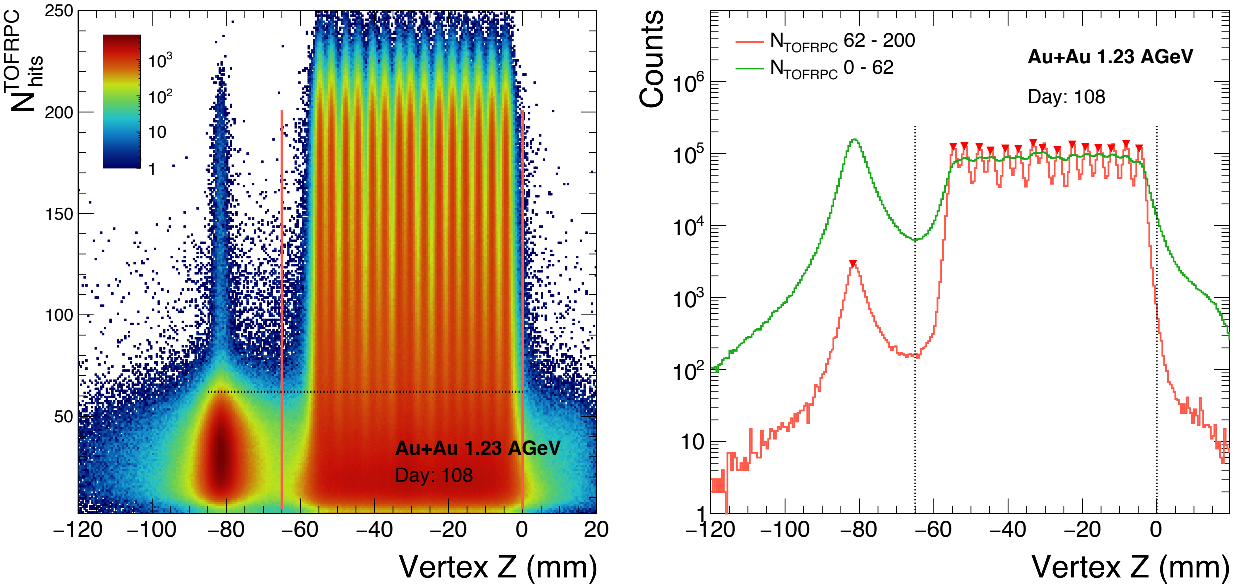

Figure 38: On the left the z-position of the reconstructed global vertices vs. hit-multiplicity in the TOF and RPC detector is shown for minimum-bias data and on the right the projection in two multiplicity intervals (indicated by the horizontal line in the left). The 15 different target strips can be clearly separated. The START detector consisting of ^{12}C can also be seen in real data. Events outside the target region between $-65 < Z < 0$ mm (vertical lines) are rejected in the analysis.

successive steps to find the target disc in which the reaction occurred and to determine the position of the reaction vertex [253]. In the first step only the correlation of the fired wires in the inner MDCs is used to select a candidate for the hit target disc including the START detector. In the second step the straight track segments obtained from the two inner MDCs are extrapolated to the z-position of the first estimate. Their point of closest approach is an estimate of the interaction vertex. Finally the fully reconstructed (Runge-Kutta fitted) tracks are used to perform a vertex fit (see section track reconstruction). The precision and efficiency of the vertex reconstruction methods are strongly dependent on the track multiplicity of the event. The resolution, defined as the deviation between the generated and reconstructed z-position in detailed detector MC simulations, can be parametrised as:

$$\sigma_{\Delta Z} \approx 4.3\text{mm}/\sqrt{N_{Tracks}}\ . \tag{31}$$

The vertex reconstruction efficiency is calculated using a full MC simulation with HGeant. However, the effects of multiple vertices from pile-up or background events are not taken into account in the simulation. The right panel in Fig. 38, TOF+RPC hit-multiplicity as a function of Z-position determined using the *reconstructed tracks* method is shown, where the 15 target strips are clearly separated. The diamond START detector consisting mainly of ^{12}C can be observed in the data located 2.8 cm in front of the first target segment. The largest fraction of the reactions are of low multiplicity, but high multiplicity events are also visible, caused by the metallisation with ^{197}Au and ^{24}Cr on the surface of the START detector (Fig. 38 left). The contribution from reactions in the START detector can be rejected by a cut on the position of the reconstructed global vertex in the z-direction, as shown in figure 38.

Event Time Determination

To ensure precise time-of-flight measurement for particle identification (PID), a good event time T_0 is essential and provided in the first step by the *START hit finder*. The timing signal of the START detector is used as the event time T_0 if a hit on the front side (X-stripes) correlates with a hit on the back side (Y-stripes) of the START detector in a time window of 0.5 ns. If no correlated hits are found between the front or back sides, a hit from one side of the START detector is chosen, which is the closest to the estimated event time calculated by the mean time-of-flight of the three fastest hits in the TOF and RPC detectors. This is done under the assumption that these fastest hits have a time-of-flight close to 7 ns because they have a velocity near $\beta \approx 1$ and a straight trajectory of 2.1 m length towards the hit position. If no correlation between the START and META detectors is found within the time window of 10 ns, the event is flagged and rejected in further analysis (see Tab. 10). After the full event and track reconstruction, the event time is further improved by the recalibration of the timing provided by the START detector and the additional combination with the measured timing and momenta information for the identified particles. The additional flight time from the ion to the target segment was corrected based on the vertex position. A preliminary particle hypothesis is assigned to each selected track based on the smallest deviation of the β-momentum and dE/dx-momentum measurements from the corresponding theoretical parameterisations. The deviation and error of the measured time-of-flight to the one calculated for the momentum of the track are stored temporarily for each of these filtered tracks. For each track, the start time is recalculated as follows:

2	both side correlate within 0.5 ns
1	back side correlates with META
0	front side correlates with META
-1	no correlation found

Table 10: T_0 Timing correlation-flag.

- The mean of all stored deviations of the measured time-of-flight using the re-calibrated start time, weighted by the corresponding errors, is calculated. The particle of interest is excluded from the calculation in order to avoid a possible auto-correlation.
- This first estimate of the event time T_0 is refined by excluding outlier hits. From the remaining deviations and the corrected start time the mean value is calculated in a second step, weighted by the errors with an additional asymmetry factor to take into account the asymmetric shape of the used momentum distribution.
- This new event time is used to correct the velocity β and the measured mass m of the particle.

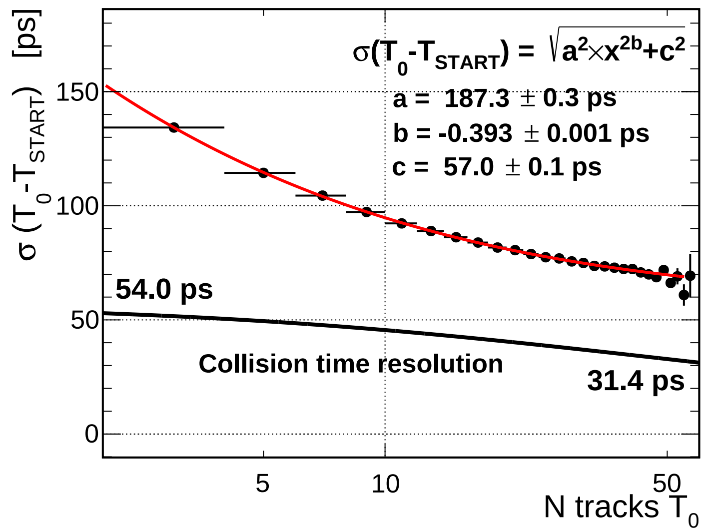

Figure 39: Event time accuracy estimated using the T_0 method. The red line shows a fit, where the contribution of the averaged single track time-measurement is taken into account via parameter a, the exponential decrease due to the addition of N tracks in the T_0 reconstruction via parameter b, and the constant time resolution of the START detector via parameter c. The lower line is the resolution of the combined timing provided by the START detector and the reconstructed T_0 as it is used in the analysis as a function of the number of tracks. The figure is taken from [268].

The result of the T_0 reconstruction method is shown in Fig. 39, where the points represent the dispersion of the time-difference between the START and the reconstructed time T_0 as a function of number of used tracks. Since all time measurements and the reconstructed time can be considered to be independent, the resolution can be split into an exponential and a constant part:

$$\sigma_{\Delta T} = \sqrt{\sigma_{T_0}^2 + \sigma_{START}^2} = \sqrt{(a \times N^b)^2 + c^2}\,, \tag{32}$$

where the coefficient a is the averaged resolution of a single track time measurement, b describes the exponential decrease of the T_0 resolution when adding N tracks and c is the constant resolution of the diamond START detector. Since the final event time is the weighted combination of individual time measurements extracted from each track convoluted with the START time, its resolution can be calculated with the following parametrisation [268]:

$$\sigma_{T_0} = \sqrt{\frac{1}{1/(a \times N^b)^2 + 1/c^2}}\,. \tag{33}$$

The resolution of the diamond detector is in general already better than 60 ps, but using this procedure the final event time resolution can be further improved to $\sigma_{T_0} = 54$ ps in peripheral and up to 31.4 ps in the most central events. This method is limited to events where the start time is measured and its deviation to the real event time is moderate. For larger time shifts a PID hypothesis cannot be made, so a full T_0-reconstruction via an iterative χ^2-minimisation method is needed. In this version the event time is reconstructed fully independent from the START detector [269]. The measured time-of-flight of each track is compared to an expected time-of-flight deduced from the measured momentum and mass hypotheses. Here the mass hypothesis of all contributing tracks are iteratively optimised to reduce the calculated χ^2.

Event Selection

To achieve a good characterisation of the events of interest, the following selection methods are generally used for different physics analyses [251, 253, 255]:

- `kGoodTRIGGER`: high multiplicity trigger PT3. In this work this flag was not used, so PT2 events are not rejected but instead the events are weighted according their downscaling factor.

- `kGoodVertexClust` and `kGoodVertexCand`: a reconstructed global vertex is existing, based on the two methods with *cluster* and *reconstructed tracks* with a χ^2 greater than zero, indicating a successful fit, and a z-position between $-65 < Z < 0$ mm along the beam axis. As shown in figure 38 this removes most of the reactions occurring in the material of the START detector. However, low multiplicity background events from the material surrounding the target region cannot be rejected with this method.

- `kGoodSTART`: there must be a measured timing signal in the START detector to allow for a correct time-of-flight measurement. An event is accepted if either correlated hits from both sides of the start detector exist or a close correlation between a hit from one side and the mean time-of-flight of the three fastest particles (see START hit finder).

- `kNoPileUpSTART`: there must be only one single START hit found within a time window of 5 to 15 ns around the first estimate of the event time as provided by the *START hit finder*. If there is a second hit found the event is rejected as a pile-up event.

- `kNoVETO`: events are accepted if there is no hit in the VETO detector in a time window of ± 15 ns around the START signal. In the case of a VETO signal inside this time window, it is expected that there was a non-interacting beam ion, before or after the event, flying through the VETO detector. The VETO detector was conceptually designed to also reject non-central events at the level of the trigger. Since spectator fragments should have on average the same velocity as the beam ion, they cannot be distinguished by their timing. Depending on the threshold on the signal of the VETO detector, spectator fragments with a cumulative charge deposition high enough can produce a

VETO hit inside this time window, which might lead to a bias in the selection of peripheral events.

- kGoodSTARTVETO: there must be no second START hit in the time interval 15 to 350 ns after the main START hit without a hit in the VETO detector in coincidence.
- kGoodSTARTMETA: there must be no second START hit in the time interval 80 to 350 ns after the main START hit with more than 4 hits in the META detectors in coincidence.

The flag kGoodSTARTVETO and kGoodSTARTMETA ensures that pile-up events are rejected, with a delayed event producing either a second START hit or additional hit multiplicity in META.

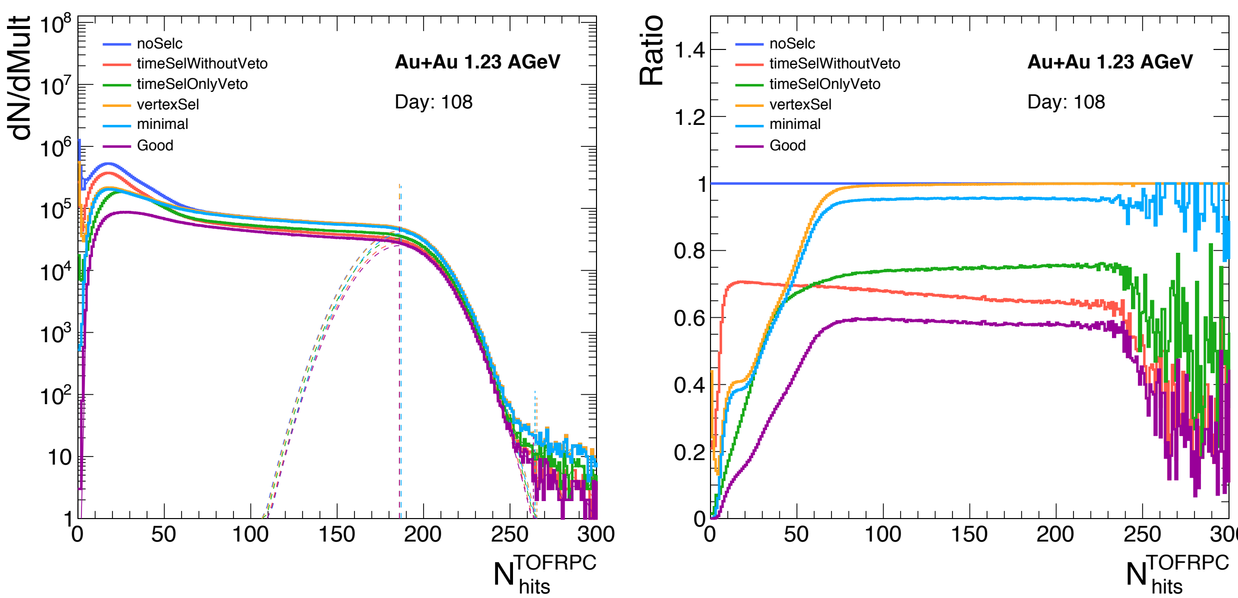

Figure 40: On the left, the TOF and RPC hit multiplicity distributions are shown after different selection methods are applied. The most central part of the distributions is fitted with a Gaussian distribution, with the lines indicating the mean values. On the right, the ratio between no selection and the individual selections is plotted.

In the left panel of Fig. 40 the TOF and RPC hit multiplicity distributions after applying different selection methods are shown. Since this observable was chosen as the main estimator for the centrality determination, any bias due to event losses was carefully studied. The right panel in Fig. 40 the ratio between the minimum-bias data (*noSelc*) without any additional selection and the events after different individual selections are plotted. To differentiate the behaviours of the methods, they are grouped according to their functionality. The light blue (*minimal*) histogram shows the distribution for the case of two vertex selections (kGoodVertexClust, kGoodVertexCand), and the successful registration of a START hit (kGoodSTART). The magenta histogram (*Good*) shows the distribution of events used in the analysis. In addition to the *minimal* criteria, all timing and pile-up selections are applied. The high-multiplicity

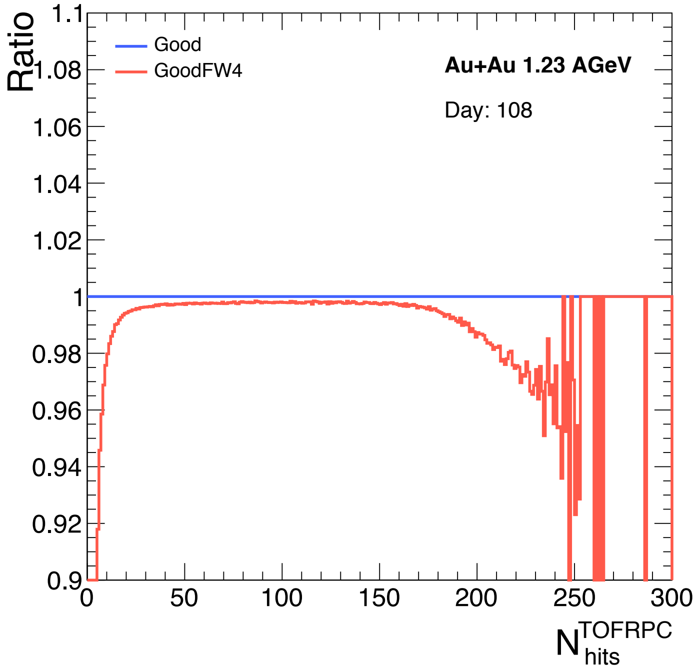

Figure 41: The ratio between data with the general selection criteria (*Good*) and the additional criteria selecting events with at least 4 hits in the FW (*GoodFW4*) is shown in red as a function of TOF and RPC hit multiplicity.

edges of the distributions are fitted with a Gaussian distribution, and their means (dashed line) are extracted for each individual day of beam time. They are found to be stable around 185 over the entire course of data collection. This is of particular importance because the characterisation of centrality classes is performed by a division of the multiplicity distribution, and any significant shift would result in a systematic bias, which depends on the performance of the `TOF` and `RPC` detectors. For a proper determination of the Event Plane (EP) at least 4 hits in the `FW` are needed, so additionally events are rejected if the number of FW-hits is below this value. This ensures that in the calculation of the EP-resolution via the two sub-event method at least two hits are in each sub-event, which reduces the effect of fluctuations. In Fig. 41 the ratio between data with the general selection criteria (*Good*) and the additional criteria selecting events with at least 4 hits in the `FW` is shown in red. An events loss of 2% is expected for the most central 10% event class (corresponding to values above $N_{\text{hits}}^{\text{TOF+RPC}} > 150$), where the multiplicities in the `FW` are low. The rejection of around 0.5% of all other mid-central events can be explained due to the wrong event timing in the `FW`.

Centrality Determination

As introduced in the section on the geometrical aspects of the reaction, it is essential for the flow analysis to know the centrality or equivalently the impact parameter range of the analysed collision events. The goal is to extrapolate the partial distribution of the triggered cross section to the total nucleus-nucleus cross section and then divide the distribution according to an experimental observable in to fractions of a given centrality according Eq. (7). There are several experimental observables considered within HADES for the determination of centrality. They provide either a measurement proportional to the charged particle density close to mid-rapidity or to the number of spectators found in the forward region. The main observables used in this analysis to estimate the event centrality is based on the summed number of hits detected by the `TOF` and the `RPC` detectors, $N_{\text{hits}}^{\text{TOF+RPC}} = N_{\text{hits}}^{\text{TOF}} + N_{\text{hits}}^{\text{RPC}}$. It generally provides large and stable acceptance over the course of data taking, but there are several systematic effects to be considered. One is the choice of the applied time window $t_{TOF} < 35$ ns and $t_{RPC} < 25$ ns to reject slow or uncorrelated hits. Another effect is the contribution of secondary particles produced in the detector material, which can be significant at large multiplicities. Additionally, the effects of occupancy play a role in high multiplicity events. Due to the partial overlap of the `RPC` cells, one particle can produce up to two hits, which results in double counting and has also to be taken into account. A similar effects can occur in two neighbouring `TOF` rods, depending on the inclination angle of the particle trajectory. A complementary measure is the number of tracks reconstructed with the `MDCs`, N_{tracks}, which has the advantage of being less contaminated by secondary particles produced in the detector material. It provides a very clean sample of particles, originating from the collision, but with the cost of a reduced available multiplicity. For a full reconstruction of the tracks in all `MDCs`, a efficient operation of all sectors is required. The third approach is the estimation of the centrality by the number of spectators in the forward region via the measurement of the total charge of fragment-hits in the `FW` in a time-of-flight window around $\beta = 0.9$.

However, it turned out that reproducing the measured distributions of $N_{\text{hits}}^{\text{TOF+RPC}}$ and N_{tracks} with events simulated with the transport model UrQMD [270], filtered through a detailed simulation of the detector response based on GEANT 3.21 [245], is challenging. Based on a phenomenological approach the measurements of $N_{\text{hits}}^{\text{TOF+RPC}}$ and N_{tracks} can instead be parameterized by quantities calculated with the *Glauber Monte Carlo* model, namely the number of participants N_{part}. The parameters are determined by a minimisation procedure, which compares the simulated multiplicity distributions with the measured ones. In a

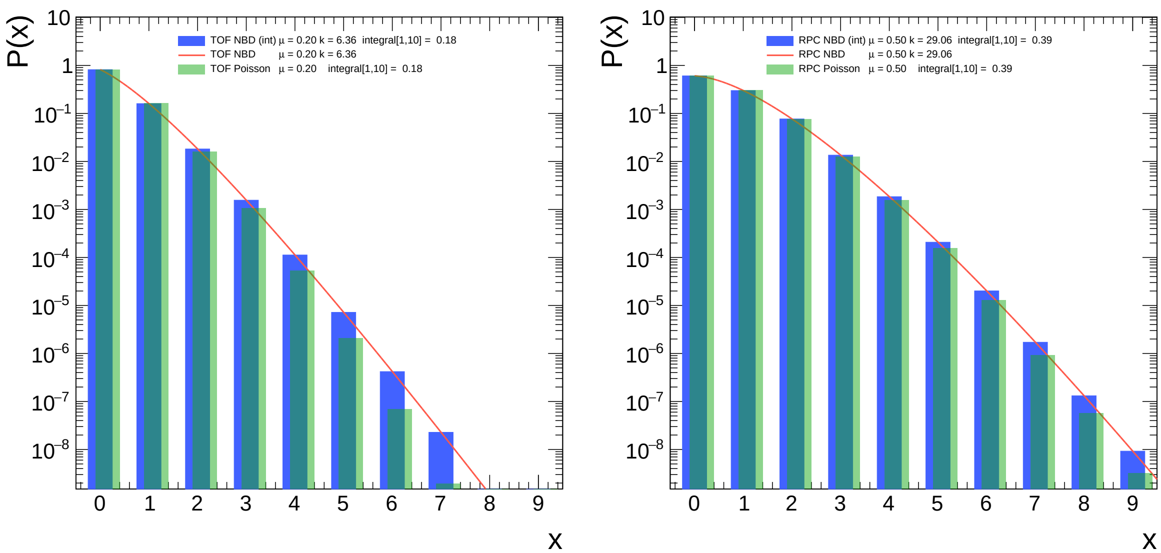

Figure 42: The NBD distributions (red curve) with the parameters for TOF (left) and RPC (right), as listed in Tab. 11. The integer valued NBD and Poisson distribution with the same mean value are shown as blue and green bars.

simple model for particle production and detection two assumption are combined. Following the wounded nucleon model [145] the measured charged particle multiplicity, N_{ch}, should on average be directly proportional to N_{part} and the event-by-event fluctuations of the number of charged particles created by each MC participant should be distributed according to a Negative Binomial probability Distribution (NBD) with a mean μ, *i.e.*:

$$P_{\mu,k}(n) = \frac{\Gamma(n+k)}{\Gamma(n+1)\Gamma(k)} \cdot \frac{(\mu/k)^n}{(\mu/k+1)^{n+k}}\,. \tag{34}$$

Here Γ is the gamma function and the dispersion parameter k is related to the relative width by $\sigma/\mu = \sqrt{1/\mu + 1/k}$. The NBD is commonly used to empirically describe charged particle multiplicities [271–275] in proton-proton collision in the high energy regime ($\sqrt{s} \gtrsim 10$ GeV). It coincides with the Poisson distribution in the case of $k \to \infty$ and with the geometric distribution in the case of $k = 1$. The deviation from a Poisson distribution reflects the degree of correlations, which can arise for different reasons.

In Fig. 42 the NBD distributions, with the parameters for `TOF` (left) and `RPC` (right) as listed in Tab. 11, are shown as red curves. The integer valued NBD and Poisson distribution with the same mean value, used for the sampling, are shown as blue and green bars. The probability for a participant to generate particles resulting in at least one detected hit in the `TOF` detector, is 18% and in the `RPC` detector 39%.

	μ	k	α
N_{TOF}	0.20	6.36	$1.64 \cdot 10^{-6}$
N_{RPC}	0.50	29.06	$1.64 \cdot 10^{-6}$
N_{tracks}	0.24	20.34	$1.10 \cdot 10^{-7}$

Table 11: The parameters obtained for the different observables.

The multiplicity distributions are generated by summing over all participants in a given event and sampling a value for each participant according to the NBD. To consider additional nonlinear multiplicity-

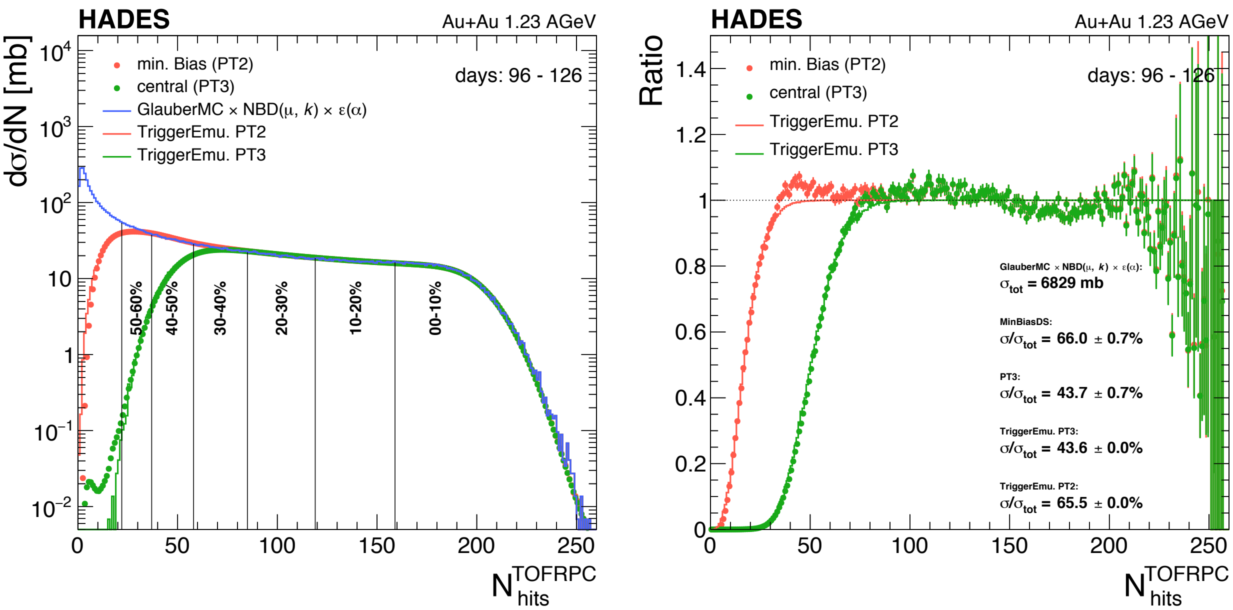

Figure 43: In the left panel the cross section as a function of $N_{\text{hits}}^{\text{TOF+RPC}}$ for the sum of TOF and RPC hits is shown for the minimum bias (PT2 trigger, red symbols) and central (PT3 trigger, green symbols) data in comparison with the Glauber MC model (blue histogram). The intervals in $N_{\text{hits}}^{\text{TOF+RPC}}$ for the 10% centrality classes are displayed. In the red and green histogram the trigger response for PT2 and PT3 is emulated with the Glauber MC simulation. The right panel shows the ratio between minimum bias and central data in comparison to the Glauber MC model. The red and green curve show the trigger response function described in the text.

dependent effects, *i.e. occupancy effects*, the value is further folded with an efficiency function. $\epsilon(\alpha) = 1 - \alpha \cdot N_{\text{part}}^2$. The values of α are listed in Tab. 11, and the parameterisation of the corresponding efficiency is obtained from a full detector simulation based HGeant [245] and events generated with the UrQMD transport model [270]. In the left panel of Fig. 43 the distribution of the cross section calculated with the Glauber MC model (blue histogram) is shown in comparison to the minimum bias (PT2, red symbols) and central (PT3, green symbols) data as a function of the sum of `TOF` and `RPC` hits $N_{\text{hits}}^{\text{TOF+RPC}}$, which are simulated individually for both detectors. For comparison, the *minimum* event selection methods are used, as shown in Fig. 40, where it was found that these criteria provided a reasonably good match to the simulated events. The red and green histograms show the emulated response of the PT2 and PT3 trigger on top of the Glauber MC simulation. The trigger response can be parameterised using the following modified error function:

$$f(x) = N_0 \cdot [1 + \text{Erf}((x - \mu)/(\sigma\sqrt{2}))] \,, \tag{35}$$

with the turning point μ and the slope σ. The derivative is conveniently a Gaussian with mean μ and sigma σ that can be utilized to simulate the smeared threshold. In the right panel of Fig. 43 the ratios between the simulated distribution of the Glauber MC model and the two data sets (PT2 and PT3) are shown, with the corresponding trigger response functions. With this method the cross section for the central PT3 data set is estimated form different estimators to be $\sigma/\sigma_{tot} = 43\%$. The trigger

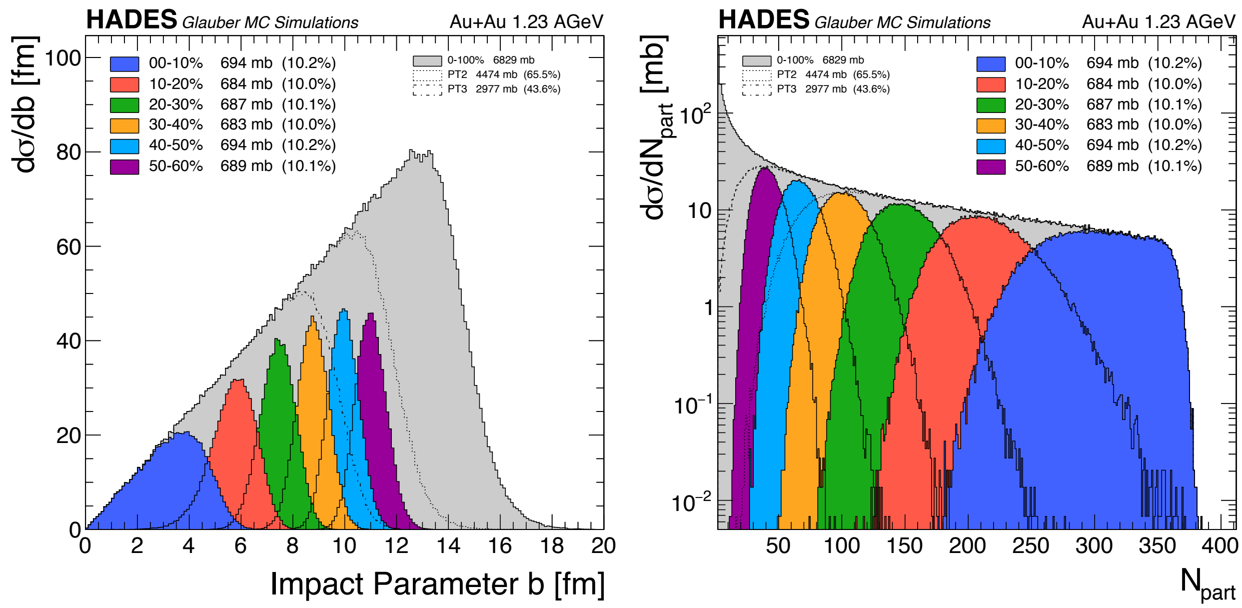

Figure 44: The distributions of the impact parameter b (left panel) and the number of participants N_{part} (right) calculated with the Glauber MC model. The grey area displays the distribution of the total Au+Au cross section, where the dotted and dashed curve represents the estimated boundary of the PT2 and PT3 triggered data set. The coloured distributions represent 10% centrality classes selected by the number of hits in the TOF and RPC detectors $N_{\text{hits}}^{\text{TOF+RPC}}$.

cross section previously calculated by using the *CTS scaler* information gives higher values of 45.8%, mainly due to the efficiency of the START detector. In the left panel of Fig. 43 the intervals in $N_{\text{hits}}^{\text{TOF+RPC}}$ are displayed for the 10% centrality classes. Due to the fluctuating nature of event multiplicities, the centrality estimation has its limitation. But an important aspect remains, namely that even with different approaches using several experimental observables the outcomes are consistent in the limits of the resolution and bias. One way to verify the accuracy and resolution is to study the distributions of the geometric quantities calculated with the Glauber MC model. In Fig. 44 the distributions of the impact parameter b (left panel) and the number of participants N_{part} (right panel) are presented. The grey area displays the distribution of the total Au+Au cross section, where the dotted and dashed curve represents the estimated boundary of the PT2 and PT3 triggered data set. The coloured distributions represent 10% centrality classes selected by the number of hits in the TOF and RPC detectors $N_{\text{hits}}^{\text{TOF+RPC}}$. The comparison between the mean values for $\langle b \rangle$ and $\langle N_{\text{part}} \rangle$ calculated for the centrality classes in intervals of $N_{\text{hits}}^{\text{TOF+RPC}}$ and in fixed intervals of impact parameter shows that they differ less than 1%. Additionally, the Glauber MC model allows to investigate systematic effects due to the model parameters, which results in variations of $\langle N_{\text{part}} \rangle$ of at most 15% for very peripheral collisions, decreasing to $3-4$% for central events. Further details are described in [142, 144]. An alternative approach [276], utilising a gamma distribution in combination with a monotonic function, was successfully used to characterize the centrality in the INDRA dataset [277]. When applied to the $N_{\text{hits}}^{\text{TOF+RPC}}$ distribution values for centrality intervals could be extracted which closely agree with the Glauber MC approach.

Event Plane Determination

Because the orientation of the colliding nuclei, described by the azimuthal angle of the *reaction plane*, is not experimentally accessible before the impact, an approximation called the *event plane* can be inferred event-wise by the azimuthal orientation of the collision products.

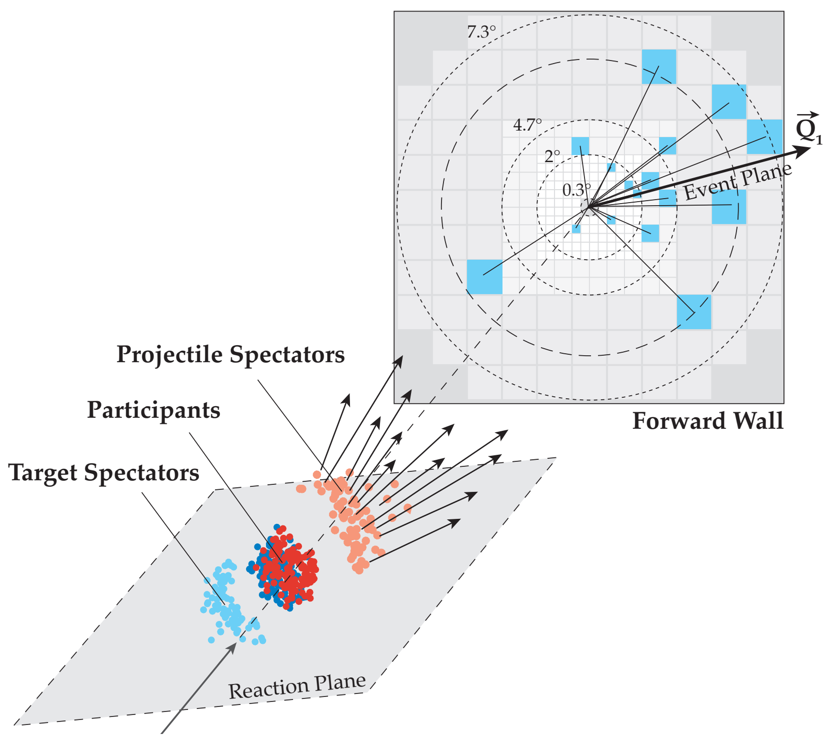

Figure 45: Sketch illustrating the event plane reconstruction using the projectile spectator hits recorded in the Forward Wall. Shown is the *reaction plane* defined by the beam axis $\vec{z}$ and the direction of the impact parameter $\vec{b}$. Oriented to this plane the *participant nucleons* (dark red and blue), as well the *target* (light blue) and *projectile spectators* (light red) are shown. The unstopped forward-going projectile spectators are detected in the cells (blue squares) of the Forward Wall and their emission angles determine the *event flow vector* $\vec{Q}_1$ and the corresponding *event plane*.

This is sketched in Fig. 45, where the *reaction plane* of a semi-central collision is shown, together with the *participant nucleons*, as well the *target* and *projectile spectators*. In the course of the collision, participating nucleons are decelerated in the central reaction region, whereby it is expected that the projectile spectator fragments continue to fly with nearly the incoming beam momentum. Their momentum distribution is modified by the Fermi motion prior to their break up [278, 279] and, due to the interaction with the expanding *participant blast*, they are further accelerated and deflected [280, 281]. Based on the analysis strategy and the properties of the experimental setup there are several methods to determine the *event plane*. To increase the measured flow signal and reduce the statistical errors, the analysis procedure is optimised for the best possible event plane resolution. This is achieved using two approaches: the exclusion of hits uncorrelated to the reaction plane and weighting according to their correlation strength to the reaction plane. The choice of weights and their optimisation have been extensively discussed in [104, 108, 138, 282–291]. It is known from experimental data [292] that the alignment of fragments relative to the reaction plane increases with their mass. Therefore, one choice for the weight which can increase the resolution would be the mass number A or charge Z of the fragments, if this is measurable in the setup. Furthermore, for particles with reconstructed trajectories, the weight can be optimised as a function of transverse momentum and rapidity. An important point here is that for the construction of odd flow vectors, the weights should be inverted for backward rapidities [138].

For the following analysis, the first-order *event plane* $\Psi_{\mathrm{EP},1}$ is chosen as the reference plane, motivated by the large directed flow expected in Au+Au collisions at SIS18 energies. From the azimuthal angles ϕ_i of the FW cells hit by spectators, the *event flow vector* $\vec{Q}_n$ of the n$^{\mathrm{th}}$ order is calculated event-wise as:

$$\vec{Q}_n = (Q_{n,x}, Q_{n,y}) = \left[\sum w_i \ \cos(n\,\phi_i),\ \sum w_i \ \sin(n\,\phi_i)\,\right] \tag{36}$$

with the individual weights $w_i = |Z_i|$, where Z_i is the charge of a given hit as determined via the signal amplitude seen by the FW cell. The selection criteria for the flight time and energy deposit for the spectators hits in the FW are discussed below. The corresponding event plane angle $\Psi_{\mathrm{EP},n}$ of the n^{th} order is determined by the following convention:

$$\Psi_{\mathrm{EP},n} = \arctan(Q_{n,y}/Q_{n,x})/n\,, \tag{37}$$

in the range $0 \leq \Psi_n < 2\pi/n$ with the arctangent evaluated for the correct quadrant. Since the measured value for Ψ_{EP} deviates from the true reaction plane angle Ψ_{RP}, its dispersion $\Delta\Psi = \Psi_{\mathrm{EP}} - \Psi_{\mathrm{RP}}$ can be quantified as the corresponding *event plane resolution* [138]:

$$\Re_n = \langle\cos(n\Delta\Psi)\rangle\ . \tag{38}$$

Because of multiple effects, the averaged distribution of FW hits is not centred around the origin, and the non-uniformities in the event-plane angular distribution must be correct, as described in following section.

Due to the finite *event plane resolution*, $\Re_n < 1$, the observed values for the flow coefficients v_n^{obs} are smaller in comparison to the values v_n related to the *reaction plane*:

Here the trigonometric subtraction identity $\cos(a-b) = \cos(a)\cos(b) + \sin(a)\sin(b)$ is used together with the assumption that the sine- and cosine-terms in the brackets are randomly distributed, uncorrelated and factorise.

$$\begin{aligned} v_n^{\mathrm{obs}} &= \langle \cos n(\phi_{lab} - \Psi_{\mathrm{EP}}) \rangle \\ &= \langle \cos n[(\phi_{lab} - \Psi_{\mathrm{RP}}) - (\Psi_{\mathrm{EP}} - \Psi_{\mathrm{RP}})] \rangle \\ &= \langle \cos n(\phi - \Delta\Psi) \rangle \\ &= \langle \cos(n\phi)\cos(n\Delta\Psi) \rangle + \langle \sin(n\phi)\sin(n\Delta\Psi) \rangle \\ &= \langle \cos(n\phi) \rangle \langle \cos(n\Delta\Psi) \rangle = v_n \cdot \Re_n \ . \end{aligned}$$

The upper relation is only valid if at least one of the sine-terms vanishes, which is true for a reflection symmetric distribution (see Eq. 29). In the analysis procedure the measured coefficients $s_n = \langle \sin(n\phi) \rangle$ can be checked to be small in comparison to the flow coefficients v_n. In the case that individual correlations between the measured emission angles are absent, the so-called *non-flow contributions*, and that the flow vector dispersion has a Gaussian distribution, the resolution can be expressed as a function of the *resolution parameter* χ [126, 137]:

Note that here the convention outlined in Ref. [248] is used, following the definition introduced in Refs. [126, 137], while the value of χ in Refs. [127, 138] is larger by a factor of $\sqrt{2}$

$$\Re_n(\chi) = \frac{\sqrt{\pi}}{2} e^{-\chi^2/2} \chi \left[I_{\frac{n-1}{2}}\left(\frac{\chi^2}{2}\right) + I_{\frac{n+1}{2}}\left(\frac{\chi^2}{2}\right) \right] , \tag{39}$$

where I_ν are the modified Bessel functions of the order ν. In Fig. 46 the dependence of the *event plane resolution* up to 6$^{\mathrm{th}}$ order as a function of the *resolution parameter* χ is shown.

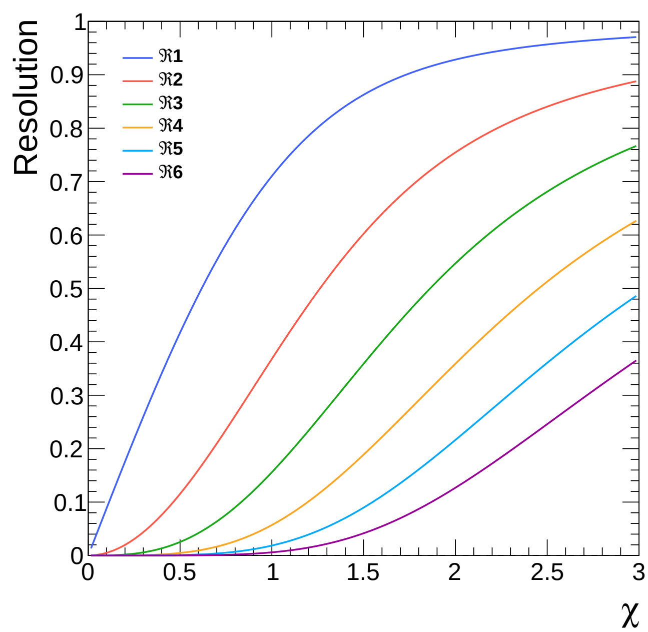

Figure 46: The dependence of the *event plane resolution* $\Re_n$ up to 6$^{\mathrm{th}}$ order as a function of the *resolution parameter* χ.

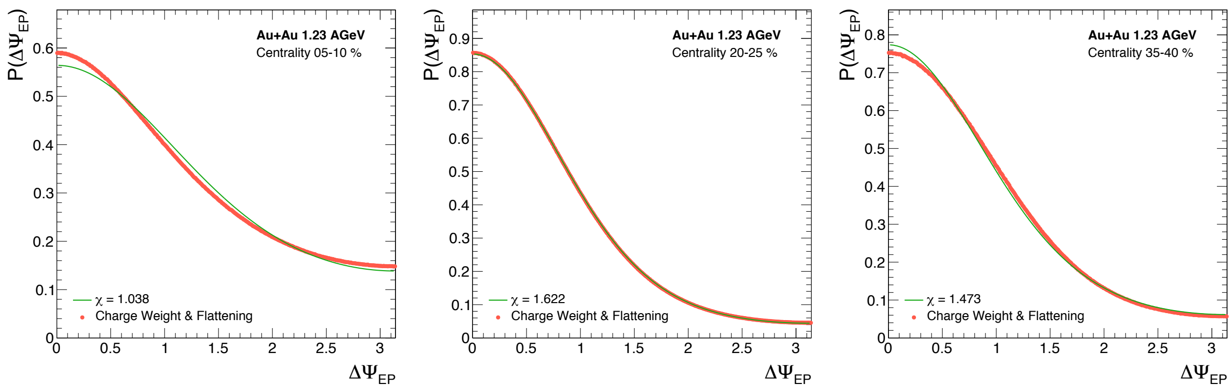

Figure 47: The probability distribution of the event plane angles Ψ_{EP} for central ($5-10\%$, left) and semi-central ($20-25\%$, middle and $35-40\%$, right) Au+Au collisions at 1.23 AGeV after the charge weighting procedure is displayed as red points. The green line shows a fit to Eq. 42, which yields the *resolution parameter* χ.

Several methods can be used to determine the *event plane resolution* $\Re_n$. In the following, the two-sub-event method is employed with three different implementations. The selected `FW` hits in a given event are randomly divided into two independent sub-events A and B of equal multiplicity with the sub-event planes $\Psi_{EP,A}$ and $\Psi_{EP,B}$. Assuming that the projectile spectators are only correlated to the reaction plane and *non-flow contributions* are absent, the `FW` hits should be independent of each other, and the resolution of the sub-events can be calculated along the lines of Eq. 38:

$$\begin{aligned} \Re_n^{\mathrm{sub}} &= \langle \cos[n(\Psi_{\mathrm{EP},A(B)} - \Psi_{\mathrm{RP}})] \rangle \\ &= \sqrt{\langle \cos[n(\Psi_{\mathrm{EP},A} - \Psi_{\mathrm{EP},B})] \rangle}\,. \end{aligned} \tag{40}$$

By replacing χ in Eq. (39) with χ^{sub} and inverting the equation, the value for χ^{sub} can be calculated. The values of the resolution parameter for the whole `FW` event is then $\chi = \sqrt{2}\,\chi^{\mathrm{sub}}$, which in turn yields the full resolution $\Re_n$ after inserting it into Eq. 39. From the distribution of the differences between the two sub-event plane angles $\Delta\Psi_{\mathrm{EP}} = |\Psi_{\mathrm{EP},A} - \Psi_{\mathrm{EP},B}|$, shown in Fig. 47 for two centrality intervals, the *resolution parameter* χ can also be calculated with an approximate method [137] using the fraction of events with larger relative angles $\Delta\Psi_{\mathrm{EP}}$ than $\pi/2$:

$$\frac{N(\Delta\Psi_{\mathrm{EP}} > \pi/2)}{N_{total}} = \frac{1}{2}\, e^{-\chi^2/2}\,. \tag{41}$$

The third implementation utilises the following parameterization of the $\Delta\Psi_{\mathrm{EP}}$ distribution [126, 136]:

$$\frac{\mathrm{d}N}{\mathrm{d}\Delta\Psi_{EP}} = \frac{\mathrm{e}^{-\chi^2}}{2}\left\{\frac{2}{\pi}(1+\chi^2) + z\,[I_0(z) + \mathbf{L}_0(z)] + \chi^2\,[I_1(z) + \mathbf{L}_1(z)]\right\} \tag{42}$$

where $z = \chi^2 \cos\Delta\Psi_{EP}$ and $\mathbf{L}_0$ and $\mathbf{L}_1$ are modified Struve functions. If the distribution is normalised to unity between 0 and π, a fit (green

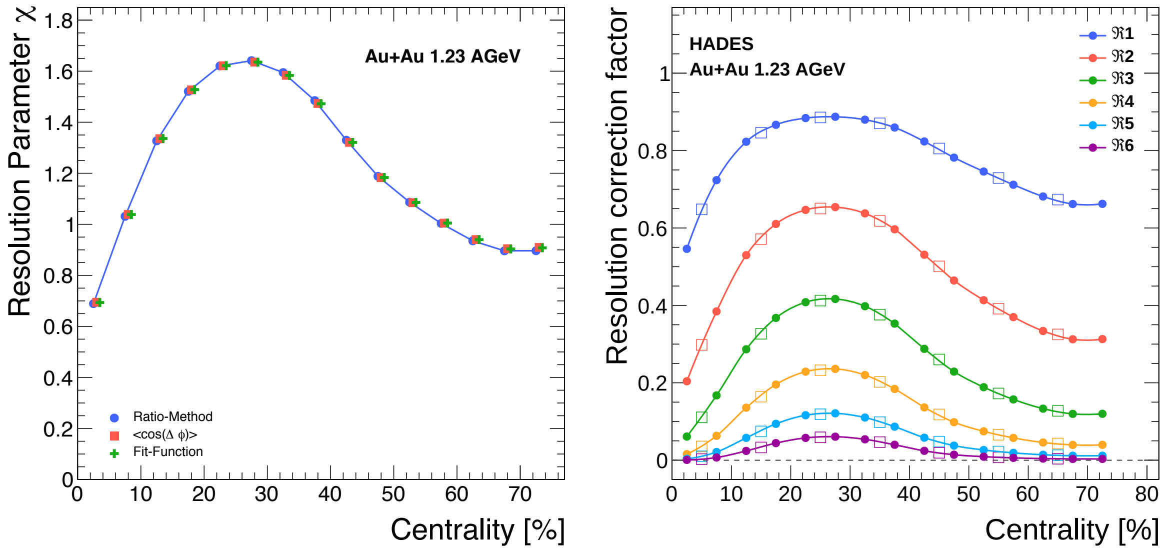

Figure 48: The resulting values for the *resolution parameter* χ from the three methods are presented on the left as a function of the event centrality. On the right the event plane resolution correction factors $\Re_n$ for the flow harmonics of different orders n as a function of the event centrality is shown. The circles correspond to centrality intervals of 5% width and the squares to 10% width (curves are meant to guide the eye).

line in Fig. 47) of Eq. 42 to the data (red dots in Fig. 47) yields the *resolution parameter* χ. Any deviation from the fit indicates additional contributions that do not originate from the directed flow of spectator fragments [108, 291]. On the left panel of Fig. 48 the *resolution parameter* χ from the three methods outlined above are presented as a function of event centrality, and the differences between them are found to be small. Based on the approximation method in Eq. 41, the resulting values for the resolution correction of different orders are summarised on the right side of Fig. 48. In the case $n = 1$ it is found to be approximately 80% and higher in the centrality range $10 - 40\%$, while it drops to a value of $\sim 50\%$ for very central collisions.

The first-order event plane angle $\Psi_{EP,1}$ is determined from the emission angles of the Forward Wall cells hit by projectile spectators and weighed by the charge obtained from the pulse heights in the corresponding cells. The hits are selected such that their flight time and energy deposit in the scintillator cells correspond to the expected values for the spectators. In Fig. 49 the selection cuts used for the flight time and signal height measured in the photomultiplier tubes for one exemplary small inner cell are shown. Individual cuts were generated for all 288 FW cells to increase the separation power for spectator fragments compared to particles from the reaction region or background reactions. The estimated peak positions for $Z = 1, 2$ up to 14 are indicated by a triangle, and the cut-off values used for each charge state are shown as red dashed lines. Depending on the position and efficiency of the FW cell, charge states up to $Z = 16$ can be identified. Between $Z = 1$ and $Z = 2$ hits are located in which two $Z = 1$ particles traverse the `FW`

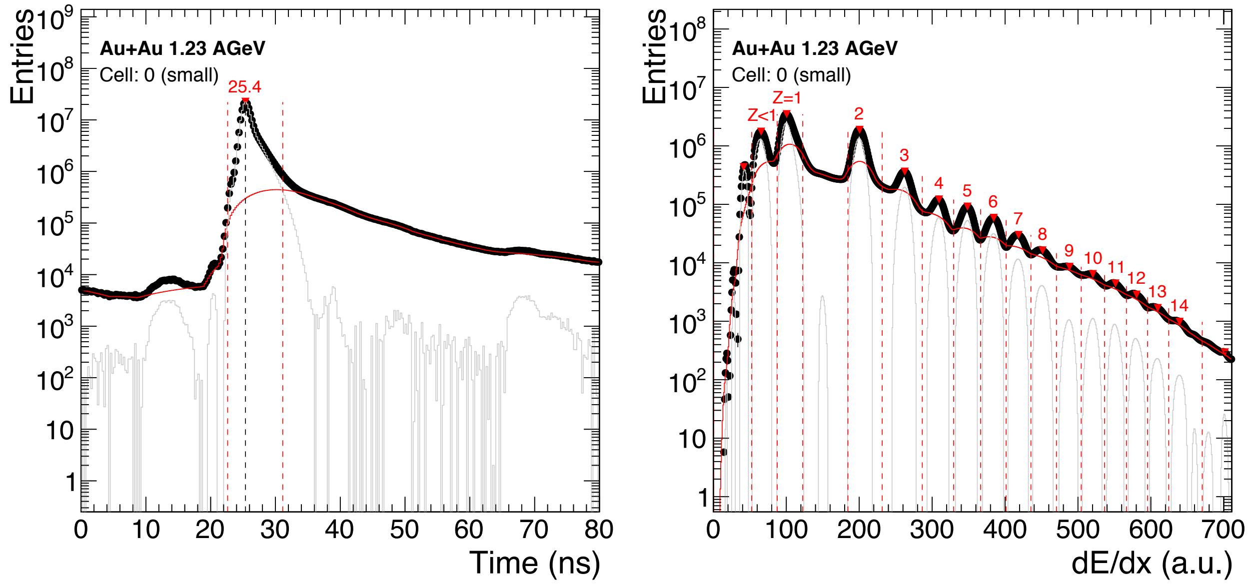

Figure 49: The time distribution (in ns) of individual FW hits in a small, inner FW cell is shown on the left. The most probable value of ~ 25 ns is indicated by a red triangle, and the minimal and maximal timing cuts used in the selection of spectators are indicated by dashed red lines. In the right plot, the charge deposition (in a.u.) in the same small FW cell, after the application of timing cuts, is shown. The estimated peak positions for $Z = 1, 2$ up to 14 are indicated by red triangles. The cut values used for each charge state are indicated by red dashed lines. The red histogram shows the background contribution estimated by the ROOT TSpectrum procedure and the grey histogram after subtraction. Both are utilised in the generation of individual cuts for timing and energy deposition.

scintillator simultaneously within a short time window, such that the readout electronics can not keep the signals apart which are produced by the two energy depositions. The piled-up signals add up to average values smaller than $Z < 2$ in accordance with previous studies [293]. Below the $Z = 1$ peak position and above the electronic noise threshold hits with a charge deposition that is lower than that for $Z = 1$ were measured in all cells of the FW array. The origin of this low signal has not been clarified. Several possible explanations have been investigated, but no firm conclusions have yet been reached. However, it turned out that the timing and azimuthal angle of the corresponding hits are correlated with those of the spectator fragments, so they are included in the sample of hits with charge $Z = 1$ in the EP determination.

Event Plane Correction

A possible detector misalignment and the movement of the beam axis, as well as time-dependent non-uniformities in the FW acceptance caused by inefficient or dead cells, result in a shift of the FW centre relative to the nominal centre of the experimental setup. Therefore, the distribution of FW hits is neither perfectly centred nor symmetric around the origin. The upper panel in Fig. 50 the average positions $\langle X_{\mathrm{FW}} \rangle, \langle Y_{\mathrm{FW}} \rangle$ of the selected spectator hits are shown throughout the beam time. To correct these variations, the standard re-centring method is applied [138]. The individual positions of the FW-hits $X_{\mathrm{FW},i}$ and $Y_{\mathrm{FW},i}$ are shifted by the first

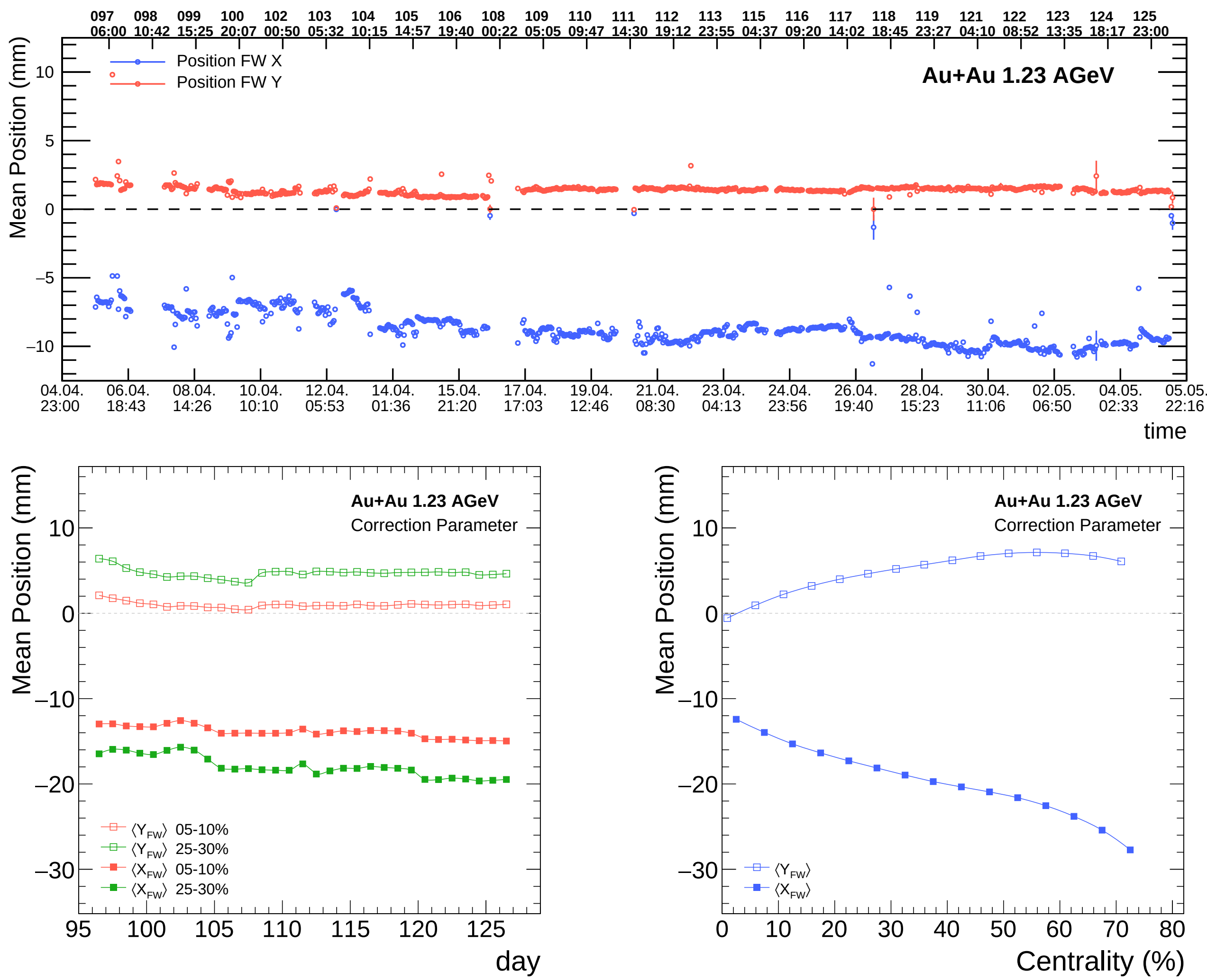

Figure 50: In the upper panel the average position $\langle X_{\mathrm{FW}}\rangle$(blue) and $\langle Y_{\mathrm{FW}}\rangle$(red) of the selected spectator hits over the full duration of the beam time is shown and in the lower panel the values for the first alignment correction for each day of the beam time in two centrality classes ($5-10\%$ and $25-30\%$) (left) and as a function of centrality in intervals of 5% (right).

moments $\langle X_{\mathrm{FW}}\rangle, \langle Y_{\mathrm{FW}}\rangle$ and divided by the second moments $\sigma_{X_{\mathrm{FW}}}, \sigma_{Y_{\mathrm{FW}}}$:

$$\begin{aligned} X'_{\mathrm{FW},i} &= (X_{\mathrm{FW},i} - \langle X_{\mathrm{FW}}\rangle)/\sigma_{X_{\mathrm{FW}}} \, , \\ Y'_{\mathrm{FW},i} &= (Y_{\mathrm{FW},i} - \langle Y_{\mathrm{FW}}\rangle)/\sigma_{Y_{\mathrm{FW}}} \, . \end{aligned} \tag{43}$$

In the lower panel of Fig. 50 the values for this first alignment correction are shown, where the correction is applied for each day of the beam time and for each 5% centrality class. From the aligned X_{FW}- and Y_{FW}-positions of the FW-hits a laboratory angle $\phi_{FW} = \arctan(Y_{\mathrm{FW}}/X_{\mathrm{FW}})$ is calculated. Using the weighted sum of these angles the first-order *event flow vector* $\vec{Q}_1$ and the *event plane angle* is calculated according to Eq. (36) and Eq. (37), using the above described weights $w_i = |Z_i|$. After charge weighting small non-uniformities in the distributions appear again, since the efficiency in the charge detection of individual cells can

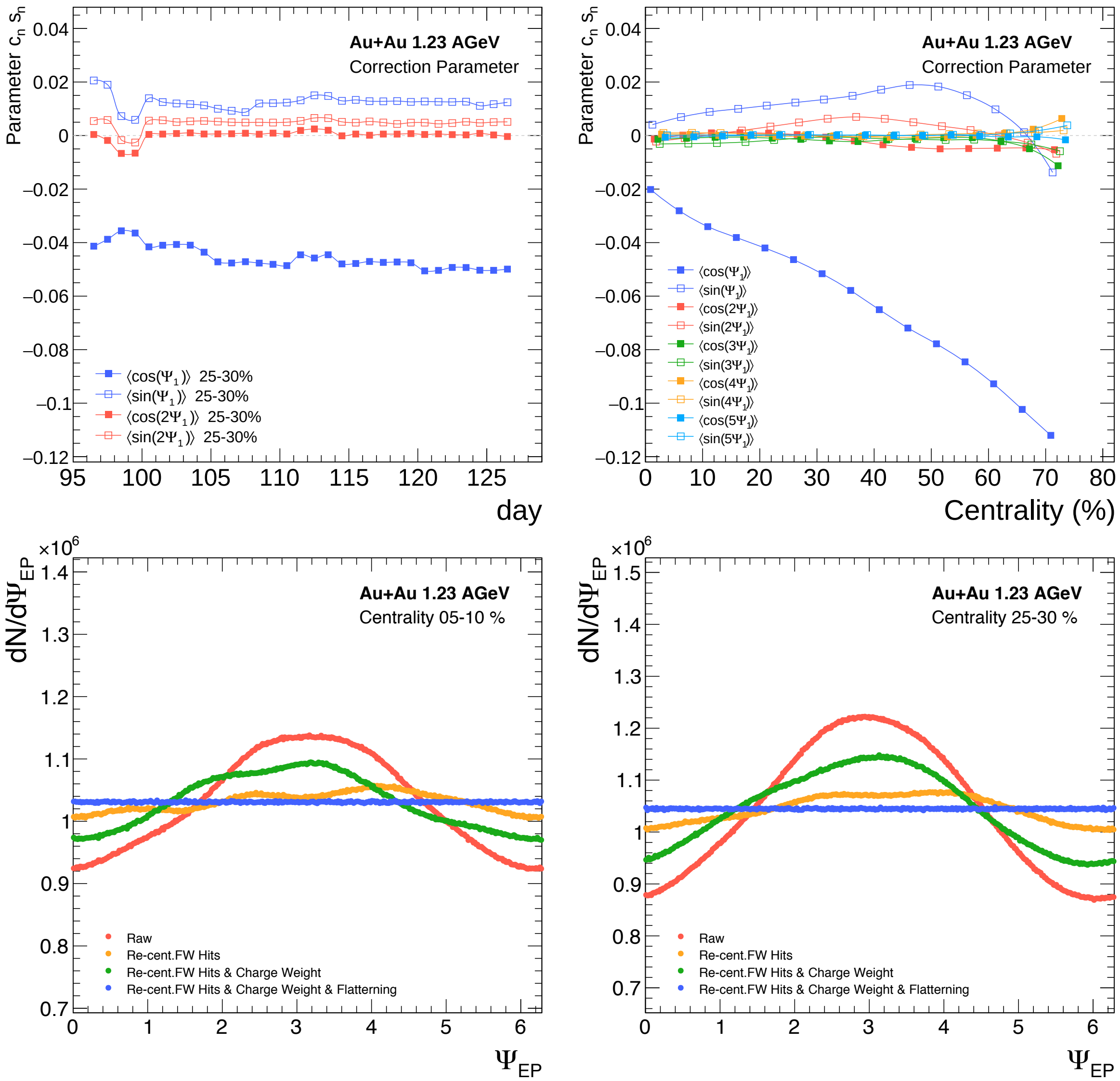

Figure 51: The values for the flattening correction c_n and s_n for the first two harmonics of the first-order EP for the centrality classes $25-30\%$ are shown for each day of the beam time (upper left) and as a function of centrality in intervals of 5% (upper right). The distribution of the event plane angles Ψ_{EP} for central ($5-10\%$, lower left) and semi-central ($25-30\%$, lower right) Au+Au collisions at 1.23 *A*GeV. Shown are the distributions before any correction (red), after applying the re-centering correction (orange), the charge weighting (green) and the final flattening correction (blue).

be quite different. These residual non-uniformities in the EP angular distribution can be removed by an additional flattening procedure [133], where the EP distribution is decomposed into a Fourier expansion:

$$\frac{dN}{d\Psi_{EP}} \propto 1 + 2\sum_{n=1}[c_n \cos(n\Psi_{EP}) + s_n \sin(n\Psi_{EP})] \;, \tag{44}$$

with the cosine $c_n = \langle \cos(n\Psi_{EP}) \rangle$ and sine-coefficients $s_n = \langle \sin(n\Psi_{EP}) \rangle$. These are calculated on an event-by-event basis up to 8$^{\text{th}}$ order for 5% intervals of centrality and each day of beam time individually, and their values are shown in the upper panel of Fig. 51. The large values for c_1 compared to the other values are a consequence of the non-uniformities

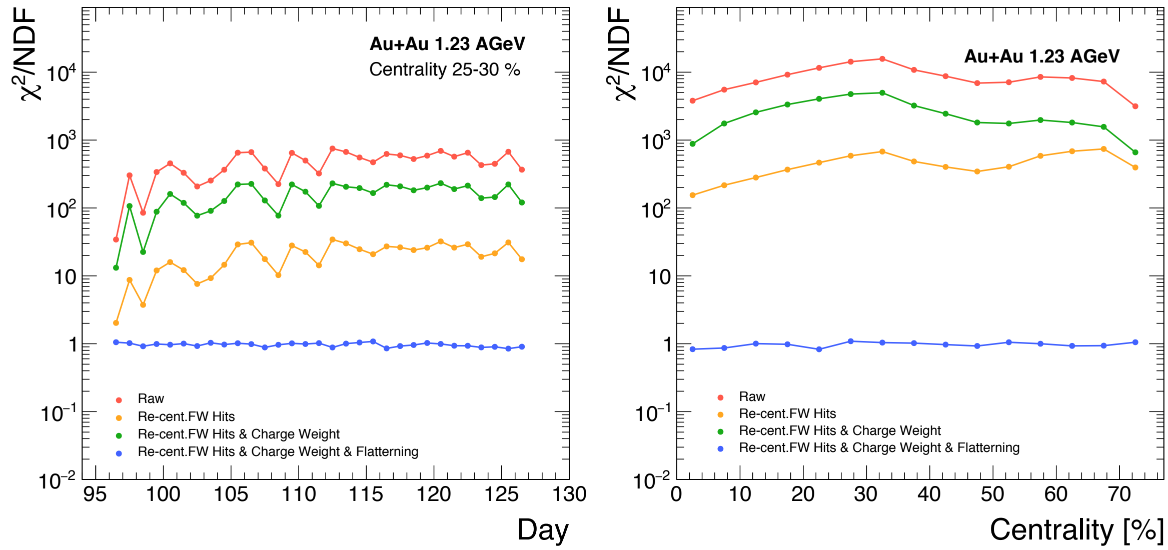

Figure 52: The least-square χ^2 over the degree of freedom to a flat distribution is shown over all days of beam time for semi-central ($25-30\%$) event in the left panel and all centralities in the right. Shown are the relative deviations before (red), after the re-centering correction (orange), after charge weighting (green) and the final flattening correction (green) is applied. After all correction are applied it reaches values around unity for all centralities and all days of the beam time.

introduced after the charge weighting. To flatten the distribution the EP angle is rotated by a corrections angle $\Psi'_{EP} = \Psi_{EP} + \Delta\Psi_{EP}$. The event plane angle Ψ_{EP} and as well its two sub-events planes $\Psi_{EP,A}$ and $\Psi_{EP,B}$ are rotated by the same corrections angle $\Delta\Psi_{EP}$, outlined in [133, 294]:

$$\Delta\Psi_{EP} = 2\sum_n \frac{1}{n}[c_n \sin(n\Psi_{EP}) - s_n \cos(n\Psi_{EP})] \tag{45}$$

In this way the flattening of the distribution does not have any effect on the event plane resolution. In the lower panel of Fig. 51 shows distributions of the event plane angles before and after applying the above described corrections. The uncorrected, raw distributions of the event plane angles $\Psi_{\mathrm{EP},1}$ in semi-central $25-30\%$ and most central $5-10\%$ classes are shown as the red curve. As a result of the re-centering correction (orange) the distributions show a more uniform pattern where residual next order harmonics are still visible. After the charge weighting (green) non-uniformities in the distributions appear again. And after the final flattening correction is applied, Ψ_{EP} is distributed uniformly in all centrality classes and remaining deviations from a flat distribution are found to be below 0.1%. To quantify possible remaining distortions, the χ^2/NDF with respect to a flat distribution is shown for all days of the beam time (left) and all centralities (right) in Fig. 52. After all corrections are applied the goodness of fit χ^2/NDF to a flat distribution reaches values around unity for all centralities for all days of the beam time.

Track Reconstruction

Charged particles traversing the cells of the drift chambers MDC ionise the counting gas and an avalanche of electrons induces electronic signals, which are read out from the sense wires. Drift cells with measurable signals on the sense wire are denoted as *fired drift cells*. The spatial informations for individual *fired drift cells* are correlated during the search for possible *track candidates*. The intersection points of the *track candidates* are matched to the nearest hit positions in TOF, RPC, PreShower or ECAL and to rings in the RICH detectors. The accuracy of the trajectory is improved by fitting it to a precise track model including the strength and orientation of the toroidal magnetic field. By utilising the measured drift time of the electron cloud from the ionised trajectory up to the sense wires, the precision of the position, originally on the order of the cell size ($5-14$ mm), can be further improved to $0.1-0.2$ mm, as shown in Fig. 24. In the reconstruction procedure the following steps are performed while searching for all possible *track candidates* [219, 296]:

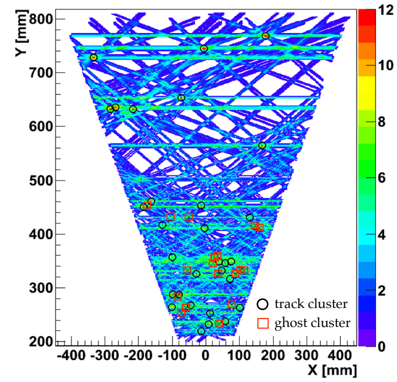

Figure 53: The projections of *fired drift cells* onto a virtual plane are shown with individual *wire clusters* up to a maximum of 12 contributing layers. Based on their particular properties *track clusters* (black circles) and *ghost clusters* (red boxes) are identified and drawn on top. The figure is adapted from [295].

- The positions of all *fired drift cells* in the inner two drift chambers and the outer two chambers are projected onto two virtual projection planes. Since the outer chambers are parallel, their projection plane is chosen to be centered in between the two, while the position and orientation of the projection plane between the inner chambers is adjusted such that all projections of the drift cells are of similar size. For the inner chambers, all projections onto the plane are implemented such that they point towards the center of the target. In Fig. 53 the spatial correlations of all *fired drift cells* projected onto a virtual plane between the inner chambers are shown with individual *wire clusters* up to a maximum of 12 contributing layers.

- *Wire clusters* are the local maxima found in these projection planes, based on the number of contributing wires and the width of the clusters. They define the intersection points of straight lines through the projection planes. With rising multiplicities the probability that fired wires cross each other at several places in the projection plane increases, resulting in so-called *ghost clusters* not originating from real particle tracks. Due to their particular properties, like their smaller average amplitudes and width, they are removed from further reconstruction. In Fig. 53 examples of identified *track clusters* are shown as black circles and *ghost clusters* as red boxes.

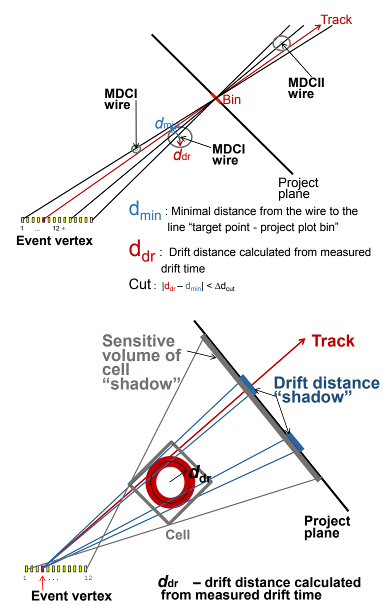

Figure 54: Illustration of the *cluster vertex finder* in the upper part, extrapolating the *wire clusters* towards a common vertex position. The scheme below shows the next step in reconstructing *track segments*, by utilizing the measured drift time information to improved the projection resolution. Figure taken from [251].

- For the inner chambers the *wire clusters* are extrapolated towards a common target position at the fixed Z-positions of the 15 target segments and the START detector, estimated by the *cluster vertex finder*, shown in the upper part of Fig. 54. The drift time information is further used to constrain the projection volume, displayed in the lower part of Fig. 54. Since the magnetic field almost vanishes in the region between the two inner and outer chambers, it is a reasonable approximation to construct straight *track segments*. In the inner chambers the estimated target position, together with the *wire clusters*, are used to construct straight *track segments* and in the outer drift chambers the *wire clusters* of one sector are extrapolated to intersection points with the inner *track segments* on the *kick plane*.

- The spatial and angular precision of the *track segments* is improved by incorporating the distance from each fired sense wire into the straight trajectory model using a minimisation procedure. The distance is inferred from the measured drift time in each cell, which is calibrated based on GARFIELD simulations [210, 296] and test measurements. Weighting factors are calculated dynamically at each step according to a Tukey weight distribution to minimise the influence of uncorrelated noise or drift times from other tracks [297]. In addition, *track segments* are rejected if the measured drift times are not compatible with the calculated drift distances. In an iterative procedure, *track segments* are flagged as *real* or *fake segments*, based on the fraction of wires shared with other segments or with segments already marked as *real*.

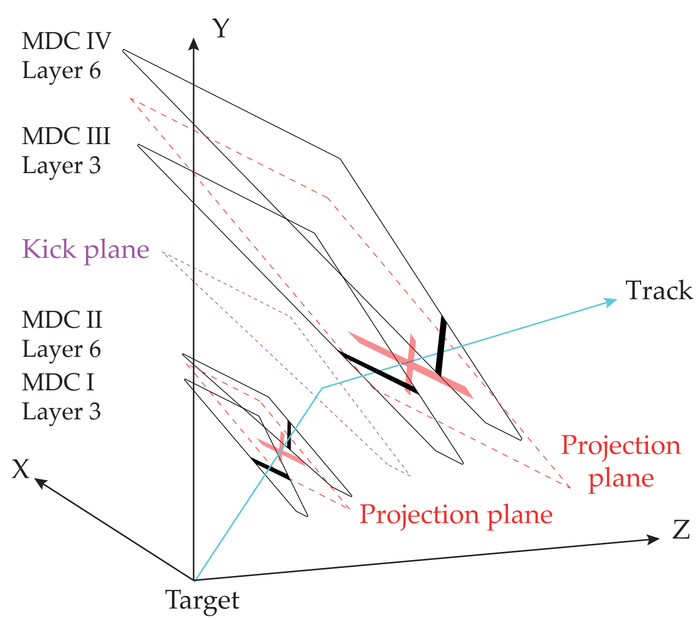

Figure 55: Principle of the track candidate search in the four MDC planes. The intersection point of the extrapolated inner track segments with kick plane is used as initial point for finding outer track segment. For each of the four MDCs one layer is shown. Figure from [219].

- The deflection of a charged particle track in the toroidal magnetic field is approximated by a momentum kick in a virtual *kick plane* between the inner and outer chambers. This kick angle is used in the extrapolation of the *track candidates* (see Fig. 55).

- In an additional iteration *fired drift cells* of the inner drift chambers, which were not assigned to the already reconstructed *track candidates*, are searched and fitted for additional *off-vertex track candidates*.
- The *track candidates* are matched to the hit points of the two `META` detectors `TOF` and `RPC` and, for electron identification, to rings of the `RICH` detector or a detected electron shower in the `PreShower` detector or `ECAL`.
- For the *momentum determination* two successive methods are used. The *spline* method utilises a three-dimensional magnetic-field map and a cubic spline to model a smooth trajectory passing through the detector hit points. The resulting momentum estimate and particle polarity is used, together with the global vertex and `META` hit information, as the initial condition for the iterative *Runge-Kutta* method. The *Runge-Kutta* method solves the equation-of-motion in a known magnetic field in a recursive way. A least-square minimisation procedure estimates the parameter of the charged-particle trajectory and, in addition, provides the specific χ^2_{RK} as a track quality criterion.

It is inherent to this combinatorial approach, that with rising multiplicities the number of possible combinations rises exponentially. In principle each inner *track segment* can be matched to maximally 3 rings in the `RICH` and each outer *track segment* to maximally 3 hits in each `TOF`, `RPC`, `PreShower` and `ECAL`. On other words, hits in `TOF`, `RPC`, `PreShower` and `ECAL` can be matched to an unlimited number of *track candidates*. It is crucial for the matching steps, that conditions are applied to reject un-physical combinations. These conditions are optimised to reject as few as possible real tracks and to select only trajectories who are as close as possible to the original particles. To quantify the quality of individual track hypothesis several *track quality parameters* are calculated in the fitting and matching steps. Following the matching step a track sorting algorithm is performed, where *track candidates* are *pre-selected* based on the following minimal requirements:

- the *track candidates* are not flagged as *fake*, have a successful fitted inner and outer segment and a matched hit or cluster in the `META` detectors.
- the Runga-Kutta track-fitting procedure has converged and the *Goodness-of-Fit* for the *track candidate* is below $\chi^2_{RK} < 1000$.
- the *track candidates* are matched to points inside the volume of the rods of the `TOF`, respectively cells of the `RPC` detector. In the y-direction the extrapolated intersection point from the Runga-Kutta

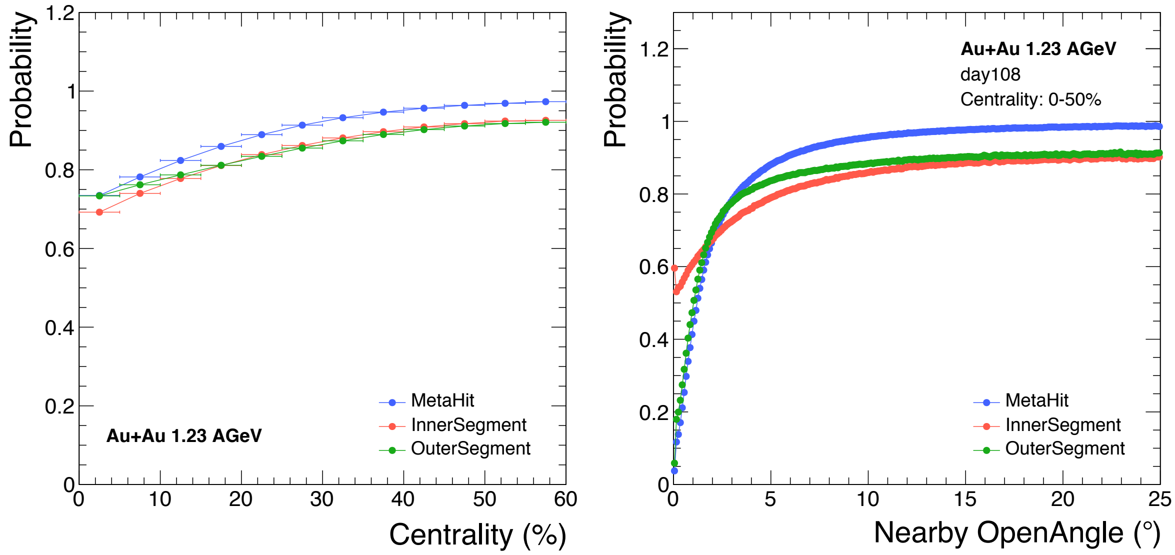

Figure 56: The probability for an uniquely *selected track* not sharing a META-hit (blue), an inner (red) or outer (green) segment with an other *track candidate* is shown as a function of centrality (left panel).

track should lie inside the dimension of the particular rod or cell. The deviation in x-direction, quantified by the *META matching quality*, *i.e.* the normalized distance between extrapolated measured position along the `META` detector, should be smaller than $Q_{MM} < 3$.

- the matched time-of-flight from the `META` hit should be below 60 ns and the calculated velocity above $\beta > 0$.

In the ideal case each real particle should have only one inner and one outer segment, and one hit or cluster in any of the time-of-flight detectors. With this assumption the list of *track candidates* are sorted according to their *Goodness-of-Fit* χ^2_{RK} and the best candidates are flagged. The contributing segment and hits/clusters can not be used again by candidates following in the list. These flagged best candidates are called *selected tracks* and their subset are the *primary tracks*, which fulfil the additional condition to have a *distance of closest approach* to the primary vertex below $d_{min} < 10$ mm. In the case that more than one particle is hitting the same rod or cell of one of the time-of-flight detectors, only the signal of the first hit is detected and the timing and position information of the faster particle will be used. For this *occupied* detector the situation can happen, that a wrong flight time is matched to a reconstructed *track candidate* with better quality parameters and the particle can not be correctly identified. In the left panel of Fig. 56 the probability for an uniquely *selected track* not sharing `META`-hits, inner or outer segments with any other *track candidate* is shown as a function of centrality. The probability that the `META`-hit of a *selected track* is shared by other *track candidates* is around 25% in most central events [251, 253]

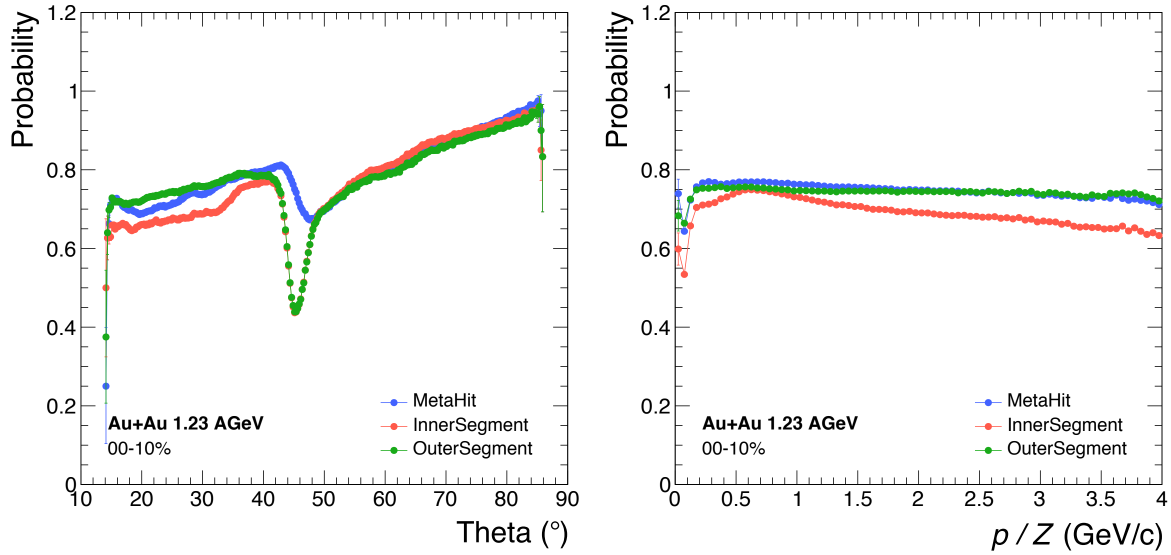

Figure 57: The probability for an uniquely *selected track* not sharing META-hit (blue), inner (red) or outer (green) segments with other *track candidates* as a function of polar angle θ (left) and as a function of rigidity p/Z (right) for the most 10% central events.

and decreases to few percent in peripheral events. The probability for sharing an inner or outer segment with any other *track candidate* is in general several percent larger than sharing a `META`-hit. The centrality dependence is the direct consequence of rising combinations due to larger multiplicities. The right panel in Fig. 56 shows the same probabilities as a function of the *opening-angle* to nearby *track candidate* in the centrality class $0-50\%$. The *nearby opening-angle* is used here as a measure for the volume around a reconstructed track, where hits or segments of a close by *track candidate* are confused and not used in the reconstruction. This effect of inefficiencies in the track reconstruction is mainly dependent on two factors, the multiplicities and owing to the geometry of the detector on the polar angle of the particle. In the left panel of Fig. 57 this probability is shown as a function of the particle polar angle θ for the most 10% central events. As already shown, the multiplicities at large polar angles are low relative to the detector granularity, resulting in values of approximately 95%. However, towards lower polar angles, the track densities and the contribution of background reactions, such as δ-electrons, in the detectors increase, leading to probabilities of approximately 70%. In the overlap region between `TOF` and `RPC`, an increase from 65% to 80% not sharing a `META`-hit can be observed because of the change in granularity between the two detectors systems. In the same polar angle region, a significant drop in the probability of a uniquely *selected track* not sharing either an inner or outer track segment towards values of approximately 45% can be seen. The right panel in Fig. 57 shows the same probabilities as a function of the particle rigidity p/Z, whereby a slight decrease towards larger rigidities is visible. At

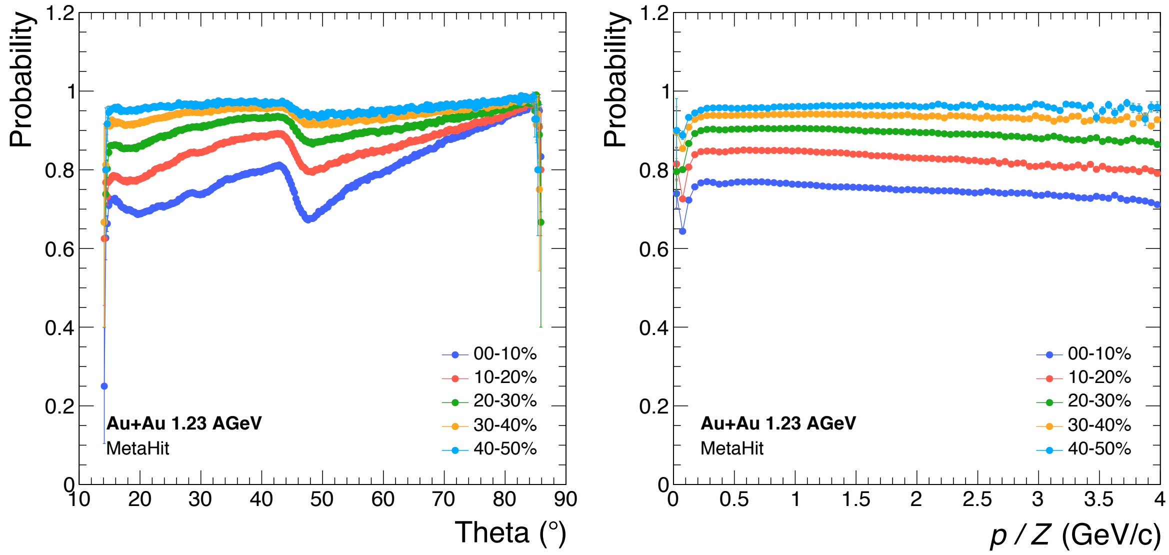

Figure 58: The probability for an uniquely *selected track* not sharing META-hit as a function of polar angle θ (left) and as a function of rigidity p/Z (right) in intervals of 10% event centrality.

large momenta the trajectories of the particles are nearly straight tracks, which in the case of low polar angle with large track densities increases the chance of hitting an already occupied `META` rod/cell. In Fig. 58 the probability of an uniquely *selected track* not sharing `META`-hit is again presented as a function of the polar angle θ on the left and as a function of rigidity p/Z on the right, but for different centrality intervals of 10% width. In general, towards peripheral centralities, the probability of not sharing a `META`-hit increases to values for single-track events, where the value would be 100%.

Occupancy

Depending on the application, several definitions of *occupancy* are used. The general one used in the context of detector readout is defined as the ratio of active cells occupied by signals to the total number of available cells. In the following, occupancy is used as a measure for the averaged track or hit multiplicity per event in a *certain active* detector element, or as a synonym for the particle flux, defined as the number of particles per event in a differential solid angle $d\omega = d\theta d\phi$ in units of $1/(°)^2$ for the polar and azimuth angle. Contrary to the approach used here, the track density can also be defined for an equal sized area with the differential solid angle $d\Omega = \sin\theta d\theta d\phi$.

The high-multiplicity environment present in heavy-ion reactions poses a challenge in terms of an efficient detection of individual charged particles. Large charged particle densities result in a high detector occupancy. Three main effects have to be considered in the context of occupancy. The first is the phase space population of particles, which means that with increasing energy, more particles are produced and, in the fixed target configuration, an increasing number of particles are emitted in the forward direction around the beam line. Second, depending on the magnetic field configuration (dipole, solenoid, or toroidal), the particles can be spread out or be collimated. The third point is the granularity of the individual sub-detectors. Ambiguities in the allocation of detector hits in the reconstruction of multiple particles result in inefficiencies which depend on the local particle densities. Non-isotropies in the flux of particles caused by flow effects generate

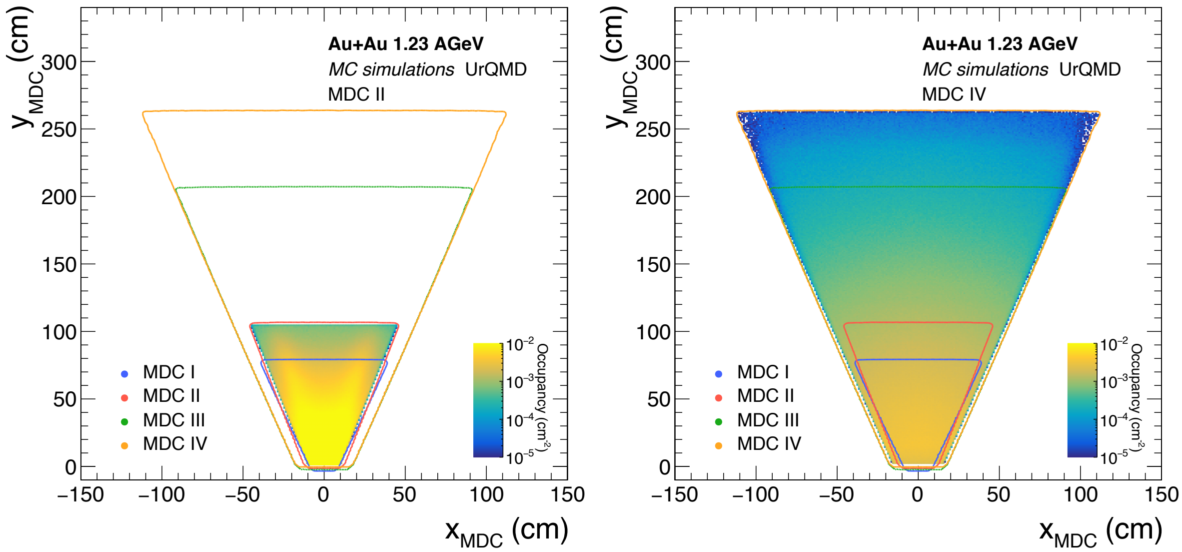

Figure 59: The occupancy in the second (left) and last (right) drift chambers (MDC II & IV) in one sector, simulated with UrQMD and GEANT for the most central event class $0 - 10\%$, is shown as function of the x- and y-coordinate along the MDC. Additionally, the contours of the other MDC chambers are overlaid.

local modulations in the particle densities. If these modulations develop hotspots in parts of the detector with reduced reconstruction efficiencies, this will distort the measurement of the flow coefficients. To account for this, any efficiency correction in the flow measurements must incorporate the orientation relative to the event plane in the correction scheme.

Distortions in the flow spectra were studied by the FOPI collaboration, where they concluded that *track-density effects lead to a loss of particles in the directed flow direction* [298]. The effects themselves could be simulated using the detector simulation based on GEANT [245], but not with sufficient accuracy to be used as a correction. An empirical method was introduced with the requirement that in symmetric collision systems the directed flow values v_1 should vanish at mid-rapidity and should be point-symmetric with respect to it. The FOPI collaboration used the so-called *quadrant method* to calculate the flow coefficients v_1 and v_2, with which it is feasible to correct the number of detected particles for each of the four quadrants relative to the event plane before calculating the final flow values. The correction factors, resulting in an effective shift of v_1, are adjusted with the assumption that the detection losses are linearly growing with the local track densities [131, 299]. Similar distortions of flow measurements due to occupancy effects are also reported by the E877 collaboration [300] and two data-driven correction methods based on the measured track density are successfully applied. In the first method a weight is assigned to each detected track that accounts for the loss of tracks in its vicinity [301]. In the other method pairs of tracks are rejected if their minimum separation in one of the

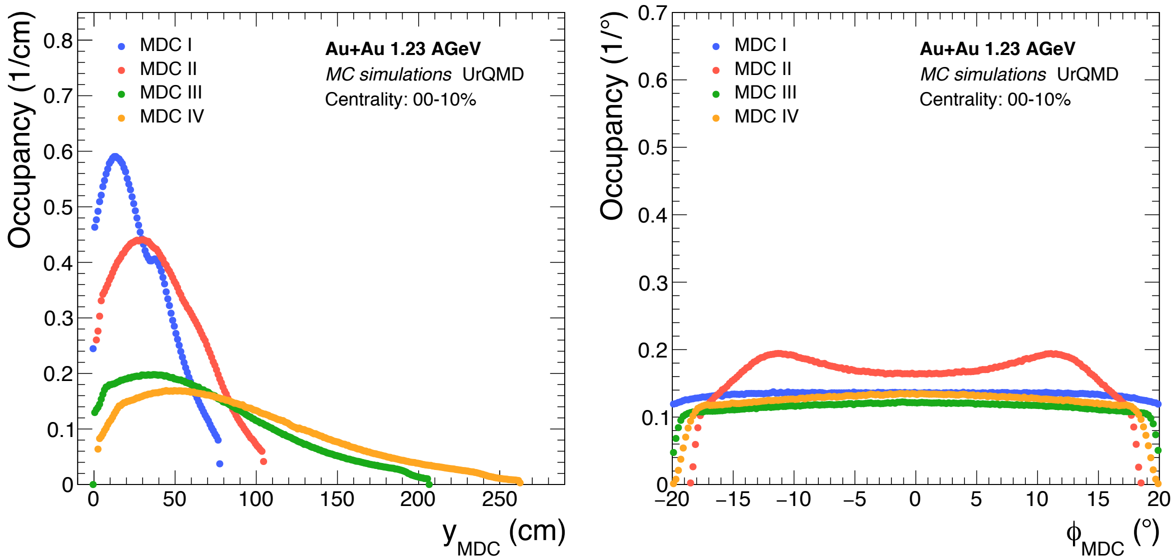

Figure 60: The occupancy projected along the y-coordinate (left) of four differently sized MDC drift chambers of a given sector, simulated with UrQMD and GEANT is shown for the most central event class $0-10\%$ in the left panel and as a function of the azimuth angle ϕ_{MDC} (right).

tracking detectors is below a certain value. The bias introduced by the cut was studied and corrected with embedded tracks [302–304]. Furthermore, the PHOBOS [305, 306] and the WA98 collaboration [307, 308] investigated occupancy effects in their detectors systems and used corrections based on Poisson statistics of multiple hits in a given detector cell.

In the case of HADES, the effect of the occupancy was studied in simulated data, generated using the UrQMD [270, 309] event-generator and GEANT 3.21 [245], combined with a detailed description of the magnetic field configuration and the detector geometry and response. The magnetic field strength in the HADES setup reaches its highest values in the centre of a given sector between the two surrounding magnetic coils and between the second and third MDC. In the upper left panel of Fig. 59 the occupancy in the second drift chamber (MDC II) is shown for the most central event class $0-10\%$ as a function of the x- and y-coordinate along the MDC. For comparison the contours of the four differently sized MDC chambers are overlaid. Since MDC II is near the magnetic field a distinctive V-shape is visible. The occupancy in MDC IV is shown in the upper right panel of Fig. 59, which exhibits a much more uniform distribution over a larger area. Both chambers show a distinctive increase in occupancy in areas closer to the beam line. In the left panel of Fig. 60 the projection of the particle flux per event along the y-direction of all MDC chambers are displayed and in right panel as a function of of the azimuth angle relative to the centre of the chamber ϕ_{MDC} (right). The maximal occupancy in the y-coordinate in units of $1/\mathrm{cm}$ is reached in the innermost chamber (MDC I) at $\sim 60\%$

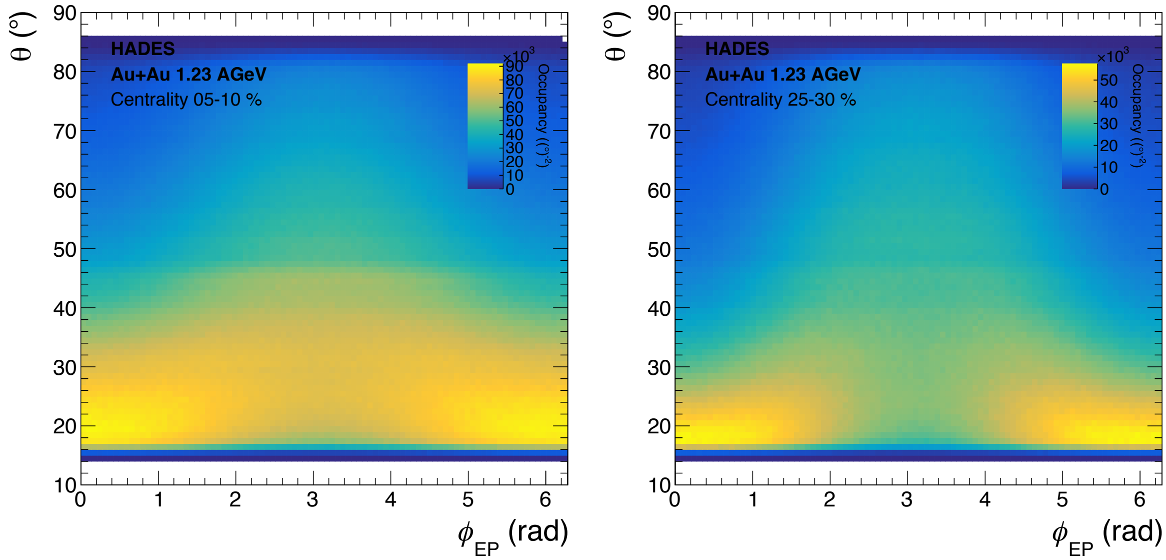

Figure 61: The track density matrices $\rho_{\text{tracks}}(\theta, \phi_{EP})$ shown as a function of the polar angle θ and the difference between the azimuth angle and the event plane angle $\phi_{EP} = \varphi - \Psi_{\text{EP}}$ for two different centrality classes (left: $5-10\%$, right: $25-30\%$).

and is nearly 3 times as high as in the outer chambers (MDC III and IV). The much smaller size of the inner chambers has the trivial effect of an increase of occupancy. The inner chambers are also directly affected by the δ-electrons produced by the incoming beam ions, which are also incorporated into the simulations. Their flux is independent of the event centrality and their emission is isotropic and not correlated with the event plane. In the first MDC a drop of particle flux per event below $\sim 50°$ can be observed, where a 5 mm thick polypropylene shield is installed to absorb a large fraction of the δ-electrons. MDC II shows an increase of a factor 2 in occupancy in comparison to the other chambers, if projected on the azimuth angle ϕ_{MDC}. The efficiency correction method extracted from MC simulations, which is commonly used to correct particle yields and spectra, was extended to include the additional effects originating from an event plane dependent flow. But it turned out that this approach was not sufficiently accurate to be used as a direct correction for the flow spectra. Several shortcomings could be identified, but were not solvable in simulation. Beside the much weaker strength of flow provided by the event-generator, the simulated particle chemistry and phase space population differs with respect to real events. Additionally, to incorporate the effects of occupancy in the different *digitizers*, modelling the detector response, on a sufficient level is a challenging task. Since in the most commonly used hadron transport code UrQMD the projectile spectator are simulated as individual protons and neutrons, a significant fraction of light nuclei are missing. This has the consequence that the event plane reconstructed by simulated protons exhibits different properties than the measured event

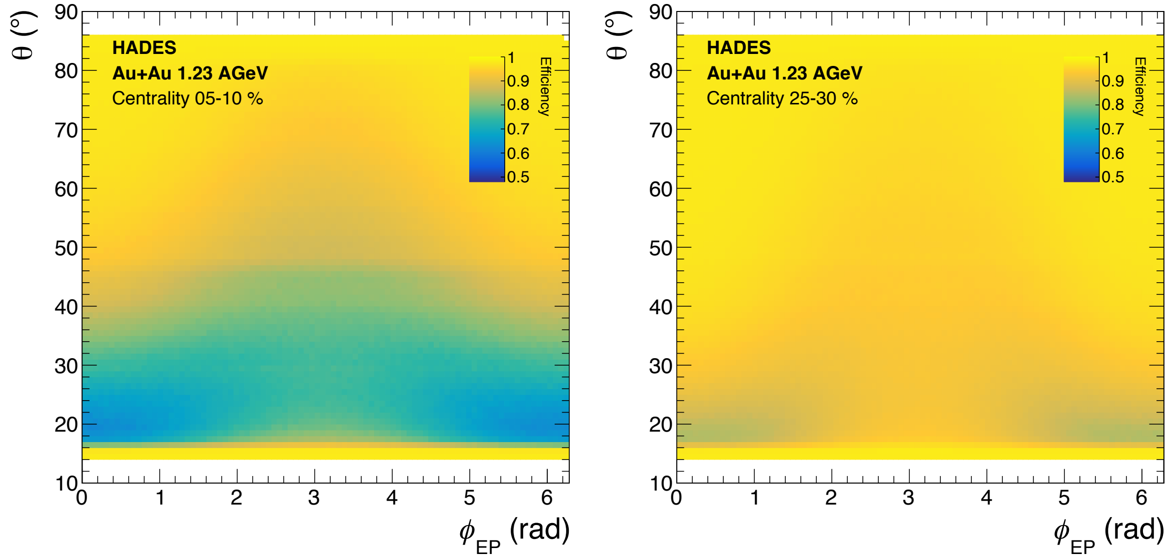

Figure 62: The efficiency matrices $\epsilon(\theta, \phi_{EP})$ as a function of the polar angle θ and the difference between the azimuth angle and the event plane angle $\phi_{EP} = \varphi - \Psi_{\mathrm{EP}}$ are shown for two different centrality classes (left: $5-10\%$, right: $25-30\%$).

plane. Consequently, several data-driven methods were investigated, utilising either local multiplicities as a function of the event plane or global observables directly sensitive to the event-by-event activity in parts of the detector. One approach that was developed is to use for each reconstructed track the local wire multiplicities in the vicinity of its fired wire to estimate the local occupancy. The advantage of such an approach is that this directly probes the reconstruction efficiency without the further need to differentiate between event multiplicities or event plane orientation. A modification of this method was successfully used as a rejection cut in the intensity-interferometry analyses of pion pairs [256, 310, 311]. In this studies, it turned out that the local wire multiplicities also showed an sensitivity to additional correlation between individual track candidates. The drawback of this method is that the full DST production had to be redone in order to provide access to this observable. Therefore, a pragmatic approach to correct for efficiency losses was proposed [312], which can be applied as weight track-by-track. The measured average local track density per event and differential solid angle $\mathrm{d}\omega = \mathrm{d}\theta \mathrm{d}\phi_{EP}$

$$\rho_{\mathrm{tracks}}(\theta, \phi_{EP}) = \mathrm{d}\langle N_{\mathrm{tracks}}\rangle / \mathrm{d}\omega \tag{46}$$

is stored for each centrality class in two-dimensional density matrices for $1° \times 1°$ intervals of the polar angle θ and relative azimuth angle $\phi_{EP} = \varphi - \Psi_{\mathrm{EP}}$.The upper panel of Fig 62 show as an example the matrices for two centrality classes ($5-10\%$ and $25-30\%$). With the following equation:

$$\epsilon(\rho_{\mathrm{tracks}}) = \epsilon_{\mathrm{single}} - c_{\epsilon}\, \rho^2_{\mathrm{tracks}} \tag{47}$$

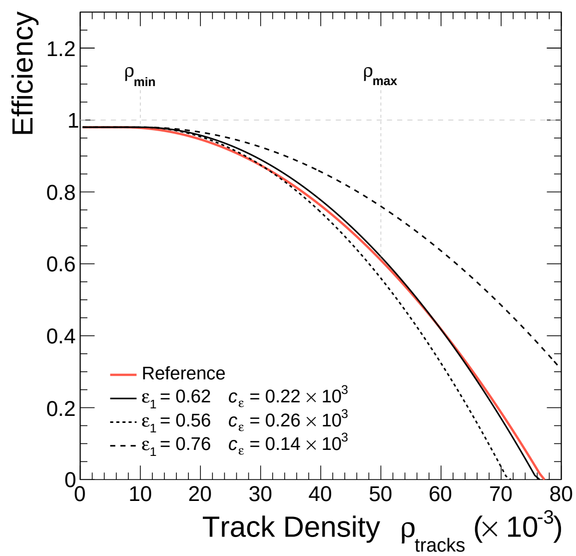

Figure 63: The efficiency of the track reconstruction as a function of the local track density (in arbitrary units) is shown as solid black line as parameterized in Eq. (47) for the nominal value of the lowest efficiency ϵ_1. The lower and upper limits (dashed and dotted lines), determined as part of the systematic uncertainty are displayed as well. For comparison the parameterization of the reference implementation [312] is shown as red line.

the relative efficiency tables $\epsilon(\theta, \phi_{EP}, \text{cent.})$ are then determined as a function of the local track density ρ_{tracks}. The calculated efficiency matrices $\epsilon(\theta, \phi_{EP})$ are displayed in Fig. 62. A similar parameterization is used in the Glauber MC approach to describe the multiplicity dependent efficiency loss in the centrality determination. The following formulation of the slope parameter c_ϵ:

$$c_\epsilon = (\epsilon_{\text{single}} - \epsilon_1)/(\rho_{\text{tracks}}^{\text{max}} - \rho_{\text{tracks}}^{\text{min}})^2 \,, \tag{48}$$

is adjusted only by the lowest efficiency ϵ_1, which is expected in the region with the highest track multiplicity $\rho_{\text{tracks}}^{\text{max}}$ reached in the most central event class. This form is convenient because it always remains between the minimum $\rho_{\text{tracks}}^{\text{min}}$ and maximum $\rho_{\text{tracks}}^{\text{max}}$ values of the track density and is independent of its normalisation and the size of the solid angle. The optimal value for the single-track efficiency of $\epsilon_{\text{single}} = 0.98$ is determined from simulations and corresponds to the region with the lowest track density, $\rho_{\text{tracks}}^{\text{min}}$ in the most peripheral centrality class. In Fig. 63 the parameterization Eq. (47) with three values for the lowest efficiency ϵ_1 and the corresponding slope parameters c_ϵ from Eq. (48) are shown. The quadratic form of Eq. 47 is motivated by MC simulations of protons and also used for deuterons and tritons, but can be different for other particles. In this phenomenological approach the parameter ϵ_1 is adjusted such that for mid-rapidity $y_{\text{cm}} = 0$ the condition $v_1 = 0$ is fulfilled for all three hydrogen isotopes, as required by the symmetry of the reaction system. The nominal value for ϵ_1 is shown together with its lower and upper limit. These limits are determined as part of the systematic uncertainty and are discussed later in this chapter. The above defined efficiency is then used to weight all tracks entering the calculation of the flow coefficients according to

$$w_{\text{eff}}(\theta, \phi_{EP}, \text{cent.}) = 1/\epsilon(\theta, \phi_{EP}, \text{cent.}) \ . \tag{49}$$

Based on the same correction method the anisotropic flow for pions [313], kaons [258], lambdas [257] and electrons [314] is studied as well. This correction method is validated by the data-driven measure previously described in the section track reconstruction. This measure, which is defined as the probability that a META-hit, an inner or an outer track segment is shared by several *track candidates*, can be extended to incorporate the azimuth angle relative to either the event plane or reaction plane. An main advantage of this approach is that in first order it is not largely biased from the procedure to determined the event plane and its resulting resolution and be both applied to data and simulations.

Particle Identification

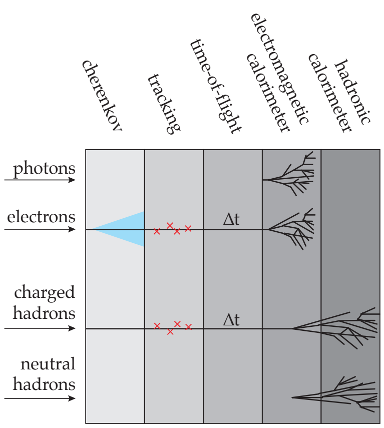

Figure 64: Particle detectors consist of several layers of specific sub-detector systems with certain sensitivity to the specific characteristics of the particle.

The detection of charged particles is based on their interactions with the active material of a detector [235], mainly due to their ionisation power. Detector systems consist of several specialised sub-detectors for different purposes. The criteria used to evaluate and design detection systems are substantially the fiducial acceptance, the granularity, the charge and mass identification, and the range and resolution of the energy or momentum measurement [315]. Owing to the intrinsic accuracy of each instrumentation, a dedicated calibration scheme is required to achieve high performance. A very important aspect of a detection setup is its architectural redundancy, which enables the cross-calibration and ensures the robustness of measurements. In Fig. 64 the several layers of detection sub-systems are sketched in a typical hierarchical structure, sorted from least-invasive measurements, *e.g.* in gaseous *Cherenkov* and *time-of-flight* detectors and than destructive ones in *electromagnetic* and *hadronic calorimeters*. For tracing the flight path of a particle through the detector setup individual position measurements are combined and for the determination of its time-of-flight at least two time measurements are needed, often at the beginning and end of the setup. From the combination of path length and flight time, the *velocity* of the particle is calculated. The velocity of a relativistic particle can be further measured using Cherenkov- or transition-radiation. Due to the *rigidity* of charged particles in the known magnetic field of the spectrometer, the *momentum* and *polarity* of a particle is measured from the curvature and direction of its trajectory. For the identification of the particle type (PID), the combination of *velocity* together with a *momentum* or *energy* measurement enables the determination

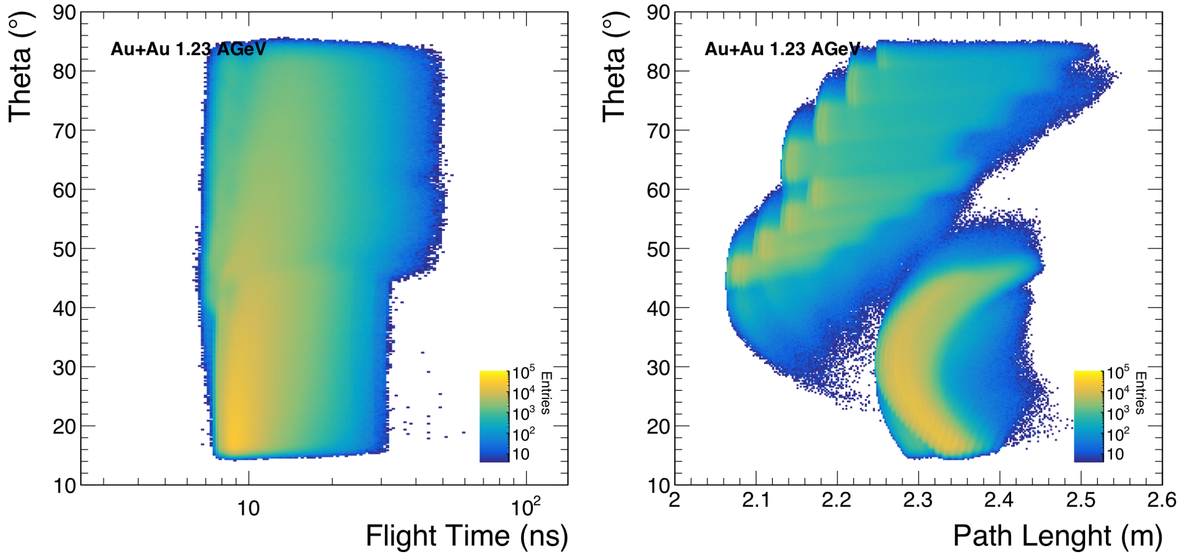

Figure 65: Distributions of the time-of-flight (left panel) and path-length (right panel) as a function of the inclination angle θ of the measured particle.

of its *mass*. The *charge* can be inferred from the measurement of its *specific energy loss* either in gaseous ionisation detectors or in scintillators. Unstable particles decay before reaching the detector setup and are thus reconstructed by their charged decay products with the *invariant mass method*. The *energy* of photons and electrons are detectable in electromagnetic, and the one of hadrons in hadronic calorimeters.

The HADES setup is primarily designed as a di-electron spectrometer (see chapter HADES). One of its main goals is to achieve an excellent electron-hadron separation, which however results in the simultaneous measurement of hadrons (π, K, p) and light nuclei (d, t, ^{3}He, ^{4}He). The time-of-flight method makes it possible to separate particles based on their mass over charge ratio, due to the excellent momentum resolution and precision of the time measurement of HADES. To achieve a good mass and charge separation a combination with the energy loss measurement is necessary.

Time-of-Flight measurement

The distributions of time-of-flight and path-length as a function of the polar angle θ of the measured particle is shown in Fig. 65. By measuring the time-of-flight of a charged particle traversing a known distance its velocity can be determined. The event time of the reaction T_0 is provided by the `START` detector and the T_0 reconstruction method, and the arrival time t_{hit} is measured in the META-detectors `TOF` and RPC. The difference results in the time-of-flight $t = t_{\text{hit}} - T_0$ of a particle.

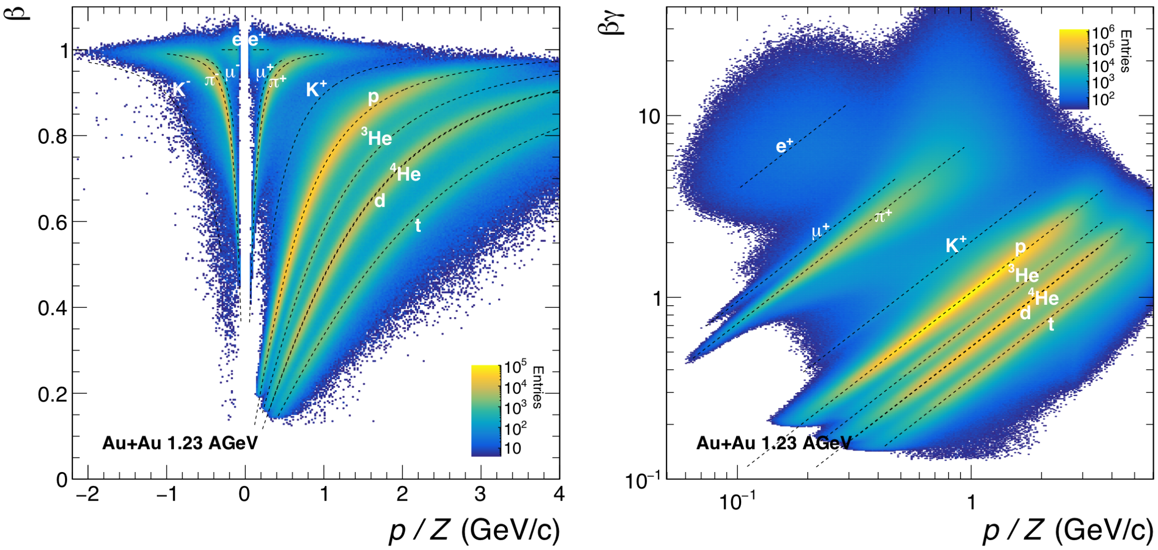

Figure 66: Correlation between rigidity p/Z and the velocity β (left) and $\beta\gamma$ (right). On the left for all selected tracks and on the right only for positive particle. The black lines correspond to the expected values for the different particle species according to the equation 51.

Here the speed of light in vacuum $c = 299.792458$ mm/ns is used as conversion unit, whereby in the following natural units are used with $c = 1$. And although in general the charge of a particle is defined as the multiple of the elementary charge $q = Ze$, in the following *charge* refers to the charge number Z.

The velocity β of a particle and the relativistic Lorentz factor can then be determined with:

$$\begin{aligned} \beta &= v/c = L/tc \ , \\ \gamma &= 1/\sqrt{1-\beta^2} \ . \end{aligned} \tag{50}$$

In the left panel of Fig. 66 the correlation between the measured rigidity p/Z and the velocity β of all *selected tracks* is shown and on the right the linear relation between rigidity p/Z and $\beta\gamma$ for positive particle. The expected values for the different particle masses m_0 is shown as the black lines, which are calculated according to the following equations:

$$\begin{aligned} \beta &= p/E = p/\sqrt{p^2+m_0^2} \\ \beta\gamma &= p/m_0 \ . \end{aligned} \tag{51}$$

In Fig. 67 the mass-over-charge ratio $m/|Z|$ measurement is displayed:

$$m/Z = \frac{p/Z}{\beta\gamma} = p/Z \cdot \sqrt{1/\beta^2 - 1} \tag{52}$$

Due to the uncertainty in the measurement of flight-time and path-length, velocities above the speed of light $\beta > 1$ can be obtained. To avoid as a result unphysical imaginary masses, the square of the masses is calculated.

Specific Energy Loss in the Drift Chambers

Knowing the velocity and charge of a particle, its differential energy loss, or stopping power, in an absorber can be calculated with the

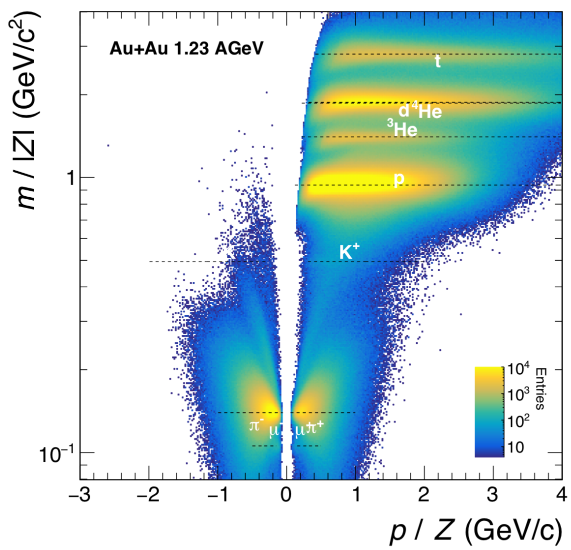

Figure 67: Correlation between the rigidity p/Z and the mass-over-charge ratio $m/|Z|$ measurement according to equation 52 is shown. The black lines correspond to the expected mass values for the different particle species.

Bethe-Bloch equation [316, 317]:

$$-\left\langle \frac{\mathrm{d}E}{\mathrm{d}x} \right\rangle = \frac{Z^2}{\beta^2} \cdot K \frac{Z_{gas}}{A_{gas}} \left[\ln \left(\beta\gamma \frac{\sqrt{2m_e c^2 W_{max}}}{I} \right) - \beta^2 - \frac{\delta}{2} - \frac{C}{Z} \right] \tag{53}$$

with $K = 0.3071$ MeV cm^2/g, Z_{gas} and A_{gas}, the atomic number and mass, and I the mean excitation energy of the gas. This results in a reasonably good expression for the differential energy loss between particle velocity $\beta\gamma \sim 0.1$, comparable to the velocity of a atomic electron, and $\beta\gamma \sim 1000$, where radiative effects arise. The expression is in first order dependent only on the velocity β, scaled by the square of the particle charge Z^2, and shows a weak dependence on the particle rest mass m_0 in W_{max}. The maximum kinetic energy which can passed to one electron in a single collision is

$$W_{max} = \frac{2m_e c^2 \beta^2 \gamma^2}{1 + 2\gamma m_e/m_0 + (m_e/m_0)^2} \tag{54}$$

There are two additional correction terms, the so-called inner shell correction C/Z, taking into account a reduced ionisations due to the screening effects of the inner atomic shells at low velocities, and the density effect correction $\delta/2$, arising from the polarisation of the atoms along the path of the particle at high relativistic velocities. Due to the polarisation, electrons are partially shielded from the Coulomb field, such that the contributions to the energy loss from these electrons decreases. In the implementation of the energy loss in the Hydra-framework the inner shell correction C/Z and the density effect correction $\delta/2$ are omitted. The $-\mathrm{d}E/\mathrm{d}x$ of a particle is calculated for the He/Iso-Butane

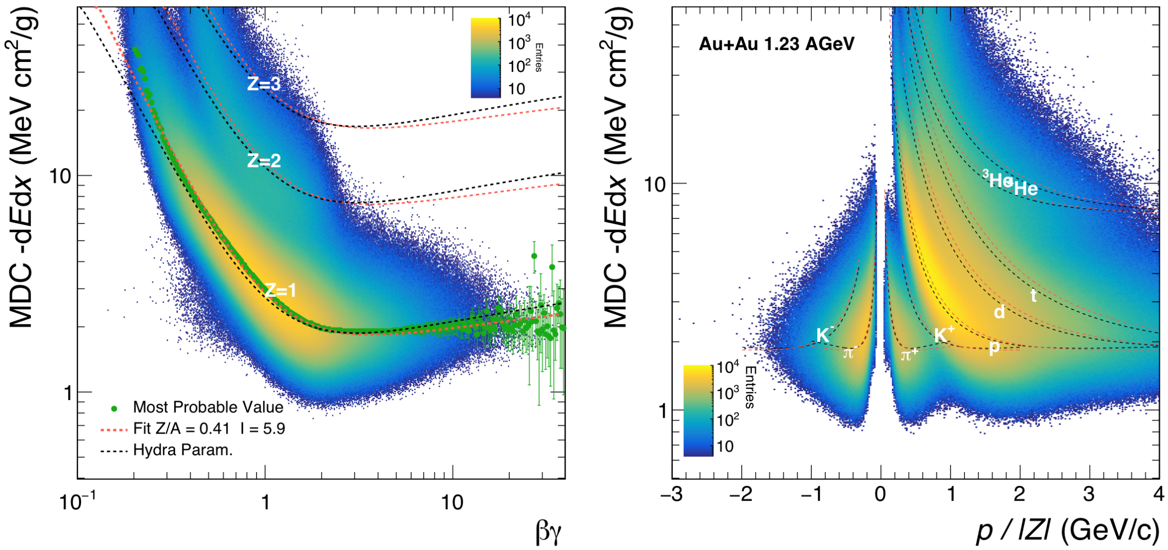

Figure 68: Distributions of the specific energy loss $-\mathrm{d}E/\mathrm{d}x$ measured in the MDC as a function of $\beta\gamma$ (left) and the rigidity p/Z (right). Black lines correspond to the expected values for the different particle species according to equation 53 as implemented in Hydra and the red lines are a fit to the most probable values for $Z = 1$, shown as green dots on the left.

gas mixture (60 : 40), with the averaged atomic charge-to-mass ratio:

$$\langle Z/A \rangle_{gas} = 0.53779 \tag{55}$$

and the values for the mean excitation energy [296, 318]:

$$I = I_0 \cdot Z_{gas} = 282.4 \text{ eV}. \tag{56}$$

Fig. 68 shows the distributions of the specific energy loss $-\mathrm{d}E/\mathrm{d}x$ measured in the MDC for charged particles as a function of $\beta\gamma$ on the left panel and the rigidity p/Z on the right. The black lines correspond to the expected most probable values for the different particle species according to equation 53 as implemented in Hydra and the red lines are a fit to the most probable values for $Z = 1$, shown as green dots on the left. The fit results in the parameters $\langle Z/A \rangle_{gas} = 0.41$ and $I = 5.9$ eV. Even through there are discrepancies between measurement and the parametrization, the general trend for the charge states $Z = 1$ and 2 as a function of $\beta\gamma$ is quite well reproduced. Since the distribution of the measured $(\mathrm{d}E/\mathrm{d}x)_{\mathrm{meas.}}$ in the MDC does not follow a Gaussian shape, the following observable is proposed [319, 320]:

$$Z_{MDC} = \ln\left[(\mathrm{d}E/\mathrm{d}x)_{\mathrm{meas.}} \,/\, (\mathrm{d}E/\mathrm{d}x)_{\mathrm{theory}}\right]. \tag{57}$$

Here $(\mathrm{d}E/\mathrm{d}x)_{\mathrm{theory}}$ is the parametrization of the energy loss shown as dashed black lines in the right panel of Fig. 68 for different particle species. In the left panel of Fig. 69 the distribution of Z_{MDC} for protons is displayed as function of measured mass-charge ratio m/Z. The $\mathrm{d}E/\mathrm{d}x$ in the MDC is measured via the *time-over-threshold* ToT of each hit

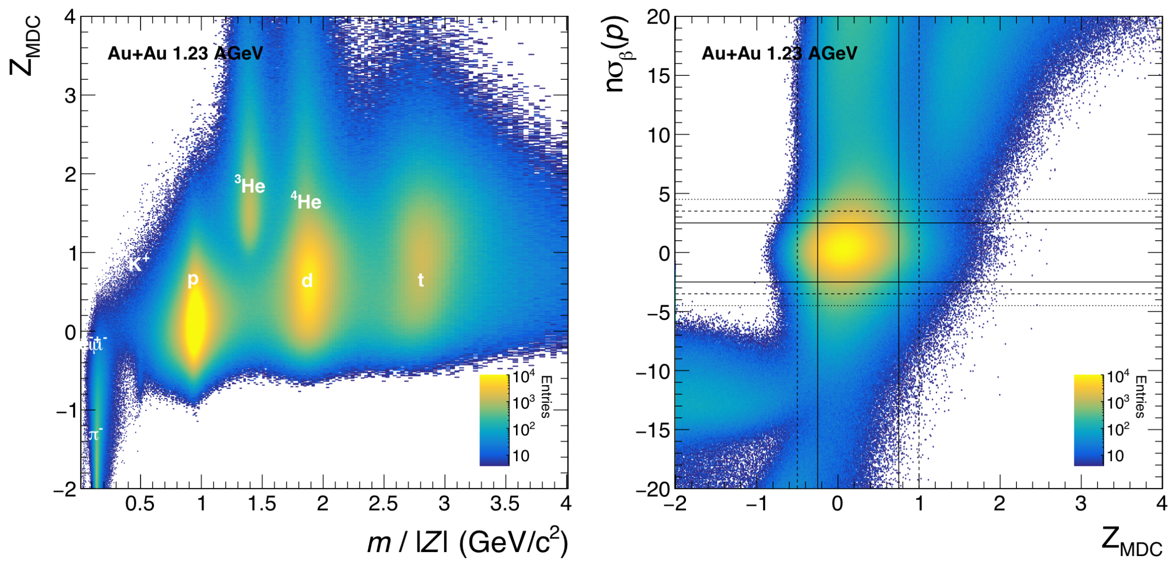

Figure 69: Correlation between Z_{MDC} and the measured mass-charge ratio m/Z for proton candidates is displayed on the left panel and the correlation between $n\sigma_\beta(p)$ and Z_{MDC} on the right. The black lines on the right correspond to the nominal selection criteria and the dashed lines to the looser ones, as summarised in Tab. 12).

in the MDC cells. A charged particle flying through a MDC cell ionises the gas mixture and electrons and ions start drifting due to the potential difference between the field and cathode wires. On their way they ionise other atoms and an avalanche is generated. The drift time depends on the gas mixture and pressure, the electric field in the cell and also on the track geometry, in particular its minimum distance to the sense wire, its impact angle and the path length in the cell. The deposited energy of the particle is then encoded in the time-width of each signal and can be fitted to the calculated energy loss from the particle momentum by the formula:

$$ToT = c_0 + c_1 \left[\log_{10} \left(\frac{\mathrm{d}E}{\mathrm{d}x} + c_3 \right) \right]^{c_2}, \tag{58}$$

with the calibration-parameters c_0, c_1, c_2 and c_3 stored for each of the four MDC planes in all six sectors, for several minimal distances and inclination angles to the wire. The Fig. 70 shows the ToT measured in the first MDC plane with a minimum distances of $d < 0.1$ mm as a function of $\mathrm{d}E/\mathrm{d}x$ for four ranges of inclination angles α. The lines are individual fits with Eq. 58. The inverse function is used to convert the measured ToT to $\mathrm{d}E/\mathrm{d}x$ values for each wire.

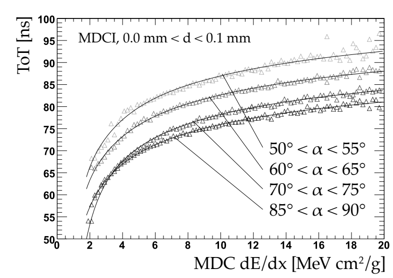

Figure 70: The ToT measured in the first MDC plane with a minimum distances below $d < 0.1$ mm for four ranges of inclination angles α as a function of $\mathrm{d}E/\mathrm{d}x$. The black lines show fits with Eq. 58 (figure from [219]).

Due to the non-Gaussian fluctuations in the individual measurements, the resolution of the cumulative specific energy loss is improved by the truncated mean method, which excludes values beyond a 3σ window around the arithmetic mean. More information on the calibration of the drift chambers can be found in [251, 321, 322].

Identification of Protons, Deuterons and Tritons

The particle identification for protons, deuterons and tritons is based on a combined measurement of time-of-flight and energy loss, as previously described. To separate particles via their bands in velocity β versus momentum (see Fig. 66), the resolutions $\sigma(p)$ are parameterized accordingly for each individual TOF rod and RPC cell. Besides the nominal cuts with a 2.5σ-window on the expected β-momentum distribution and a Z_{MDC}-cut between -0.25 and 0.75 for protons and -0.25 to 0.5 for deuteron and tritons, also looser criteria are used (see Tab. 12). In Fig. 69 the correlation between $n\sigma_\beta(p)$ and Z_{MDC} for the proton candidates is shown, with the black solid lines representing the nominal cuts and the dashed lines the looser selection criteria. The total numbers, of analyzed events, together with the mean number of identified proton, deuteron and triton candidates are summarised in Tab. 13. In Fig. 71 the mean number of analyzed proton, deuteron and triton candidates according the nominal selection criteria is shown for the full duration of the beam time. The variations are mainly driven by the performance of individual sectors and are discussed in the section on reconstruction inefficiencies.

	$n\,\sigma_\beta(p)$
nominal	2.5
loose	3.5
very loose	4.5

Z_{MDC}	p	d and t
nominal	$-0.25 : 0.75$	$-0.25 : 0.50$
loose	$-0.50 : 1.00$	$-0.50 : 0.75$

Table 12: Selection criteria for β-momentum and the Z_{MDC}-cut values for very loose, loose and nominal cuts.

	N_{evt}	$\langle M_{\mathrm{prot.}}\rangle$	$\langle M_{\mathrm{deut.}}\rangle$	$\langle M_{\mathrm{trit.}}\rangle$
Total	$3.39 \cdot 10^9$	17.7	6.1	1.6
$0-10\%$	$7.29 \cdot 10^8$	27.8	9.9	2.4
$10-20\%$	$7.35 \cdot 10^8$	19.7	7.0	1.9
$20-30\%$	$7.79 \cdot 10^8$	13.7	4.7	1.3
$30-40\%$	$6.68 \cdot 10^8$	10.5	3.4	0.9

Table 13: Number of analyzed events after all selection cuts, N_{evt}, and the mean multiplicities of identified proton, deuteron and triton candidates according to the nominal selection criteria is shown for the different centrality classes.

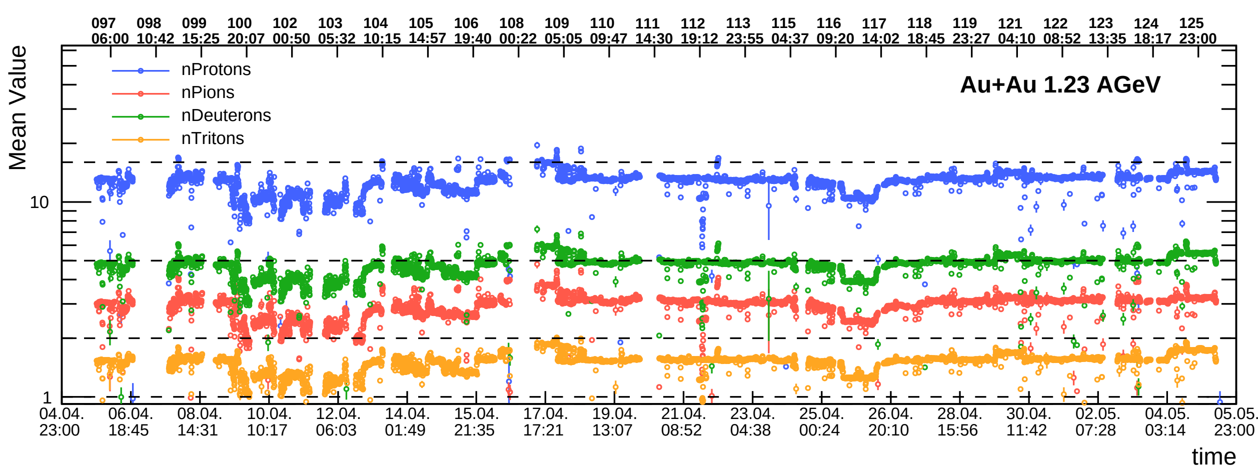

Figure 71: The mean number of analysed proton, deuteron, pions and triton candidates according the nominal selection criteria over the full duration of the beam time is shown.

Purity

The purity of the particle identification procedure is determined for each rapidity and transverse momentum interval used in the analysis and is extracted from simulated data or by fitting the measured mass distributions, which can take a non-trivial from. In Fig. 72 the distributions of the mass-to-charge ratios for protons, deuterons and tritons are shown for mid-rapidity and the same p_t interval. The purity is estimated from the fraction of MC true (correctly reconstructed and identified) particles. In the left panel it is visible that a possible contamination of the proton sample comes mainly from pions and ^{3}He. Since the protons are the charged particles with the largest abundance, their purity is in general far higher than 98% over a large region of phase space. The main candidate for being falsely identified as deuterons are ^{4}He, and in the case of tritons they are ^{6}He, having nearly the same mass-to-charge ratio (see Tab. 14). The effect of a residual contamina-

	m_0 (GeV/c^2)	Z	m_0/Z (GeV/c^2)
p	0.938	1	
d	1.876	1	
t	2.809	1	
^{3}He	2.809	2	1.405
^{4}He	3.727	2	1.864
^{6}He	5.603	2	2.802
^{6}Li	5.603	3	1.868
^{7}Li	6.535	3	2.178

Table 14: Mass m_0, charge Z and their ratio for light nuclei.

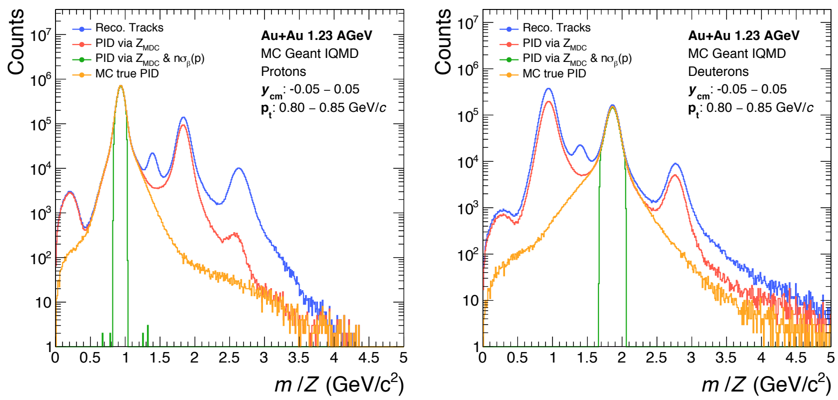

Figure 72: The simulated distributions of the mass-to-charge ratio for protons, deuterons and tritons at mid-rapidity and the same p_t interval. All reconstructed tracks (blue), after applying the Z_{MDC} window (red), with additional the beta-momentum selection (green) and the true MC sample (orange) are shown.

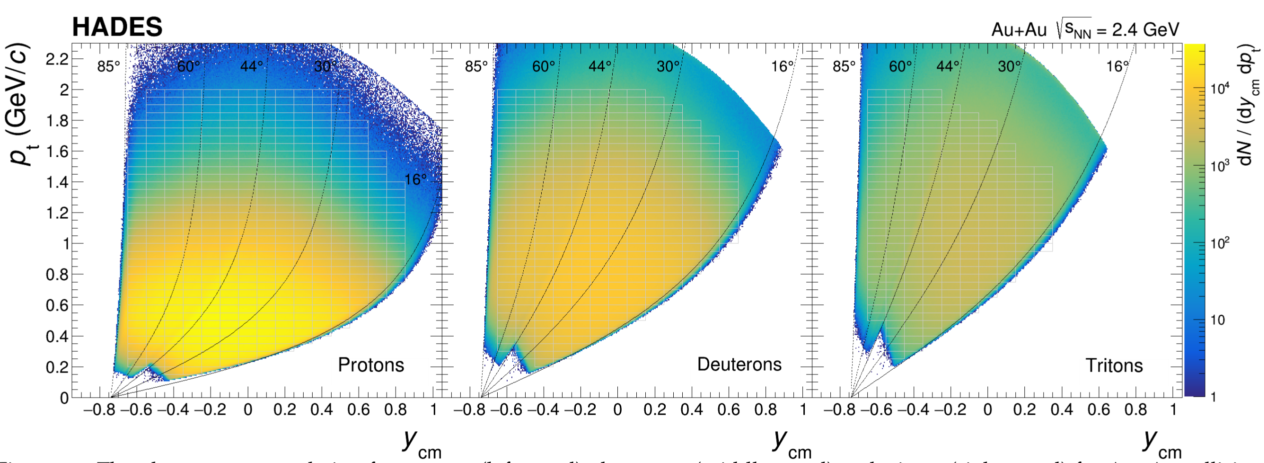

Figure 73: The phase space population for protons (left panel), deuterons (middle panel) and tritons (right panel) for Au+Au collisions at 1.23 *A*GeV as a function of the centre-of-mass rapidity y_{cm} and transverse momentum p_t (the dashed lines correspond to the polar angles θ in the laboratory system).

tion from Helium and Lithium isotopes on the flow results was found to be negligible. Phase space intervals are only included in the final result, if the estimated purity was higher than 80%, independent of centrality. Furthermore, the intervals should be completely covered by the detector acceptance, excluding outlier bins at the edge of the detector acceptance. The phase space coverage for the identified particles is shown in Fig. 73, overlaid with the bins, for which in the following results for flow coefficients are shown.

Non-uniform acceptance and reconstruction inefficiencies

The flow analysis method based on single track measurements, correlated to an independently measured event plane, should not be influenced by any non-uniformity or limitation of the detector acceptance. However, in real data a systematic bias of the flow measurement is observed depending on the sensitivity of individual sectors. Any bias in the flow measurement due to non-uniform acceptance and reconstruction efficiencies can be traced back to two main correlated aspects. Neither is the EP distribution perfectly flat (see section Event Plane Determination), nor is the accuracy of the azimuthal-angle reconstruction homogeneous over the whole detector system. Furthermore, any significant movement of the beam position with respect to the center of the Forward-Wall and the MDC chambers can introduce azimuthal asymmetries by simultaneously modifying the relative azimuth angles between the two sub-systems. Small asymmetries inside individual sectors, as well as effects of their alignment, can add up and can be increased by any non-uniformity in the detection efficiency of the MDCs in each sector. The performance of the drift chambers crucially dependents on the stability of the drift velocity of the electrons produced

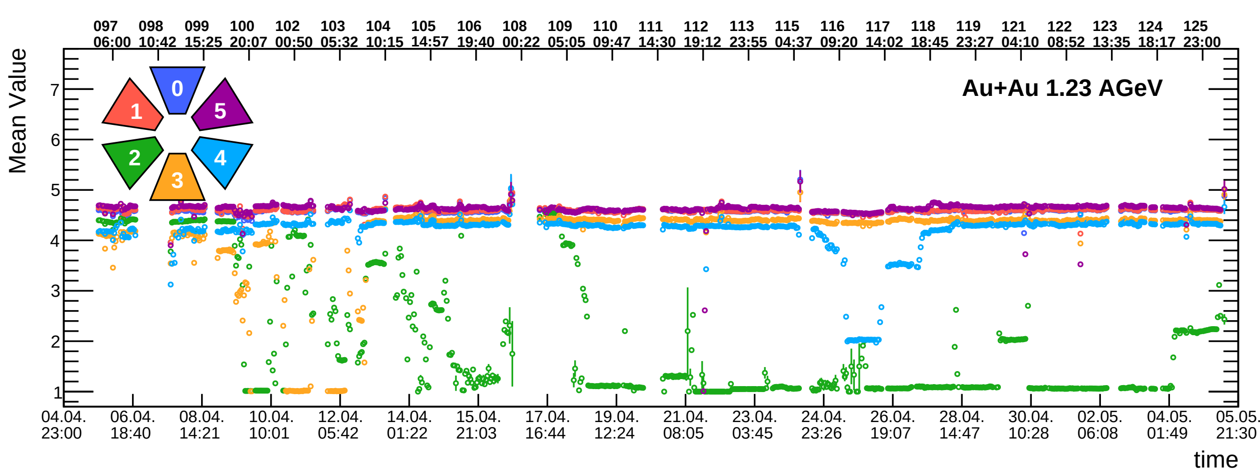

Figure 74: The mean number of identified protons in each sector as a function of beam time. Since the performance of the upper sectors 0, 1 and 5 is equivalent over time the points of sectors 0 and 1 are overlaid by the ones of sector 5. Sector 2 (green) is most of the time switched off or running with low performance.

in the primary ionization. The drift velocity itself depends on the temperature, pressure and mixture of the drift gas and furthermore on the strength of the electric field. The condition of the chambers was constantly monitored during the beam time. The properties of the gas mixture were rather constant, whereby the high voltage settings of individual MDCs were either automatically adjusted in the case of small current spikes, or were manually re-adjusted or switched off in the case of instabilities [252]. Switching off or running one chamber at lower voltage results in a significant drop of the efficiencies of the whole sector. In Fig. 74 the mean number of identified protons in each sector as a function of the beam time is shown. The upper sectors 1, 0 and 5 show a continuously high performance over the whole beam time, whereas the lower sectors were running in several periods with lower performance.

In a dedicated analysis, based on the mean number of identified pions per sector, the performance of each sector was evaluated file-by-file. If the measured mean number of pions in one sector deviated more than ±5% from the truncated mean estimated for a given day, the sector was marked as inefficient and stored in a list to be excluded in several analyses [254]. In Fig. 75 the fraction of files in this list as function of the number of efficient sectors is shown. Only in a small fraction of files (6%) all sectors were identified to be fully operational at the same time. In 70% of the cases only 5 sectors were fully efficient. In Fig. 76 the number of efficient sectors based on this condition is shown as a function of the beam time.

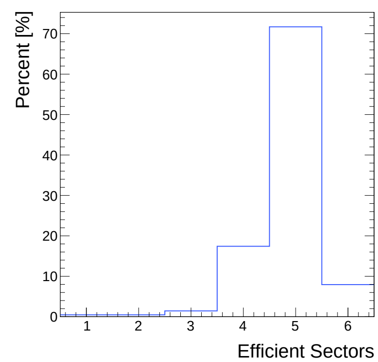

Figure 75: The fraction of files in the exclusion list as a function of the number of efficient sectors.

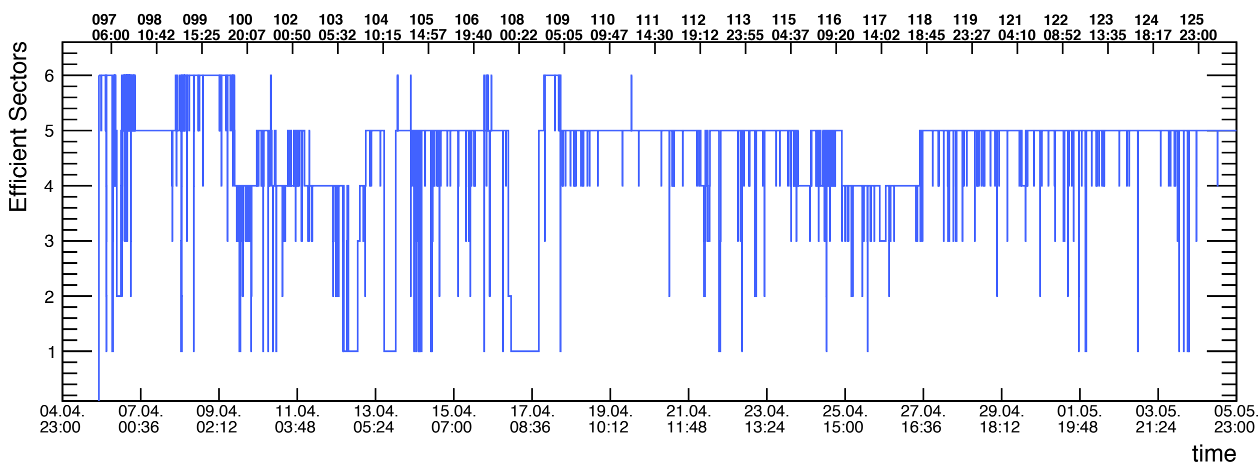

Figure 76: The number of efficient sectors as a function of the beam time.

Toy Model Monte Carlo

To investigate the convoluted effects of a non-uniform geometric acceptance and reconstruction efficiency the averaged centroid of the XY-positions $\langle\cos(\phi_{lab})\rangle$ and $\langle\sin(\phi_{lab})\rangle$ of all identified particles (protons, deuterons, tritons and charged pions) over the full detector coverage are calculated as a function of the beam time. Here the most 20% central events are used in combination with the common event selection methods. Additionally, to further reduce any fluctuations, e.g. due to beam intensity or PID performance, only events are used where at least 5 selected tracks could be reconstructed. In the upper panel of Fig. 77 the values are shown, which in the perfectly symmetric case should be zero. The effect of the geometric acceptance due to missing sectors on the flow studies can be estimated in toy model MC simulations. 300 events with 120 particles each are generated via MC sampling for each time step. According to the time dependent list of efficient sectors, as shown in Fig. 76, particles in the azimuthal intervals corresponding to ineffi-

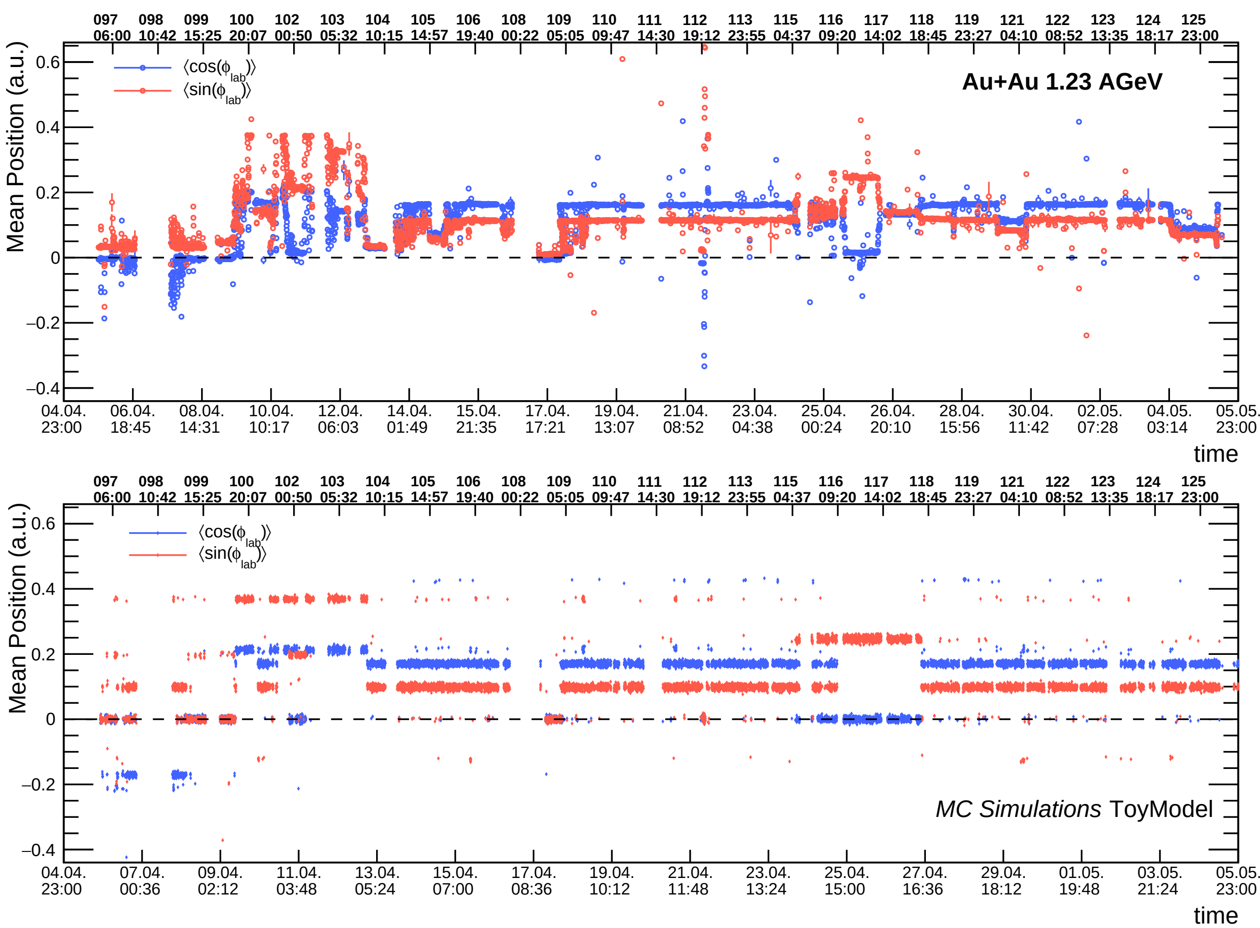

Figure 77: In the upper panel the averaged centroid XY-positions $\langle\cos(\phi_{lab})\rangle$ and $\langle\sin(\phi_{lab})\rangle$ of all identified particles (protons, deuterons, tritons and charged pions) over the full detector coverage for the most 20% central events are shown as a function of the beam time. In the lower panel the toy model MC simulation results, including only the effects of detector acceptance, are presented.

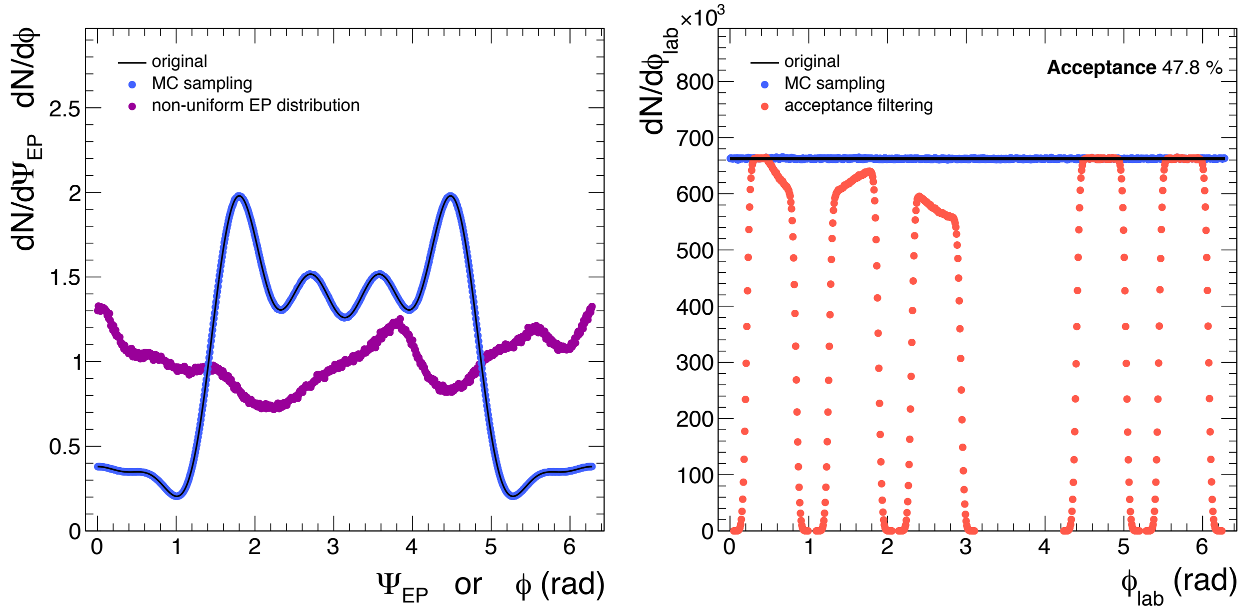

Figure 78: In the left panel the input function (black line) depending on the single-particle azimuthal angles ϕ used for the MC sampling (blue points), and the distribution of the non-uniform event plane angle Ψ_{EP} is shown in purple points. On the right panel the azimuthal angles ϕ_{lab} rotated into the detector coordinate system by an random event plane angle are presented for the input function (black line) and for the MC sampled particles (blue points). In red the acceptance filtered distribution, where one complete sector and smeared gaps between the sectors are excluded, is shown. To illustrate only the effect of acceptance, here a flat distributed event plane is used, whereby the non-uniform one in purple (left) is additionally used for the calculation, shown in the Fig. 79.

cient sectors are excluded, but no further inhomogeneities are included. Additionally, the acceptance gaps between each sector of around 24° including a Gaussian smearing of 2° at the edges are included in the simulations. The outcome of the MC simulation is shown in the lower panel of Fig. 77 as a function of the beam time. The general trend of the measured values of $\langle \cos(\phi_{lab}) \rangle$ and $\langle \sin(\phi_{lab}) \rangle$, as presented in the upper panel, can be emulated by the simulation quite well. Remaining differences can be attributed to the individual detection efficiency and inhomogeneities in each sector. Averaged values for higher harmonics of $\langle \cos(n\phi_{lab}) \rangle$ and $\langle \sin(n\phi_{lab}) \rangle$ are also studied up to the 8th order exhibiting in general similar trends in data and simulation. To understand further the various effects on the measurement of higher order flow coefficients caused by a non-uniform acceptance and efficiency in combination with a non-uniform event plane, a second toy model MC simulation is assessed. In this idealised scenario the distributions of the particle angles are simulated according to flow values up to the 6th harmonic and are rotated by an event plane angle randomly chosen from a flat probability distribution into the detector coordinate system. The flow values used here are similar to the measured values for protons in the backward hemisphere. In the left panel of Fig. 78 the input function (black line) used for the MC sampling (blue points) is shown, and on the right panel the same angles are shown in blue after rotation by the event plane angle. The acceptance filtered distribution, where the complete sector 2 (60°) and smeared gaps between the sectors are excluded, is shown in red. Additionally, event-by-event

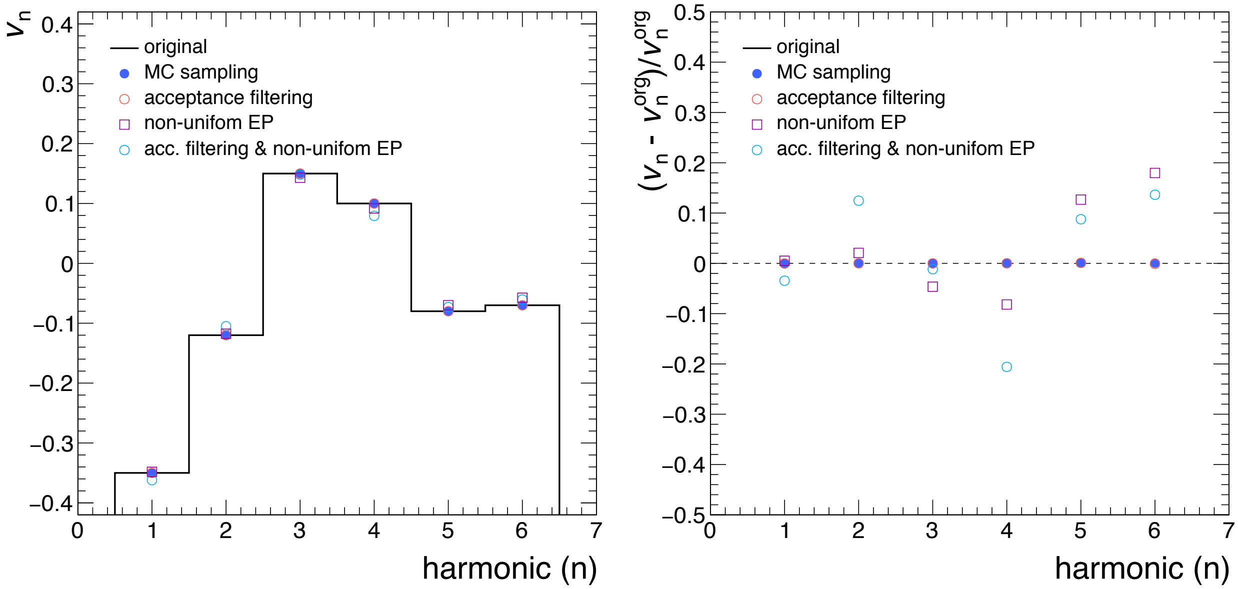

Figure 79: In the left panel the original values for the flow coefficients used in the simulations are shown as black histogram and in the right panel the relative differences to these original values are shown. The values calculated with MC sampling with ideal event plane (blue dots) and the acceptance filtered ones (red open dots) exhibit no significant modification. In purple the values calculated from angles rotated by a non-uniform event plane distribution (see red curve in left panel of Fig. 78) are shown and the additional acceptance filtered values are displayed in cyan.

fluctuations of the efficiency in the detector system are included in the simulation, as visible in the three first sectors. In total 6×10^6 events each with around 80 particles are sampled. The original values for the flow coefficients used in the simulations are shown as the black histogram in the left panel of Fig. 79. No significant modification due to the MC sampling (blue dots) and the acceptance filtering (red open dots) could be observed. In the case of a rotation with a non-uniform event plane distribution (purple symbols in the left panel of Fig. 78), the calculated flow coefficients are generally damped to smaller values (shown as purple squares). The combination of a non-uniform event plane and an acceptance filter results in a non-trivial behaviour with increased or damped values. In the right panel of Fig. 79 the relative differences to the original values are shown. It should be pointed out that the non-uniformity of the event plane assumed in this study is exaggerated to the level of 15% to illustrate the effect. Two conclusions can be drawn from this MC study. First, one should make sure that the event plane distribution is flattened. As described in the section Event Plane Determination, this is done below the 0.1% level, with values for the least-square χ^2 over the degree of freedom around unity in comparison to a flat distribution. Second, any bias in the flow measurement due to the performance of individual sectors has to be corrected or the effect has to be estimated and included in the systematic uncertainties. In the following both approaches are discussed.

Sector exclusion

With this method the possible magnitude of the effect is estimated by a comparison of several flow analyses, done with different combinations of deliberately excluded sectors [323]. After a survey of different possible combinations of excluded sectors, finally six versions were chosen and their differences were included in the systematic uncertainties. The *default* analysis-run uses only sectors which are marked as fully efficient according to the described sector list. The next variation excludes the problematic sector 2 from the analysis. To symmetrize the acceptance further the opposite sector (sector 5) is also excluded from the analysis. In the most extreme case the acceptance used in the flow analysis is divided into the fully-efficient upper half sectors (5, 0, 1) and the partially-efficient lower sectors (2, 3, 4). To investigate possible effects due to the time-dependent sector selection, in one variation all sectors are used independent of their performance.

Track weighting

To account for non-uniformities in the azimuthal-angle distribution of reconstructed tracks, for each interval in y_{cm}, p_{t} and ϕ_{lab} two different weights are calculated as:

$$w_{\mathrm{mean}}(\phi_{lab}, y_{\mathrm{cm}}, p_{\mathrm{t}}) = N(\phi_{lab}, y_{\mathrm{cm}}, p_{\mathrm{t}}) / \langle N(y_{\mathrm{cm}}, p_{\mathrm{t}}) \rangle_{\phi_{lab}} , \quad (59)$$

$$w_{\mathrm{max}}(\phi_{lab}, y_{\mathrm{cm}}, p_{\mathrm{t}}) = N(\phi_{lab}, y_{\mathrm{cm}}, p_{\mathrm{t}}) / N_{max}(y_{\mathrm{cm}}, p_{\mathrm{t}}) . \quad (60)$$

where $\langle N(y_{\mathrm{cm}}, p_{\mathrm{t}}) \rangle_{\phi_{lab}}$ is the number of tracks averaged and $N_{max}(y_{\mathrm{cm}}, p_{\mathrm{t}})$ is the maximum number of tracks over the full range of ϕ_{lab}, while $N(\phi_{lab}, y_{\mathrm{cm}}, p_{\mathrm{t}})$ is the number of tracks within the given interval.

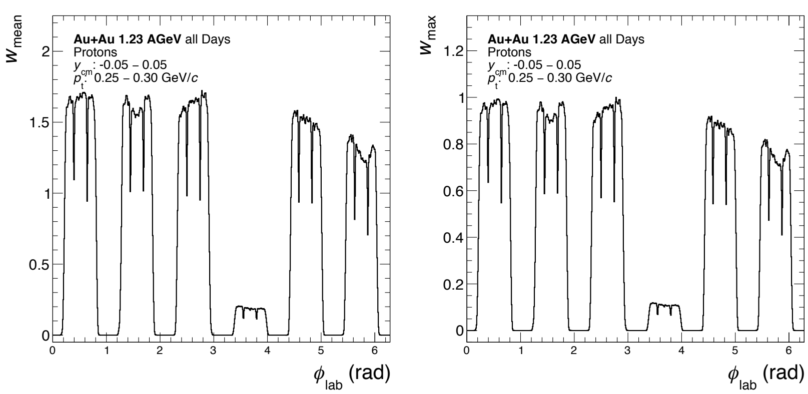

Figure 80: The weights $w_{\mathrm{mean}}(y_{\mathrm{cm}}, p_{\mathrm{t}})$ and $w_{\mathrm{max}}(y_{\mathrm{cm}}, p_{\mathrm{t}})$ as a function of the azimuthal angle ϕ_{lab} for protons in the same interval of y_{cm} and p_{t} averaged over the whole beam time for the most central events $(0 - 10\%)$.

In Fig. 80 the distribution of the weights $w_{\mathrm{mean}}(y_{\mathrm{cm}}, p_{\mathrm{t}})$ and $w_{\mathrm{max}}(y_{\mathrm{cm}}, p_{\mathrm{t}})$ as a function of the azimuthal angle ϕ_{lab} for protons in the same intervals of y_{cm} and p_{t} for the most central events $(0 - 10\%)$ is presented, calculated after integrating the track distribution over all days of the

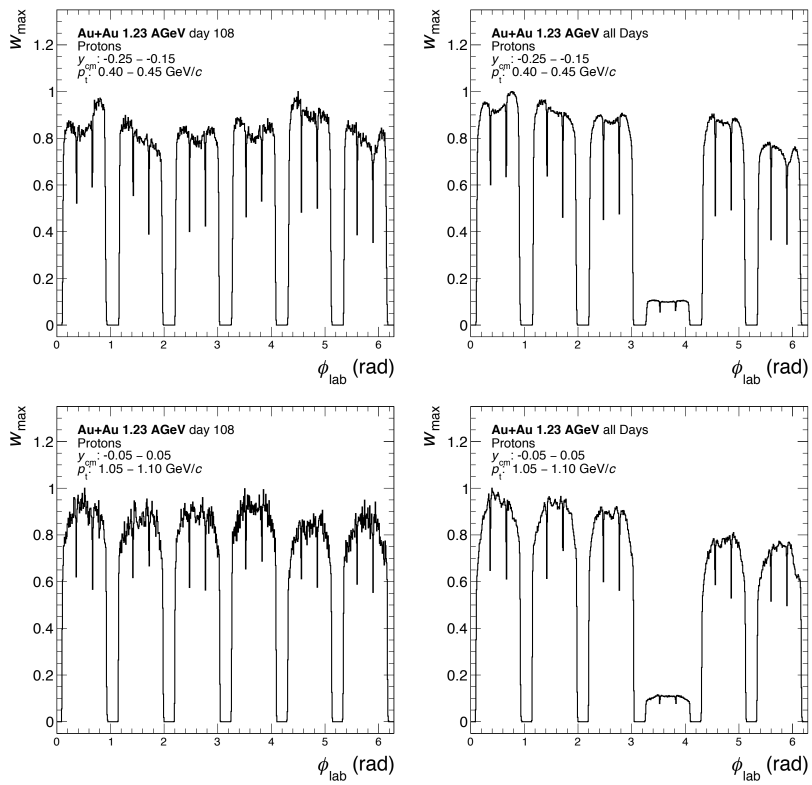

Figure 81: The weight $w_{\max}(y_{\rm cm}, p_{\rm t})$ as a function of the azimuthal angle ϕ_{lab} for protons in different interval of $y_{\rm cm}$ and $p_{\rm t}$ (upper and lower row) calculated for day 108 (left) and all days (right) in the most central events $(0-10\%)$.

beam time. In Fig. 81 the distribution of the weight $w_{\max}(y_{\rm cm}, p_{\rm t})$ as a function of the azimuthal angle ϕ_{lab} for protons in different interval of $y_{\rm cm}$ and $p_{\rm t}$ (upper and lower row) calculated for day 108 (left) and all days (right) for the most central events $(0-10\%)$ are shown. The data-driven correction of any efficiency loss in the detector by track weighting was extensively tested, but the effect in the case of a perfectly flattened event plane distribution turned out to be minimal and the quantitative difference to the un-weighted approach are far below the estimated systematic uncertainties. The disadvantage of the track weighting procedure is that correction matrices as a function of phase space ($\phi_{lab}, y_{\rm cm}, p_{\rm t}$) for each particle species, centrality class and day of data taking have to be provided separately. Its advantage is that beside non-uniformities due to track reconstruction, also inhomogeneities due to PID can be re-weighted. Since with the track weighting method only inefficiencies can be corrected, for the correction of azimuthal anisotropies due to holes in the acceptance further flattening methods are needed [138, 294]. The averaged values of $\langle\cos(n\phi_{lab})\rangle$ and $\langle\sin(n\phi_{lab})\rangle$ for harmonic n up to the $8^{\rm th}$ order can be used for re-centering the track distribution and are shown in upper panel of Fig. 77 for $n = 1$. Further studies [324, 325] show that correlated biases due to detector non-uniformity can be successfully corrected with a data-driven correction procedure described in [294]. Due to practical reasons and the smallness of the effect, far below the systematic uncertainties, for the results of the flow measurements shown in the following the track flattening methods are omitted. But it should be noted that in the case of flow measurements based on multi-particle correlations the corrections for non-uniformity can not be neglected [326, 327].

Systematic uncertainties

The systematic uncertainties for the measured flow harmonics v_n are estimated by varying individual conditions in the analysis-procedure. In general they can be separated into global effects affecting all data points of a given centrality class the same way, like the uncertainties originating from the determination of the event plane and its resolution correction, and systematic uncertainties which depend on phase space. The latter arise from multiple effects of the measurement in different parts of the detector and are partially correlated. The main contributors are the uncertainties from the quality selection criteria applied to the tracks (Track Quality), the correction procedure for reconstruction inefficiencies caused by high track densities (Occupancy), the procedures for particle identification (PID) and the effects of an azimuthally non-uniform detector acceptance (Acceptance). They are determined separately for each particle-type (proton, deuteron and triton), the order of the flow harmonics v_n, the centrality class and the y_{cm}- and p_{t}-interval. The bin size is chosen to be 50 MeV/c in transverse momentum and 0.1 units of rapidity, symmetric around mid-rapidity. It is checked that the resolution in transverse momentum and rapidity in most of the analyzed phase space bins is far below the bin size. On the other side, the relative small bin-size allows to assume that the variation of the reconstruction efficiency inside each bin is negligible[4]. These systematic uncertainties are represented by boxes in the figures with the final results and are evaluated in the corresponding tables (see next chapter) and are in general larger than the statistical errors. A summary of the analysis conditions of the nominal analysis run and the modifications applied in the variational analysis runs are listed in Tab. 15. Beyond these main contributions other sources of uncertainty are studied, either with consistency checks, MC simulations or the embedding of simulated protons in the real data. It turned out that no significant deviations are observed for these sources. For completeness they are summarised at the end of this chapter. To estimate the total systematic uncertainty for each measured point of the nominal analysis run, the standard deviation over all variational runs is determined, including the nominal one. To suppress jumps or outliers due to statistical fluctuations the standard deviation is calculated by weighting

[4] If a re-binning due to the statistical uncertainty is necessary the ReBin-Method of the TProfile2D-Class is used to preserve independently the weights and entries of each bin.

Table 15: Conditions of the nominal analysis run and the variations used to estimate the systematic uncertainties.

$n\,\sigma_\beta(p)$	Z_{MDC}	χ^2_{RK}	Q_{MM}	DCA (mm)	ϵ_{min}	Sectors
Nominal						
< 2.5	nominal	< 1000	< 3	< 10	0.62	only good
Track Quality						
				< 8		
				> 2		
			< 0.5			
			> 0.5			
		< 15				
		< 200				
Occupancy						
					no Corr.	
< 2.5	nominal				0.56	
< 2.5	nominal				0.76	
< 3.5	loose				0.56	
< 3.5	loose				0.76	
PID						
< 4.5	nominal					
< 3.5	nominal					
< 3.5	loose					
< 4.5	loose					
< 2.5	loose					
reference PID						
Acceptance						
						excl. sec. 2
						excl. sec. 2&5
						upper half
						lower half
						no sec. excl.

the contributing values by their statistical errors[5] and is explicitly not truncated, as can be done by statistical significance checks, like the *Barlow criterion* [328]. The set of variational runs is chosen on one hand such that the magnitude of the variations is always within the corresponding resolution of the detector or the size of the correction. On the other hand, it should have a significant contribution to the total uncertainty. Since several of the systematic effects are correlated, this approach allows to evaluate the total systematic uncertainty at a chosen confidence level (CL) [329] without the need to evaluate the individual contributions and their correlations separately.[6]. With the assumption that the chosen variations represent a good estimate for values normally distributed around the nominal value, we define a confidence interval of 99% for the total systematic uncertainties as 2.5 times the standard deviation. The resulting uncertainties are averaged over several neighboring bins to have continuous values for the uncertainty over phase space without large variations between bins[7]. Only values in phase space bins are shown that are fully within the detector acceptance with a PID purity above 80% (for detail see previous section about purity). Further, bins at the edge of the acceptance are only shown, if there are no significant deviation between backward- and forward-rapidities of

[5] Since the flow coefficients are mean values the standard error of the mean provided by the TProfile2D-Class is used.

[6] The procedure here was motivated by a similar approach (see Appendix of [330]).

[7] This smoothing was done with a kernel algorithm implemented in the ROOT class TH2::Smooth() with an adjusted 5×5 matrix.

the first two harmonics v_1 and v_2, indicating that the estimation of the systematic uncertainties in these bins are safely under control.

Calculations of ratios Since the individual flow coefficients are calculated from the same data sample, their systematic uncertainties should be correlated. The systematic uncertainties for a composite flow-observable, like the ratio v_4/v_2^2, are then determined directly by calculating the observable under investigation for all systematic variations following the same procedure, as described above for the single harmonics. Instead of explicitly propagating the errors of the individual components, this approach takes care of the correlated part and thus avoids an over-estimation of the errors.

Track selection As already discussed in the section on track reconstruction the quality of the tracks is mainly controlled by the three parameters: the *Goodness-of-Fit* χ^2_{RK}, the *META matching quality* Q_{MM} and the *Distance of Closest Approach DCA* to the reaction vertex. In general, constraining the track quality parameter to small values results in a selection of more accurately reconstructed tracks with less contribution from mismatched hit points or background. But similar to the systematic effects due to the PID selection any restrictive selection results in a non-uniform loss of reconstructed tracks, here mostly at the edges and corners of each sector. To preserve the initial azimuthal distribution as un-biased as possible over a large phase space, no restrictions on χ^2_{RK} and Q_{MM} are applied in the default analysis, beside the maximal threshold values already used by the track sorting algorithm (see Tab. 16). For the *DCA* a maximum value of 10 mm is used, motivated by similar values used in the analysis of weakly decaying hadrons [253, 331]. The *narrow selection criteria* in χ^2_{RK}, Q_{MM} and *DCA* are optimized to enhance the fraction of accurate track candidates, but to keep simultaneously the resulting bias due to the deformations of the azimuthal angle distribution at a minimum. With the *biased criteria* very accurate track candidates are excluded from the analysis resulting in non-uniform loss of tracks in other parts of the detector, probing the deformation of the angle distribution. This approach of splitting the total sample allows to differentiate between the effects of a non-uniform accuracy in the momentum- and angular-reconstruction, and the contribution from background and mismatched hit points in the flow results. For the estimation of the systematic uncertainty each track quality parameter is modified individually to the narrow or the biased versions, resulting in six additional analysis runs.

	χ^2_{RK}	Q_{MM}	*DCA* (mm)
nominal	< 1000	< 3	< 10
narrow	< 200		
	< 15		
		< 0.5	
			< 8
biased		> 0.5	
			> 2

Table 16: Track selection criteria for the nominal, the narrow and biased analysis runs.

Particle Identification The trivial effect of the variation of the selection criteria for the particle identification is that broader selection cuts are

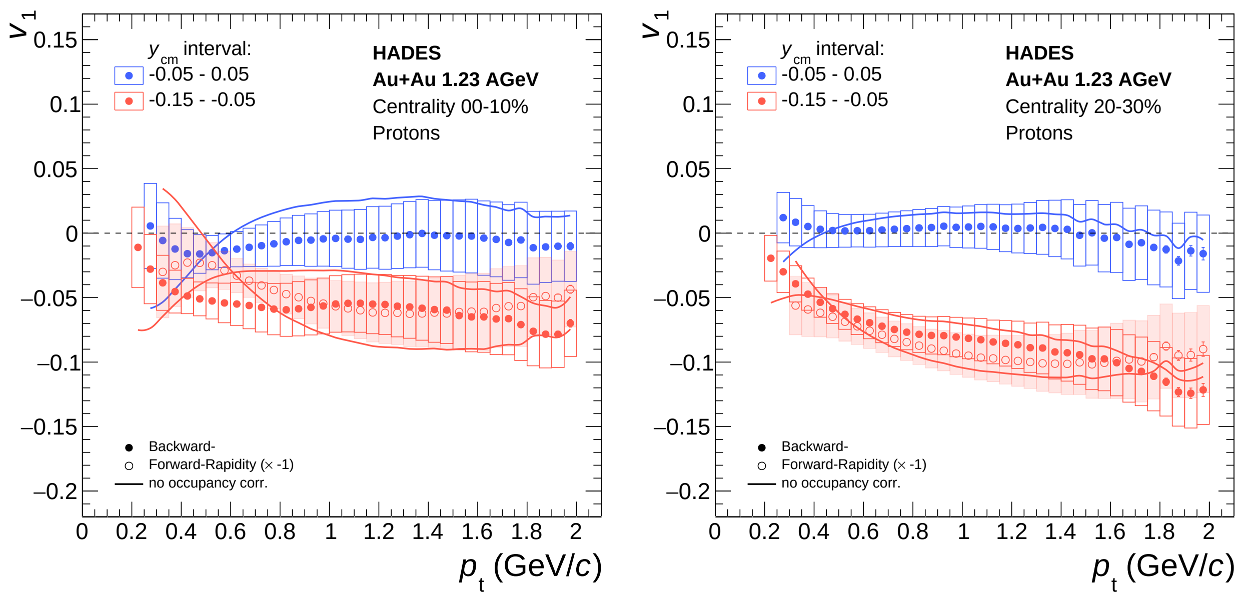

Figure 82: Results for v_1, including their total systematic uncertainties, are shown for protons in two centrality classes, $0-10\%$ (left) and $20-30\%$ (right). To illustrate the effect of the occupancy correction the version without correction is overlaid as solid lines.

expected to include more contamination by misidentified particles, but on the other side provide higher statistics. Since all variations in the PID selection results in continuous identification efficiencies as a function of p_t and y_{cm}, no large systematic effects are expected from the PID efficiency alone. Impurities in the sample of particles, however, will modify the corresponding flow result. Since the protons have the largest abundance, their selected sample has in general a purity of far more than 98% in most parts of the phase space (see Fig. 73). The contamination at very high momenta results from misidentified pions, deuterons and ^{3}He. The high purity region for deuterons is much smaller, due to the additional contamination mainly by ^{4}He, having nearly the same mass-to-charge ratio. The rejection power of ^{4}He strongly depends on the dE/dx resolution. For the triton the region of high purity shrinks down to only few phase-space bins at backward rapidities. Further detailed studies show that the main systematic effect concerning the flow analysis is that a restrictive PID selection criterium does modify the azimuthal particle distribution in an non-trivial way, resulting in a significant bias of the flow result. The chosen selection criteria are a compromise between acceptable impurities in the sample and a maximized phase-space coverage with a minimal biased azimuthal distribution. Beside the nominal PID cuts, also five further combinations of β-momentum and Z_{MDC} selections with broader criteria are used (see Tab. 12). In addition, also the reference PID method implemented in the Hydra-framework as part

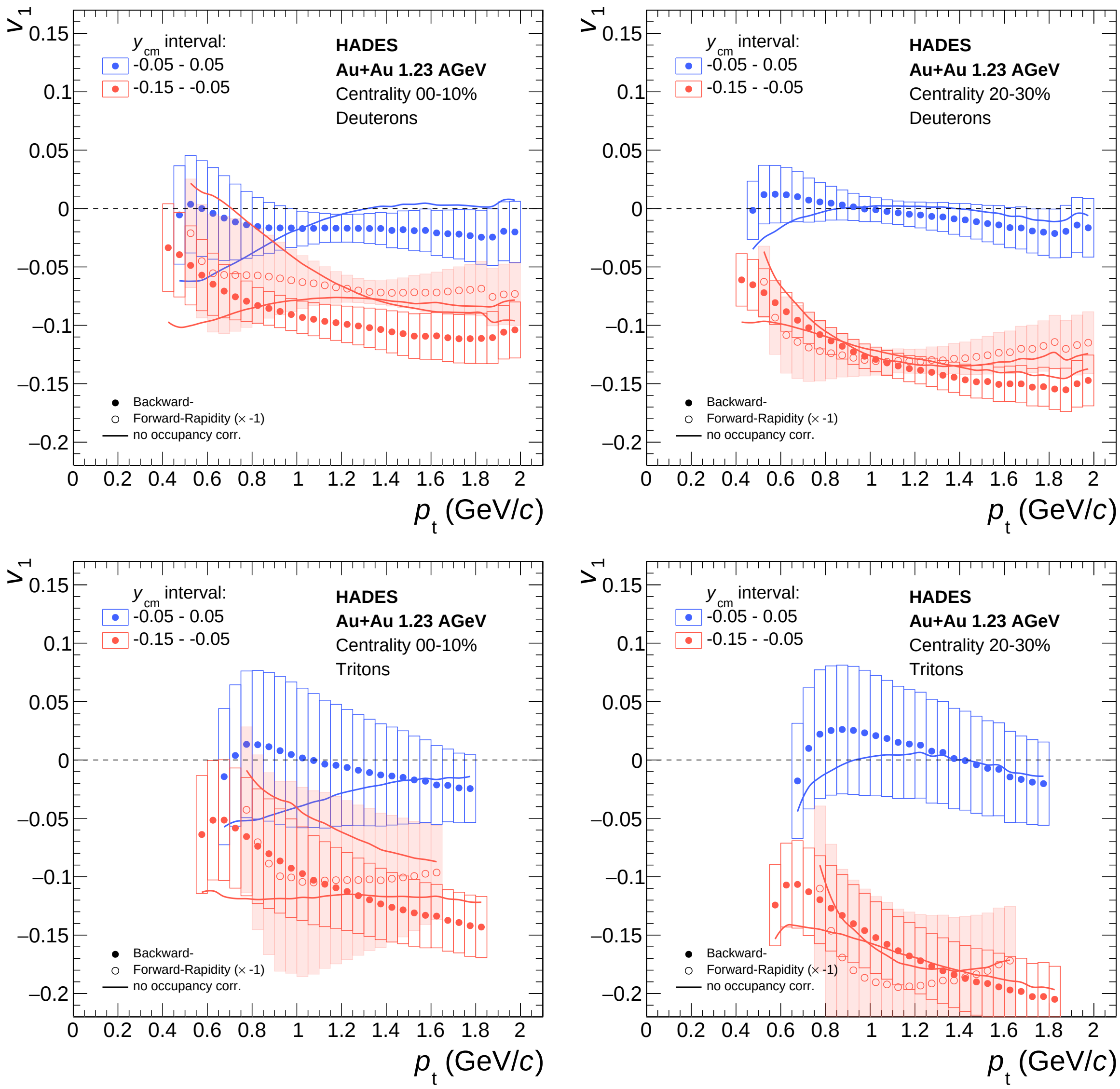

Figure 83: Results for v_1, including their total systematic uncertainties, are shown for deuterons and tritons (upper and lower row) in two centrality classes, $0-10\%$ (left) and $20-30\%$ (right). To illustrate the effect of the occupancy correction the version without correction is overlaid as solid lines.

of T_0-reconstruction is included in the evaluation of the systematic uncertainties.

Occupancy The correction parameter ϵ_1 (see Eq. 48) with its nominal value of 0.62, already discussed in a previous section, is adjusted in such a way that the v_1 flow values are symmetric around mid-rapidity and as close as possible to zero at mid-rapidity for all three hydrogen isotopes and all centrality classes. The lower limit of 0.56 and the upper of 0.76 for ϵ_1 are motivated by the observation that inside this parameter range for the occupancy correction the odd flow values v_1 and v_3 as a function of p_t are still compatible within errors with zero at mid-rapidity and

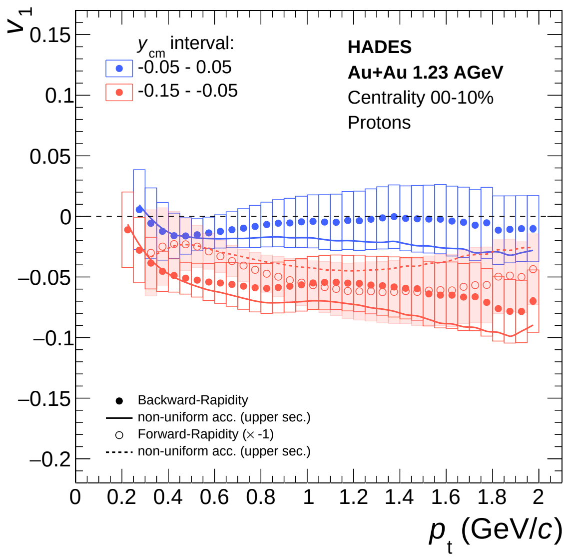

Figure 84: Results for v_1, including their total systematic uncertainties, are shown for protons in two centrality classes, $0-10\%$ (left) and $20-30\%$ (right). Additionally, the results from the variation run, where only the upper sectors (5, 0 and 1) are used, are plotted on top as solid lines.

symmetric between forward- and background rapidities. In Fig. 82 the v_1 flow results for protons, including the total systematic uncertainties, are shown for the two centrality classes $0-10\%$ and $20-30\%$. To illustrate the effect of the occupancy correction the version without correction is overlaid as solid lines. The same is presented for deuterons and tritons for two centrality classes $0-10\%$ and $20-30\%$ in Fig. 83. To include the correlated effects of particle selection and occupancy correction, two variations of ϵ_1 are combined with one broader PID selection in β-momentum and Z_{MDC}. Due to the working principle of the correction method, the far edges of the phase space with very low track multiplicity are in general over-corrected. To preserve these regions in the systematic uncertainty evaluation, an additional analysis run with no occupancy correction is included, resulting in a total of five variation runs.

Acceptance In general, the flow analysis method is based on single track measurements, correlated to an independently measured event plane and should therefore not be influenced by any non-uniformity of the detector acceptance. To verify this the various effects caused by a non-uniform acceptance of particles are studied with a Toy Model MC simulation. No significant modification of the original flow coefficient due to acceptance is observed, as long the initial correlation between individual track and the EP is preserved (see Fig. 79). However, in real data neither the EP distribution is perfectly flat, nor is the accuracy of the azimuthal-angle reconstruction homogeneous over the whole detector system. Additional effects of the alignment of individual sectors

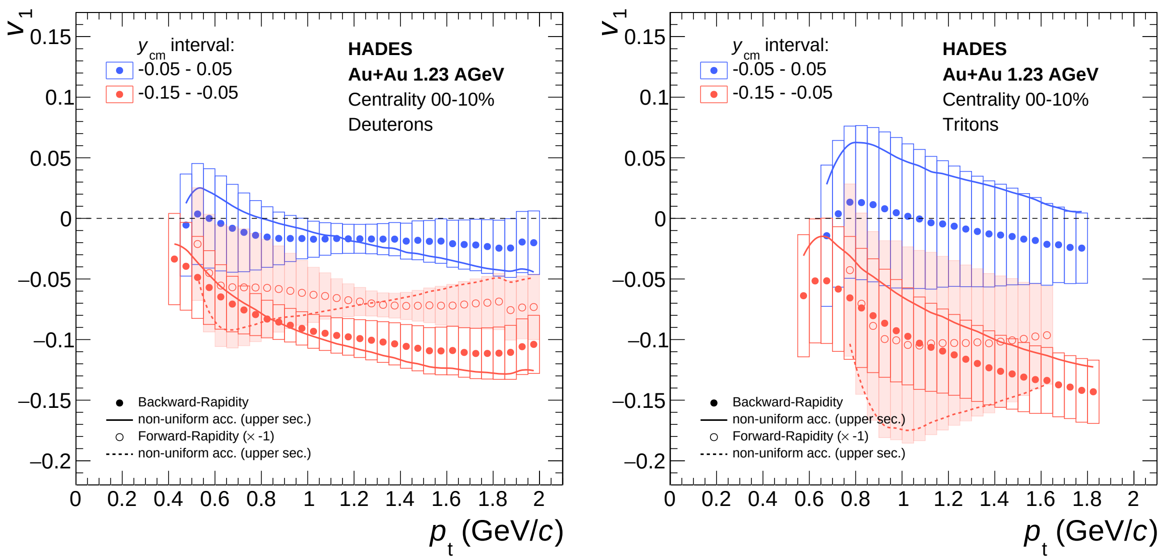

Figure 85: Results for v_1, including their total systematic uncertainties, are shown for deuterons and tritons for the centrality class $0-10\%$. Additionally, the results from the variation run where only the upper sectors (5, 0 and 1) are used are plotted on top as solid lines.

also play a role. Furthermore, slight shifts of the beam position w.r.t the center of the Forward-Wall and the MDC chambers, simultaneously modifying the azimuth angels in the two sub-system, can introduce azimuthal asymmetries. Small asymmetries of any origin can be increased by the acceptance due to an non-uniform weighting of individual tracks depending on their orientation. In comparison to higher order flow coefficients, the effect described here is most prominent for the directed flow v_1 and, since it is mainly governed by the geometry of the detector, there is only a very weak dependence on centrality. In Fig. 84 the flow results v_1 for protons are shown for the two centrality classes $0-10\%$ and $20-30\%$ and in Fig. 85 the flow results v_1 for deuterons and tritons for the centrality classes $0-10\%$. Additionally, the variation run where only the upper half of sectors (5, 0 and 1) are used, is plotted on top as solid lines. To describe the full picture of the systematic effects caused by the non-uniform detector acceptance five additional variation runs where chosen, where individual or several sectors are excluded [323]:

- In the *default* analysis run only sectors, which are marked as being fully efficient according to a time-dependent selection list, are used [254].

- On top of the *default* condition, the problematic sector 2 was excluded from the analysis. This is in line with most other analyses of hadrons [251, 253].

- In addition to sector 2, the opposite sector 5 was excluded from the analysis. This condition imposes a more symmetric acceptance, but provides a maximal acceptance with 4 remaining sectors (0, 1, 3, 4).

- In order to investigate two extreme cases the full acceptance was divided into the upper half sectors (5, 0, 1) or the lower sectors (2, 3, 4) in the flow analysis.
- To include possible effects of the time-dependent sector selection, a variation run is used which includes all sectors independent of their efficiency.

Consistency checks are important to examine the analysis strategy and to inspect the scientific validity of the results inside the evaluated systematic uncertainties. They are used to find mistakes in the measurement which should be corrected for. In general, any discrepancy in the measurement should not be added to the systematic uncertainties itself. If accessible, the effect underlying the measurement deficiencies should rather be understood and be covered by the independently estimated systematic uncertainties [328]. For the above discussed systematic uncertainties three consistency checks where primarily used:

- *Measurement symmetry*: Due to the symmetric longitudinal expansion of the collision system in the center-of-mass frame, the value of all flow coefficients should be symmetric around mid-rapidity. The odd harmonics are point- and the even ones reflection-symmetric. This is checked either via point-by-point comparisons between backward- and forward rapidities or via a fit with a polynomial function describing this symmetry.
- *Zero-crossing*: the direct consequence of the symmetry condition is that all odd flow coefficients v_1, v_3 and v_5 should cross zero at mid-rapidity, whereby the even coefficients v_2, v_4 and v_6 should have a maximum or minimum there. The p_t-differentiated odd flow values are therefore checked to be compatible within errors with $v_1 = 0$ and $v_3 = 0$ at mid-rapidity.
- *Vanishing residual sine-terms*: Due to the reflection symmetry in the transverse plane and the assumption that the angular distribution is symmetrically distributed around the reaction plane (see Eq. 29) any sine-term should vanish for all orders. The main source of the residual sine-term is the result of the interplay of non-uniformities in the reconstructed angular distribution and the remaining small anisotropies in the EP-distribution. It is a reasonable assumption that any systematic effect introducing sine-terms should also give rise to cosine-terms of the same magnitude. This residual systematic effect is investigated for all harmonics over all variational runs and was found to be of smaller or similar magnitude than the systematic uncertainties estimated via the methods discussed above.

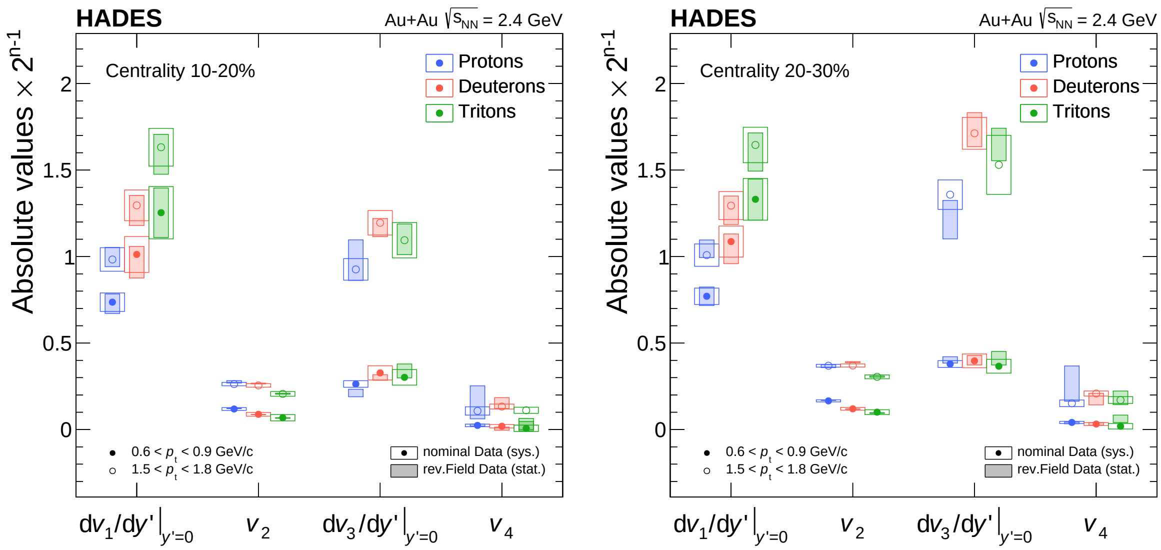

Figure 86: Comparison of the flow coefficients reconstructed from the total dataset and with data taken with reversed field polarity. Shown are the absolute values $|dv_1/dy'|_{y'=0}|$, $|v_2|$, $|dv_3/dy'|_{y'=0}|$ and $|v_4|$ measured at mid-rapidity for two exemplary p_t intervals and the two centrality classes ($10-20$ % and $20-30$ %). The data points are scaled for visibility. For the data with reversed field polarity only the statistical uncertainties and for the nominal values the systematic uncertainties are shown.

Beyond the checks on symmetry, the following conditions were studied:

- The condition of *non-negative probabilities* in the Fourier series is a useful tool to constrain or cross check the results for one or the combination of several measured flow harmonics. It prohibits the observation of a non-physical *negative particle emission* (also know as *Bochner's theorem*). In evaluating the Fourier series, it is clear that in the case that one harmonic coefficient v_n of any order being larger than 0.5 or lower than -0.5, negative probabilities arise in the angular distribution. To overcome non-physical negative probabilities in the angular distribution the following coefficients in the Fourier series have to compensate this effect.

- *Time-dependent systematic effects*: the analyses for all variational runs are also performed for each day of data taking separately. This makes it possible to investigate whether any systematic trends appear in the course of the whole data taking period.

- *Magnetic field polarity*: Another systematic check is performed by analyzing data that was recorded with a reversed magnetic field setting. In this configuration the bending direction of positively and negatively charged particles are swapped such that they are measured by different areas in the outer two `MDC` layers, as well as `TOF` and RPC. No significant differences between the two settings are found, as shown in Fig. 86.

- *Higher order* flow coefficients of 7th and 8th order were analyzed, but appeared to be insignificant with the statistical uncertainties.

Experimental Results

In the following chapter the full set of experimental results for the individual Fourier coefficients and their systematic uncertainties in the 40% most central events are presented and now also submitted for publication [332]. Preliminary values for the three first flow harmonics v_1 to v_3 were already shown in [333–336]. Results on measured flow coefficients v_1 to v_6 for protons, deuterons and tritons in selected regions of phase space in the centrality range $20 - 30\%$, shown in the Figures 87 and 91, are published in [337] and are discussed in the following with an emphasis of their systematic uncertainty and the residual sine-terms. This centrality range is chosen since the measured flow values are in general relatively high and the corrections due to the event plane resolution smaller than in other centrality classes. In particular, this enables the measurement of significant values for the higher harmonics. For the time being this chapter will be limited to the description of the data with a simple polynomial fit in the context of forward- and backward symmetries. The discussion and interpretation of the extracted parameters, as well as the comparison with other experimental measurements and theoretical models are postponed to the next chapter. In the left column of Fig. 87 the p_t dependence of the flow coefficients v_1, v_3 and v_5 at backward rapidities in the interval of $-0.25 < y_{cm} < -0.15$ are shown and in the right column their y_{cm} dependence for values averaged over the p_t interval $1.0 < p_t < 1.5$ GeV/c. The p_t interval used here provides a good compromise between large values in all flow harmonics and sufficient statistics. Above $p > 1$ GeV/c in momentum the reconstruction efficiency is rather flat, which makes it possible to average over this large p_t-range without a dedicated efficiency correction. The rapidity dependence for the values of the odd flow coefficients exhibits a typical *S-shape* with values being consistent with zero at mid-rapidity $y_{cm} = 0$ and being point-symmetric relative to it. The values for v_1 develop a clear mass dependence when moving away from mid-rapidity with smaller values for protons than deuterons and tritons $|v_1|(\mathrm{p}) < |v_1|(\mathrm{d}) < |v_1|(\mathrm{t})$. The mass ordering for v_1 is also visible in the p_t-dependence in the shown rapidity interval, whereas for v_3 and v_5 a mass hierarchy can not be

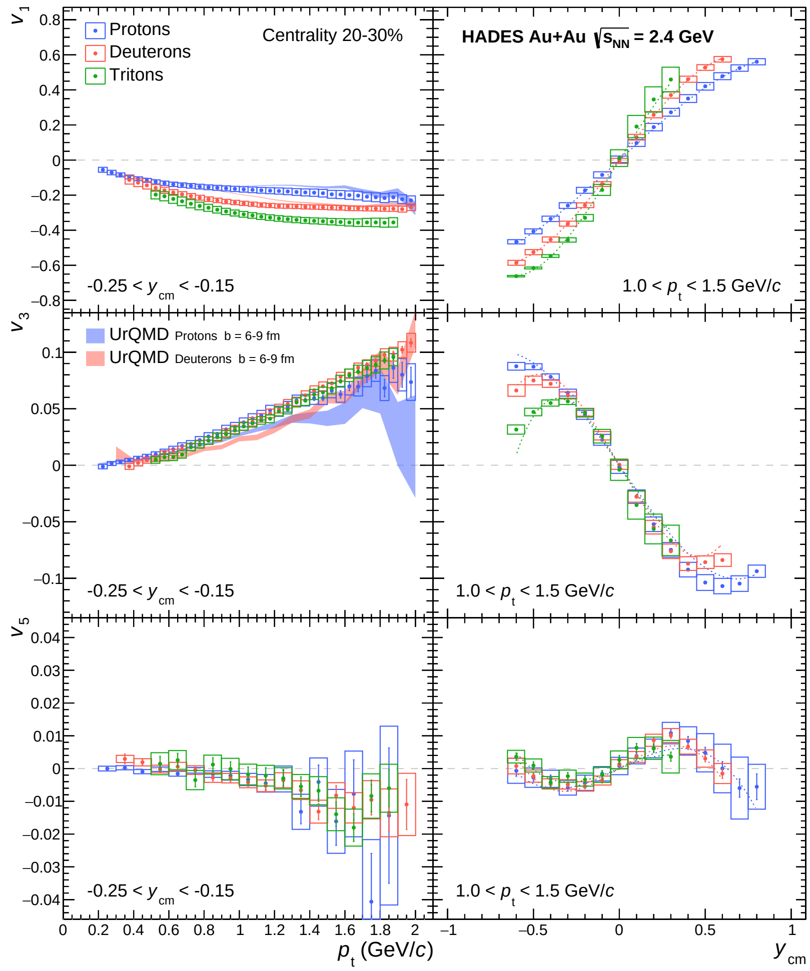

Figure 87: The p_t dependences of the odd flow coefficients v_1, v_3 and v_5 in the semi-central $(20-30\%)$ event class for protons, deuterons and tritons are presented in the left column for the rapidity interval $-0.25 < y_{cm} < -0.15$ and the corresponding y_{cm} dependences averaged over the p_t interval $1.0 < p_t < 1.5$ GeV/c in the right column. The upper row displays the values of v_1, the middle row the ones of v_3 and the lower row the ones of v_5. The systematic uncertainties are shown as open boxes and fits to the data points with the Eq. (61) as dashed coloured curves. The p_t dependences of v_1 and v_3 for protons and deuterons are compared with UrQMD model predictions, depicted as shaded areas [338]. The figure is published in [337].

verified due to the larger uncertainties. It is remarkable that the sign of v_3 is opposite to the negative one of v_1 and v_5. Around mid-rapidity the values of v_3 are comparable for the three isotopes, but at larger rapidity values v_3 develops a clear mass hierarchy $|v_3|(\mathrm{p}) > |v_3|(\mathrm{d}) > |v_3|(\mathrm{t})$, which however is inverted in relation to the values for v_1. Also the maximum shows up at larger rapidity and larger flow values for protons compared to that for deuterons and subsequently to that for tritons. For v_5, due to the larger uncertainties, a hierarchy between the isotopes can not be identified, but from the data it can be deduced that at backward- and forward rapidities further zero crossing exists.

To demonstrate the symmetry of the measurements as a function of rapidity y_{cm} the odd harmonics are fitted with the following function:

$$v_n^{odd}(y_{cm}) = v_{n1}\, y_{cm} + v_{n3}\, y_{cm}^3 \qquad (61)$$

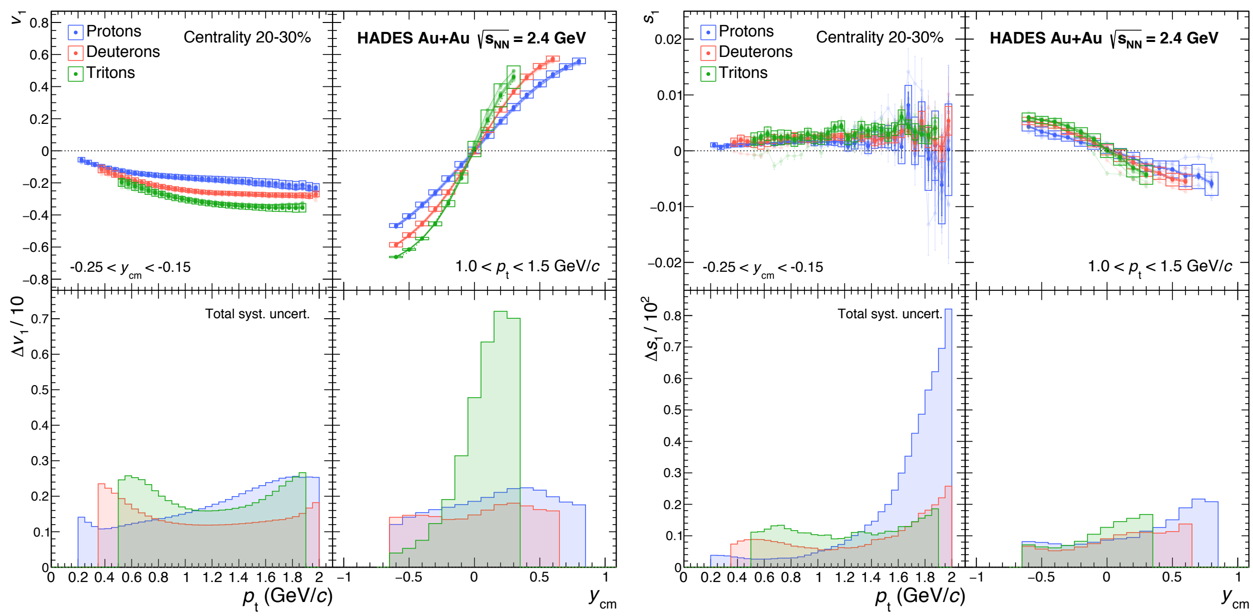

Figure 88: The values for v_1, shown in the left panel, and the measured values for s_1 in the right panel, are overlaid with the results from the variations runs. The total systematic uncertainties for v_1 and s_1, calculated from the distribution of these variation runs, are shown as boxes in the upper row and as absolute values in the lower row.

The results for free unbound protons and deuterons from the UrQMD model calculations with the Skyrme potential for a hard EOS in semi-central events ($b = 6 - 9$ fm) coupled with a coalescence procedure [338] are shown as shaded areas in the p_t-spectra. A good description for the v_1 values of the free unbound protons can be observed, while discrepancies are visible between model and data for the deuterons. At large p_t values where v_1 saturates, the difference between data and model becomes small for deuterons. Although UrQMD model calculations describe in general the rise of v_3 as a function of p_t and converges at large p_t, small deviations to data are visible at intermediate p_t.

In the upper row of the left panel of Fig. 88 the values for the cosine-term v_1 are shown and the corresponding measured values for the sine-term s_1 in the right panel. The total systematic uncertainties for v_1 and s_1, shown as boxes in the upper row and as absolute values in the lower row, are calculated from the distribution of the variation runs (see chapter Systematic uncertainties) as of 99% confidence interval range symmetric around the nominal value. The values of the systematic

	Protons		Deuterons		Tritons	
	p_t bins	y_{cm} bins	p_t bins	y_{cm} bins	p_t bins	y_{cm} bins
Total syst. uncert.	0.011 – 0.026	0.012 – 0.022	0.012 – 0.024	0.013 – 0.018	0.016 – 0.027	0.004 – 0.072
PID	0.006 – 0.018	0.008 – 0.018	0.005 – 0.014	0.003 – 0.011	0.013 – 0.024	0.003 – 0.060
Track Quality	0.004 – 0.018	0.006 – 0.011	0.003 – 0.014	0.004 – 0.013	0.011 – 0.019	0.004 – 0.021
Occupancy	0.013 – 0.021	0.011 – 0.022	0.010 – 0.026	0.007 – 0.019	0.006 – 0.029	0.005 – 0.028
Acceptance	0.006 – 0.029	0.013 – 0.024	0.014 – 0.022	0.013 – 0.018	0.017 – 0.031	0.002 – 0.070

Table 17: Range of systematic uncertainty values of v_1.

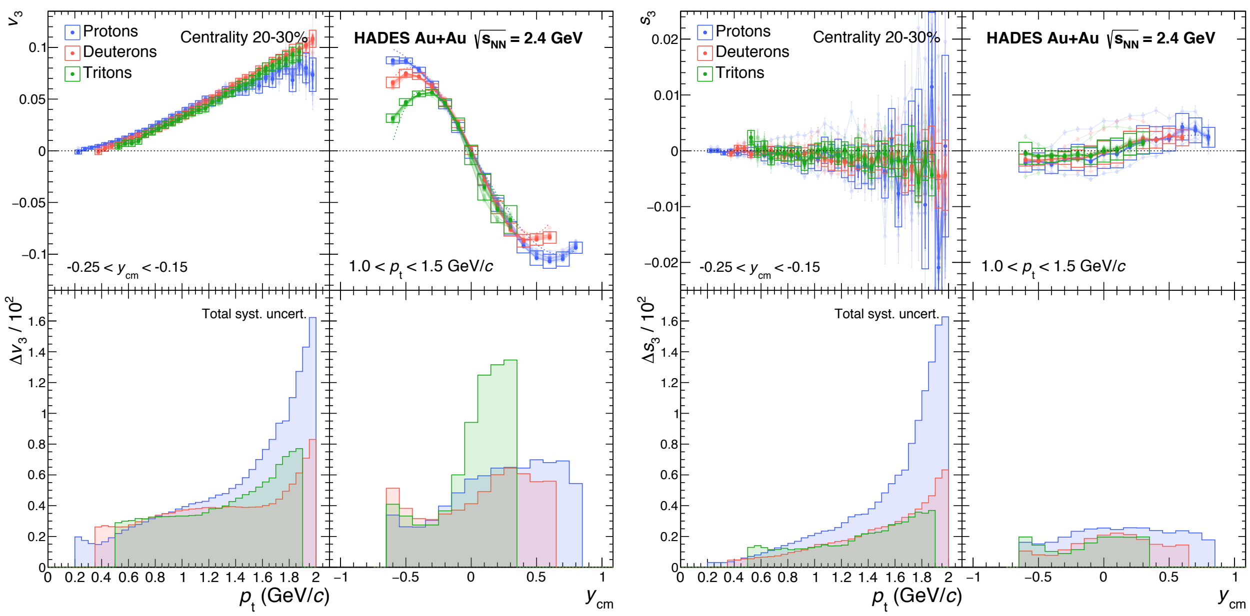

Figure 89: The values for v_3, shown in the left panel, and the measured values for s_3 in the right panel, are overlaid with the results from the variations runs. The total systematic uncertainties for v_3 and s_3, calculated from the distribution of these variation runs, are shown as boxes in the upper row and as absolute values in the lower row.

uncertainties for v_1 shown in the Fig. 88 are listed in Tab. 17 for the different particle species. To illustrate the weight of the individual contributions to the total uncertainty, the uncertainty of PID, Track Quality, Occupancy and Acceptance are calculated in the same general approach using only variational run of the same class. For the odd flow coefficients the dominating contribution arises from the correction procedure for reconstruction inefficiencies caused by high track densities (Occupancy) and the effects of an azimuthally non-uniform detector acceptance (Acceptance). In general the sine-term $s_n = \langle \sin(n\phi) \rangle$ should vanish in a perfectly corrected measurement, whereas any non-zero residual value indicates also a bias of the cosine-terms of the same and following orders due to the non-uniformities in the detector. As shown in Fig. 88, the values of s_1 and its uncertainty Δs_1 are far below the values of v_1 and its uncertainty. The values for v_3 and s_3 are presented as a function of y_{cm}- and p_t in the upper row of the left and right panels of Fig. 89, overlaid by the systematic uncertainties resulting from the different variations runs, shown as boxes in the upper row

	Protons		Deuterons		Tritons	
	p_t bins	y_{cm} bins	p_t bins	y_{cm} bins	p_t bins	y_{cm} bins
Total syst. uncert.	0.0015 – 0.0162	0.0026 – 0.0070	0.0026 – 0.0083	0.0031 – 0.0064	0.0029 – 0.0077	0.0027 – 0.0135
PID	0.0004 – 0.0073	0.0012 – 0.0048	0.0003 – 0.0046	0.0010 – 0.0040	0.0009 – 0.0052	0.0012 – 0.0101
Track Quality	0.0007 – 0.0205	0.0018 – 0.0046	0.0009 – 0.0083	0.0013 – 0.0053	0.0012 – 0.0066	0.0012 – 0.0028
Occupancy	0.0024 – 0.0086	0.0015 – 0.0088	0.0031 – 0.0063	0.0027 – 0.0084	0.0040 – 0.0055	0.0030 – 0.0086
Acceptance	0.0005 – 0.0205	0.0027 – 0.0072	0.0010 – 0.0090	0.0031 – 0.0066	0.0021 – 0.0088	0.0024 – 0.0125

Table 18: Range of systematic uncertainty values on v_3.

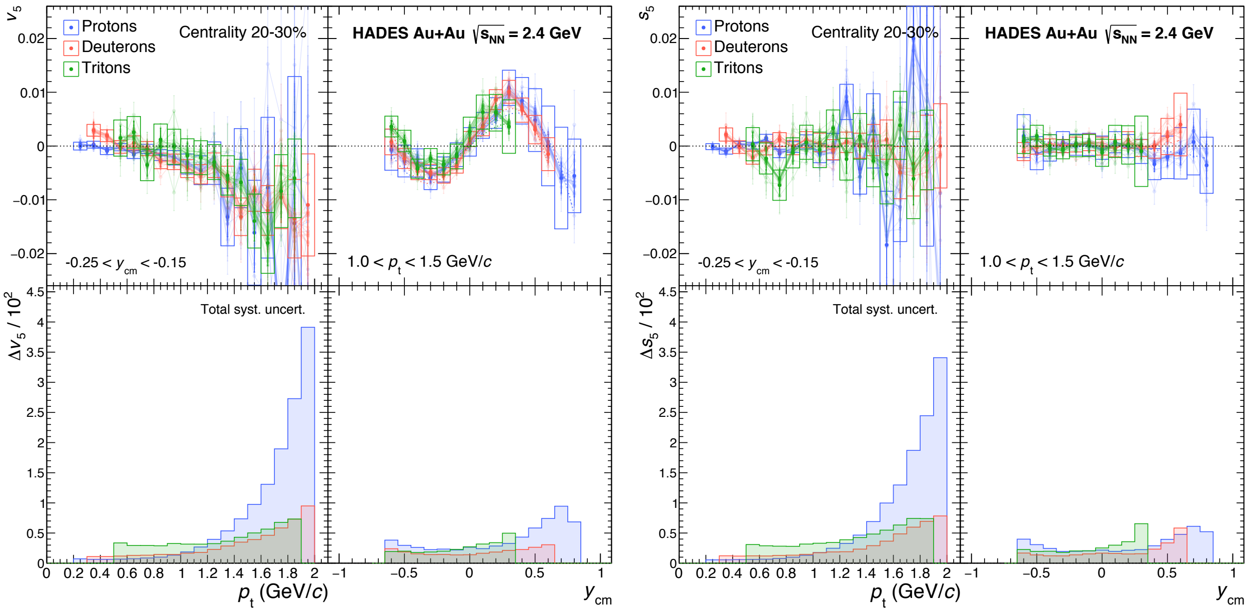

Figure 90: The values for v_5, shown in the left panel, and the measured values for s_5 in the right panel, are overlaid with the results from the variations runs. The total systematic uncertainties for v_5 and s_5, calculated from the distribution of these variation runs, are shown as boxes in the upper row and as absolute values in the lower row.

and as absolute values in the lower row. The values of the systematic uncertainties for v_3 are summarised in Tab. 18 for the different particle species.

The comparison between the two panels of Fig. 89 shows that the values of s_3 and their uncertainties Δs_3 are smaller by one magnitude than the values of v_3.The values for v_5 and s_5 as a function of y_{cm} and p_{t} are presented in the upper row of the left and right panels of Fig. 90, overlaid by the systematic uncertainties resulting from the different variations runs, shown as boxes in the upper row and as absolute values in the lower row. The values of the systematic uncertainties for v_5 are summarised in Tab. 19 for the different particle species. The comparison between the two panels of Fig. 90 shows that the values of s_5 and its uncertainties Δs_5 are smaller by one magnitude than the values of v_5.

	Protons		Deuterons		Tritons	
	p_{t} bins	y_{cm} bins	p_{t} bins	y_{cm} bins	p_{t} bins	y_{cm} bins
Total syst. uncert.	0.0006 – 0.0391	0.0022 – 0.0094	0.0011 – 0.0095	0.0014 – 0.0031	0.0029 – 0.0073	0.0018 – 0.0050
PID	0.0003 – 0.0231	0.0011 – 0.0068	0.0004 – 0.0046	0.0005 – 0.0018	0.0013 – 0.0042	0.0009 – 0.0031
Track Quality	0.0006 – 0.0314	0.0024 – 0.0107	0.0012 – 0.0111	0.0012 – 0.0042	0.0032 – 0.0077	0.0020 – 0.0059
Occupancy	0.0006 – 0.0209	0.0012 – 0.0074	0.0008 – 0.0043	0.0010 – 0.0033	0.0022 – 0.0060	0.0015 – 0.0047
Acceptance	0.0007 – 0.0584	0.0027 – 0.0099	0.0013 – 0.0128	0.0014 – 0.0031	0.0028 – 0.0079	0.0016 – 0.0036

Table 19: Range of systematic uncertainty values on v_5.

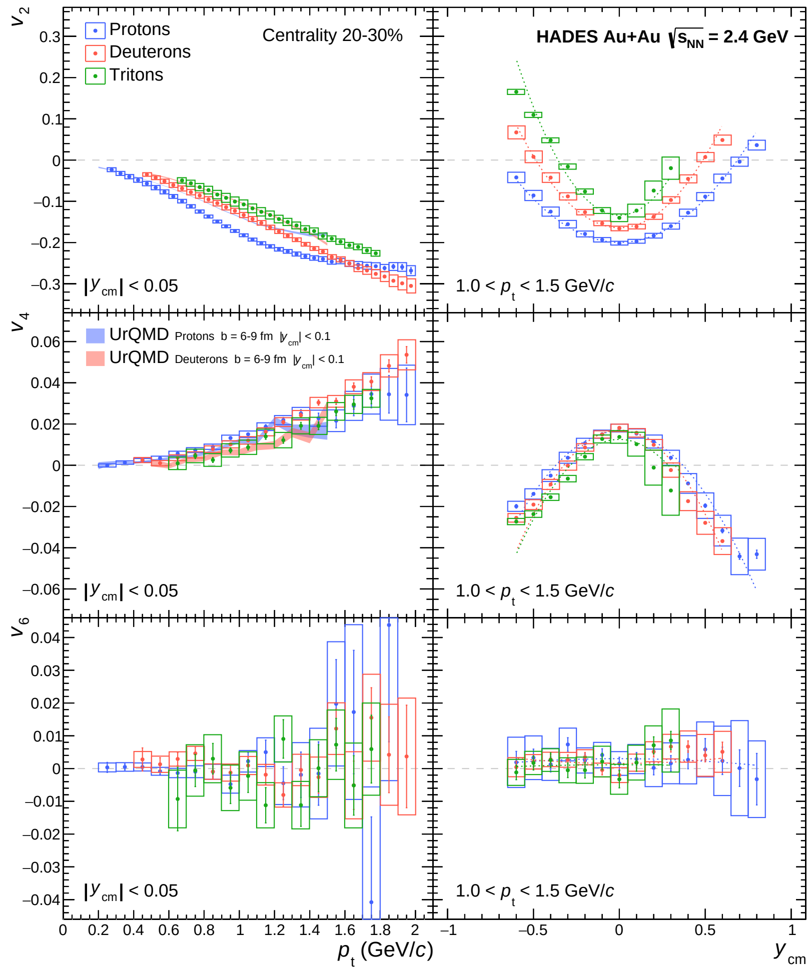

Figure 91: The p_t dependences of the even flow coefficients v_2, v_4 and v_6 in the semi-central $(20-30\%)$ event class for protons, deuterons and tritons are presented in the left column in the rapidity interval $|y_{cm}| < 0.05$ and the corresponding y_{cm} dependences averaged over the p_t interval $1.0 < p_t < 1.5$ GeV/c in the right column. The upper row displays the values of v_2, the middle row the ones of v_4 and the lower row the ones of v_6. The systematic uncertainties are shown as open boxes and fits to the data points with the Eq. (62) as dashed coloured curves. The p_t dependences of v_2 and v_4 for protons and deuterons are compared to UrQMD model calculations [338] in the rapidity interval $|y_{cm}| < 0.1$ depicted as shaded areas. The figure is published in [337].

In Fig. 91 the p_t dependences around mid-rapidity $|y_{cm}| < 0.05$ of the flow coefficients v_2, v_4 and v_6 are presented in the left column and their y_{cm} dependences for values averaged over the p_t interval $1.0 < p_t < 1.5$ GeV/c in the right column. For v_2 around mid-rapidity a clear mass ordering can again be observed $|v_2|(\mathrm{p}) > |v_2|(\mathrm{d}) > |v_2|(\mathrm{t})$ up to $p_t = 1.5$ GeV/c. This mass hierarchy becomes even more pronounced when moving away from mid-rapidity. Also, the zero-crossing for protons shows up at larger rapidity compared to that for deuterons and subsequently to that for tritons in the same p_t-interval. A mass ordering for v_4 is visible $|v_4|(\mathrm{p}) > |v_4|(\mathrm{d}) > |v_4|(\mathrm{t})$, but less significant than for v_2, whereas the zero-crossing for the three isotopes shows up at almost the same rapidities. The sign of the v_4 values at mid-rapidities is opposite to the negative v_2 values. Due to the large uncertainties for v_6 only an upper limit for the values can be derived, but no conclusion on its behavior as a function of p_t and y_{cm} is possible. Similar to the

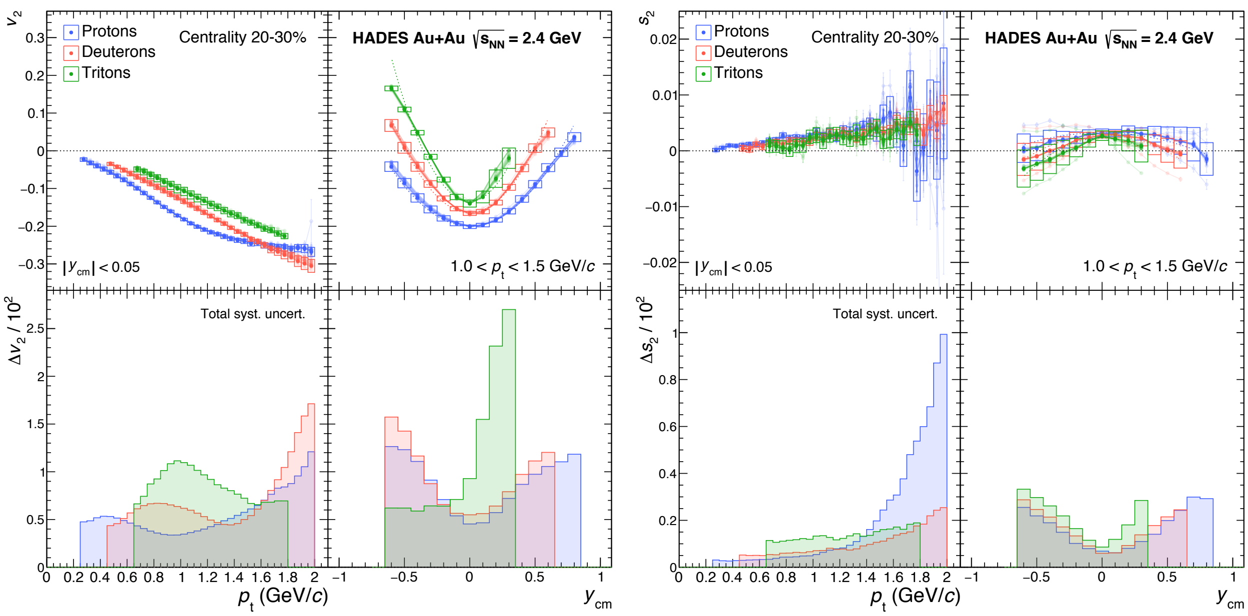

Figure 92: The values for v_2, shown in the left panel, and the measured values for s_2 in the right panel, are overlaid with results from the variations runs. The total systematic uncertainties for v_2 and s_2, calculated from the distribution of this variation runs, are shown as boxes in the upper row and as absolute values in the lower row.

odd flow coefficients the symmetry of the flow values as a function of rapidity $y_{\rm cm}$ are demonstrated for the even harmonics via the following parabolic-function:

$$v_n^{even}(y_{\rm cm}) = v_{n0} + v_{n2}\, y_{\rm cm}^2 \quad (62)$$

A good agreement between data and fit can be observed for v_2 and v_4 for all three isotopes around mid-rapidity. At the largest forward rapidity interval slightly smaller values for proton v_2 and v_4 can be seen. Also the first rapidity interval for tritons shows smaller v_2 and v_4 values in comparison to the fit. The UrQMD model provides a good description of v_4 for protons [338], while discrepancies between the measured v_2 for protons and deuterons and the model predictions can be observed at large $p_{\rm t}$-values, whereas the deviations in low $p_{\rm t}$-range are small. It should be noted that the UrQMD model calculations are averaged over a slightly larger interval around mid-rapidity $|y_{\rm cm}| < 0.1$.

In the upper row of the left and right panels of Fig. 92 the values for v_2 and s_2 as a function of $p_{\rm t}$ and $y_{\rm cm}$ are presented. In addition, the systematic uncertainties resulting from the different variation runs are

	Protons		Deuterons		Tritons	
	$p_{\rm t}$ bins	$y_{\rm cm}$ bins	$p_{\rm t}$ bins	$y_{\rm cm}$ bins	$p_{\rm t}$ bins	$y_{\rm cm}$ bins
Total syst. uncert.	0.003 – 0.012	0.005 – 0.013	0.004 – 0.017	0.005 – 0.016	0.007 – 0.011	0.006 – 0.027
PID	0.001 – 0.009	0.002 – 0.010	0.001 – 0.011	0.002 – 0.008	0.003 – 0.007	0.004 – 0.024
Track Quality	0.002 – 0.013	0.002 – 0.006	0.002 – 0.019	0.002 – 0.009	0.004 – 0.009	0.003 – 0.012
Occupancy	0.005 – 0.009	0.005 – 0.016	0.006 – 0.009	0.006 – 0.016	0.006 – 0.010	0.006 – 0.013
Acceptance	0.001 – 0.013	0.003 – 0.015	0.001 – 0.019	0.004 – 0.019	0.005 – 0.010	0.005 – 0.025

Table 20: Range of systematic uncertainty values on v_2.

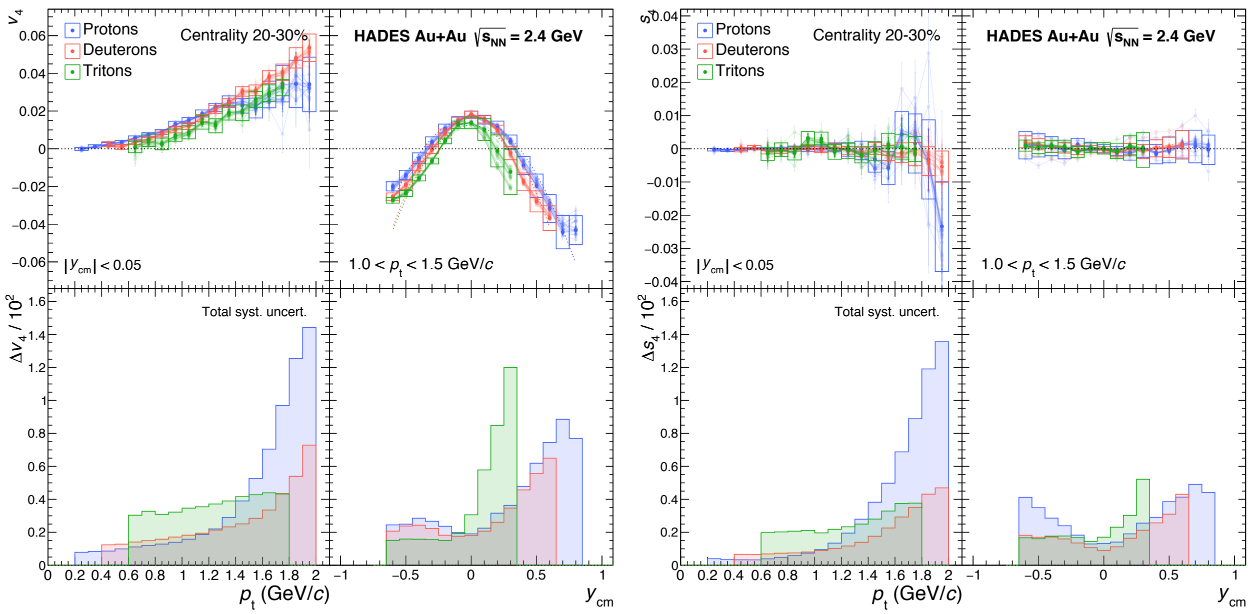

Figure 93: The values for v_4, shown in the left panel, and the measured values for s_4 in the right panel, are overlaid with the results from the variations runs. The total systematic uncertainties for v_4 and s_4, calculated from the distribution of these variation runs, are shown as boxes in the upper row and as absolute values in the lower row.

included shown as boxes in the upper row and as absolute values in the lower row. The values of the systematic uncertainties for v_2 are shown in Tab. 20 for the three hydrogen isotopes. In comparison to the odd harmonics the weight of the individual contributions to the total systematic uncertainty are for the even flow coefficients of roughly equal size. As shown in Fig. 92, the value of s_2 and its uncertainty Δs_2 are in most regions of the phase space consistent with zero and their magnitude is about one order smaller than the one of v_1. In the upper row of the left and right panel of Fig. 93 the values for v_4 and s_4 as a function of p_t and y_{cm} are displayed. In addition, the systematic uncertainties resulting from the different variation runs are included shown as boxes in the upper row and as absolute values in the lower row. The values of the systematic uncertainties for v_4 are shown in Tab. 21 for the three hydrogen isotopes. As shown in Fig. 93, the values of s_4 and its uncertainties Δs_4 are overall consistent with zero and their magnitude is far below the one of the measured values of v_4.

	Protons		Deuterons		Tritons	
	p_t bins	y_{cm} bins	p_t bins	y_{cm} bins	p_t bins	y_{cm} bins
Tot. syst. uncert.	0.0008 – 0.0144	0.0019 – 0.0089	0.0012 – 0.0073	0.0018 – 0.0065	0.0030 – 0.0044	0.0015 – 0.0120
PID	0.0002 – 0.0092	0.0008 – 0.0059	0.0004 – 0.0045	0.0006 – 0.0039	0.0013 – 0.0026	0.0006 – 0.0090
Track Quality	0.0004 – 0.0161	0.0013 – 0.0062	0.0008 – 0.0076	0.0007 – 0.0024	0.0022 – 0.0051	0.0011 – 0.0051
Occupancy	0.0012 – 0.0082	0.0018 – 0.0104	0.0015 – 0.0052	0.0015 – 0.0091	0.0026 – 0.0040	0.0018 – 0.0078
Acceptance	0.0004 – 0.0165	0.0016 – 0.0078	0.0012 – 0.0085	0.0015 – 0.0055	0.0031 – 0.0044	0.0013 – 0.0114

Table 21: Variation values nominal, min. and max. v_4

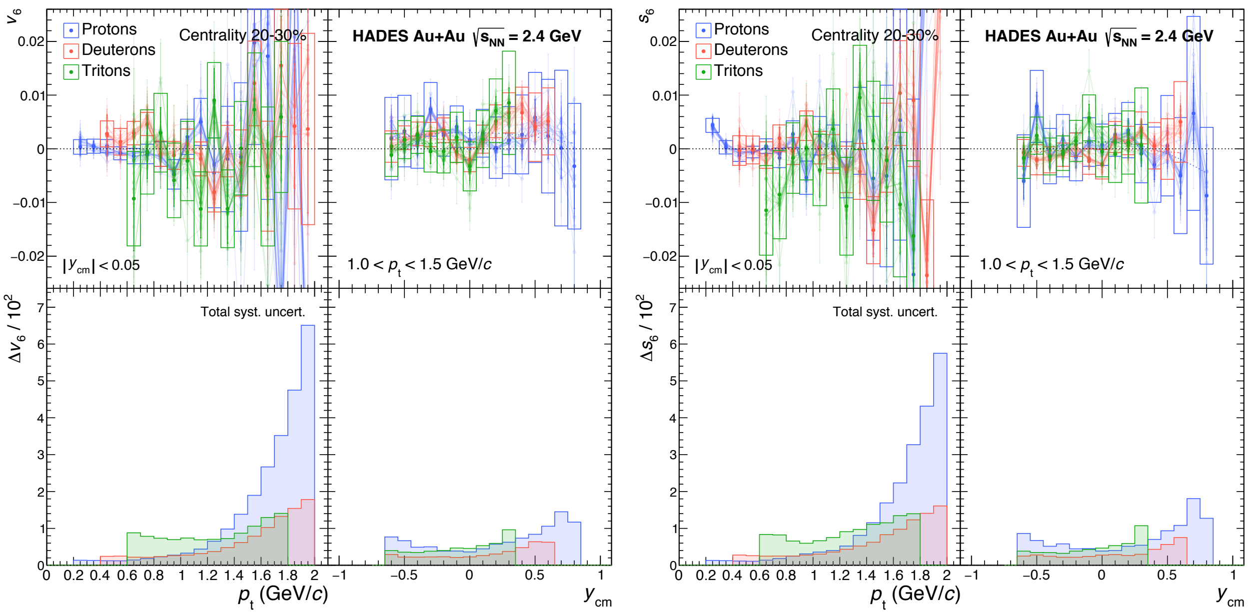

Figure 94: The values for v_6, shown in the left panel, and the measured values for s_6 in the right panel, are overlaid with the results from the variations runs. The total systematic uncertainties for v_6 and s_6, calculated from the distribution of these variation runs, are shown as boxes in the upper row and as absolute values in the lower row.

In the upper row of the left and right panel of Fig. 94 the values for v_6 and s_6 as a function of p_t and y_{cm} are presented. In addition, the systematic uncertainties resulting from the different variation runs are included shown as boxes in the upper row and as absolute values in the lower row. The values of the systematic uncertainties for v_6 are shown in Tab. 22 for the different particle species. As shown in Fig. 94, the values of v_6 and s_6 are dominated by their statistical uncertainties which are a of similar magnitude.

	Protons		Deuterons		Tritons	
	p_t bins	y_{cm} bins	p_t bins	y_{cm} bins	p_t bins	y_{cm} bins
Tot. syst. uncert.	0.0012 – 0.0651	0.0036 – 0.0145	0.0022 – 0.0178	0.0021 – 0.0064	0.0069 – 0.0141	0.0035 – 0.0096
PID	0.0006 – 0.0359	0.0021 – 0.0091	0.0012 – 0.0100	0.0010 – 0.0035	0.0029 – 0.0074	0.0018 – 0.0071
Track Quality	0.0012 – 0.0874	0.0042 – 0.0200	0.0027 – 0.0246	0.0023 – 0.0086	0.0090 – 0.0178	0.0045 – 0.0114
Occupancy	0.0008 – 0.0322	0.0015 – 0.0099	0.0011 – 0.0094	0.0008 – 0.0033	0.0047 – 0.0110	0.0024 – 0.0107
Acceptance	0.0014 – 0.0735	0.0044 – 0.0138	0.0024 – 0.0191	0.0024 – 0.0069	0.0062 – 0.0148	0.0033 – 0.0083

Table 22: Range of systematic uncertainty values on v_6.

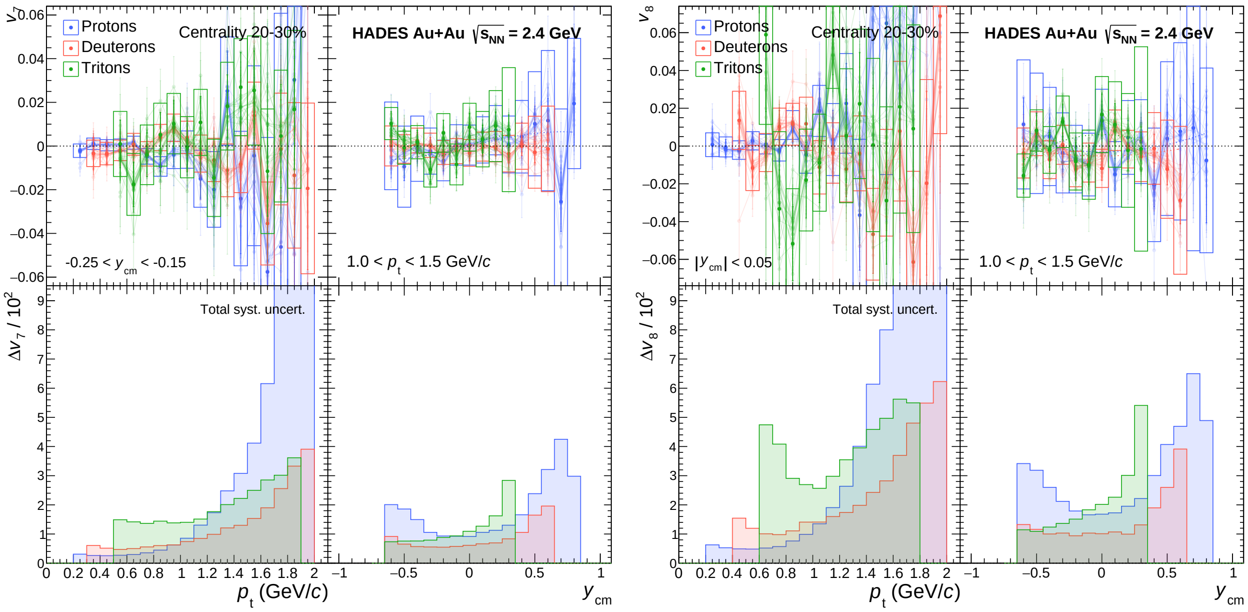

Figure 95: The measured values for v_7, shown in the left panel, and for v_8 in the right panel, are overlaid with the results from the variations runs. The total systematic uncertainties for v_7 and v_8, calculated from the distribution of these variation runs, are shown as boxes in the upper row and as absolute values in the lower row.

Presented are in Fig. 95 the p_t dependence of the flow coefficient v_7 in the backward rapidity interval $-0.25 < y_{cm} < -0.15$ (left panel) and v_8 around mid-rapidity $|y_{cm}| < 0.05$ (right panel) and their y_{cm} dependence for values averaged over the p_t interval $1.0 < p_t < 1.5$ GeV/c. From the spectra it can be seen that due to the dominating statistical uncertainties only an upper bound can be obtained. Since the measured values of the residual sine-terms for s_7 and s_8 have similar systematic uncertainties, the upper limit for the absolute accuracy of the measurement of v_7 can be estimated as 0.02 and for v_8 as 0.03 for protons up to $p_t < 1.5$ GeV/c.

	Protons		Deuterons		Tritons	
	p_t bins	y_{cm} bins	p_t bins	y_{cm} bins	p_t bins	y_{cm} bins
			v_7			
Total syst. uncert.	0.0026 – 0.1732	0.0092 – 0.0425	0.0047 – 0.0391	0.0055 – 0.0196	0.0137 – 0.0361	0.0074 – 0.0284
PID	0.0012 – 0.0793	0.0028 – 0.0297	0.0025 – 0.0260	0.0027 – 0.0152	0.0062 – 0.0172	0.0041 – 0.0149
Track Quality	0.0032 – 0.2778	0.0098 – 0.0619	0.0066 – 0.0536	0.0065 – 0.0226	0.0159 – 0.0595	0.0065 – 0.0495
Occupancy	0.0015 – 0.0699	0.0028 – 0.0288	0.0019 – 0.0172	0.0024 – 0.0093	0.0092 – 0.0182	0.0049 – 0.0211
Acceptance	0.0031 – 0.1886	0.0103 – 0.0333	0.0048 – 0.0406	0.0055 – 0.0195	0.0139 – 0.0332	0.0091 – 0.0238
			v_8			
Total syst. uncert.	0.0048 – 0.2445	0.0166 – 0.0650	0.0098 – 0.0623	0.0094 – 0.0391	0.0257 – 0.0562	0.0109 – 0.0541
PID	0.0018 – 0.1510	0.0073 – 0.0414	0.0049 – 0.0461	0.0049 – 0.0218	0.0150 – 0.0332	0.0055 – 0.0301
Track Quality	0.0054 – 0.3414	0.0209 – 0.0726	0.0111 – 0.0851	0.0105 – 0.0503	0.0335 – 0.0668	0.0120 – 0.1024
Occupancy	0.0030 – 0.1477	0.0067 – 0.0398	0.0054 – 0.0442	0.0042 – 0.0166	0.0169 – 0.0498	0.0107 – 0.0258
Acceptance	0.0057 – 0.2802	0.0164 – 0.0885	0.0129 – 0.0527	0.0110 – 0.0422	0.0241 – 0.0617	0.0103 – 0.0463

Table 23: Range of systematic uncertainty values on v_7 and v_8.

Directed flow

The directed flow coefficient v_1 measured for protons is shown in Fig 96 in various p_t and y_{cm} intervals. The upper left panel shows v_1 as a function of the centre-of-mass rapidity y_{cm} in several p_t intervals of 50 MeV/c width for semi-central events ($20-30\%$). While v_1 is consistent with zero at mid-rapidity as expected due to the symmetry of the collision system, the y_{cm} dependence has a typical *S-shape*, which is stronger at higher than at lower transverse momenta. The p_t dependence of the proton v_1 is shown in the upper right panel of Fig. 96 for four exemplary rapidity intervals, chosen symmetrically

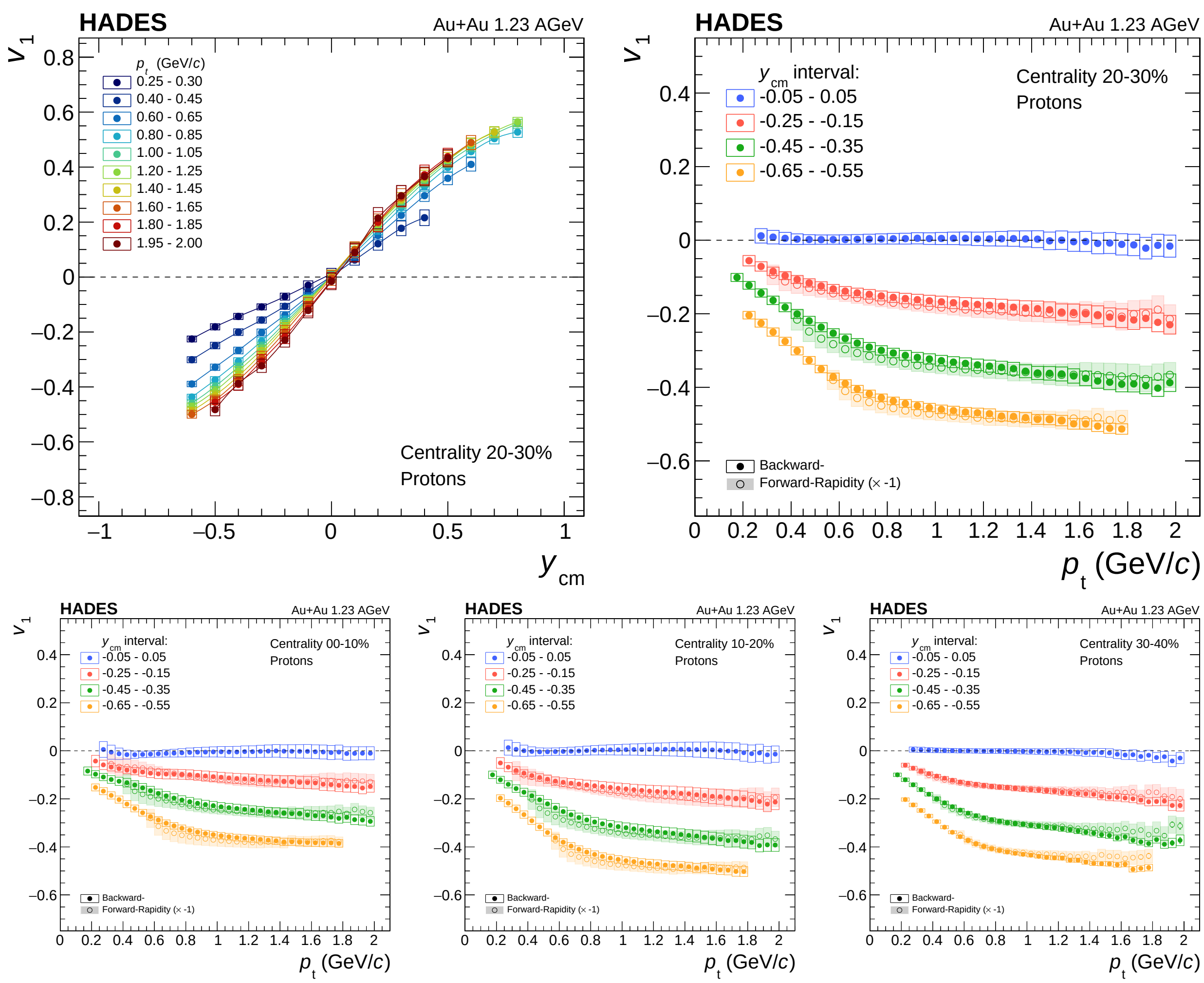

Figure 96: The directed flow (v_1) of protons in semi-central events ($20-30\%$) as a function of the centre-of-mass rapidity y_{cm} in transverse momentum intervals of 50 MeV/c width are shown (upper left panel, lines are to guide the eye. The p_t intervals are shown in the legend). The proton v_1 as a function of p_t in several rapidity intervals, chosen symmetrically around mid-rapidity, are displayed for different centrality ranges (upper right and lower panel). The values measured in the forward hemisphere (open symbols) have been multiplied by -1. The systematic uncertainties are displayed here as empty- and dashed-filled boxes.

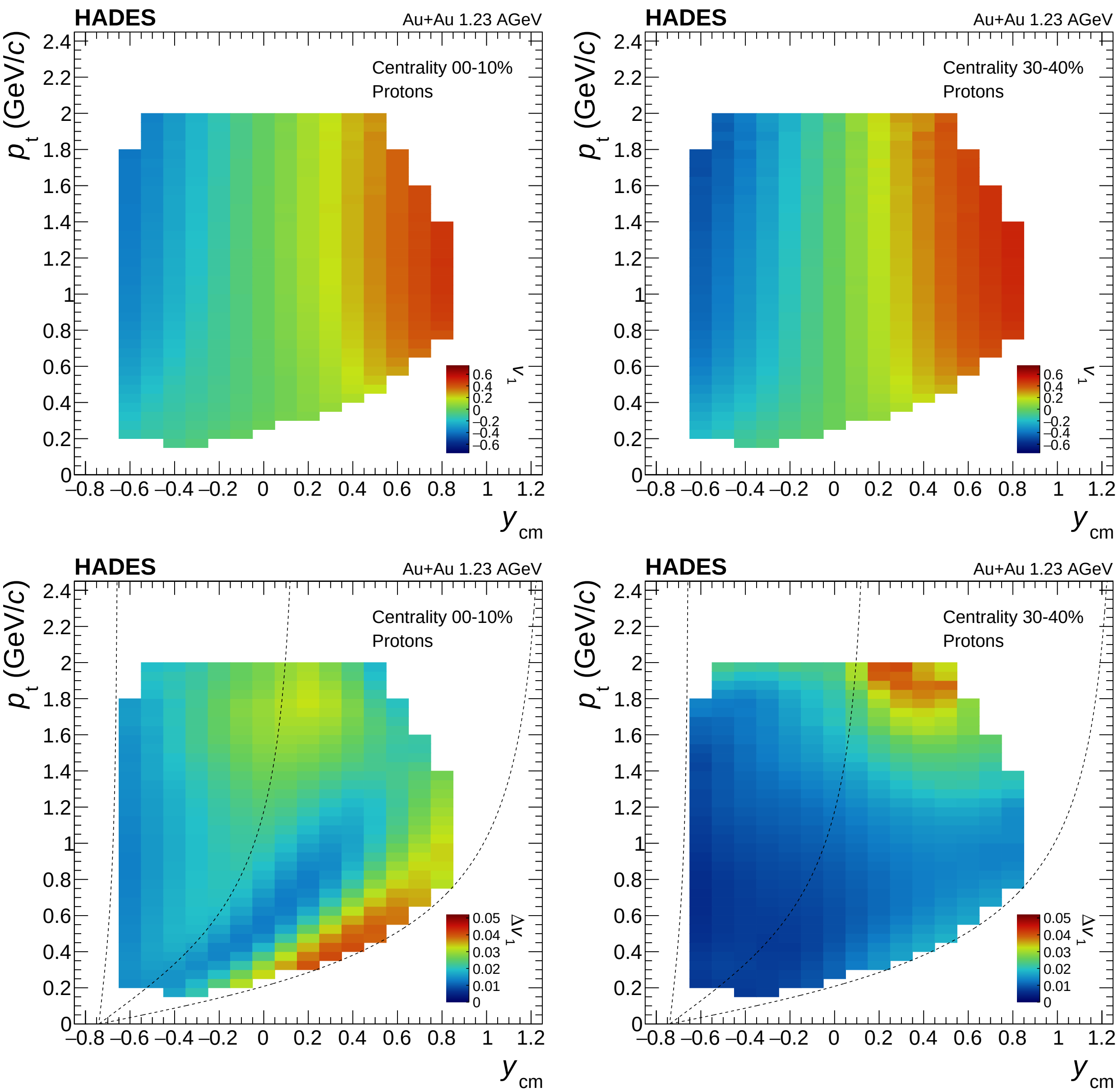

Figure 97: In the upper row the values for the directed flow coefficient v_1 for protons as a function of p_t and y_{cm} for two centrality classes ($0-10\%$ and $30-40\%$) are shown and in the lower row the absolute values of the systematic uncertainty. The dashed lines in the lower panels show the theta angles 15°, 44° and 85° and corresponds to the lower acceptance edges, the overlap between TOF and RPC detectors and the upper acceptance edges of the detector system.

around mid-rapidity in the same semi-central ($20-30\%$) event class. The values measured in the forward hemisphere (open symbols) have been multiplied by -1 for a direct comparison with the backward rapidity values (filled symbols). In the lower panel the p_t dependence in three other centrality classes ($0-10\%$, $10-20\%$, $30-40\%$) is displayed and the comparison shows that the centrality dependence is very moderate, only in the most central event class slightly smaller values are observed. The measured proton v_1 shows a good agreement well within systematic errors between forward and backward rapidity

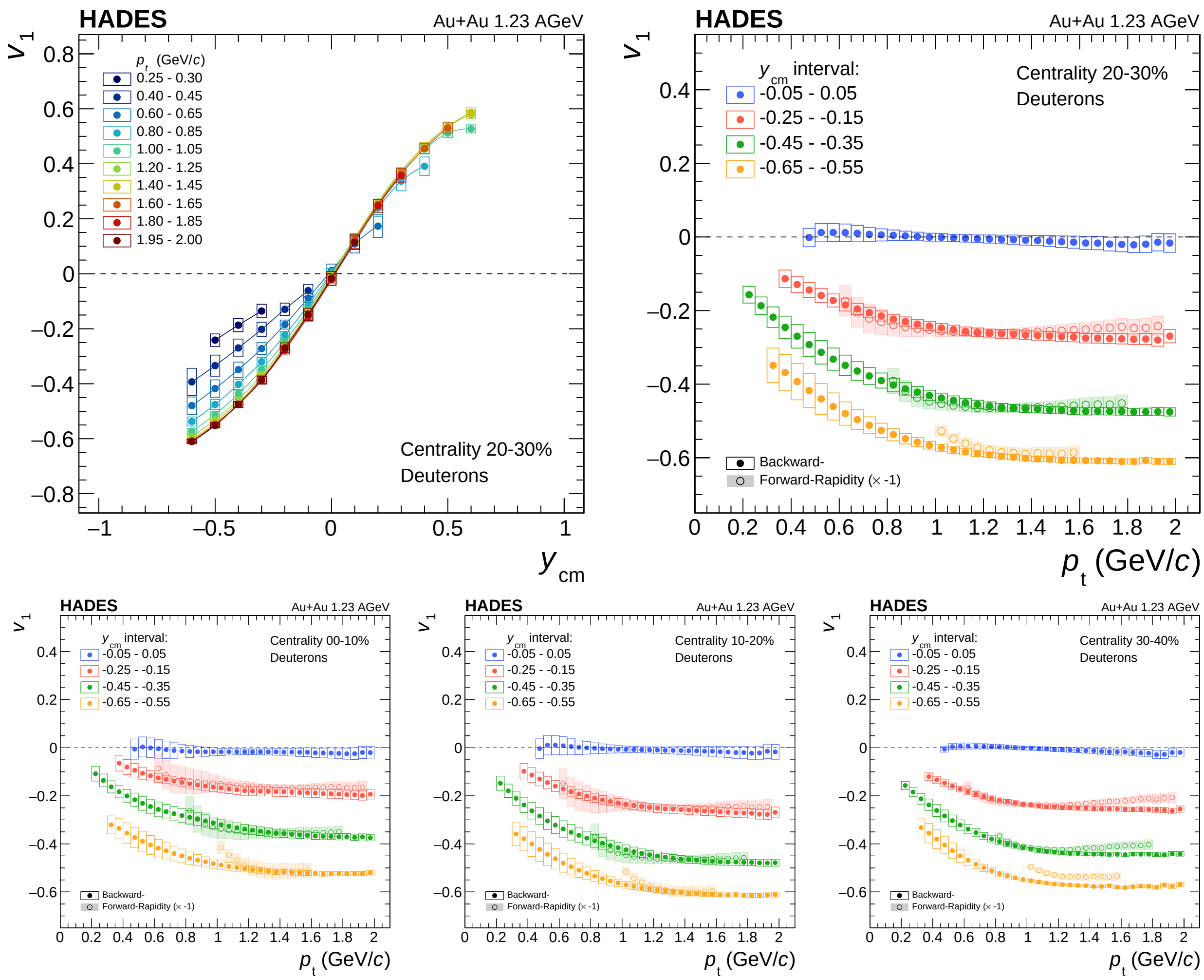

Figure 98: The same as shown in Fig. 96 for the directed flow (v_1) of deuterons.

intervals. The p_t spectra exhibit an almost linear rapid rise $v_1 \propto p_t$ in the region $p_t < 0.6$ GeV/c and then increase only moderately till they saturate for $p_t > 1$ GeV/c. The upper row of Fig. 97 shows the measured v_1 values as a function of p_t and y_{cm} for the two centrality classes ($0-10\%$ and $30-40\%$) and in the lower row the absolute values of the systematic uncertainty. Here the contribution of the occupancy to the systematic uncertainty is clearly visible in the low polar angular region (lower right corner), where its is most dominant in the most central event class and the effect vanishes in the more peripheral central class. In the higher p_t region, in forward rapidities, the effects of the track reconstruction and particle identification quality are noticeable as contribution to the systematic uncertainties. A similar behavior is observed in the p_t and y_{cm} dependences for v_1 of deuterons (Fig. 98) and tritons (Fig. 99). The centrality dependence is also in the case of

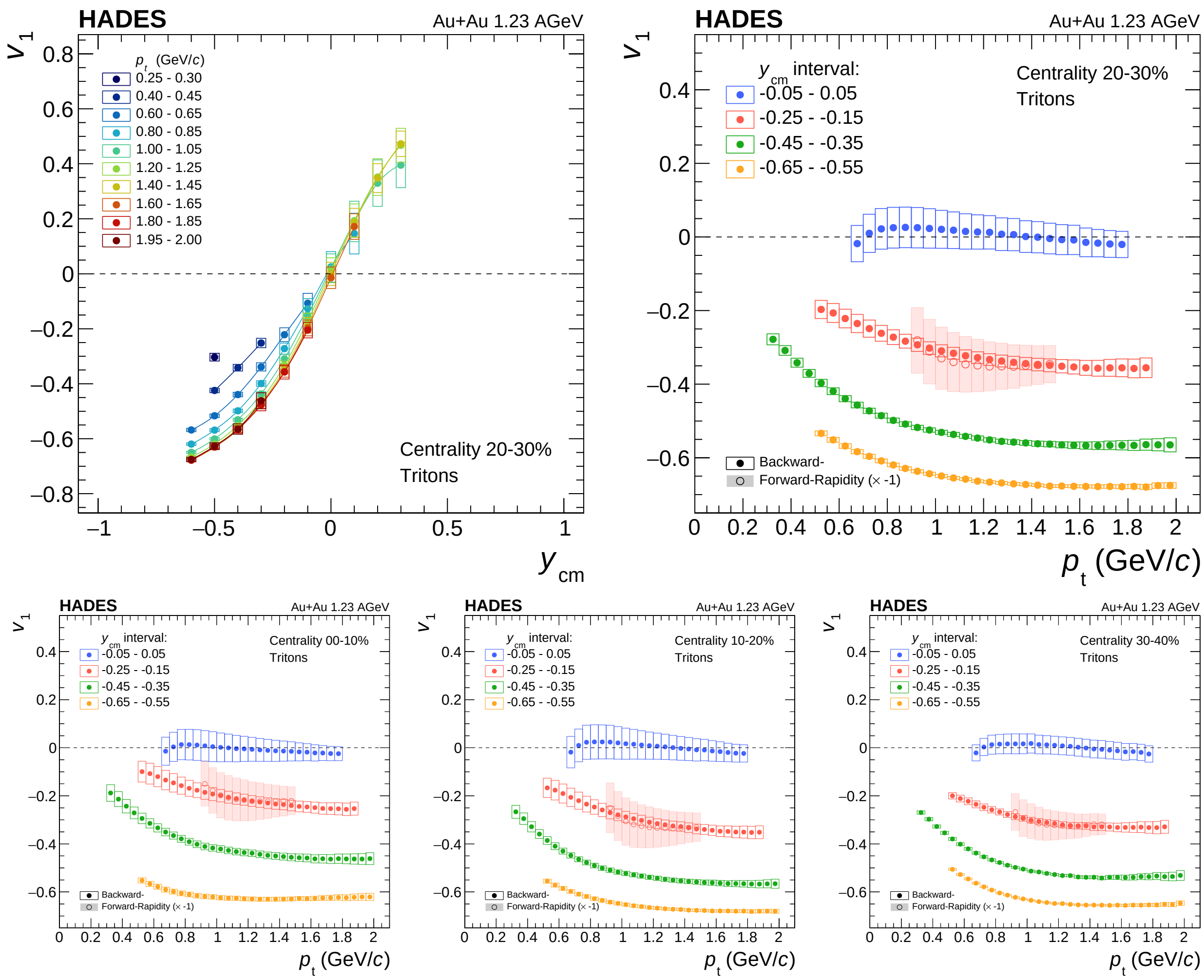

Figure 99: The same as shown in Fig. 96 for the directed flow (v_1) of tritons.

deuteron and triton v_1 moderate, the values for the most central event class being only slightly smaller in comparison to the peripheral classes. For the $|y_{\mathrm{cm}}|$ interval $0.55 - 0.65$ and the centrality class $20 - 30\%$ the saturation values of v_1 are $|v_1^{\mathrm{prot.}}| \approx 0.5$, $|v_1^{\mathrm{deut.}}| \approx 0.6$ and $|v_1^{\mathrm{trit.}}| \approx 0.7$. This means that the dependence of v_1 on rapidity gets more pronounced with increasing mass of the particle, such that as a consequence the slope at mid-rapidity increases. The qualitative difference between the three hydrogen isotopes is that the region between the transition of the almost linear rise $v_1 \propto p_{\mathrm{t}}$ at low p_{t}-values to saturated v_1-values increase with particle mass.

Elliptic flow

The upper left panel of Fig. 100 shows the v_2 values for protons as a function of y_{cm} for the centrality range $20-30\%$. The absolute values of v_2 are largest at mid-rapidity and decrease towards forward and backward rapidities until they reach zero at rapidities of approximately $|y_{\mathrm{cm}}| \approx 0.7$. The p_{t} dependence of v_2 is shown in the upper right panel of Fig. 100 for four exemplary rapidity intervals. At mid-rapidity the v_2 values decrease continuously with p_{t} proportional to $v_2 \propto p_{\mathrm{t}}^2$ in the region $p_{\mathrm{t}} < 0.8$ GeV/c and from there only moderately until it saturates at values around 2 GeV/c. In the lower panel of Fig. 100 the

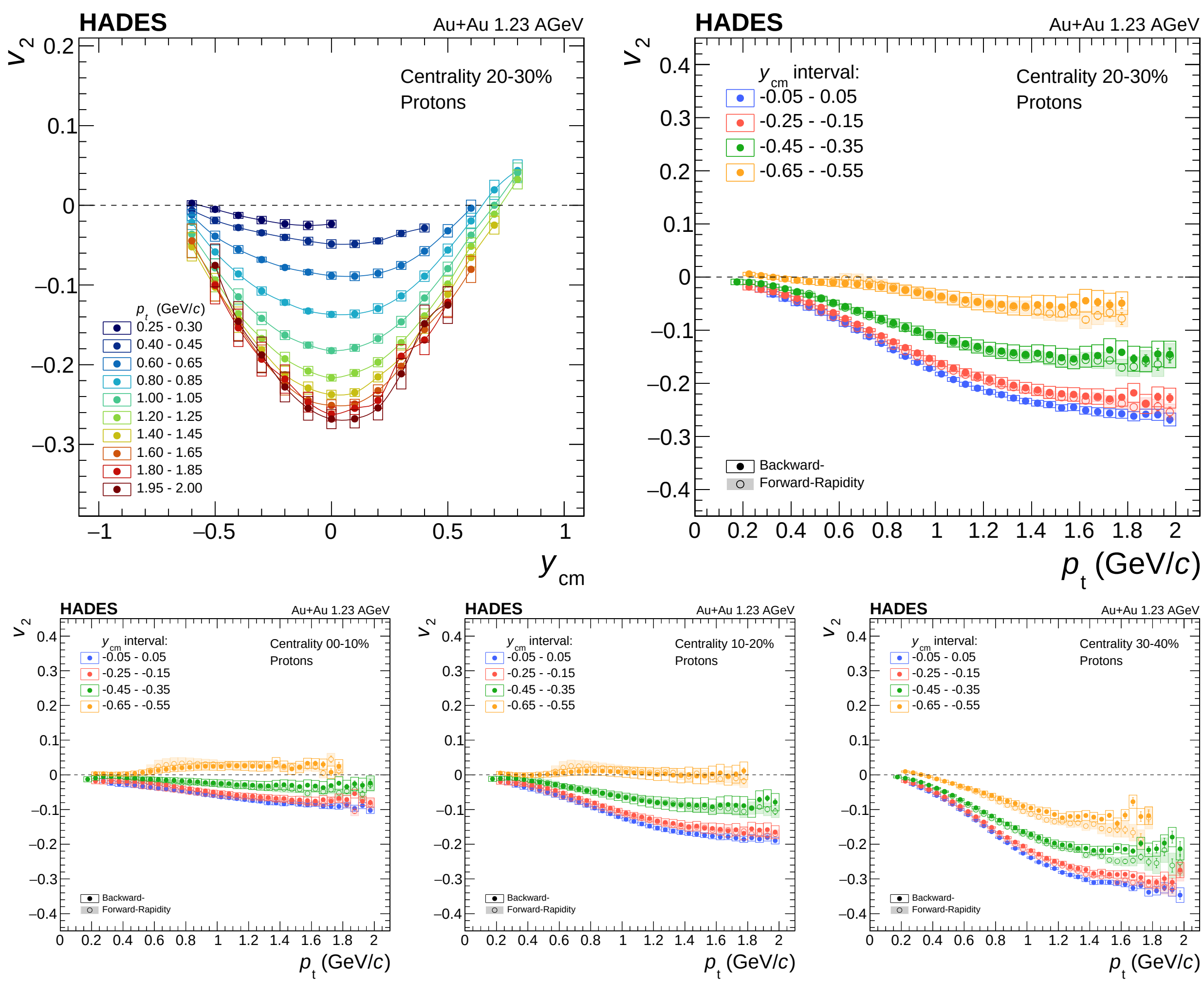

Figure 100: The elliptic flow (v_2) of protons in semi-central events ($20-30\%$) as a function of the centre-of-mass rapidity y_{cm} in transverse momentum intervals of 50 MeV/c width are shown (upper left panel, lines are to guide the eye. The p_{t} intervals are shown in the legend). The proton v_2 as a function of p_{t} in several rapidity intervals, chosen symmetrically around mid-rapidity, are displayed for different centrality ranges (upper right and lower panel). The systematic uncertainties are displayed here as empty- and dashed-filled boxes.

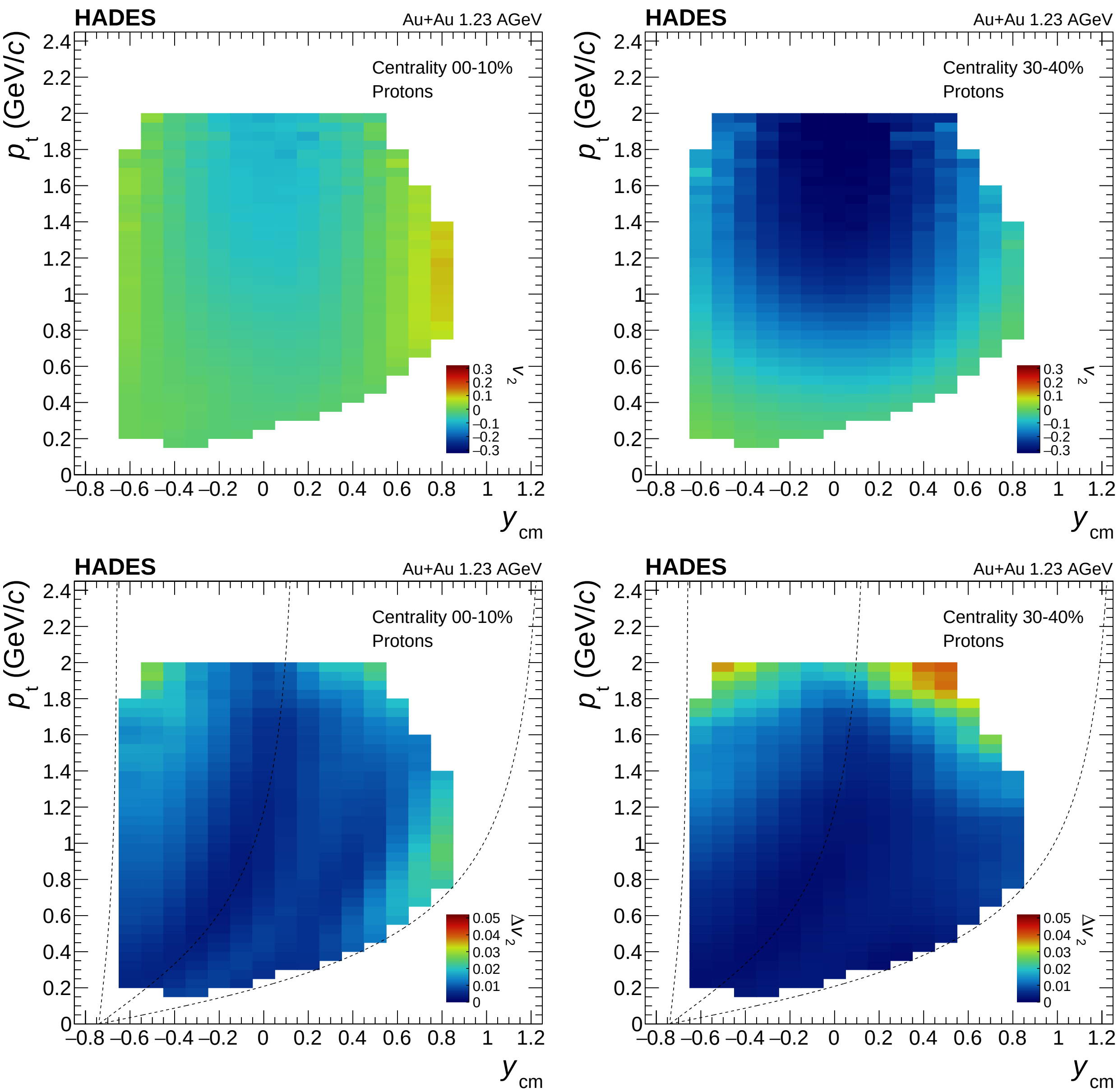

Figure 101: In the upper row the values for the elliptic flow coefficient v_2 for protons as a function of p_t and y_{cm} for two centrality classes ($0-10\%$ and $30-40\%$) are shown and in the lower row the absolute values of the systematic uncertainty. The dashed lines in the lower panels show the theta angles 15°, 44° and 85° and corresponds to the lower acceptance edges, the overlap between TOF and RPC detectors and the upper acceptance edges of the detector system.

p_t dependence of v_2 for the three other centrality classes is shown and the comparison of the p_t spectra reveals that there is a continuous rise of the highest absolute values at mid-rapidity, going from the most central events to the semi-central. With increasing absolute v_2 values the zero crossing in the y_{cm} dependences moves to larger rapidities. The upper row of Fig. 101 shows the measured v_2 as a function of p_t and y_{cm} for the two centrality classes ($0-10\%$ and $30-40\%$) and in the lower row the absolute values of the systematic uncertainty are displayed. Here small effects due to the high occupancy are recognizable in the

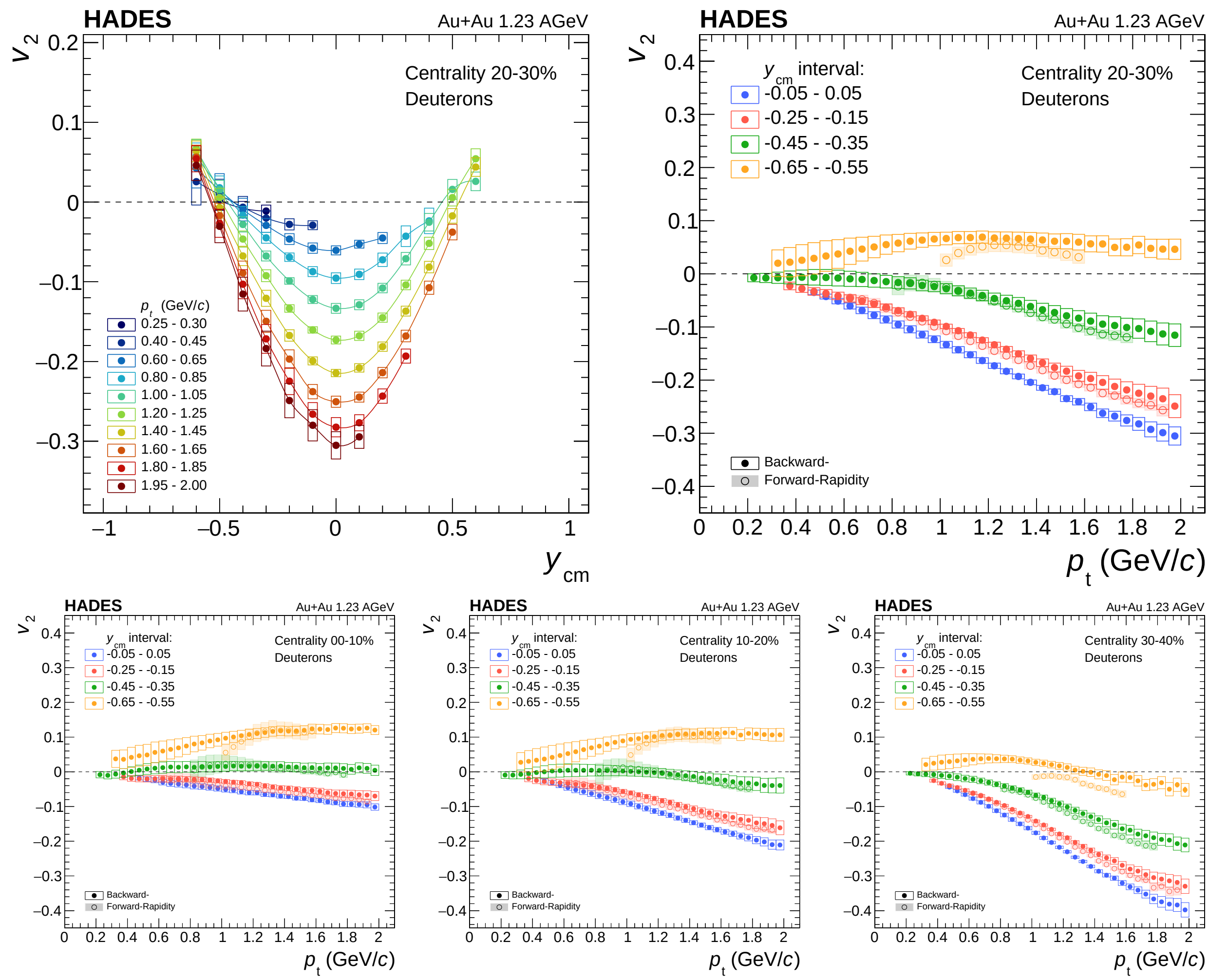

Figure 102: The same as shown in Fig. 100 for the elliptic flow (v_2) of deuterons.

low polar angular region (lower right corner) in the most central event class and vanish when going to more peripheral events. In the higher p_t region at forward and backward rapidities the influence of particle misidentification are noticeable as contribution to the systematic uncertainty (here for the protons mainly ^{3}He). In the centrality class $30-40\%$ the effects of increasing impurities in the protons selection can be seen as small discontinuities in the spectra at large p_t-values. The v_2 values of the misidentified heavier particles are in general larger resulting into a systematic shift of the measured v_2 values for the protons. This effect is not so pronounced in the deuteron and triton sample. In the Fig. 102 and 103 the v_2 values for deuterons and tritons as a function of p_t and y_{cm} are shown, again for the centrality range $20-30\%$ in the upper row and in the lower row the p_t-spectra for the other centrality classes. In general, the drop with p_t for protons is faster than for deuterons which

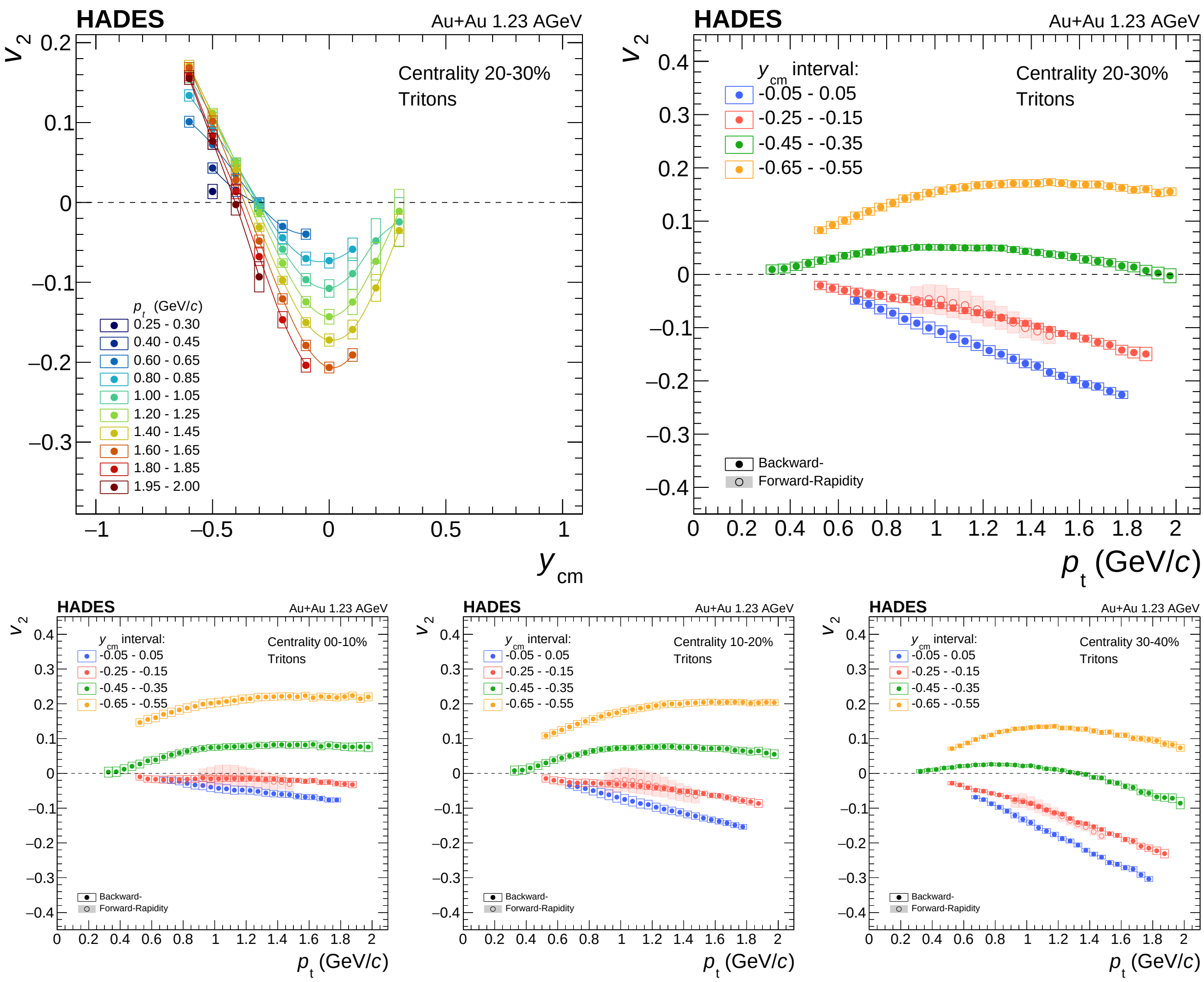

Figure 103: The same as shown in Fig. 100 for the elliptic flow (v_2) of tritons.

is in turn faster than for tritons. While there is a pronounced saturation at large p_t-values for protons, such a behavior can not be observed for deuterons and tritons. A strong dependence on the particle type is also observable for the rapidity distributions of v_2. While for protons a zero crossing is found at rapidities of $|y_{cm}| \approx 0.7$, the distributions for deuterons are significantly narrower, such that they cross zero already at $|y_{cm}| \approx 0.5$ and v_2 changes sign for larger centre-of-mass rapidities. For tritons this change of sign already happens around $|y_{cm}| \approx 0.35$. In comparison to mid-rapidity at larger backward and forward rapidities the p_t-spectra exhibit a different shape, where it rises from zero at $p_t = 0$ up to a maximum value at intermediate p_t and then decreases again towards higher p_t.

Triangular flow

The triangular flow coefficient v_3 measured for protons is shown in Fig 104 in various p_t and y_{cm} intervals. The left panel shows v_3 as a function of the centre-of-mass rapidity y_{cm} in several p_t intervals of 50 MeV/c width for the semi-central events ($20-30\%$). The rapidity dependence of the v_3-values shows a typical *S-shape*, similar in shape to the one of v_1, however, with the opposite sign and narrower in shape. Like in the case of v_1 the values for v_3 are consistent with zero at mid-rapidity. The p_t dependence of the proton v_3 is shown in the right panel of Fig. 104 for four exemplary rapidity intervals,

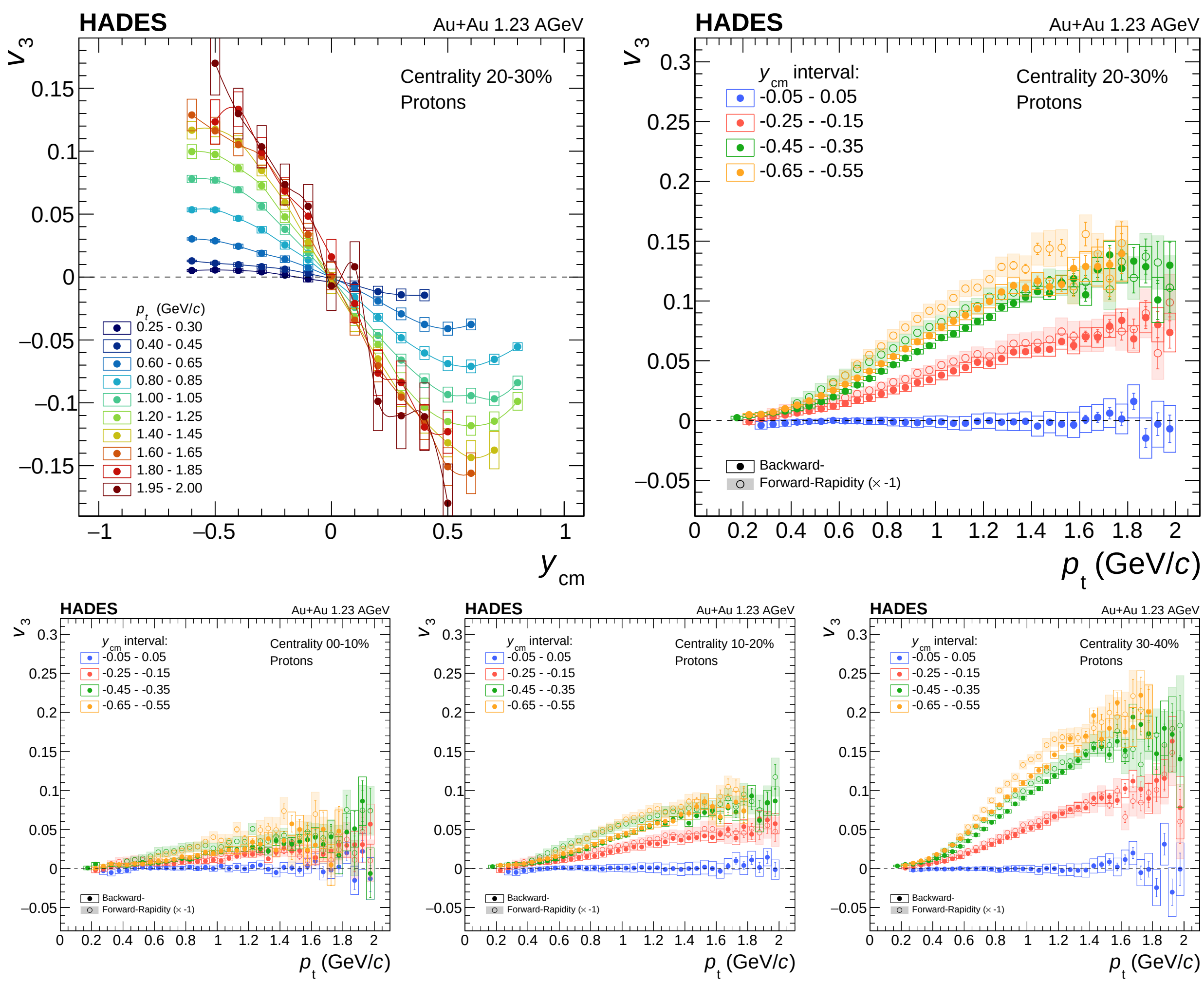

Figure 104: The triangular flow (v_3) of protons in semi-central events ($20-30\%$) as a function of the centre-of-mass rapidity y_{cm} in transverse momentum intervals of 50 MeV/c width are shown (upper left panel, lines are to guide the eye. The p_t intervals are shown in the legend). The proton v_3 as a function of p_t in several rapidity intervals, chosen symmetrically around mid-rapidity, are displayed for different centrality ranges (upper right and lower panel). The values measured in the forward hemisphere (open symbols) have been multiplied by -1. The systematic uncertainties are displayed here as empty- and dashed-filled boxes.

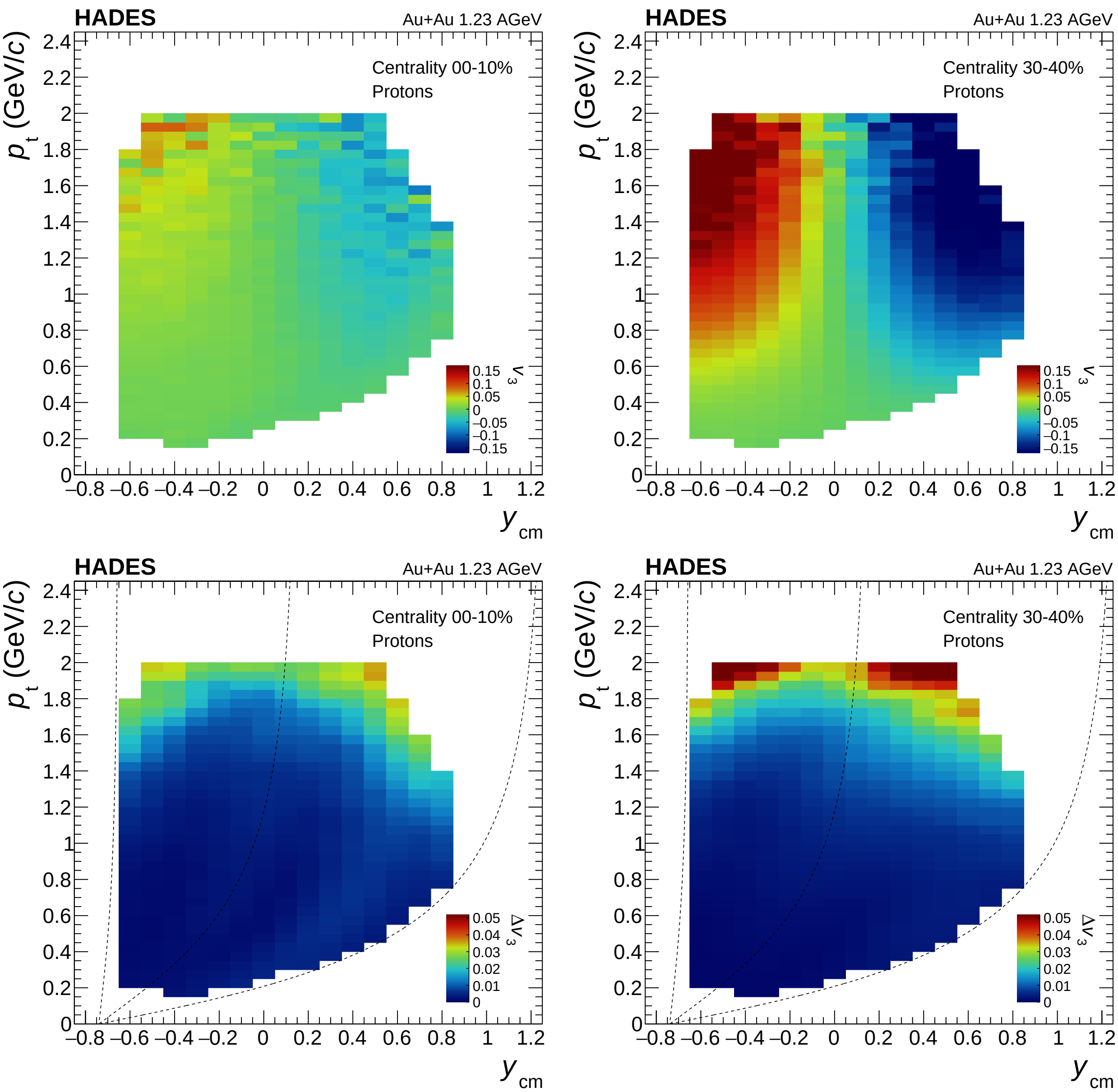

Figure 105: In the upper row the values for the triangular flow coefficient v_3 for protons as a function of p_t and y_{cm} for two centrality classes ($0-10\%$ and $30-40\%$) are shown and in the lower row the absolute values of the systematic uncertainty. The dashed lines in the lower panels show the theta angles 15°, 44° and 85° and corresponds to the lower acceptance edges, the overlap between TOF and RPC detectors and the upper acceptance edges of the detector system.

chosen symmetrically around mid-rapidity in the same semi-central $(20-30\%)$ event class. The values measured in the forward hemisphere (open symbols) have been multiplied by -1 for a direct comparison with the backward rapidity values (filled symbols). In the lower panel the p_t dependence in three other centrality classes $(0-10\%$ $, 10-20\%$ $, 30-40\%)$ is displayed. The measured proton v_3 shows a good agreement well within systematic uncertainties for rapidity intervals between $|y_{cm}| < 0.3$. In comparison to the almost linear rise of $v_1 \propto p_t$ in the region $p_t < 0.6$ GeV/c, the p_t spectra of v_3 rises only moderately

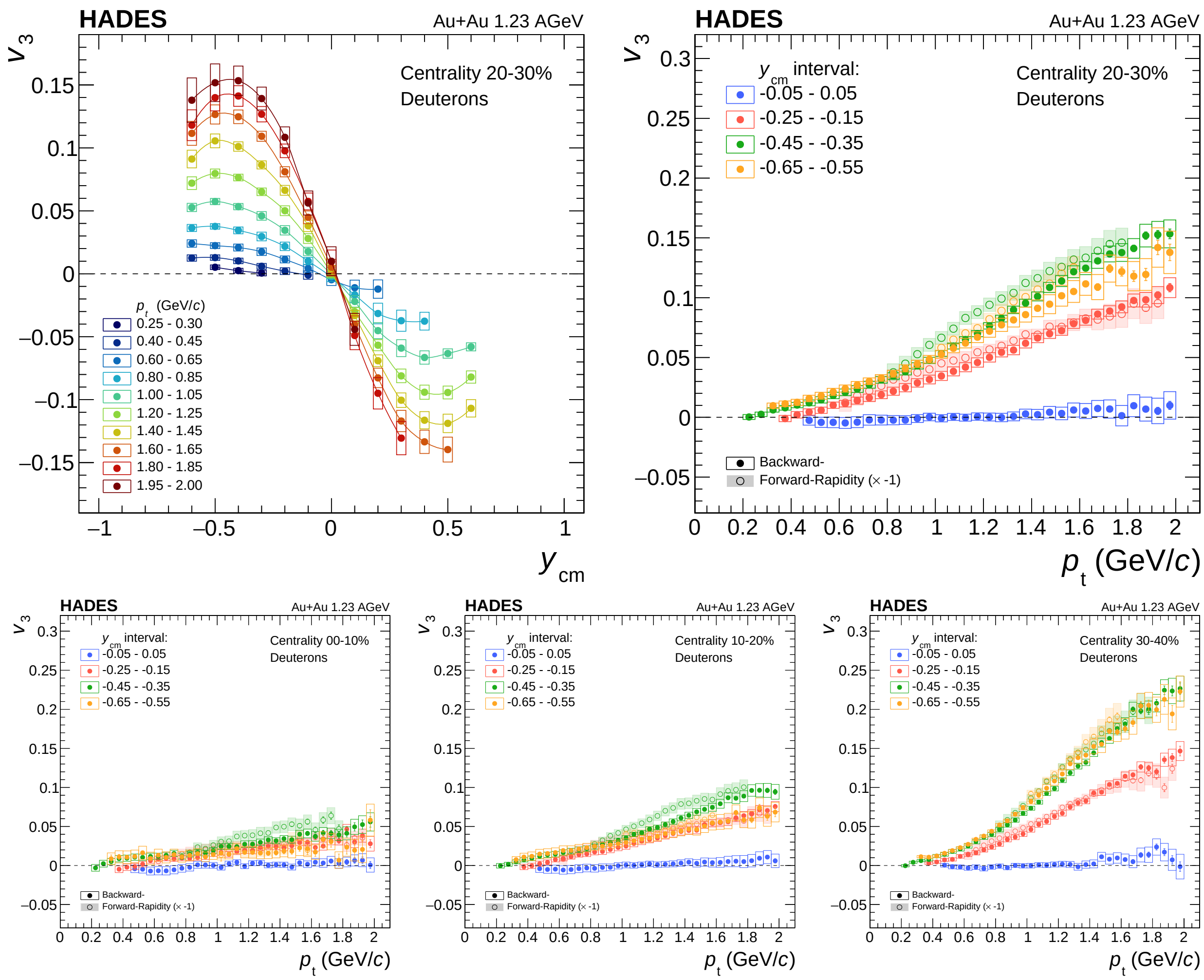

Figure 106: The same as shown in Fig. 104 for the triangular flow (v_3) of deuterons.

and then increase nearly linear. In contrast to the p_t spectra of v_1, where a saturation at high p_t can be seen, this can not be clearly observed for v_3. The upper row of Fig. 105 shows the measured v_3 as a function of p_t and y_{cm} for the two centrality classes ($0-10\%$ and $30-40\%$). In the lower row the absolute values of the systematic uncertainty are displayed, where a rise is clearly visible in the higher p_t region. As already shown in the left panel of Fig. 89, the p_t and y_{cm} dependence of v_3 in one exemplary rapidity ($-0.25 < y_{cm} < -0.15$) and one p_t-interval ($1.0 < p_t < 1.5$ GeV$/c$) compared for protons, deuterons and tritons are within the uncertainties very similar. Only at very large rapidity mass hierarchy can be observed. The same can observed for v_3 for the deuterons (Fig. 106) and for the tritons (Fig. 107), with similar p_t-dependence and slight shift of the maxima in rapidity for the three hydrogen-isotopes, found at $|y_{cm}| \approx 0.5$ (protons), ≈ 0.4 (deuterons)

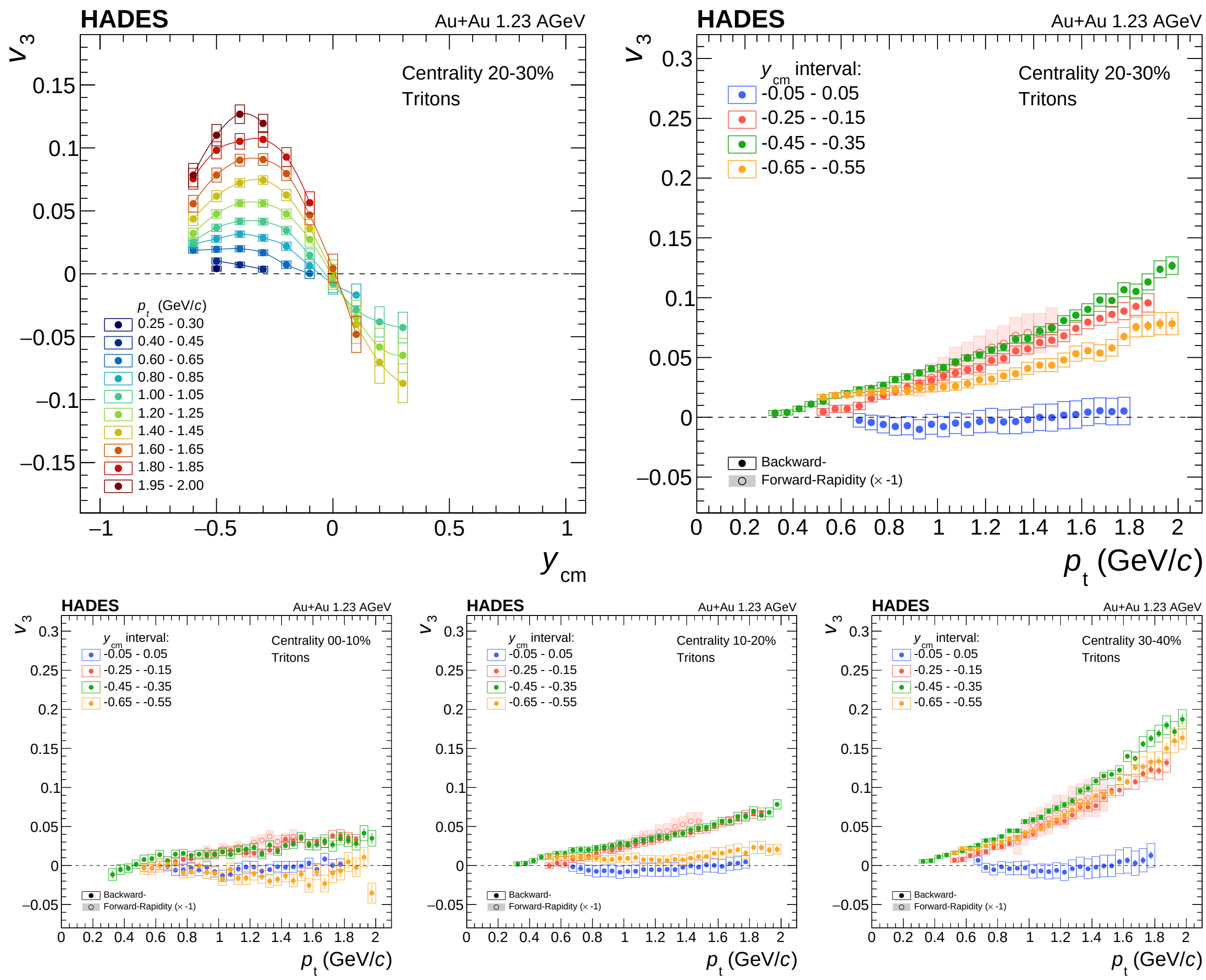

Figure 107: The same as shown in Fig. 104 for the triangular flow (v_3) of tritons.

and ≈ 0.3 (tritons). The pronounced centrality dependence for deuteron and triton is also similar to the one of the protons.

Quadrangular flow

The upper left panel of Fig. 108 shows the v_4 values for protons for the centrality range $20-30\%$ as a function of y_{cm} in transverse momentum intervals of 200 MeV/c width. The values of v_4 are largest at mid-rapidity and decrease towards forward and backward rapidities until they reach zero at rapidities of approximately $|y_{\mathrm{cm}}| \approx 0.4$. The p_{t} dependence of v_4 is shown in the upper right panel of Fig. 108 for four exemplary rapidity intervals. At mid-rapidity the v_4 values increase only moderately with p_{t}. In the lower panel of Fig. 108 the p_{t} dependence of v_4 for the three other centrality classes $(0-10\%\ , 10-20\%\ , 30-40\%)$

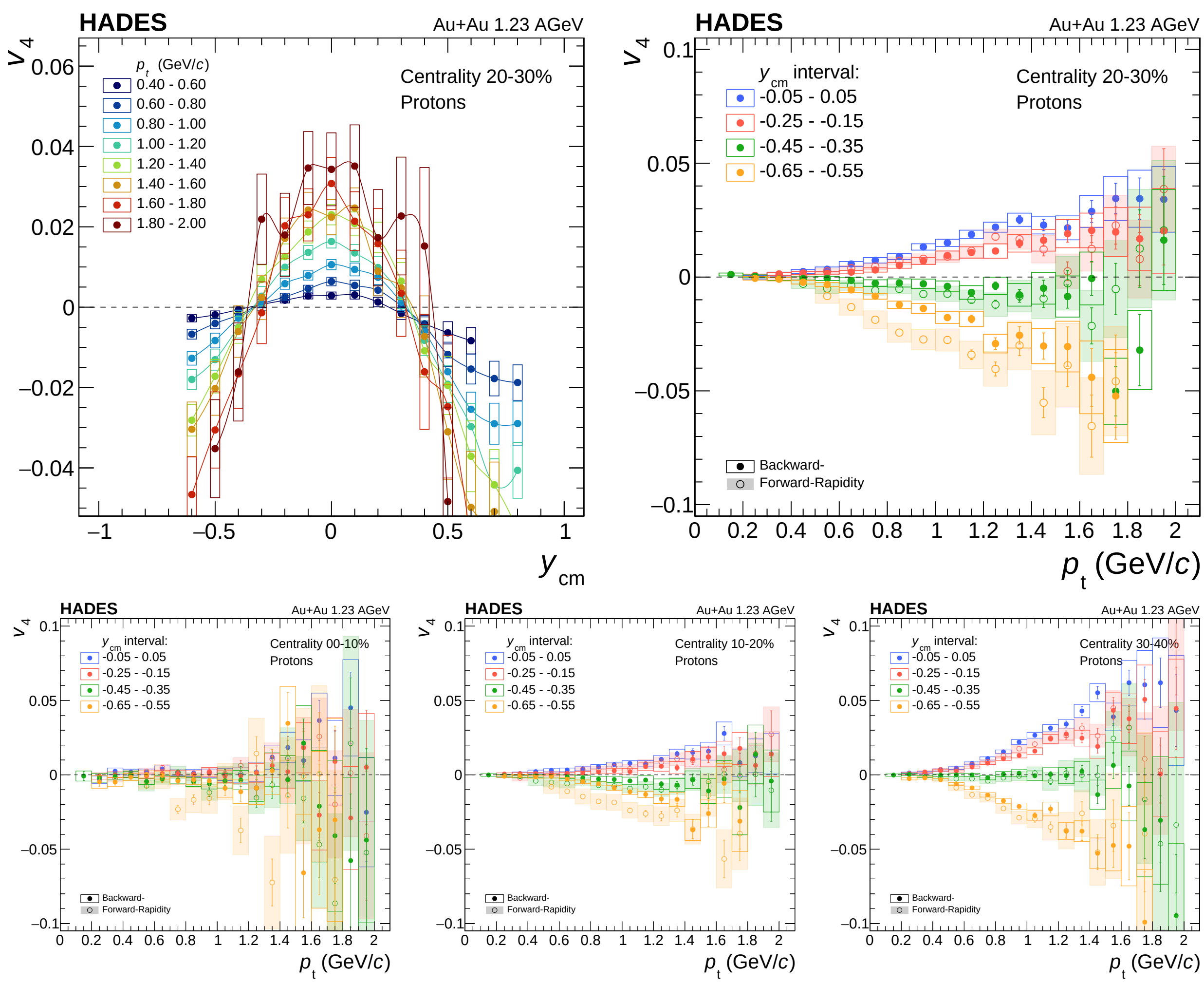

Figure 108: The quadrangular flow (v_4) of protons in semi-central events $(20-30\%)$ as a function of the centre-of-mass rapidity y_{cm} in transverse momentum intervals of 200 MeV/c width are shown (upper left panel, lines are to guide the eye. The p_{t} intervals are shown in the legend). The proton v_4 as a function of p_{t} (100 MeV/c width) in several rapidity intervals, chosen symmetrically around mid-rapidity, are displayed for different centrality ranges (upper right and lower panel). The systematic uncertainties are displayed here as empty- and dashed-filled boxes.

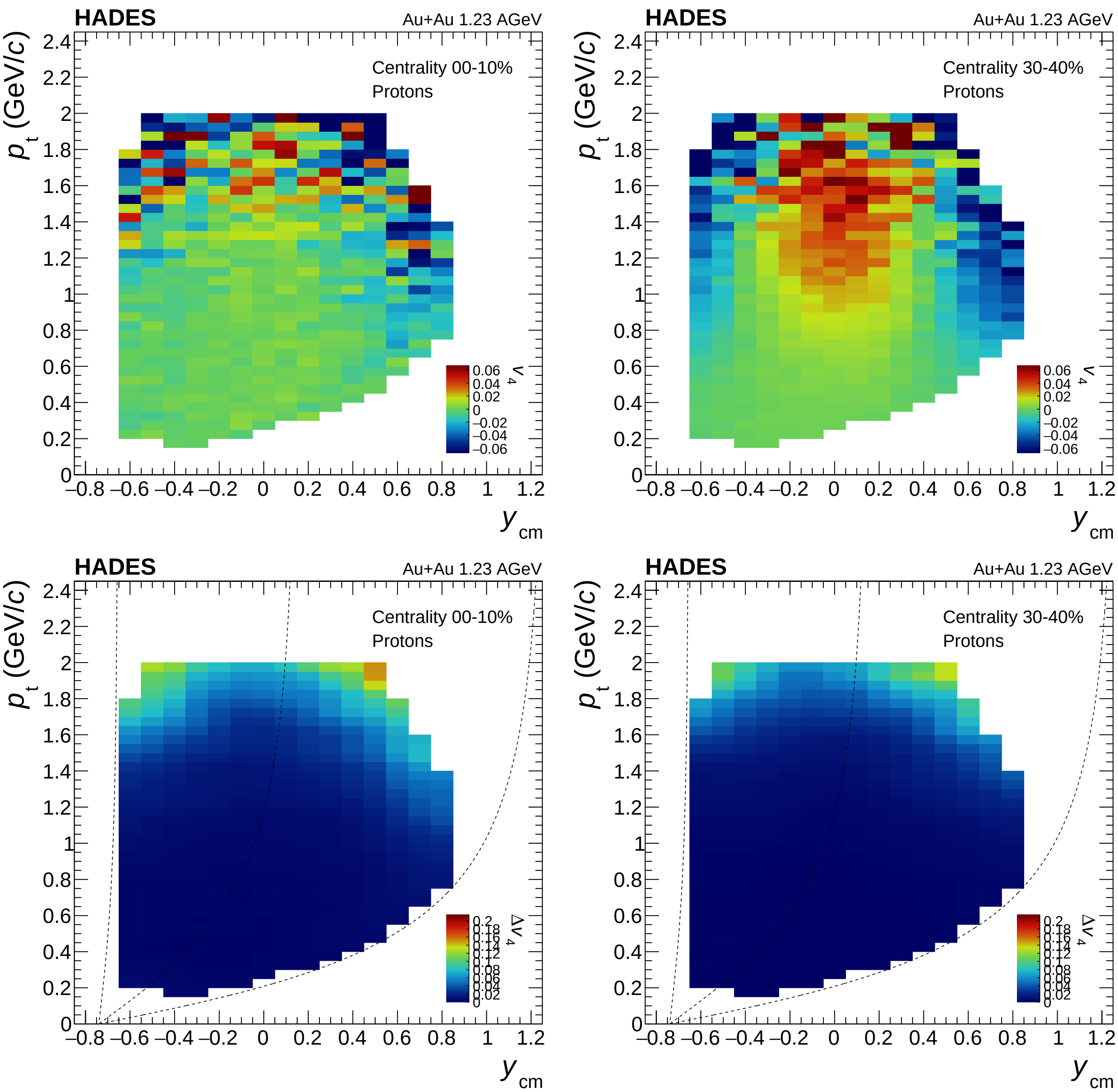

Figure 109: In the upper row the values for the quadrangular flow coefficient v_4 for protons as a function of p_t and y_{cm} for two centrality classes ($0-10\%$ and $30-40\%$) are shown and in the lower row the absolute values of the systematic uncertainty. The dashed lines in the lower panels show the theta angles 15°, 44° and 85° and corresponds to the lower acceptance edges, the overlap between TOF and RPC detectors and the upper acceptance edges of the detector system.

is shown and the comparison of the p_t spectra reveals that there is an increase of the absolute values, going from the most central events to the semi-central. The upper row of Fig. 105 shows the measured v_4 as a function of p_t and y_{cm} for the two centrality classes ($0-10\%$ and $30-40\%$). In the lower row the absolute values of the systematic uncertainty are displayed, where a rise is clearly visible in the higher p_t region. In the Fig. 110 and 111 the v_4 values for deuterons and tritons as a function of p_t and y_{cm} are shown, again for the centrality range $20-30\%$ in the upper row and in the lower row the p_t-spectra for the

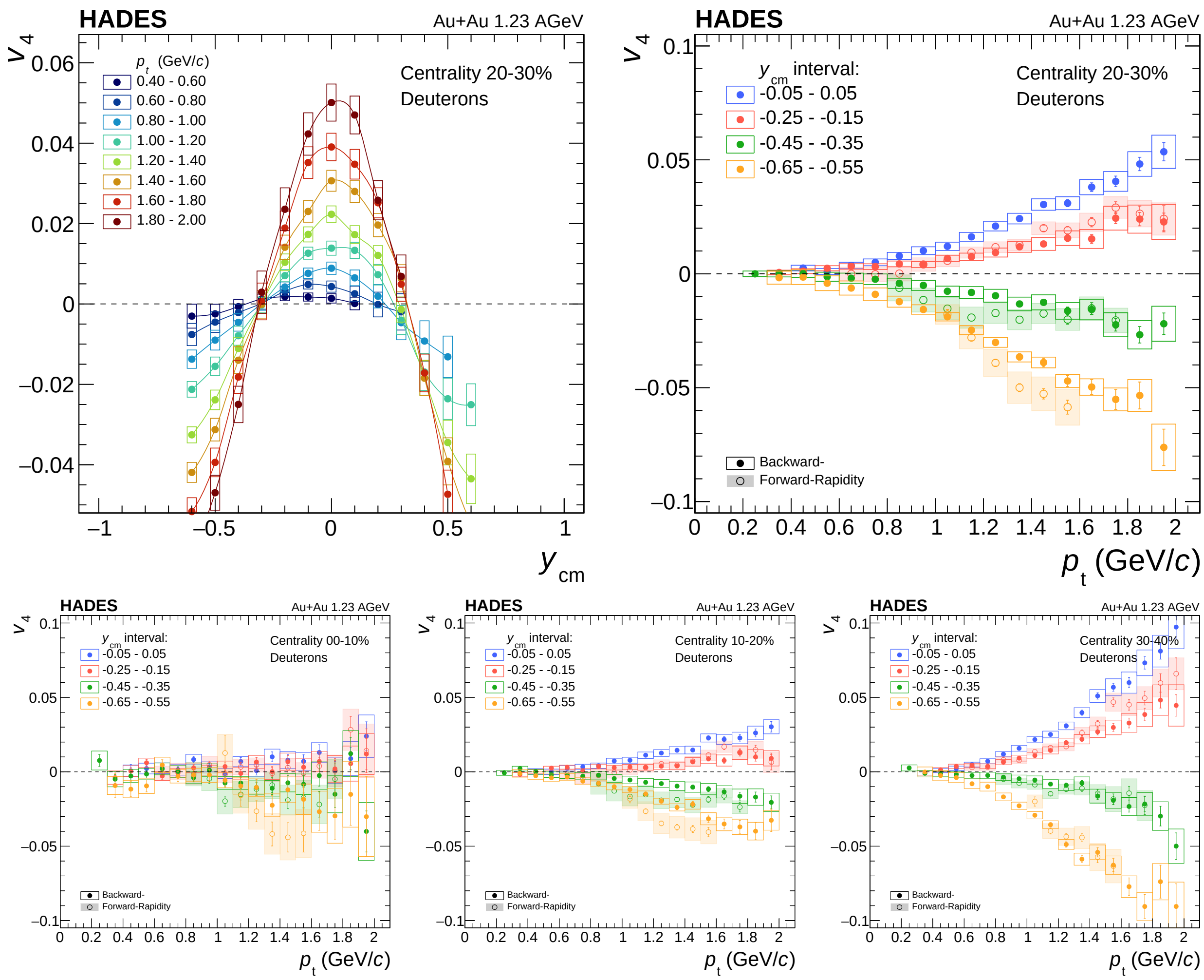

Figure 110: The same as shown in Fig. 108 for the quadrangular flow (v_4) of deuterons.

other centrality classes ($0 - 10\%$, $10 - 20\%$, $30 - 40\%$). The rapidity distributions are similar in shape to the ones measured for v_2 for the corresponding particle, but have an opposite sign. Also, they for are narrower for v_4 than for v_2, so that zero is crossed at smaller $|y_{cm}|$ values. For the different particle species this is found to be at $|y_{cm}| \approx 0.35$ (protons), ≈ 0.3 (deuterons) and ≈ 0.25 (tritons). The increase of the absolute v_4 values with p_t is also significantly less pronounced as in the case of v_2. Therefore, in contrast to the case of v_2, no saturation or even a maximum is observed at higher p_t.

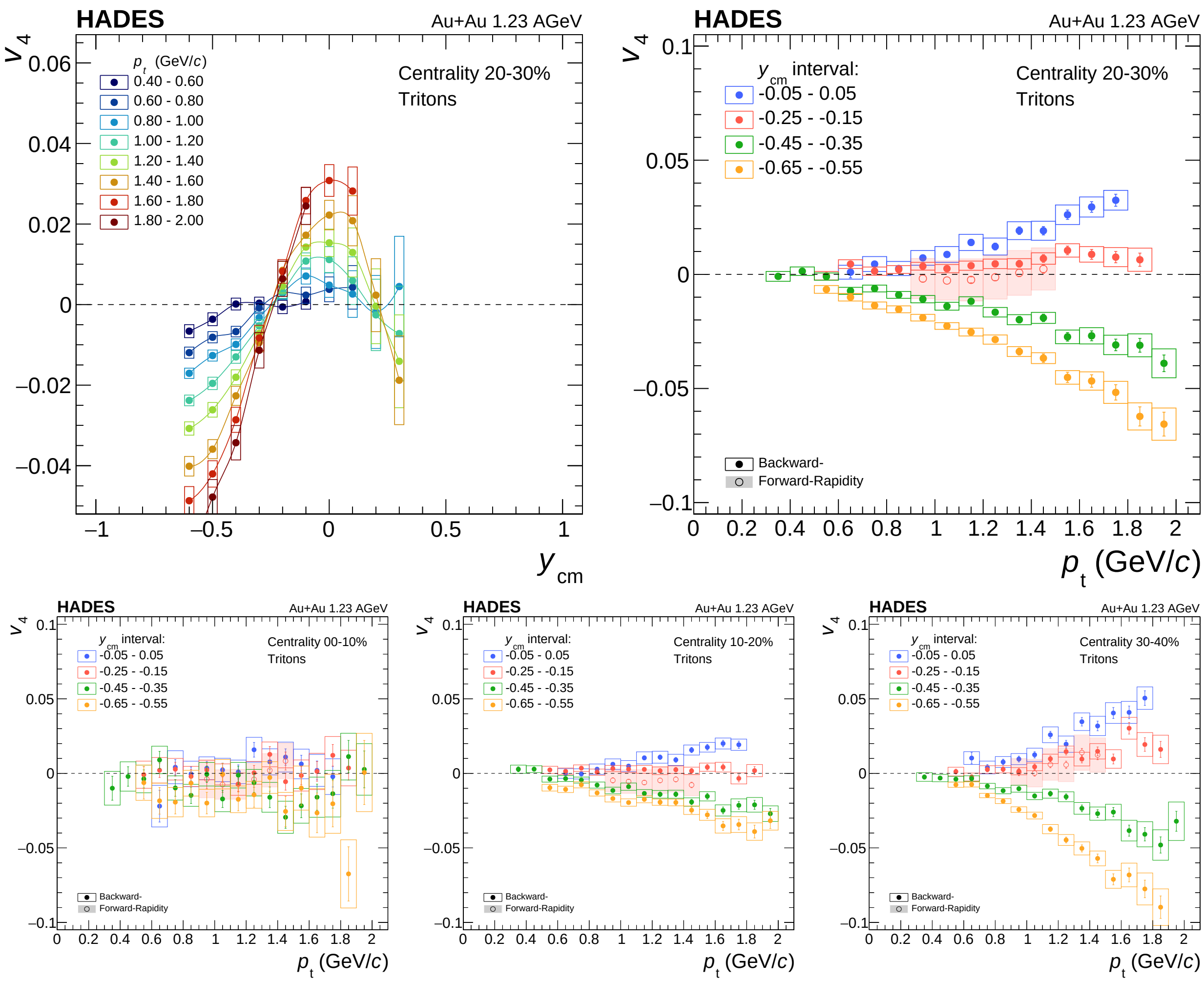

Figure 111: The same as shown in Fig. 108 for the quadrangular flow (v_4) of tritons.

Discussion

The previously presented data for the measured flow harmonics are in the following discussed individually concerning their scaling properties and whether the data can be parameterized in any way. Considering the large number of measured data points a parametrization allows to organize the data and to systematically quantify the general properties as functions of transverse momentum, rapidity or centrality. The comparison of the hydrogen isotopes allows studying any mass-ordering. We start with the rapidity-dependent parameterization of the data averaged over one large p_t-interval to visualize the three-dimensional representation of the angular emission pattern relative to the reaction plane. An energy dependent comparison of the p_t-integrated values of $dv_1/dy'|_{y'=0}$ and v_2 at mid-rapidity with previously measured experimental world data is summarised in the next section. The p_t dependence of v_2 at mid-rapidity is also compared with results from other experiments in the same energy regime. In the next step, the parameters that characterize the rapidity dependence of the data points are extracted as a function of p_t within small intervals, such that features depending on the centrality and particle type can be discussed. In contrast to the polynomial parameterization, commonly used to describe the data, a general, phenomenological parameterization of the p_t- and rapidity-dependence, based on hydro-dynamically motivated *Blast Wave models*, is proposed. The scaling between various flow coefficient, predicted by ideal hydrodynamics and confirmed by transport model calculations, are presented. To study the origin of this behaviour, the measured flow coefficients are related to the initial geometrical properties of the collisions by scaling the flow coefficients v_2 and v_4 measured in different centrality classes with the eccentricities calculated with Glauber MC simulations. Furthermore, a scaling between the flow coefficients v_2 and v_4 of the three hydrogen isotopes according to their nuclear mass number A is observed and discussed within the picture of nucleon coalescence. This chapter concludes with a comparison of selected experimental data with several state-of-the-art transport model calculations, with emphasis on the sensitivity of the presented data to different implementations of the equation-of-state.

The total amount of individual data points sums to around 17k, if only the first four flow coefficients in the four centrality ranges are counted with 470 phase-space bins for the protons, 365 for the deuterons and 249 for the tritons.

A three-dimensional representation of the angular emission pattern relative to the reaction plane is shown in Fig. 112 for protons. It is constructed by using the rapidity-dependent parametrizations of the individual odd and even flow coefficients v_n up to order 6, as shown in Fig. 87 and 91:

$$
\begin{aligned}
v_n^{odd}(y_{\mathrm{cm}}) &= v_{n1}\, y_{\mathrm{cm}} + v_{n3}\, y_{\mathrm{cm}}^3 \\
v_n^{even}(y_{\mathrm{cm}}) &= v_{n0} + v_{n2}\, y_{\mathrm{cm}}^2
\end{aligned}
\tag{63}
$$

into the cosine of the Fourier series:

$$1/\langle N\rangle\,(dN/d\phi) = 1 + 2\sum v_n \cos(n\phi)\,. \tag{64}$$

v_{11}	0.906 ± 0.049
v_{13}	-0.321 ± 0.099
v_{31}	-0.220 ± 0.008
v_{33}	0.156 ± 0.021
v_{51}	0.025 ± 0.005
v_{53}	-0.065 ± 0.019
v_{20}	-0.200 ± 0.003
v_{22}	0.422 ± 0.031
v_{40}	0.017 ± 0.001
v_{42}	-0.121 ± 0.011
v_{60}	0.003 ± 0.002
v_{62}	-0.003 ± 0.011

Table 24: The parameters as extracted with a fit of Eq. (63) to the proton sample averaged over the interval $1.0 < p_t < 1.5$ GeV/c in the semi-central $(20-30\%)$ event class, as shown in Fig. 87 and 91.

The values of the parameters for the p_t-interval $1.0 < p_t < 1.5$ GeV/c in the semi-central $(20-30\%)$ event class are listed in Tab. 24. The combination of flow coefficients, including higher order one, results in a larger azimuthal resolving power and an accurate description of the three-dimensional emission shape. The general approach to obtain the event shape by combining the multi-differential measurements of the

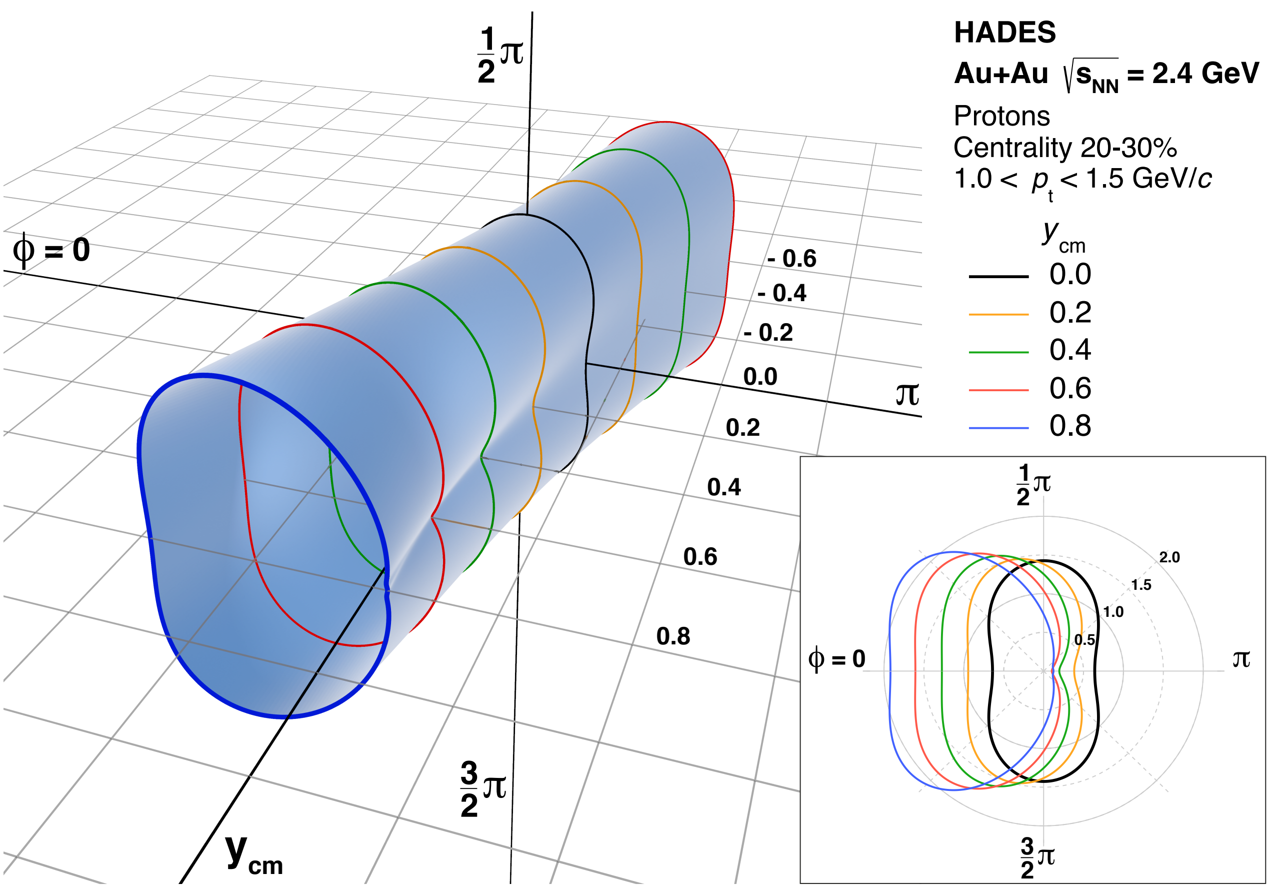

Figure 112: Angular emission pattern of protons with respect to the reaction plane $1/\langle N\rangle\,(dN/d\phi)$ for semi-central $(20-30\%)$ events, integrated over the p_t interval $1.0-1.5$ GeV/c. The flow coefficients of the orders $n = 1-6$ as listed in Tab. 24 are used. The insert panel shows slices corresponding to different forward rapidities. The figure is published in [337].

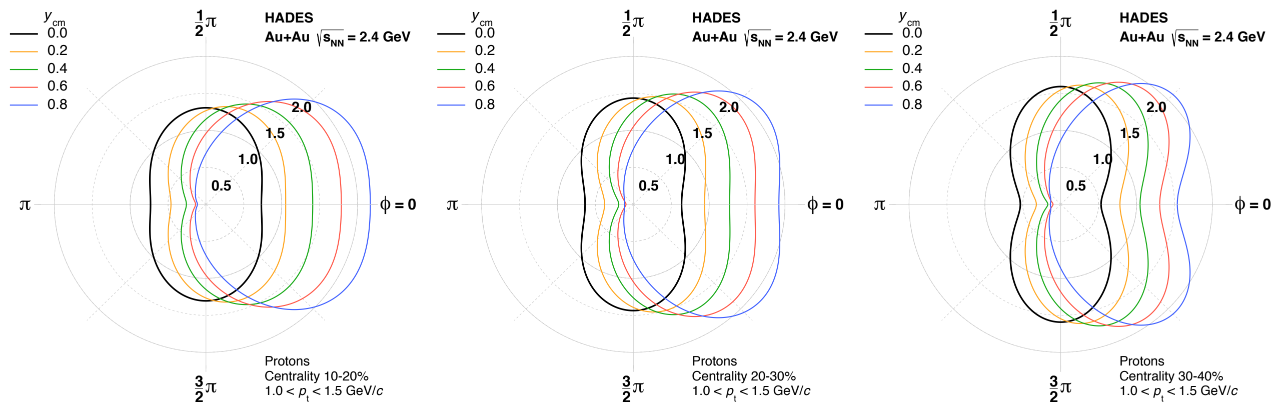

Figure 113: The angular emission pattern of protons with respect to the reaction plane $1/\langle N\rangle\,(dN/d\phi)$ for three centrality intervals of 10% width. It should be noted that the orientation is inverted with respect to the insert in Fig. 112, with $\phi = 0$ showing in both cases into the direction of the projectile spectator.

Fourier coefficients was first proposed in Ref. [127] and allows for a three-dimensional characterisation of heavy-ion collisions in different representations [128, 337, 339]. The insert panel in Fig. 112 shows the azimuthal distribution in polar coordinates in slices corresponding to different rapidity intervals in the forward region. At mid-rapidity (black line) a dipole shape centred around the beam axis with its long axis perpendicular to the reaction plane can be observed. Since the values for the odd coefficients vanish at mid-rapidity, the form is mainly defined by the negative v_2 values, corresponding to a preferred out-of-plane emission, and the positive v_4 values, which result in an additional contribution simultaneously into and out of the reaction plane. Moving away from mid-rapidity the value for v_2 increases and the value for v_4 decreases, where it crosses zero und changes its sign to positive or negative values at forward- and backward-rapidity. A sign change means that the symmetry axis of v_2 is rotated by 90° and the one of v_4 by 45° about their orientation at mid-rapidity. The contributions by the odd coefficients increase going from mid-rapidity to target and projectile rapidities, which results in an asymmetric shape and a shift of the centroid towards the spectator side. A more triangular shape develops, where the tip of the triangle aligned with the reaction plane shows in the opposite direction of the spectators. Additionally, it is observable that the tip of the triangle evolves a pronounced indentation going from mid-rapidity to spectator rapidities. This complicated smooth event shape can only be described by the combination of several flow harmonics. In Fig. 113 the same as the insert in the Fig. 112 is shown for two additional centrality classes.

Centrality and Mass Number Dependence

The directed and triangular flow at mid-rapidity can be quantified by their slope $dv_1/dy'|_{y'=0}$ and $dv_3/dy'|_{y'=0}$ which is defined relative to the scaled rapidity $y' = y_{\mathrm{cm}}/y_{\mathrm{mid}}$, with $y_{\mathrm{mid}} = 0.74$ as mid-rapidity in the laboratory system. The scaled rapidity is useful for the comparison of measurements at different beam energies (as shown later in Fig. 116), since it removes the trivial dependence of the slopes on the rapidity gap between target and beam projectile. The slopes are here defined as the linear term v_{n1} of the cubic function in Eq. 63, which has been used to fit the measured data on odd flow coefficients:

$$\begin{aligned} dv_1/dy'|_{y'=0} &= v_{11} \cdot y_{\mathrm{mid}} \\ dv_3/dy'|_{y'=0} &= v_{31} \cdot y_{\mathrm{mid}} \, . \end{aligned} \tag{65}$$

Aberrancy is used to define the third derivative of a curve, a measure of its non-circularity [340].

Similarly, the deviation from a linear rapidity-dependence, called in the following *aberrancy*, is quantified by the coefficients v_{n3} of Eq. 63:

$$\begin{aligned} d^3v_1/dy'^3|_{y'=0} &= v_{13} \cdot y^3_{\mathrm{mid}} \\ d^3v_3/dy'^3|_{y'=0} &= v_{33} \cdot y^3_{\mathrm{mid}} \, . \end{aligned} \tag{66}$$

In the upper panels of Fig. 114 the extracted slopes of v_1 (left) and v_3 (right) are displayed for two different p_{t} intervals ($0.6 < p_{\mathrm{t}} < 0.9$ GeV/c and $1.5 < p_{\mathrm{t}} < 1.8$ GeV/c) and the four centrality classes considered in this analysis. The slope of v_1 exhibits no significant centrality dependence for all particles and p_{t} intervals, except for the very central class where dv_1/dy' is smaller than for the other centralities. The positive slope values mean that the orientation of the directed flow is towards the direction of the projectile spectators. The increase of the slope of v_1 from most-central up to intermediate centralities and the significant mass hierarchy is in qualitative agreement with p_{t}-integrated measurements by FOPI [131, 341, 342] and with earlier measurements of the PlasticBall [139] and EOS [343] collaborations at similar or smaller beam energies. For the slope of v_3 a continuous increase of the absolute value $|dv_3/dy'|$ is visible, with values almost identical for the different particles at all centralities. In the lower panels of Fig. 114 the corresponding values for the *aberrancy* of v_1 (left) and v_3 (right) are shown for the same p_{t} intervals and centrality classes. The *aberrancy* for v_1 exhibits only a moderate centrality dependence but a clear mass ordering, where the small values for the most central class are consistent within uncertainties with an vanishing curvature. The curvature of v_3 shows almost identical values for the lower p_{t}-interval for each particle-type at all centralities, while for the larger p_{t}-interval an centrality dependent increase can be seen. In the upper panels of Fig. 115 the measured values of v_2 (left) and v_4 (right) at mid-rapidity

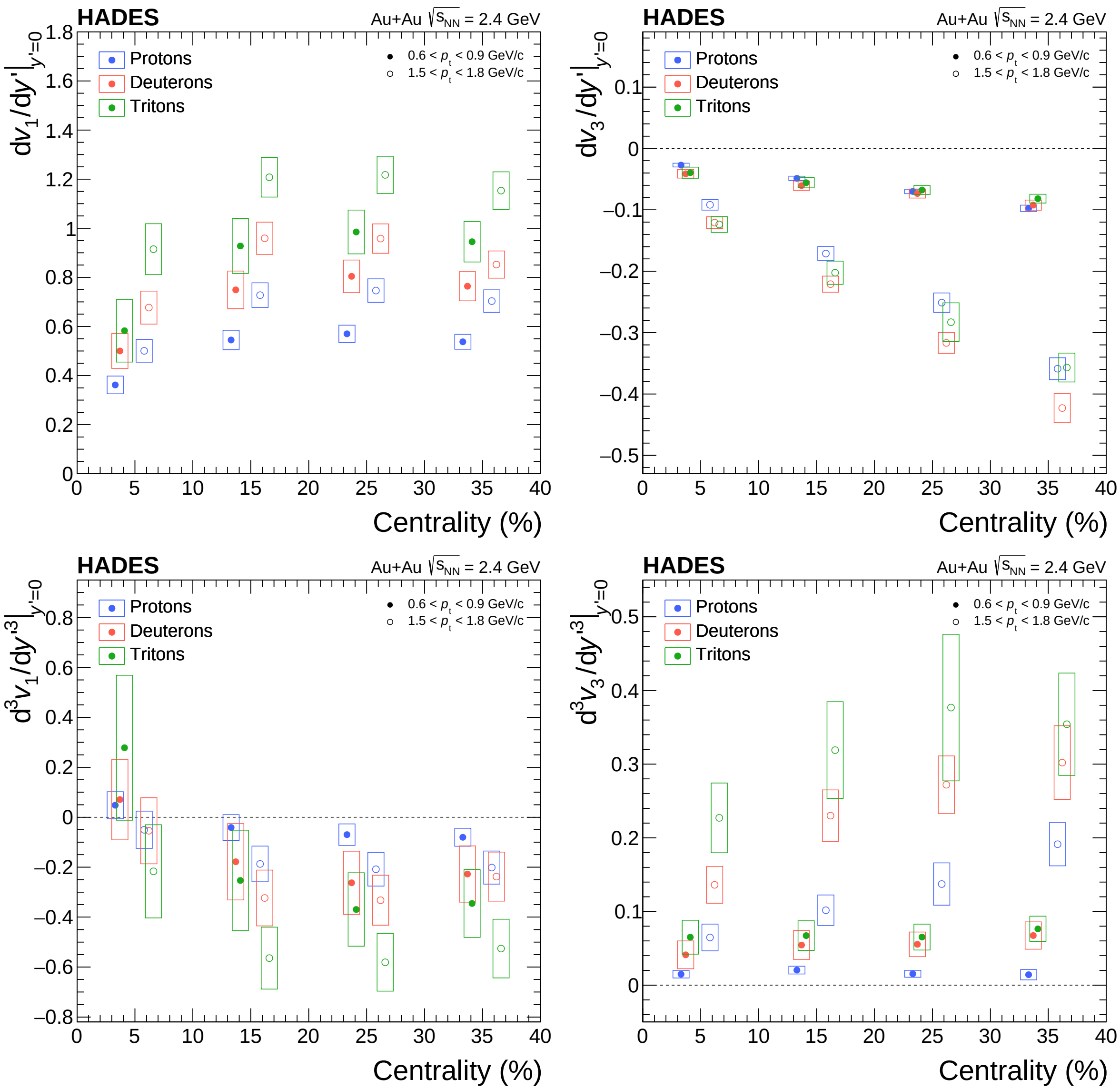

Figure 114: The slope $dv_1/dy'|_{y'=0}$ (upper left) and $dv_3/dy'|_{y'=0}$ (upper right), the aberrancy $d^3v_1/dy'^3|_{y'=0}$ (lower left) and $d^3v_3/dy'^3|_{y'=0}$ (lower right) of the directed and triangular flow of protons, deuterons and tritons in two transverse momentum intervals at mid-rapidity for Au+Au collisions at $\sqrt{s_{\mathrm{NN}}} = 2.4$ GeV in four centrality classes. Systematic uncertainties are displayed as boxes.

are displayed and in the lower panels the curvatures $d^2v_2/dy'^2|_{y'=0}$ (left) and $d^2v_4/dy'^2|_{y'=0}$ (right), extracted by the quadratic term v_{n2} in Eq. 63:

$$
\begin{aligned}
d^2v_2/dy'^2|_{y'=0} &= v_{22} \cdot y^2_{\mathrm{mid}} \\
d^2v_4/dy'^2|_{y'=0} &= v_{42} \cdot y^2_{\mathrm{mid}} \,.
\end{aligned}
\tag{67}
$$

Larger values of the curvature result in a narrower rapidity distribution which will cross zero at smaller y_{cm} values. The sign shows if the shape is convex or concave around mid-rapidity. The values of v_2 show a similar dependence on the reaction centrality as the triangular flow. The

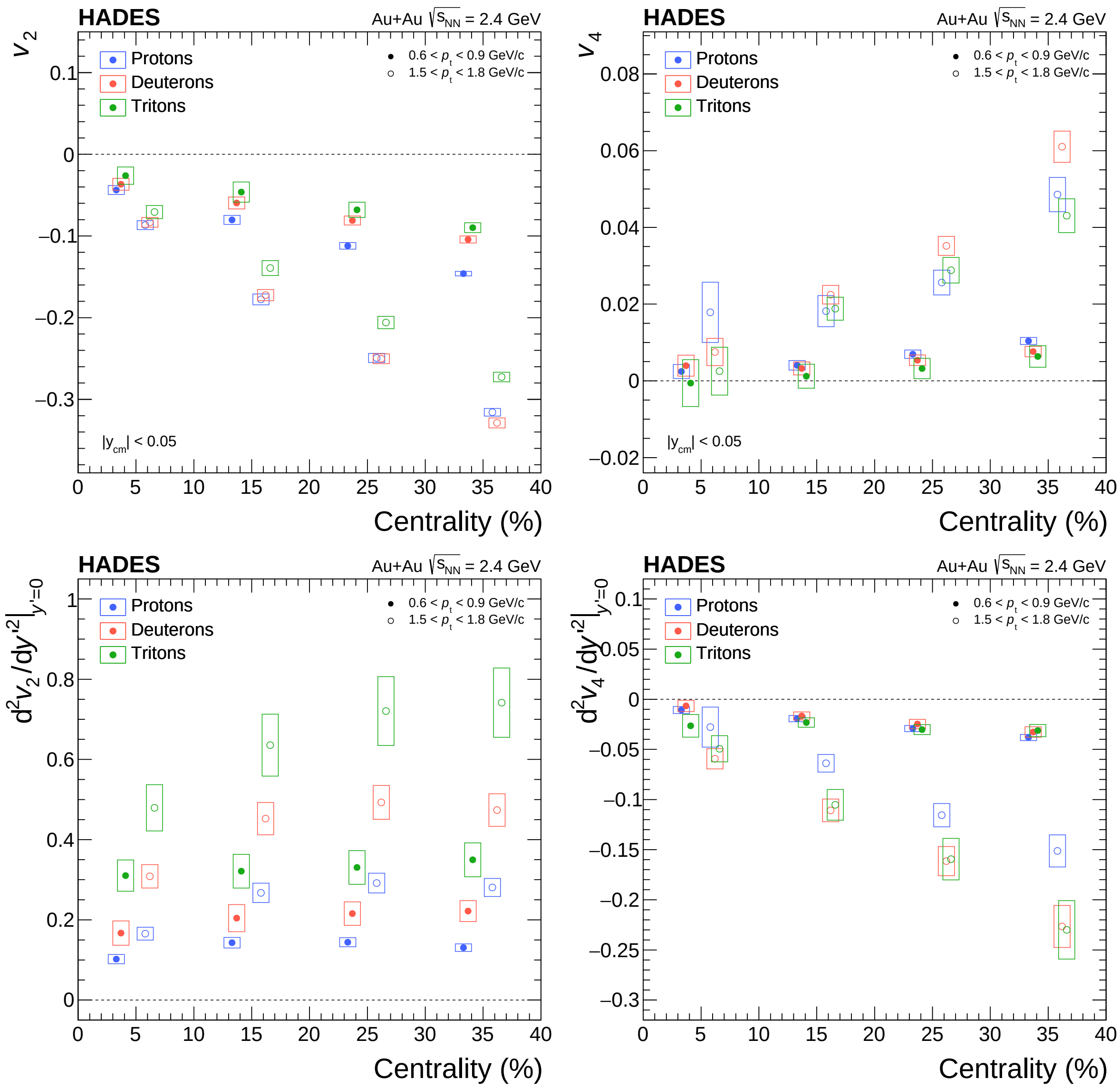

Figure 115: The values of the elliptic flow v_2 (upper left) and quadrangular flow v_4 (upper right), as well as the curvatures $d^2v_2/dy'^2|_{y'=0}$ (lower left) and $d^2v_4/dy'^2|_{y'=0}$ (lower right) of protons, deuterons and tritons in two transverse momentum intervals at mid-rapidity for Au+Au collisions at $\sqrt{s_{\mathrm{NN}}} = 2.4$ GeV in four centrality classes. Systematic uncertainties are displayed as boxes.

absolute value $|v_2|$ increases roughly linearly with centrality, while v_4 exhibits a stronger increase. For the lower p_t interval a mass ordering is visible for v_2 and v_4 in all centrality classes, while in the higher p_t region only the v_2 values for tritons are different from the one of protons and deuterons. The v_4 values do not exhibit any systematic ordering. In Fig. 115 the curvatures of v_2 and v_4 are displayed. As expected, the curvature of v_2 shows a clear mass ordering, with the tritons having the most narrow shape, followed by the deuterons and the protons (see Section on elliptic flow). This is not observed for $d^2v_4/dy'^2|_{y'=0}$, since for all hydrogen isotopes the values and widths are very similar (see Section on quadrangular flow). The slopes of v_1 and v_3 and the values of v_2 and v_4 at mid-rapidity exhibit a systematic decrease towards central events, which is in line with the assumption, that in perfect central collisions any anisotropies vanish.

Comparison with other Experiments

Since this is the first measurement of v_3 and v_4 in this energy regime only compilations of existing data on transverse momentum integrated directed flow v_1 and elliptic flow v_2 at mid-rapidity can be presented here in Fig. 116 and 117 in comparison with the results of this analysis. There are indications, that in the FOPI data a significant v_3 and v_4 for protons and in particular for fragments (deuterons) was observed.However, this has never been published [131]. The upper limits on the higher flow coefficients were determined by E877 at the AGS [132] with an absolute accuracy of approximately 10% consistent with zero for v_3 [133] and at most 2% for v_4 [134].

In the Ref. [131] it is remark that due to the finite azimuthal resolution, the measured higher Fourier components turn out to be small.

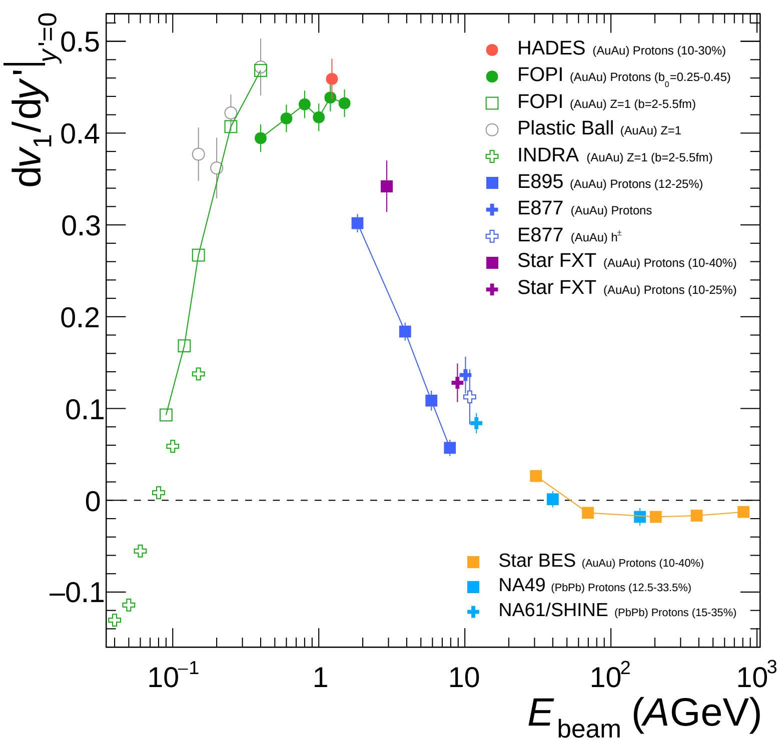

Figure 116: Compilation of directed flow measurements as a function of the beam energy E_{beam}. Shown is the v_1 slope at mid-rapidity $dv_1/dy'|_{y'=0}$ relative to the scaled rapidity $y' = y_{\text{cm}}/y_{\text{mid}}$. The p_t-integrated value for protons in Au+Au collisions at 1.23 *A*GeV ($10-30\%$ centrality) is presented as a red point. Available world data on $dv_1/dy'|_{y'=0}$ in the same or similar centrality interval in Au+Au or Pb+Pb collisions is shown for nuclei with $Z = 1$ (INDRA [108], FOPI [108, 341], Plastic Ball [101, 292]) for protons (FOPI [131], E895 [344], E877 [133], NA61/SHINE [345], NA49 [346], STAR [347–349]) and for inclusive charged particles (E877 [132, 350]).

The beam energy dependence of the slope of v_1 shows a rise from negative values below $E_{\text{beam}} \approx 0.1$ *A*GeV up to positive values with a maximum at around $E_{\text{beam}} \approx 1$ *A*GeV and then drops to negative values close to zero at higher beam energies. It should be noted that

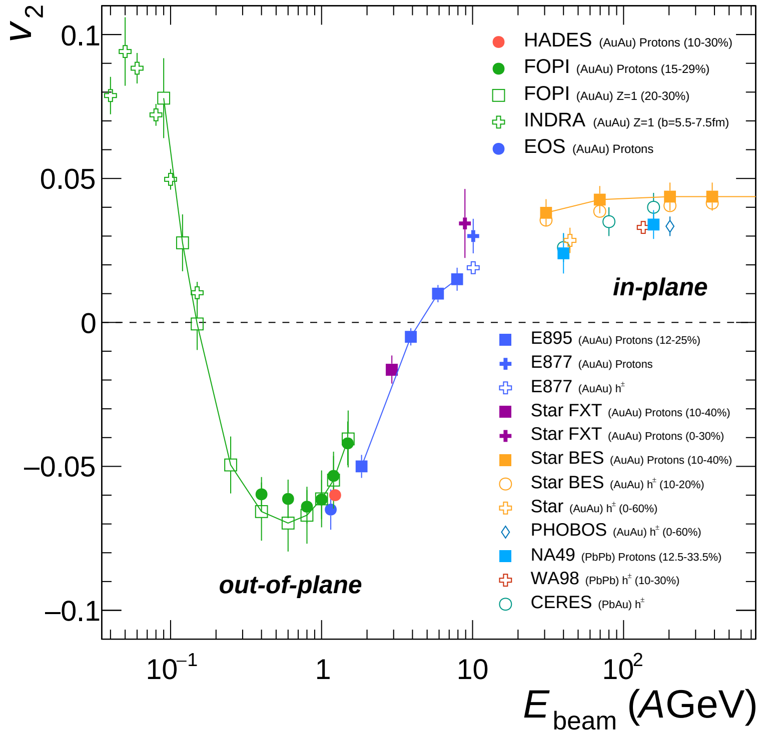

Figure 117: Compilation of p_t integrated elliptic flow v_2 measurements at mid-rapidity as a function of the beam energy E_{beam}. The result for protons in Au+Au collisions at 1.23 AGeV ($10-30\%$ centrality) from this analysis is represented by the red point. Shown are also data on v_2 in the same or similar centrality ranges in Au+Au or Pb+Pb(Pb+Au) collisions for nuclei with $Z = 1$ (INDRA [108] FOPI [108, 352], for protons (FOPI [131, 352], EOS/E895 [153]), for inclusive charged particles (E877 [132], CERES [353], WA98 [307], STAR [354, 355], PHOBOS [306]) and for charged pions (NA49 [346]).

the proton data of FOPI [131] (solid green points) have a lower p_t cut, which is beam-momentum dependent and therefore results in a systematic decrease of the values compared to results with a fixed p_t cut. The measurements for protons by E895 [344, 351] (sold blue squares) also exhibits systematically smaller values compared to other measurements in the same energy range. The measured value from HADES at 1.23 AGeV falls into the region where the observable v_1 flow is maximal. The values of v_2 at mid-rapidity also exhibit a very distinct energy dependence, as shown in Fig. 117. At beam energies of $0.1 \lesssim E_{\text{beam}} \lesssim 5$ AGeV the particle emission is out-of-plane with values for v_2 being negative. The passage time of the spectator matter is long enough to cause the squeeze-out effect [96, 107], where the pressure in the fireball pushes particles into the direction which is not blocked by spectators. At higher energies the particle emission is in-plane, as a particle can freely follow the pressure gradients into this direction, due to the much shorter passage times compared to the expansion time. The integrated v_2 obtained in this analysis for Au+Au collisions at 1.23 AGeV is in the region where out-of-plane emission is still very strong and also in good agreement with other measurements by EOS [153] and FOPI [131, 352]. The p_t dependent values of v_2 for protons measured in a narrow rapidity interval $|y_{\text{cm}}| < 0.05$ around

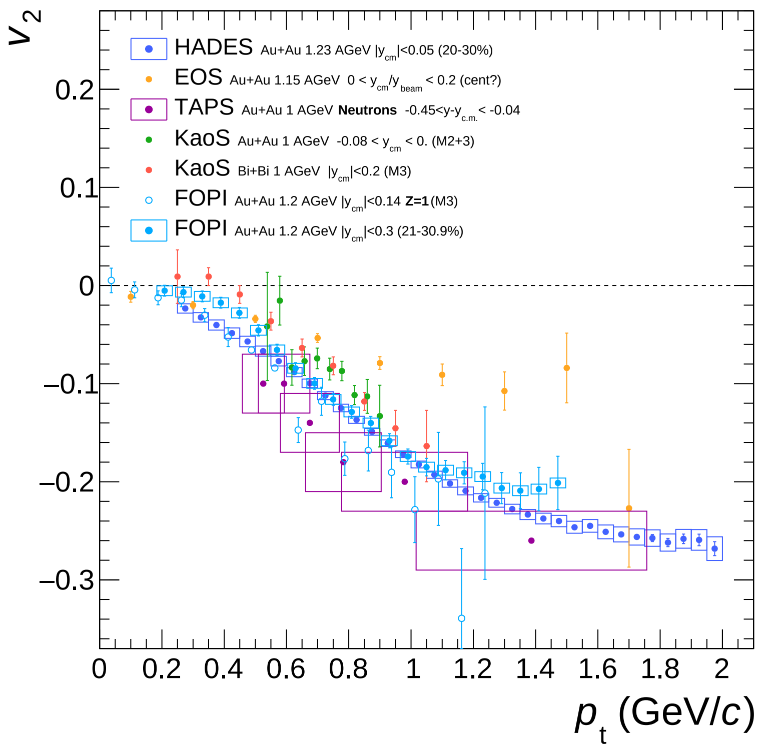

Figure 118: The elliptic flow (v_2) at mid-rapidity of protons in semi-central ($20-30\%$) Au+Au collisions at 1.23 *A*GeV as a function of p_t, in comparison with data of EOS [153, 356], KaoS [357, 358] and FOPI [131, 352] and TAPS (neutrons) [359] in the same energy region and similar centrality selection. The systematic uncertainties are shown as boxes. For the TAPS data the horizontal size of the boxes is derived from the neutron velocity measurement. The deviation of the EOS spectra might be caused by a different centrality range selection [153, 356].

mid-rapidity in the centrality class $20-30\%$ are compared with results of other experiments in the same energy region (EOS [153, 356], KaoS [357, 358] and FOPI [352]) in Fig. 118. Within uncertainties and considering the slight differences in beam energies, a good agreement with the other data sets is found. Additionally the measurement of neutron flow by TAPS [359] is shown, where the horizontal size of the boxes indicate the p_t intervals derived from the velocity measurement of the neutrons. The deviation of the EOS spectra might be caused by a different centrality range used in the analysis, which could not be clearly determinate from in the publication [153, 356].

General Parameterization

In the following, a simultaneous phenomenological parameterization of the rapidity and transverse momentum dependence of the measured Fourier coefficients is described, which results in a reasonable agreement over a large region of phase space, centrality and particle types. This two-dimensional fit incorporates several empirical assumptions and provides a useful description of the data with only four free parameters. In Fig. 119 the rapidity-dependence of the flow coefficients v_1 to v_5 are shown for protons averaged over the p_t interval

$1.0 < p_{\mathrm{t}} < 1.5$ GeV/c in the semi-central $(20-30\%)$ event class. In the left panel of Fig. 119 the zero-crossing at forward- and backward-rapidities can be only observed for v_5, with its *turning point* y_{tp} (indicated by the vertical line) much closer to mid-rapidity than for v_3 and for v_1:

Here a *turning point* is a stationary point with either a relative maximum or a relative minimum of a differentiable function at which the derivative changes sign.

$$|y_{tp}|(v_1) > |y_{tp}|(v_3) > |y_{tp}|(v_5)\ . \tag{68}$$

A similar observation can be made in the right panel of Fig. 119 for the even harmonics, where the zero intercept y_{zi} of v_4 is closer to mid-rapidity than for v_2:

$$|y_{zi}|(v_2) > |y_{zi}|(v_4)\ . \tag{69}$$

For the rapidity dependence, a polynomial of the cubic or quadratic form (see Eq. 63) describes the data around mid-rapidity very well, but might need further terms for the description at large backward- and forward-rapidities. A better agreement can be achieved by using trigonometric functions, such as:

$$\begin{aligned} v_n^{odd}(y_{\mathrm{cm}}) &= v_n^{\mathrm{sat}} \cdot \sin(y_{\mathrm{cm}}/y_{tp} \cdot \pi/2) \\ v_n^{even}(y_{\mathrm{cm}}) &= v_n^{\mathrm{sat}} \cdot \cos(y_{\mathrm{cm}}/y_{zi} \cdot \pi/2)\ . \end{aligned} \tag{70}$$

For even harmonics, y_{zi} characterises the position of the zero intercept and v_n^{sat} the value at mid-rapidity, and for odd harmonics y_{tp} is the location of the maximal absolute value v_n^{sat}, which corresponds here to the first turning point in forward-rapidities. In Fig. 119 the fit of the trigonometric (solid line) and the polynomial (dotted line) functions to the

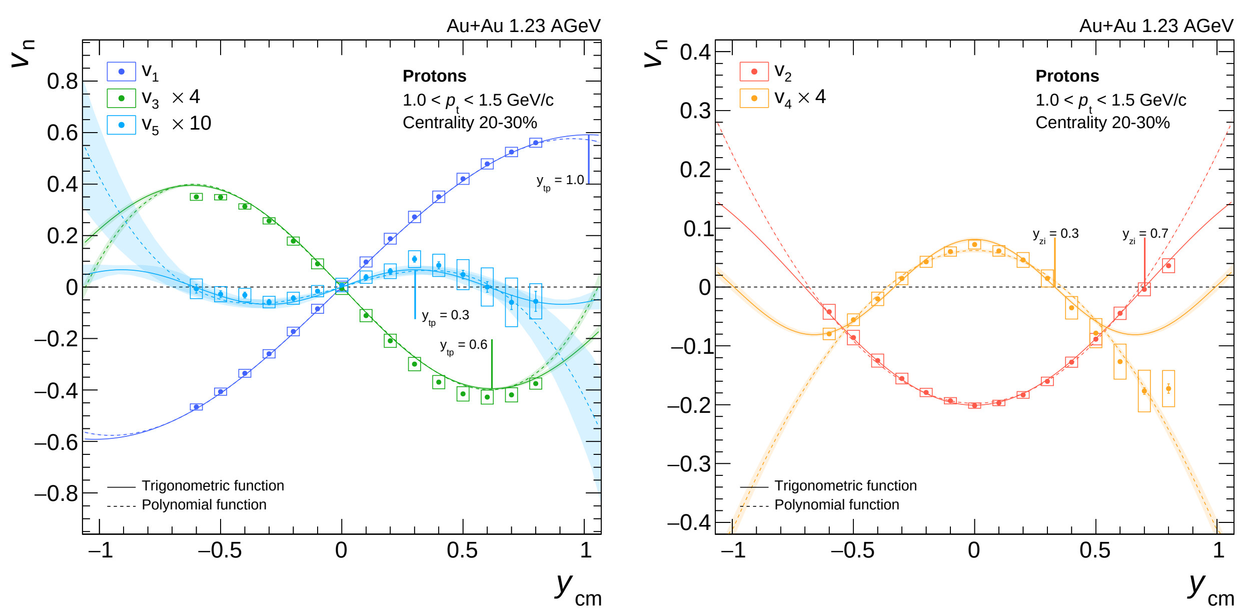

Figure 119: The y_{cm} dependences of the odd flow coefficients v_1, v_3, and v_5 (left panel) and of the even flow coefficients v_2 and v_4 (right panel) are presented for protons averaged over the p_{t} interval $1.0 < p_{\mathrm{t}} < 1.5$ GeV/c in the semi-central $(20-30\%)$ event class. The data is fitted with the trigonometric function in Eq. 70 (solid line) and with the polynomial function in Eq. 63 (dotted line). At forward-rapidities, the turning points y_{tp} for the odd harmonics and the zero intercept y_{zi} for the even harmonics are indicated by vertical lines. For visibility, the values of the higher order flow coefficients are multiplied by a factor. The coloured bands depict the uncertainties of the individual fits.

data are shown, both describe a similar behaviour around mid-rapidity. It should be pointed out that the characterisation of the rapidity dependence can also be performed with *Legendre* [360] or *Chebyshev polynomials* [361], which might indicate that the full emission pattern can be described in terms of *multipole moments* with *spherical harmonics* [123, 362].

The hydrodynamic inspired *Blast Wave model*, characterising an expanding thermal source with a radial velocity profile [119, 120], can be extended to also incorporate azimuthal dependencies [133, 346, 363–367]. In the *Blast Wave model* the single-particle density $\varrho(p_t, \phi)$ is obtained from the emission function $S(x, p)$ by integrating over the space-time evolution of the system:

$$\varrho(p_t, \phi) = \int d^4x \, S(x, p) \, . \tag{71}$$

It can be modelled using Cooper-Frye formalism [182], if it is assumed that particles decouple at *local thermal equilibrium* with a temperature T and in the velocity field which describes the collective expansion of the fireball. Recalling the shorthand notation $\varrho(p_t, \phi)$ in Eq. 20 for the single-particle density in azimuth angle and transverse momentum, the Fourier coefficients can be expressed as:

$$v_n(p_t) = \frac{\int_0^{2\pi} \cos(n\phi) \; \varrho(p_t, \phi) \; d\phi}{\int_0^{2\pi} \varrho(p_t, \phi) \; d\phi} \tag{72}$$

The analytical solution of the ϕ-dependence in momentum space results in [364]:

$$v_n(p_t) = \frac{\int_0^{2\pi} \cos(n\phi_s) \;\; I_n(\alpha_t(\phi_s)) \, K_1(\beta_t(\phi_s)) \; d\phi_s}{\int_0^{2\pi} \; I_0(\alpha_t(\phi_s)) \, K_1(\beta_t(\phi_s)) \; d\phi_s} \, . \tag{73}$$

where I_n and K_n are the modified Bessel functions of the order n, and the arguments $\alpha_t(\phi_s) = (p_t/T) \sinh(\rho(\phi_s))$, $\beta_t(\phi_s) = (m_t/T) \cosh(\rho(\phi_s))$ depend on the radial flow rapidity $\rho(\phi_s)$, with the azimuthal angle ϕ_s in coordinate space. The ϕ_s-dependence of the particle emission can be either formulated radially directed outwards from the center of the expanding emission source or be perpendicular to the emission surface [366]. The azimuthal modulation can be incorporated into the magnitude of the radial flow rapidity with the additional parameter ρ_n:

$$\rho(\phi_s) = \rho_0(1 + 2\rho_n \;\cos(n\phi_s)) \; . \tag{74}$$

The angular dependence in Eq. 73 can not be solved further analytically. But numerically it can be shown [367, 368], that in the relevant range of the parameter space (T, ρ_0, ρ_n) the p_{t} spectra for the flow coefficients of different order can be approximated in the form of a ratio of the modified Bessel functions of the first kind I_n of the n^{th} order:

$$v_n(p_t) = v_n^{\text{inf}}\ I_n(p_t/\chi)/I_0(p_t/\chi)\ , \tag{75}$$

where v_n^{inf} is the value reached at infinite p_t and χ is a free parameter that controls the momentum scale. Expanding the Eq. 75 as a Taylor series, the leading terms can be approximated in form of a *sigmoid function*:

$$v_n(p_t) = v_n^{\text{sat}} \cdot \tanh(p_t/p_0)^a\ , \tag{76}$$

with nearly identical behaviour at low p_t, but saturating at v_n^{sat} for large p_t values. The parameter p_0 is used to scale the momentum range and the exponent a is mainly needed to adjust the shape at low momenta. In Fig. 120 the p_t dependences of the flow coefficients v_1 to v_5 for protons in the semi-central $(20-30\%)$ event class are shown, for the odd harmonics in the rapidity interval $-0.25 < y_{\text{cm}} < -0.15$ in the left panel and the even ones at mid-rapidity in the right panel. Both parametrizations, Eq. 75 (dashed lines) and of Eq. 76 (solid lines) are compared to the data, with the uncertainties of the individual fits to the different order of the flow coefficients shown as coloured bands.

Similar forms of the parametrization as in Eq. 75 are given with further terms for v_1 in Ref. [133, 363] and for v_2 in Ref. [364]. Generalized solutions for even v_n are outlined in Ref. [367–369], but with a different order of the Bessel function in the numerator $v_{2n} = I_n(x)/I_0(x)$.

The parametrization with the trigonometric function in Eq. 76 is motivated by similar solutions given in Ref. [364] and [370]. It should be noted that v_n^{sat} for the second harmonic is related to the p_t^2-weighted v_2 [371] (denoted first as $\bar{\alpha}$ in [372]).

Three observations can directly be made when characterizing the p_t-dependence of the data. The first is that any anisotropy vanishes for $p_t \to 0$, which results in zero values for all flow coefficients. The second is that v_1 shows in general an almost linear and v_2 an approximately quadratic growth in the region of low transverse momenta, which is

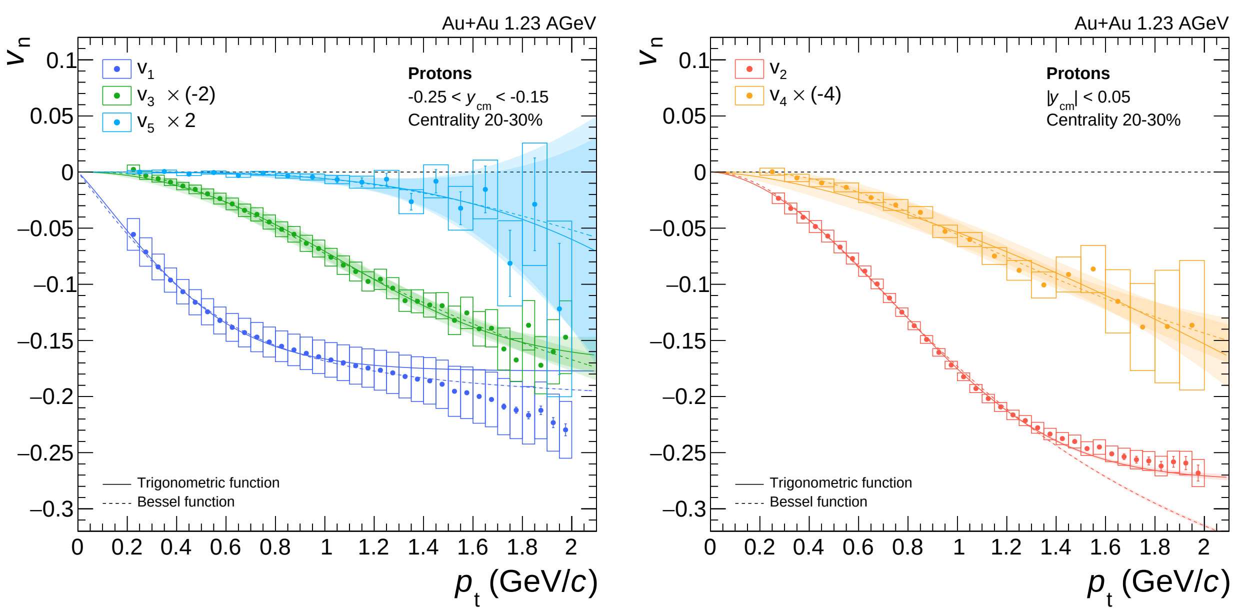

Figure 120: The p_t dependences of the odd flow coefficients v_1, v_3 and v_5 in the rapidity interval $-0.25 < y_{\text{cm}} < -0.15$ (left panel) and of the even flow coefficients v_2 and v_4 in the rapidity interval $|y_{\text{cm}}| < 0.05$ (right panel) are presented for protons in the semi-central $(20-30\%)$ event class. The data is fitted with the trigonometric function in Eq. 76 (solid line) and with the Bessel function in Eq. 75 (dotted line). For visibility, the values of the higher order flow coefficients are multiplied by a factor, and positive values also with -1. The coloured bands depict the uncertainties of the individual fits.

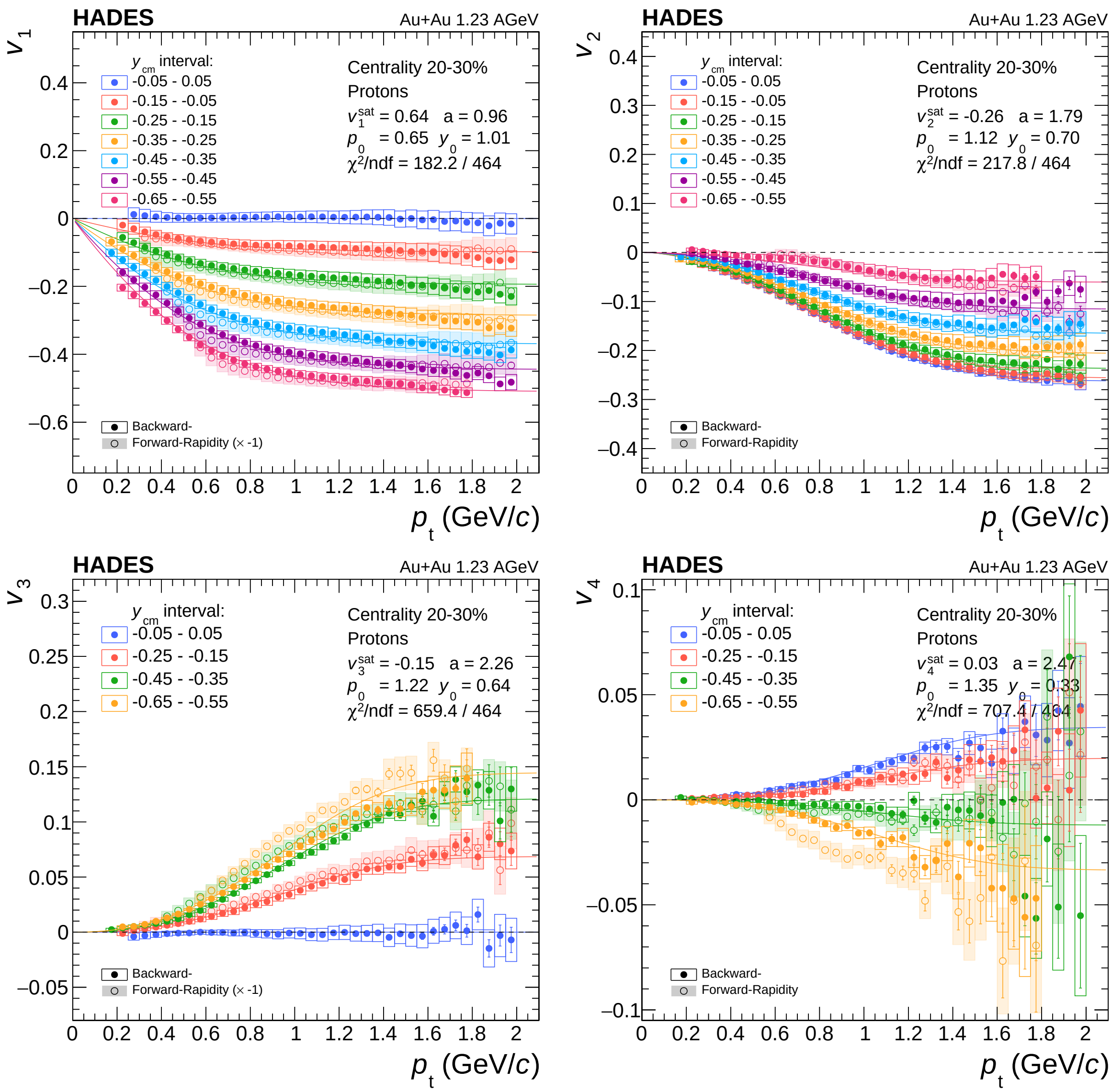

Figure 121: The p_{t} dependences of the flow coefficients v_1, v_2, v_3 and v_4 for the different rapidity interval are presented for protons in the semi-central $(20-30\%)$ event class. The data is fitted with Eq. 77, with resulting values for the fit parameters listed in Tab. 25.

supported by analytic considerations [113] and is also observed by other experiments [131, 133, 153, 352, 373]. The hypothesis that for the higher order flow coefficients a proportionality of the form $v_n(p_{\mathrm{t}}) \propto p_t^n$ at low p_{t} is verified. The third is that a saturation of v_1 and v_2 at large momenta can here be observed for the first time in this energy regime. However, for the higher flow coefficients v_3, v_4 and v_5 a saturation behaviour can not be directly concluded from the measured data. Combining both trigonometric functions of Eqs. 70 and 76, the following p_{t} and rapidity dependent form of a parameterisation can be given:

$$\begin{aligned} v_n^{odd}(p_t, y_{\mathrm{cm}}) &= v_n^{sat} \cdot \tanh(p_t/p_0)^a \cdot \sin(y_{\mathrm{cm}}/y_{tp} \cdot \pi/2) \\ v_n^{even}(p_t, y_{\mathrm{cm}}) &= v_n^{sat} \cdot \tanh(p_t/p_0)^a \cdot \cos(y_{\mathrm{cm}}/y_{zi} \cdot \pi/2)\ . \end{aligned} \quad (77)$$

In Fig. 121 the p_t-dependence in several rapidity intervals is shown for the centrality class $20-30\%$. The curves show the fit with Eq. 77, resulting in the parameter values listed in Tab. 25. The extracted parameter v_n^{sat} is the maximal saturation value at high p_t and has a maximal absolute value for odd harmonics at the turning point and for the even harmonics at mid-rapidity. A fit using the p_t-dependence

Table 25: Extracted values for the parameters v_n^{sat}, p_0, a and y_{tp}, y_{zi} from the fit with the parametrization Eq. (77) to the proton flow data in four centrality classes. The goodness of fit is also shown as χ^2/NDF.

Centrality	v_n^{sat}	p_0	a	y_{tp} y_{zi}	χ^2/NDF
			v_1		
$00-10\%$	0.630 ± 0.007	0.70 ± 0.02	0.95 ± 0.04	1.40 ± 0.01	153.7/464
$10-20\%$	0.666 ± 0.015	0.66 ± 0.01	1.00 ± 0.03	1.09 ± 0.03	129.7/464
$20-30\%$	0.638 ± 0.010	0.65 ± 0.01	0.96 ± 0.03	1.01 ± 0.02	182.2/464
$30-40\%$	0.608 ± 0.008	0.68 ± 0.01	0.84 ± 0.02	1.00 ± 0.01	328.5/464
			v_2		
$00-10\%$	-0.104 ± 0.004	1.29 ± 0.07	1.31 ± 0.06	0.51 ± 0.00	284.8/464
$10-20\%$	-0.198 ± 0.003	1.20 ± 0.02	1.63 ± 0.03	0.59 ± 0.00	155.3/464
$20-30\%$	-0.263 ± 0.002	1.12 ± 0.01	1.79 ± 0.02	0.70 ± 0.00	217.8/464
$30-40\%$	-0.328 ± 0.001	1.05 ± 0.00	1.92 ± 0.01	0.80 ± 0.00	1113.6/464
			v_3		
$00-10\%$	-0.058 ± 0.007	1.58 ± 0.16	1.82 ± 0.08	0.55 ± 0.02	428.2/464
$10-20\%$	-0.095 ± 0.002	1.31 ± 0.03	2.12 ± 0.04	0.57 ± 0.01	449.4/464
$20-30\%$	-0.145 ± 0.002	1.22 ± 0.01	2.26 ± 0.02	0.64 ± 0.01	659.4/464
$30-40\%$	-0.203 ± 0.003	1.14 ± 0.01	2.36 ± 0.02	0.71 ± 0.01	648.7/464
			v_4		
$00-10\%$	0.092 ± 0.101	6.10 ± 5.35	1.61 ± 0.27	0.27 ± 0.01	359.1/464
$10-20\%$	0.023 ± 0.003	1.43 ± 0.13	2.42 ± 0.16	0.31 ± 0.00	568.3/464
$20-30\%$	0.035 ± 0.003	1.35 ± 0.07	2.47 ± 0.09	0.33 ± 0.00	707.4/464
$30-40\%$	0.053 ± 0.003	1.27 ± 0.05	2.58 ± 0.07	0.37 ± 0.00	596.2/464

of Eq. 75 yields a similar good agreement with the measurements at lower p_t, but results in a deviation at large p_t, since it is not saturating at finite values. This generalised parameterization can be used as a tool to simplify the comparison to model predictions.

Scaling Properties

Hydrodynamic calculations [371, 374] investigated the relationship between the initial geometrical anisotropy and the equation-of-state to the resulting flow anisotropy in terms of v_2 and v_4. The conclusion was that both, the hydrodynamic evolution and the geometric configuration [375], can contribute to finite values of v_2 and v_4, and hence a general relation between them should exist. Following this reasoning the proportionality $v_n \approx v_2^{n/2}$ was proposed [376] and further theoretical considerations suggested the scaling $v_4/v_2^2 = 0.5$ in an ideal fluid scenario [377]. A later calculation [367], as well as measurements at RHIC [378, 379] and LHC [380–382], showed that this ratio yields larger values if flow fluctuations are considered in addition. In the energy regime around 1 *A*GeV the IQMD transport model suggested that the ratio of 0.5 would decrease after including initial-state effects, if flow

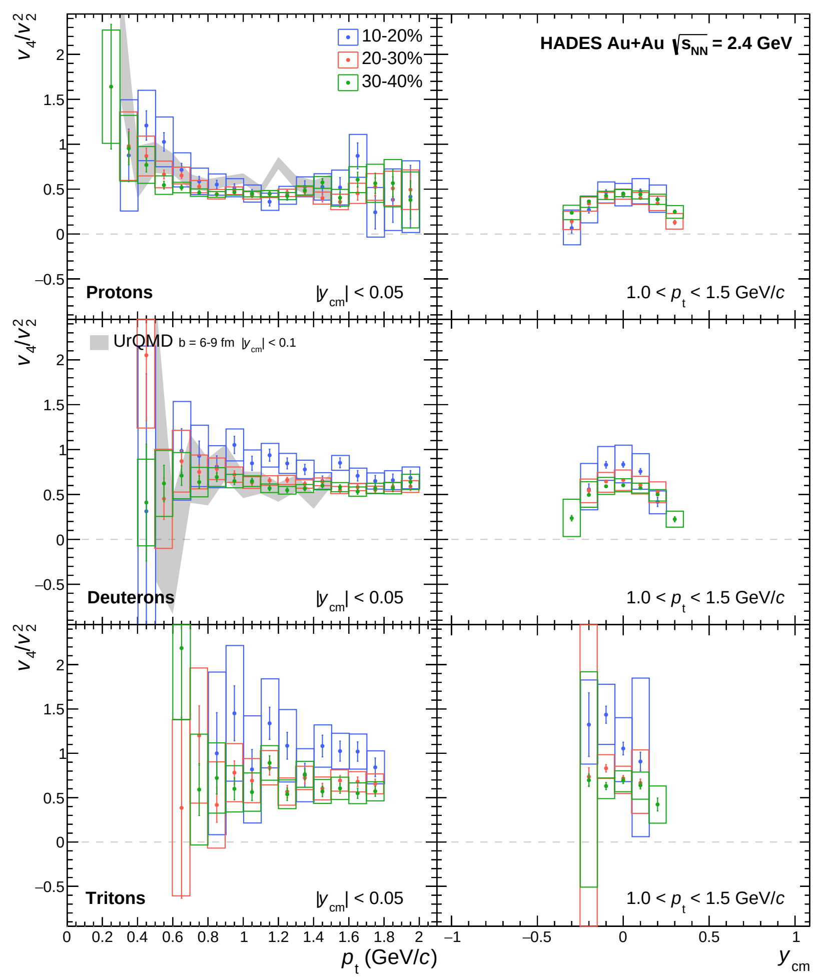

Figure 122: The ratio v_4/v_2^2 for protons (upper row), deuterons (middle row) and tritons (lower row) in Au+Au collisions at 1.23 *A*GeV for three different centralities. The left column displays the values as a function of p_t at mid-rapidity ($|y_{cm}| < 0.05$) and in the right column the values averaged over the interval $1.0 < p_t < 1.5$ GeV/c are shown as a function of rapidity. Systematic errors are represented by open boxes. UrQMD model predictions for protons and deuterons are depicted as grey shaded areas [338]. The figure is published in [337].

coefficients in relation to the participant plane are analyzed [383]. It was shown that the v_2 should be proportional to the initial eccentricity of the reaction. The `UrQMD` transport model provides a good description of v_1 and v_4 of protons [338] with discrepancies to the measured v_2, but can reproduce the measured ratio v_4/v_2^2 at mid-rapidity for protons and deuterons. Similar calculation from the transport model `SMASH` [384], for the case of nucleon flow (protons and neutrons), shows also that the value of 0.5 is reached in the p_t region above 0.75 GeV/c. In the left panels of Fig. 122 the ratio v_4/v_2^2 at mid-rapidity as a function of p_t is shown. For protons an almost p_t independent value around 0.5 is observed at p_t above 0.6 GeV/c for the three centrality intervals shown, while in the case of deuterons and tritons it is systematically above 0.5, both without significant p_t dependence. `UrQMD` model predictions are displayed as grey-shaded bands. In the right panels of Fig. 122 the rapidity-dependence of the ratio is shown. The values of 0.5 are only

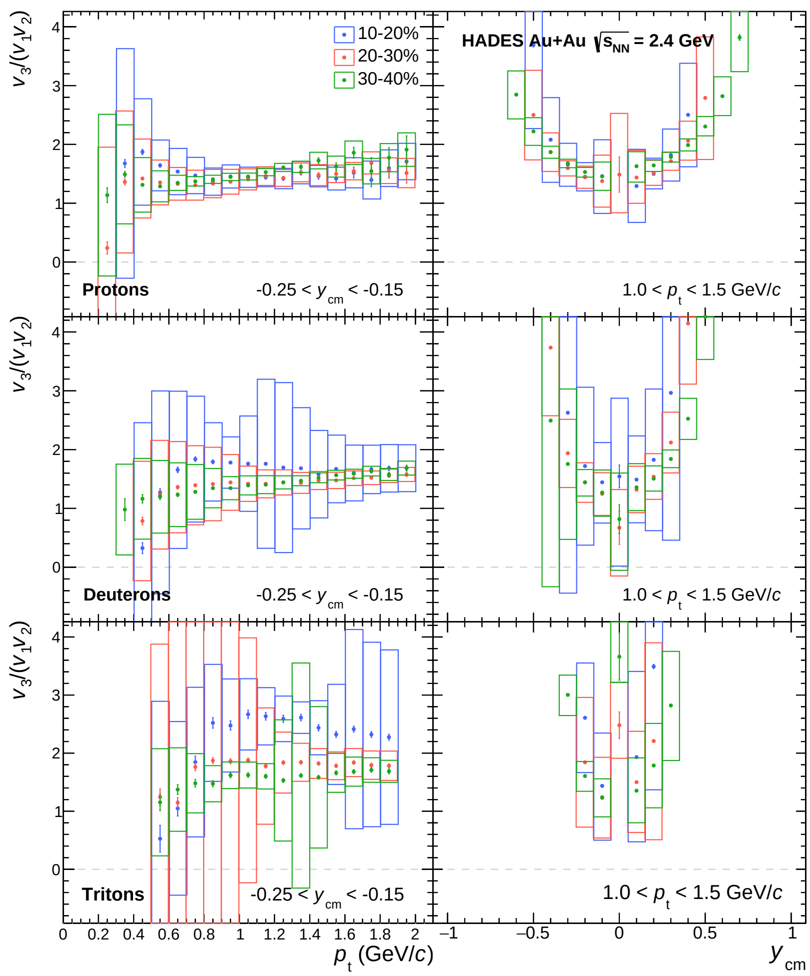

Figure 123: The ratio $v_3/(v_1 v_2)$ for protons (upper row), deuterons (middle row) and tritons (lower row) in Au+Au collisions at 1.23 *A*GeV for three different centralities. The left column displays the values as a function of p_t for the rapidity interval $-0.25 < y_{cm} < -0.15$ and in the right column the values averaged over the interval $1.0 < p_t < 1.5$ GeV/c are shown as a function of rapidity. Systematic errors are represented by open boxes.

reached by the data at mid-rapidity and it is found to be lower moving away from mid-rapidity. The ratio $v_3/(v_1 v_2)$ is shown in a similar way in Fig. 123. The p_t dependence is presented here in the rapidity interval $-0.25 < y_{cm} < -0.15$, with values above 1.4 for the protons and deuterons. It should be noted that a reliable determination of this ratio around mid-rapidity is not possible, because the odd flow coefficients reach values around zero. The UrQMD model calculation [338] yields for protons and deuterons comparable values. The relatively large value of this ratio indicates that the flow coefficients are connected to the same origin, be it the initial geometry of the collision or the dynamic evolution of the reaction system up to the later stages. To answer this question systematic model calculations are needed. Until now only calculations for v_4/v_2^2 and $v_3/(v_1 v_2)$ from the above described transport models [338, 383, 384] are available and no results from a calculation with a hydro-dynamical model for our energy regime has been published. Since the flow coefficients are here measured relative to the first order reaction plane determined from the projectile spectators, the effects of fluctuations, as dominant for higher energies, should not be relevant in this energy regime [298].

Geometrical Scaling

To investigate to what extent the geometrical properties of the collision system determine the observed flow pattern, we recall the description of the collision geometry given in the introduction. The anisotropic shape and orientation of the initial state of the overlapping region is characterized by the corresponding moments of order n for the eccentricity ε_n and the phase angles ψ_n relative to the reaction plane:

$$\varepsilon_n = \frac{\sqrt{\langle r^n \cos(n\phi)\rangle^2 + \langle r^n \sin(n\phi)\rangle^2}}{\langle r^n \rangle} \tag{78}$$

$$\psi_n \equiv \mathrm{atan2}(\langle r^n \sin(n\phi)\rangle, \langle r^n \cos(n\phi)\rangle) + \frac{\pi}{n}, \tag{79}$$

with $r = \sqrt{x^2 + y^2}$, $\phi = \tan^{-1}(y/x)$ and x, y as the nucleon coordinates in the plane perpendicular to the beam axis, where x is oriented in the direction of the impact parameter. In the following, we use the participant nucleon distribution in the transverse plane within the Glauber-MC approach [142, 143] to calculate ε_n of order n. In Fig. 124 the spatial nucleon distribution for one Glauber MC event is displayed with an impact parameter $b = 6$ fm. The participating nucleons are plotted as full coloured dots, the spectators as light coloured dots and their size corresponds to the nucleon-nucleon cross section σ_{NN} used in the calculation. The corresponding average impact parameter $\langle b \rangle$, the average participant eccentricities $\langle \varepsilon_2 \rangle$ and $\langle \varepsilon_4 \rangle$ with their systematic model uncertainties describing the initial nucleon distribution for

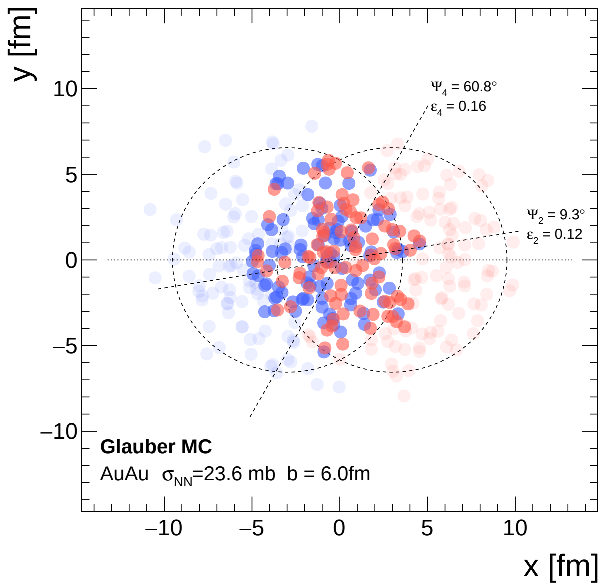

Figure 124: The spatial nucleon distribution within one Glauber MC event is displayed, where the dashed circles indicate the radius R of each of the two gold nuclei with an impact parameter $b = 6$ fm. The participating nucleons are plotted as full coloured dots, and the spectators as light coloured dots and their size corresponds to the nucleon-nucleon cross section σ_{NN}. The anisotropic shape of the overlapping region is characterized by the corresponding moments ε_n and the phase angles ψ_n relative to the reaction plane.

the different centrality classes, as calculated using the Glauber-MC approach [142] are listed in Tab. 26. The values for $\langle \varepsilon_2 \rangle$ and $\langle \varepsilon_4 \rangle$ are

Table 26: Parameters describing the initial nucleon distribution for the different centrality classes as calculated within the Glauber-MC approach [142]. Listed are the corresponding average impact parameter $\langle b \rangle$, the average participant eccentricities $\langle \varepsilon_2 \rangle$ and $\langle \varepsilon_4 \rangle$ with their systematic model uncertainties and their standard deviation σ_{ε_2} and σ_{ε_4}.

Centrality class	$\langle b \rangle$	$\langle \varepsilon_2 \rangle$	σ_{ε_2}	$\langle \varepsilon_4 \rangle$	σ_{ε_4}
$00-10$	3.13	0.121 ± 0.007	0.067	0.124 ± 0.009	0.067
$10-20$	5.70	0.235 ± 0.010	0.089	0.183 ± 0.009	0.094
$20-30$	7.37	0.325 ± 0.008	0.109	0.250 ± 0.010	0.121
$30-40$	8.71	0.401 ± 0.009	0.129	0.323 ± 0.012	0.148
$40-50$	9.86	0.466 ± 0.010	0.153	0.400 ± 0.011	0.174
$50-60$	10.91	0.529 ± 0.009	0.067	0.483 ± 0.015	0.199

shown in the left panel of Fig. 125 for the different centrality classes. In addition, the reaction plane eccentricity ε_{RP} in the fixed reference frame is displayed and for the order $n = 2$ the eccentricity ε_2 coincides with the *participant eccentricity* $\varepsilon_{\text{part}}$ [385–387]:

$$\varepsilon_{RP} = \frac{\sigma_y^2 - \sigma_x^2}{\sigma_y^2 + \sigma_x^2} \; , \; \varepsilon_{\text{part}} = \frac{\sqrt{(\sigma_y^2 - \sigma_x^2)^2 + 4\sigma_{xy}^2}}{\sigma_y^2 + \sigma_x^2} \; . \tag{80}$$

The moments of the spatial distribution in x- and y-direction used here are the mean $\langle x \rangle$ and $\langle y \rangle$, the variance and the covariance:

$$\sigma_x^2 = \langle x^2 \rangle - \langle x \rangle^2 \; , \; \sigma_y^2 = \langle y^2 \rangle - \langle y \rangle^2 \; , \; \sigma_{xy}^2 = \langle xy \rangle - \langle x \rangle \cdot \langle y \rangle \; . \tag{81}$$

In the right panel of Fig. 125 the elliptic flow v_2 measured at mid-rapidity is shown for all three investigated particle species after dividing it by the event-by-event averaged second-order participant eccentricity $v_2 / \langle \varepsilon_2 \rangle$. Remarkably, this scaling results in almost identical values for all centrality classes at high transverse momenta, indicating that the

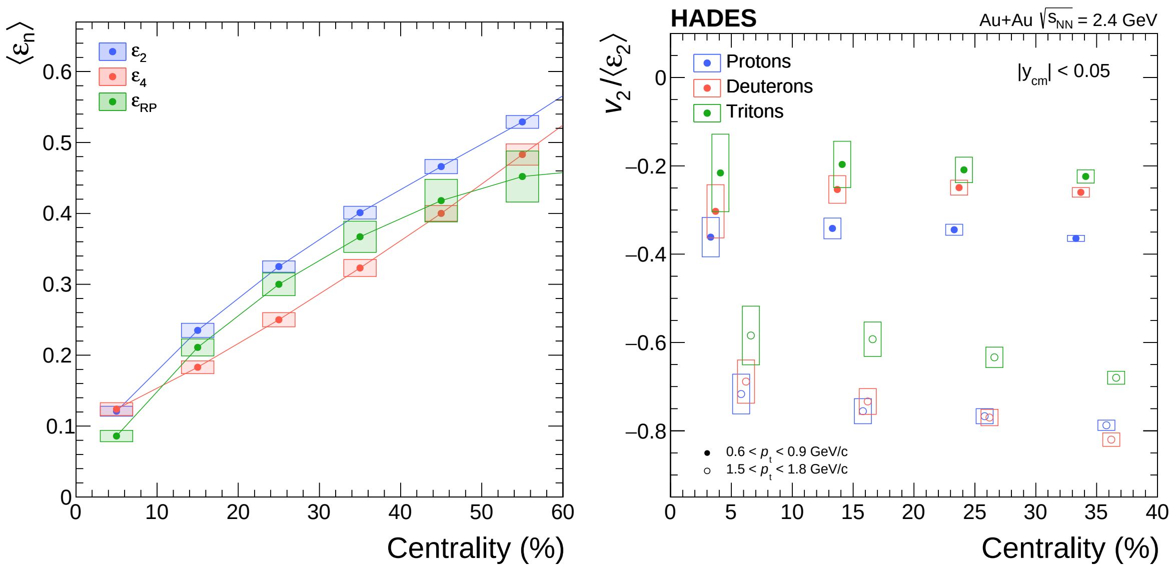

Figure 125: The average participant eccentricities $\langle\varepsilon_2\rangle$ and $\langle\varepsilon_4\rangle$ and the reaction plane eccentricity ε_{RP} in the fixed reference frame are shown with their systematic model uncertainties for the different centrality classes (left panel). The elliptic flow v_2 of protons, deuterons, and tritons in two transverse momentum intervals at mid-rapidity in Au+Au collisions at 1.23 *A*GeV for four centrality classes. The values are divided by the second-order eccentricity $v_2/\langle\varepsilon_2\rangle$. Systematic uncertainties are displayed as boxes.

centrality dependence of the elliptic flow of particles emitted at early times is to a large degree already determined by the initial nucleon distribution. It is not immediately clear how the flow pattern can be directly related to the initial participant distribution, since the elliptic flow at these beam energies is mainly the result of the so-called squeeze-out effect, caused by the passing spectators. This scaling is also shown in Fig. 126, where in the left panel the elliptic flow v_2 measured at mid-rapidity for protons as a function of p_t is displayed for different

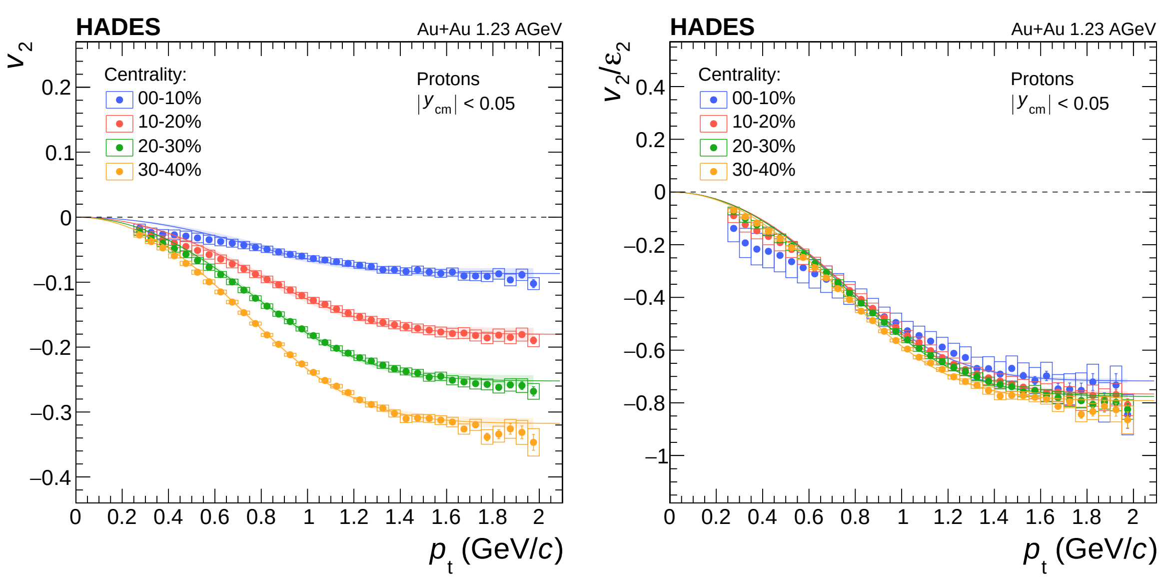

Figure 126: Elliptic flow v_2 of protons in four different centrality classes as a function of p_t around mid-rapidity (left) and v_2 scaled by the eccentricity $\langle\varepsilon_2\rangle$ of the same centrality interval (right). The lines are fits with the trigonometric function in Eq. 76.

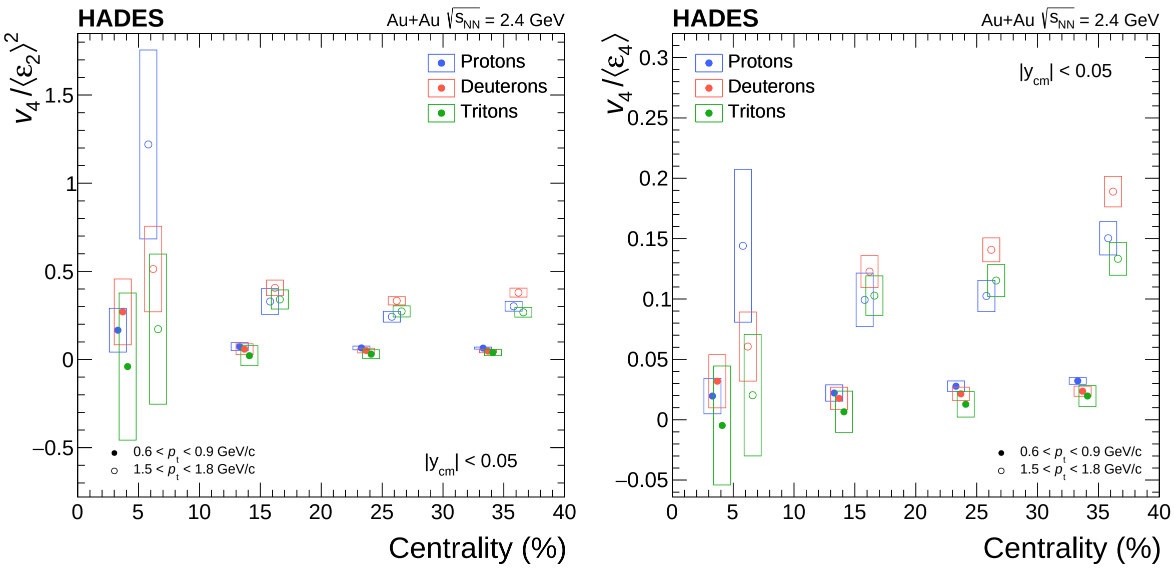

Figure 127: Same as in the right panel of Fig. 125, but for the quadrangular flow divided by the square of second-order eccentricity, $v_4/\langle\varepsilon_2\rangle^2$ (left), and by the fourth-order eccentricity, $v_4/\langle\varepsilon_4\rangle$ (right).

centralities and in the right panel the scaled values $v_2/\langle\varepsilon_2\rangle$. The eccentricity scaled spectra for the protons show a saturation at similar values of around -0.8, which is also reproduced by the parametrization with Eq. 76. It has been argued that *flow saturation* at large momenta [388, 389], observed first at SPS and RHIC, might be the results of *surface emission*, where particles with the maximal velocity can preserve their orientation, since the probability of leaving the outer shell of the reaction region without further interactions or absorption is higher than

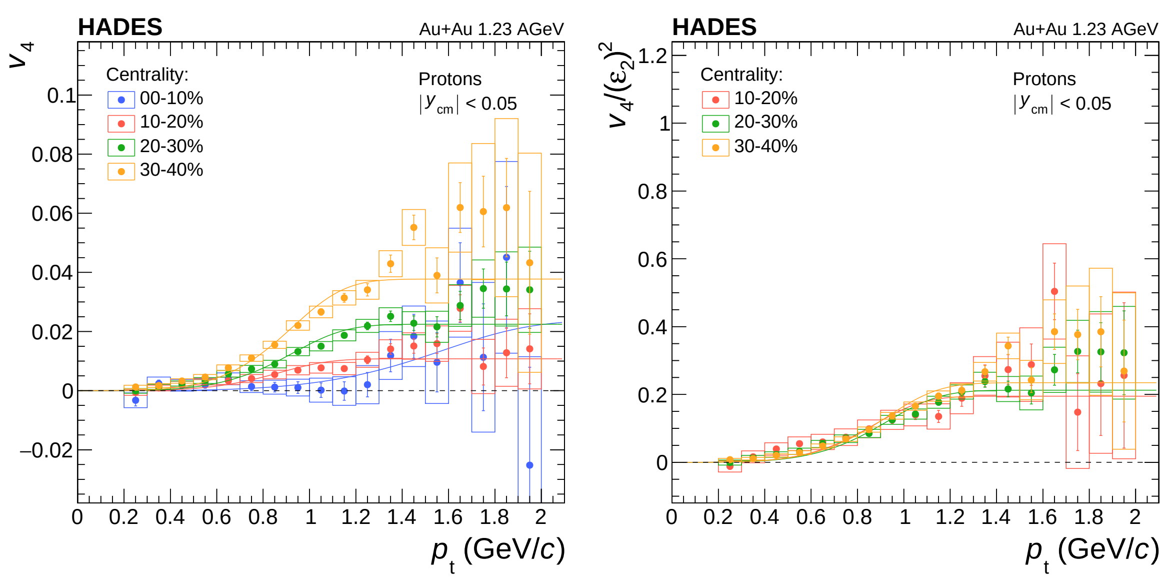

Figure 128: Same as in the Fig. 126, but for the scaled quadrangular flow. The values in the right are divided by the square of second order eccentricity, $v_4/\langle\varepsilon_2\rangle^2$. The lines are fits with the trigonometric function in Eq. 76.

from the central core. The scaling of v_2 works less well at lower p_t, which suggests that particles emitted at later times are less affected by the initial state geometry. Also, a scaling of v_4 with ε_2^2 is observed, as is depicted in the left panel of Fig. 127 which presents $v_4/\langle\varepsilon_2\rangle^2$ for different centralities in two transverse momentum intervals. To illustrate this, in Fig. 128 the quadrangular flow v_4 measured at mid-rapidity for protons as a function of p_t is displayed and in the right panel the scaled values $v_4/\langle\varepsilon_2\rangle^2$ in the same centrality classes. The fixed relation between v_2 and v_4, shown in the ratio v_4/v_2^2 (see Fig. 122), and the individual eccentricity scalings $v_2/\langle\varepsilon_2\rangle$ and $v_4/\langle\varepsilon_2\rangle^2$, might point to a common origin of the Fourier decomposition, where v_4 is a second order correction ($\propto \langle\varepsilon_2\rangle^2$) to the overall emission pattern defined at mid-rapidity by v_2. This is contrary to the case at very high collision energies, where higher order flow coefficients are related to initial state fluctuations and independent from another. In this scenario one would also expect v_4 to rather scale with ε_4. While this might be observable also here at lower p_t, $v_4/\langle\varepsilon_4\rangle$ is not independent of centrality in the high p_t region, *i.e.* for particles emitted at early times, as demonstrated in the right panel of Fig. 127.

Nucleon Coalescence

Usually, the *coalescence model* implies that the invariant spectrum of composite particles is proportional to the *product* of the invariant spectra of its constituents particles [390–393]. The momentum p_A of the composite nucleus is the sum of the momenta p of its A constituent nucleons, if their distance in phase space is negligible:

$$p_A = A\ p\ ,\ \ \delta p \rightarrow 0\ ,\ \ \delta\phi \rightarrow 0\ . \tag{82}$$

In the following only the transverse spectra at mid-rapidity are considered. Recalling the triple differential invariant distribution Eq. 19 with its shorthand notation given in Eq. 20, the single-particle density in azimuth angle and transverse momentum can be expressed as:

$$\varrho(p_t,\phi) = \frac{1}{2\pi}\,\frac{dN}{p_\mathrm{t}\,dp_\mathrm{t}}\left(1 + 2\sum_{n=1}^{\infty} v_n(p_\mathrm{t})\cos(n\phi)\right)\ . \tag{83}$$

With the assumption that the single-particle densities of the constituent neutrons and protons are equal[8], the particle density of the composite nucleus follows in the coalescence picture as:

$$\varrho_A(Ap_t,\phi) = B_A\ \varrho(p_t,\phi)^A\ . \tag{84}$$

The coalescence parameter B_A is a phase space dependent factor, describing the probability for nucleons to coalesce. This factor incorporates multiple effects and the exact treatment can depend on kinematic

[8] In the references [370, 394–396] the analytic expressions for flow coefficients from the *coalescence model* are outlined for the case of quark or parton recombination, but the key arguments are the same and exclusively based on momentum addition in the case of negligible small distances in phase space between their constituents.

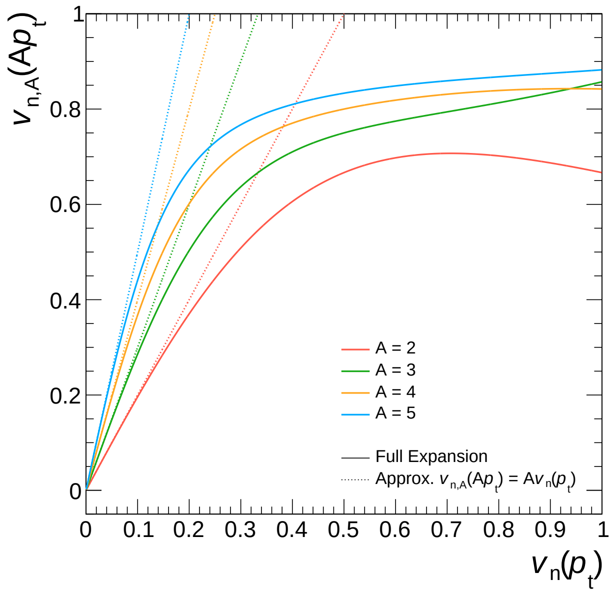

Figure 129: The dependence of $v_{n,A}(A\,p_{\mathrm{t}})$ for nuclei of mass number A as a function of the single nucleon $v_n(p_{\mathrm{t}})$ is displayed for the expansion with the correction term as given in Eq. (87) as solid lines and for the approximations as dotted lines, both in the case of only one specific harmonic coefficient.

and quantum mechanical considerations (*i.e.* the respective wave functions), the quantum numbers (spin and isospin) of the constituents, and the spatial extension of the source [397–399]. However, recalling the ratio defined in Eq. 21 which is used to calculate the Fourier coefficients, the coalescence parameter B_A drops out if it has no ϕ-dependence [370, 396]:

$$v_{n,A}(Ap_t) = \frac{\int_0^{2\pi} \cos(n\phi)\ B_A\ \varrho(p_t,\phi)^A\ d\phi}{\int_0^{2\pi}\ B_A\ \varrho(p_t,\phi)^A\ d\phi} \tag{85}$$

Further simplifying the single-particle density such that only one specific coefficient v_n is considered at a time:

$$\varrho(p_t,\phi) = \varrho(p_t)(1+2v_n(p_t)\ \cos(n\phi))\ , \tag{86}$$

the azimuthal density of a composite particle can be expressed by the following relations:

$$\begin{aligned}
v_{n,A=2}(A\,p_{\mathrm{t}}) &= 2\,v_n(p_{\mathrm{t}})\,\frac{1}{1+2\,v_n^2(p_{\mathrm{t}})}\\
v_{n,A=3}(A\,p_{\mathrm{t}}) &= 3\,v_n(p_{\mathrm{t}})\,\frac{1+v_n^2(p_{\mathrm{t}})}{1+6\,v_n^2(p_{\mathrm{t}})}\\
v_{n,A=4}(A\,p_{\mathrm{t}}) &= 4\,v_n(p_{\mathrm{t}})\,\frac{1+3\,v_n^2(p_{\mathrm{t}})}{1+12\,v_n^2(p_{\mathrm{t}})+6\,v_n^4(p_{\mathrm{t}})}\\
v_{n,A=5}(A\,p_{\mathrm{t}}) &= 5\,v_n(p_{\mathrm{t}})\,\frac{1+6\,v_n^2(p_{\mathrm{t}})+2\,v_n^4(p_{\mathrm{t}})}{1+20\,v_n^2(p_{\mathrm{t}})+30\,v_n^4(p_{\mathrm{t}})}\ .
\end{aligned} \tag{87}$$

If the correction term is neglected, the expressions are reduced to the simple scaling relation $v_{n,A}(A\,p_{\mathrm{t}}) = A\,v_n(p_{\mathrm{t}})$. The latter corresponds

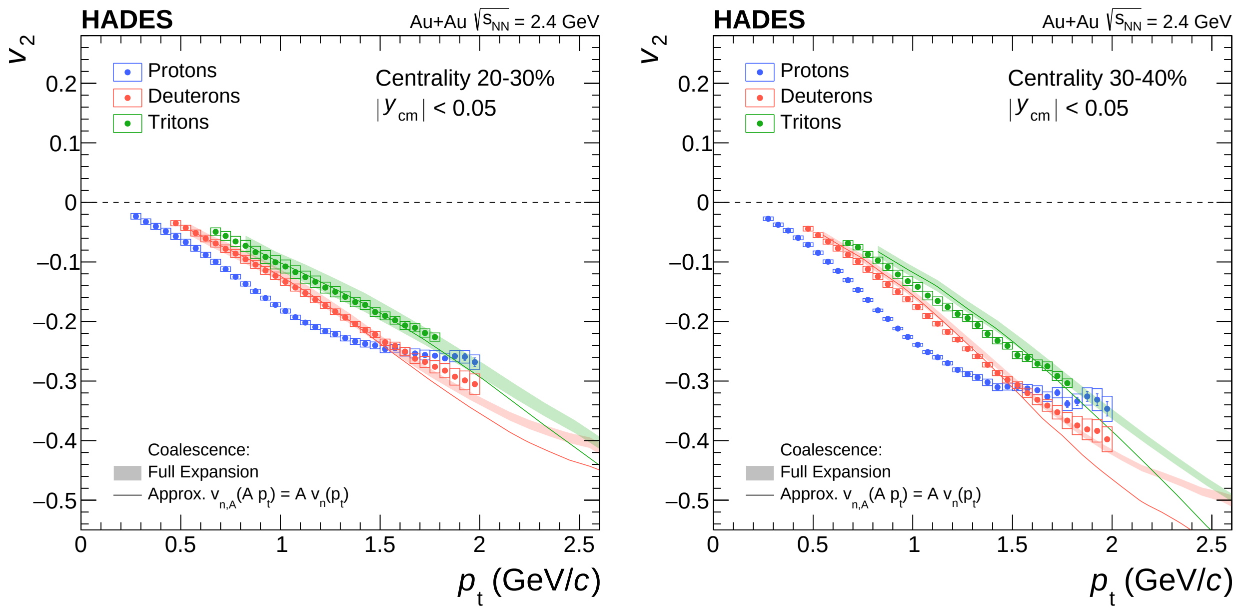

Figure 130: Elliptic flow (v_2) of protons, deuterons, and tritons in two centrality classes $20-30\%$ (left) and $30-40\%$ (right) in Au+Au collisions at 1.23 AGeV as a function of p_t at mid-rapidity ($|y_{cm}| < 0.05$). Systematic uncertainties are displayed as boxes. The solid lines represent the proton distribution after scaling according to the approximation $v_{n,A}(A\,p_t) = A\,v_n(p_t)$. The coloured bands depict the results as calculated from the proton spectrum, including its systematic uncertainties, for the nucleon coalescence scenario with higher order terms as given in Eq. (87).

to the common approximation within a naive nucleon coalescence scenario, where one would expect that the observed flow coefficients scale with the nuclear mass number A. In Fig. 129 the dependence of $v_{n,A}(A\,p_t)$ for nuclei of mass number A as a function of the single nucleon $v_n(p_t)$ is displayed as solid lines for the expansion with the correction term as given in Eq. (87) and for the approximations as dotted lines, both in the case of only one specific harmonic coefficient. It can be seen that the approximation holds for small values of $v_{n,A} < 0.2$ and that the correction term prevents $|v_{n,A}|$ to rise beyond the maximal value of 1. The p_t dependences of v_2 measured at mid-rapidity for protons, deuterons and tritons is shown in Fig. 130. The coloured bands depict the results as calculated from the proton spectrum, including its systematic uncertainties, for the nucleon coalescence scenario with higher order terms as given in Eq. (87) and the solid lines represent the proton distribution after scaling according to the approximation $v_{n,A}(A\,p_t) = A\,v_n(p_t)$. Both parameterizations achieve a reasonable agreement with the v_2 values measured for deuterons and tritons, whereby the parameterization with correction terms shows a better description of the deuterons up to the highest p_t. It should be noted though, that this kind of parameterization is only observed in the region around mid-rapidity, where all odd flow coefficients are zero and the elliptic flow is the predominant component in the azimuthal distribution compared to the next non-zero flow coefficient v_4.

To test, whether the v_4 itself is compatible with the nucleon coalescence picture and whether the contribution of v_4 to the composite

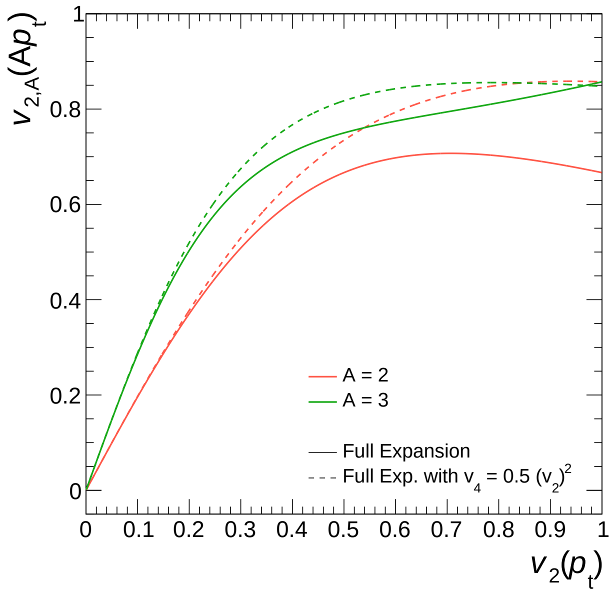

Figure 131: The dependence of $v_{n,2}(A\,p_\mathrm{t})$ for a nuclei with mass numbers $A = 2$ and 3 on the single nucleon $v_n(p_\mathrm{t})$ is displayed as dashed lines for the calculation with Eq. (89) which includes the additional contribution of v_4, assuming the relation $v_4 = 0.5\,v_2^2$. The solid lines represent the expansion with the correction term as given in Eq. (87) as in Fig. 129 in the case of only one specific harmonic coefficient.

v_2 spectra is significant enough to be visible in the measured data, vice versa the contribution of v_2 to the composite v_4 spectra, the single-particle density Eq. (86) has to be extended with an additional term:

$$\varrho(p_t,\phi) = \varrho(p_t)(1 + 2v_2(p_t)\ \cos(2\phi) + 2v_4(p_t)\ \cos(4\phi))\,. \qquad (88)$$

The extension of Eq. 87 results in following relations:

$$\begin{aligned} v_{2,A=2}(A\,p_\mathrm{t}) &= 2\,v_2(p_\mathrm{t})\,\frac{1 + v_4(p_\mathrm{t})}{1 + 2\,v_2^2(p_\mathrm{t}) + 2v_4^2(p_\mathrm{t})} \\ v_{2,A=3}(A\,p_\mathrm{t}) &= 3\,v_2(p_\mathrm{t})\,\frac{1 + v_2^2(p_\mathrm{t}) + 2\,v_4(p_\mathrm{t}) + v_4^2(p_\mathrm{t})}{1 + 6\,v_2^2(p_\mathrm{t}) + 6\,v_2^2 v_4(p_\mathrm{t}) + 6\,v_4^2(p_\mathrm{t})}\,. \end{aligned} \qquad (89)$$

Fig. 131 displays the dependence of $v_{2,A}(A\,p_\mathrm{t})$ for a nuclei with mass numbers $A = 2$ and 3 on the single nucleon $v_2(p_\mathrm{t})$ as dashed lines for the calculation with Eq. (89) which includes the additional contribution of v_4, assuming the in the previous section established relation $v_4 = 0.5\,v_2^2$. For comparison, the curves already presented in Fig. 129 are shown as well.

In Fig. 132 the same v_2 values are shown as in Fig. 130 but compared to the single-harmonic expansion according to Eq. (87) (coloured bands) and the mixed order calculation as given in Eq. (89), which includes the additional contribution of v_4 (dashed lines). In the p_t-regions covered by measurements the modification of the composite v_2-spectra due to the contribution of v_4 is found to be marginal. A similar extension of

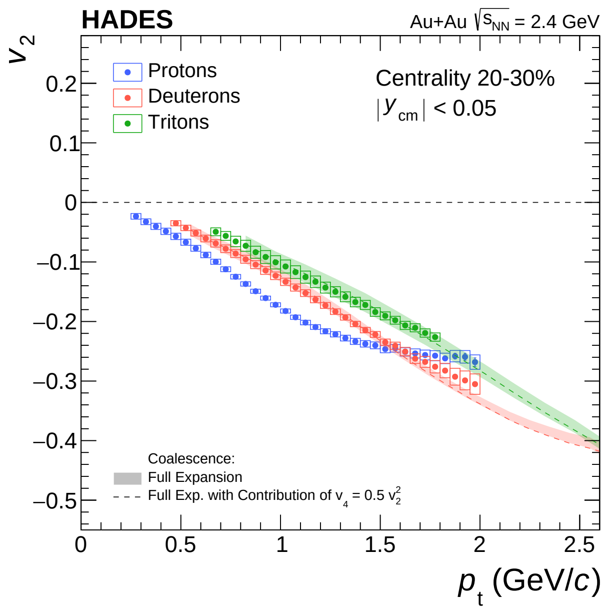

Figure 132: Elliptic flow (v_2) of protons, deuterons, and tritons (same as in Fig. 130) shown with the single harmonic expansion according to Eq. (87) (coloured bands) and the mixed order calculation as given in Eq. (89), which includes the additional contribution of v_4 assuming the relation $v_4 = 0.5\, v_2^2$.

Eq. 87 for v_4 with the contribution of v_2 results in the following relation:

$$\begin{aligned} v_{4,A=2}(A\, p_\mathrm{t}) &= \frac{2\, v_4(p_\mathrm{t}) + v_2^2(p_\mathrm{t})}{1 + 2\, v_2^2(p_\mathrm{t}) + 2\, v_4^2(p_\mathrm{t})} \\ v_{4,A=3}(A\, p_\mathrm{t}) &= \frac{3\, v_4(pt) + 3\, v_2^2(p_\mathrm{t})}{1 + 6\, v_2^2(p_\mathrm{t}) + 6\, v_4^2(p_\mathrm{t})}\,. \end{aligned} \tag{90}$$

Here next higher-order corrections as well as the mixed terms between v_2 and v_4 are neglected for the case of $A = 3$ and with the assumed relation between v_2 and v_4 this reduces to:

$$\begin{aligned} v_{4,A=2}(A\, p_\mathrm{t}) &= 4\, v_4(p_\mathrm{t})\, \frac{1}{1 + 4\, v_4(p_\mathrm{t}) + 2\, v_4^2(p_\mathrm{t})} \\ v_{4,A=3}(A\, p_\mathrm{t}) &= 9\, v_4(p_\mathrm{t})\, \frac{1}{1 + 12\, v_4(p_\mathrm{t}) + 6\, v_4^2(p_\mathrm{t})}\,. \end{aligned} \tag{91}$$

This results in the simple approximation $v_{n,A}(A\, p_\mathrm{t}) = A^2\, v_n(p_\mathrm{t})$, if the higher-order corrections are omitted. In Fig. 133 the dependence of $v_{4,A}(A\, p_\mathrm{t})$ for nuclei with mass numbers $A = 2$ and 3 as a function of the single nucleon $v_4(p_\mathrm{t})$ is displayed as solid lines for the mixed flow coefficient calculation according to Eq. (91), which includes the additional contribution of v_2. The dotted lines show for comparison the single harmonic expansion with the correction term as given in Eq. (87), as already shown in Fig. 129. The simple approximation $v_{n,A}(A\, p_\mathrm{t}) = A^2\, v_n(p_\mathrm{t})$ is represented by the dashed lines and coincides for small values $v_n < 0.1/A$ with the mixed flow coefficient calculation according to Eq. (91). Figure 134 presents a comparison of these different approximations with the data for the centrality classes $20-30\%$

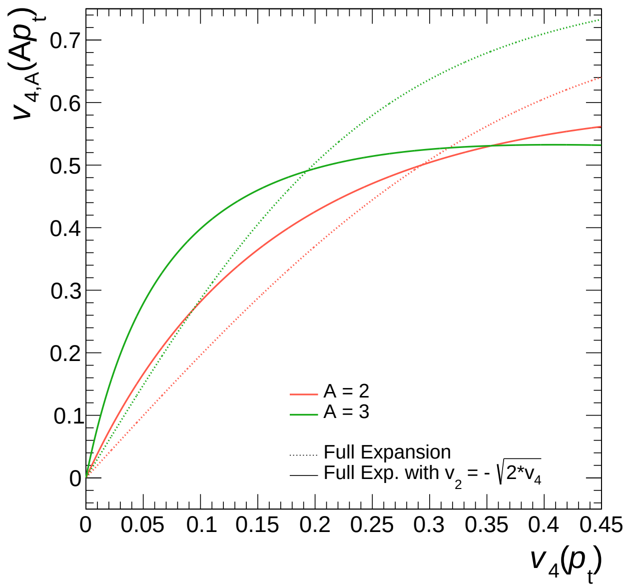

Figure 133: The dependences of $v_{4,A}(A\,p_\mathrm{t})$ for nuclei with mass number $A = 2$ and 3 as a function of the single nucleon $v_4(p_\mathrm{t})$ is displayed as solid lines for the calculation with Eq. (91), which includes the additional contribution of v_2, assuming the relation $v_2 = -\sqrt{2\,v_4}$. The dotted lines represent the single harmonic expansion with the correction term as given in Eq. (87). Note the different scale compared to in Figs. 129 and 131.

and $30-40\%$. While the relation given in Eq. 87 does not provide a good description of the data, the extended version of Eq. 91 results in a very good agreement with the deuteron and triton data. Also, the simple relation $v_{n,A}(A\,p_\mathrm{t}) = A^2\,v_n(p_\mathrm{t})$ is quite close to the data points, indicating that the higher order corrections are small.

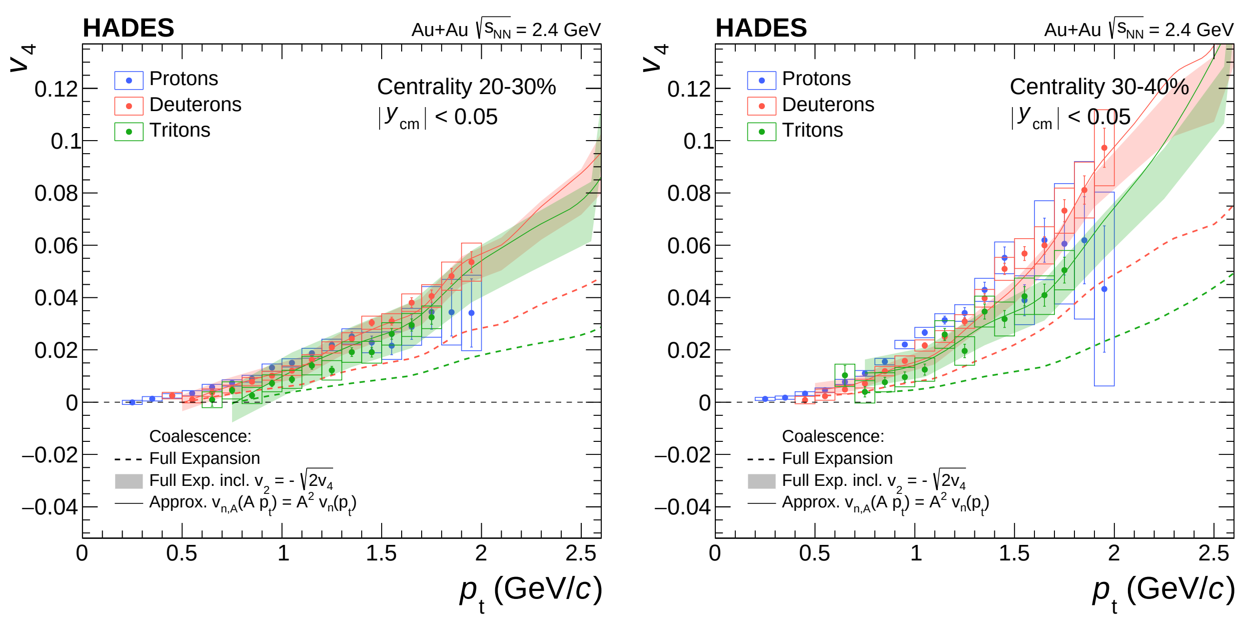

Figure 134: Quadrangular flow (v_4) of protons, deuterons and tritons in two centrality classes $20-30\%$ (left) and $30-40\%$ (right). The dashed curves represent the proton distribution after scaling according to the higher order nucleon coalescence scenario given in Eq. (87). The coloured bands depict the results as calculated with Eq. (91) which includes the additional contribution of v_2 assuming the relation $v_2 = -\sqrt{2\,v_4}$. The solid curves show the result for the simple approximation $v_{n,A}(A\,p_\mathrm{t}) = A^2\,v_n(p_\mathrm{t})$.

Transport Model Simulations

In the following, we compare a selected set of measured flow data with the calculations performed with several transport models. The emphasis was on the implementation of density-dependent mean-field potentials describing the EOS of dense nuclear matter in these models. There are basically two different categories of transport codes, where, due to the highly non-linear nature, the relativistic transport equations are numerically solved, either by simulations with test particles in the density based *Boltzmann-Uehling-Uhlenbeck* `BUU` approach or within an event based many-body approach, the *quantum molecular dynamics* `QMD` (see here for a brief introduction).

Besides the variety of approaches to formulate the mean-field potentials in microscopic transport simulations [149, 150], collision dynamics are also influenced by other ingredients that have to be accurately determined. For instance, the initial construction of realistic ground-state nuclei before collision must be constrained. In addition, the microscopic nucleon-nucleon collisions in the medium need to be treated in detail, where the effects of Pauli blocking, the formulation of effective particle masses, and the modifications of interaction cross-sections in a dense medium are important. Further, the production and emission mechanism of hadrons, mesons, and light nuclei from the expanding and thermalising medium have to be understood. Compromises between the accuracy of the simulated processes and the practicability in terms of computation time often have to be made. The evaluation of higher-order flow coefficients requires a large number of simulated events to obtain sufficient statistics. For a detailed review of the different approaches used for transport simulations see [147, 148].

Previous investigations were based on measurements of integrated values of the directed and elliptic flow coefficients as a function of beam energy [125, 152, 159, 160, 162, 169], only partially constrained by their transverse momentum dependence [170]. The information from the multi-differential data, including higher-order flow coefficients, will provide better discriminating power. As representative examples of a broad range of publicly available transport codes, the predictions of two QMD models, `JAM` [400] and `UrQMD` [401], and one BUU model, `GiBUU` [402, 403], are considered here. The versions and key properties

Model	EOS	K (MeV)	m^*/m	mom-dep.
JAM 1.90591 [400]	NS1	380	0.83	no
	MD1	380	0.65	yes
	MD4	210	0.83	yes
UrQMD 3.4 [401]	Hard	380		no
GiBUU 2019 (patch7) [402]	Skyrme 12	240	0.75	no

Table 27: Used versions of the transport models with the implemented potential characterised by the incompressibility modulus $K(\rho_0) = 380$ MeV (hard) and 210 MeV (soft), and the effective mass m^*/m, both constrained at normal nuclear matter density of $\rho_0 = 0.168$ fm^{-3}. JAM is based on the relativistic mean-field potential RMF of the Walecka type, and UrQMD and GiBUU on a non-relativistic momentum-independent potential of the Skyrme type. The GiBUU Skyrme 12 parameterization is based on the recommendation for code comparison in Ref. [150].

of the different implementations are listed in Tab. 27. Usually, the potentials are parameterised by the incompressibility modulus $K(\rho_0) =$ 380 MeV (hard) and 210 MeV (soft), and the *Landau effective mass* m^*/m, both constrained at normal nuclear matter density of $\rho_0 = 0.168\ \mathrm{fm}^{-3}$ (see for further explanation). The `JAM` code is used with three different EOS implementations, based on the relativistic mean-field `RMF` approach: hard momentum independent `NS3`, hard momentum dependent `MD1` and soft momentum dependent `MD4`. The `UrQMD` code is employed with a *hard* momentum independent EOS, and `GiBUU` with a *soft* momentum independent EOS (Skyrme 12), both utilising a non-relativistic Skyrme-like potential. Further, the effects of isospin-dependent potentials are not included in the model calculations, even though they are in principle essential for this purpose. It should be noted that the evaluation was also performed with other potentials in `JAM` and `GiBUU` and with other transport models (`smash` and `IQMD`), but these results are not shown here for the sake of brevity. Because a comprehensive comparison is beyond the scope of this work, in the following rather the discriminative power of the data, owing to its accuracy, will be highlighted. In general, the uncertainties of the data are below the spread of the model predictions shown here.

After the compilation of this comparison, several updates of the transport codes used here were published or are in progress: `UrQMD` version 3.5 [404–406] was released, `JAM`, previously written in Fortran, was rewritten in `C++` introducing several updates to the mean-field potentials in version 2.1 [407, 408] and the `GiBUU` code in its recent version of 2021 was released.

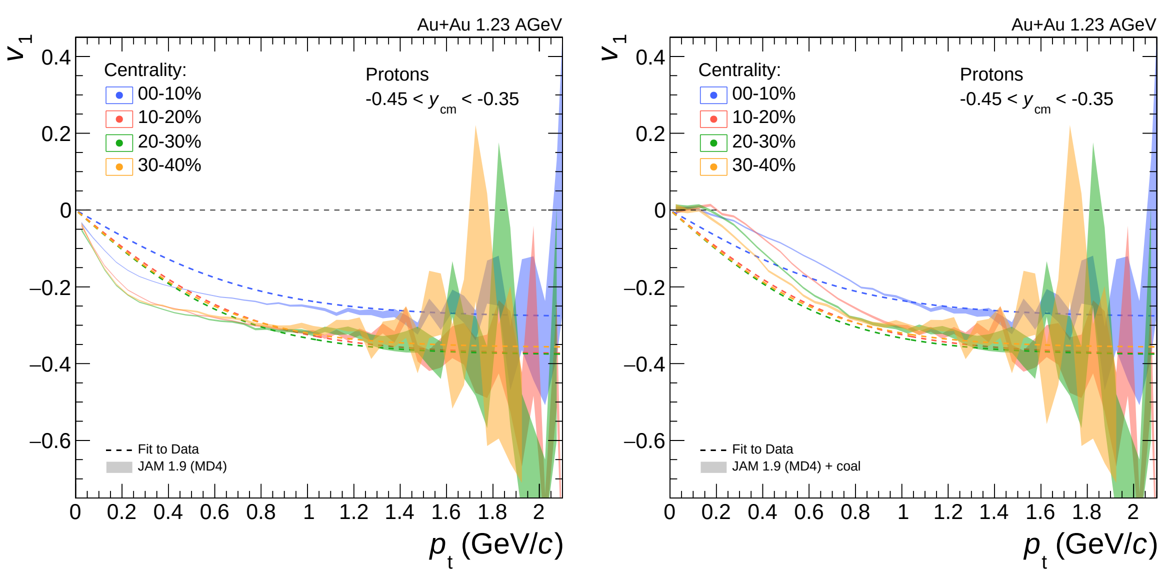

Figure 135: The p_t dependences of the directed flow v_1 for protons in the backward-rapidity interval $-0.45 < y_{cm} < -0.35$ in the four centrality classes are presented in both panels. The measurements are represented by parameterizations of the data point according to Eq. 76. The JAM calculations with soft momentum dependent potential MD4 are shown as coloured band, without (left) and with the application of the light clusters formation (right).

Since the models used here do not apply dedicated mechanisms for producing light clusters, we restrict the comparison to protons only. A common treatment of cluster formation should allow using the data on deuteron and triton flow as additional constraints. To test the effects caused by the generation of light clusters, two algorithms based on the concept of *nucleon coalescence* are implemented as a task in the `UniGen` framework [409] and can be consistently applied to the output of various event generators. The first is based on the approach used in combination with `UrQMD` [410, 411] (with predecessor implementations in `ARC` [412, 413], and `RQMD` [398, 412, 414]) and the another is based on a first implementation in the Dubna-Cascade model `DCM` [415] and its successor `DCM-QGSM` [416, 417], `LAQGSM` and `CEM` [418], or in `Geant4` [419].

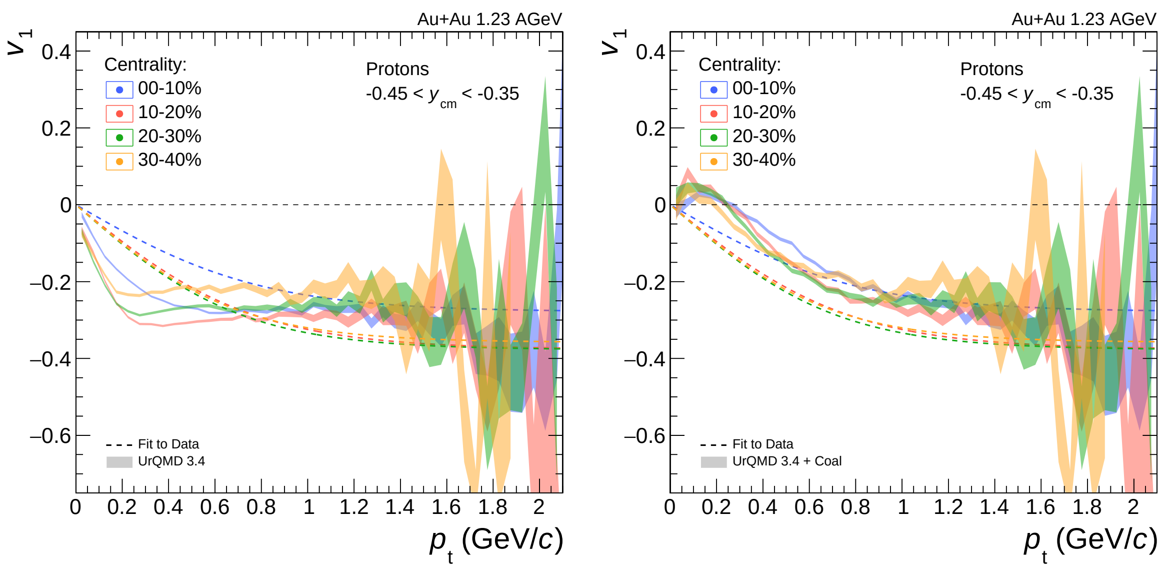

Figure 136: The same as in Fig. 135 in comparison to UrQMD calculations without (left) and with the application of the light clusters formation (right).

In Fig. 135 parameterisations of the measured p_t dependences of the directed flow v_1 according to Eq. 76 are shown for protons in the backward-rapidity interval $-0.45 < y_{cm} < -0.35$ for four centrality classes. The data points are omitted for clarity. The `JAM` calculations with the soft momentum-dependent potential `MD4` are shown as coloured bands. The spectra without any modifications are presented on the left and after the application of the light-cluster formation on the right. Similar results are shown in Fig. 136 for `UrQMD` simulations. In the high p_t region above > 1 GeV/c, the v_1 spectra before and after the cluster formation are essentially identical. In the low p_t region, a strong attenuation of the absolute v_1 values can be observed in both transport models, if the cluster formation is applied. The procedure of light nuclei production thus modifies the flow spectra of protons and has to be constrained to simultaneously reproduce the rapidity

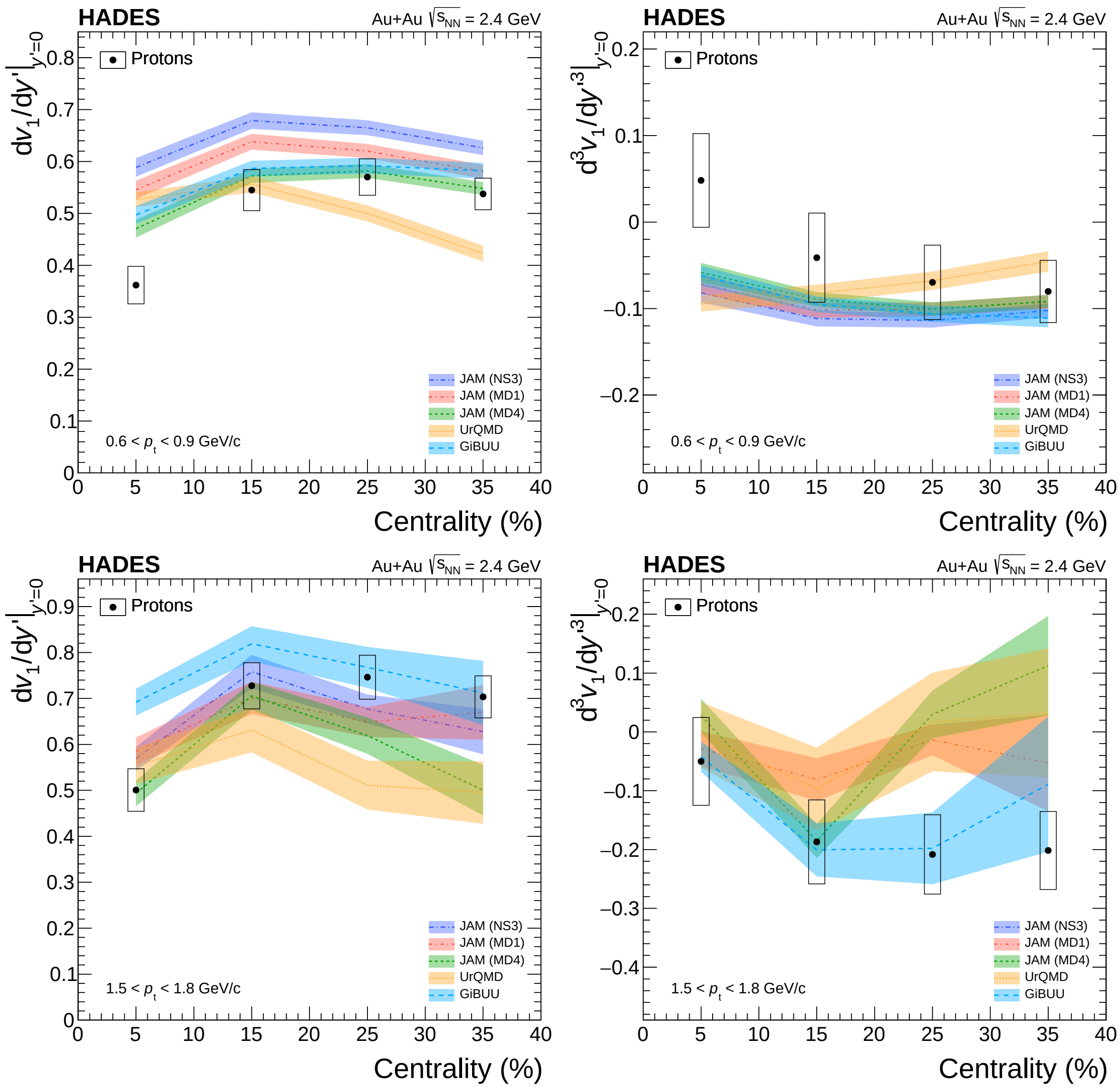

Figure 137: The slope $dv_1/dy'|_{y'=0}$ (left) and the aberrancy $d^3v_1/dy'^3|_{y'=0}$ (right) of the directed flow of protons in the two transverse momentum intervals $0.6 < p_t < 0.6$ GeV/c (upper panels) and $1.5 < p_t < 1.8$ GeV/c (lower panels) at mid-rapidity. Systematic uncertainties are displayed as boxes. The data are compared to several model predictions (see text for details).

and transverse momentum spectra of protons and light nuclei. In general, the flow coefficients of unbound protons, deuterons, and tritons generated through cluster formation exhibit sensitivity to the details of their production mechanisms, interfering with the interpretation of the effects of mean-field potentials. A simple explanation might be that an *attractive* potential will result in localised higher particle phase-space densities and, subsequently, a higher probability for the formation of light nuclei, which can reduce the flow of unbound nucleons. In comparison with the approach presented here for cluster formation at a certain freeze-out time, dynamical approaches in the production and

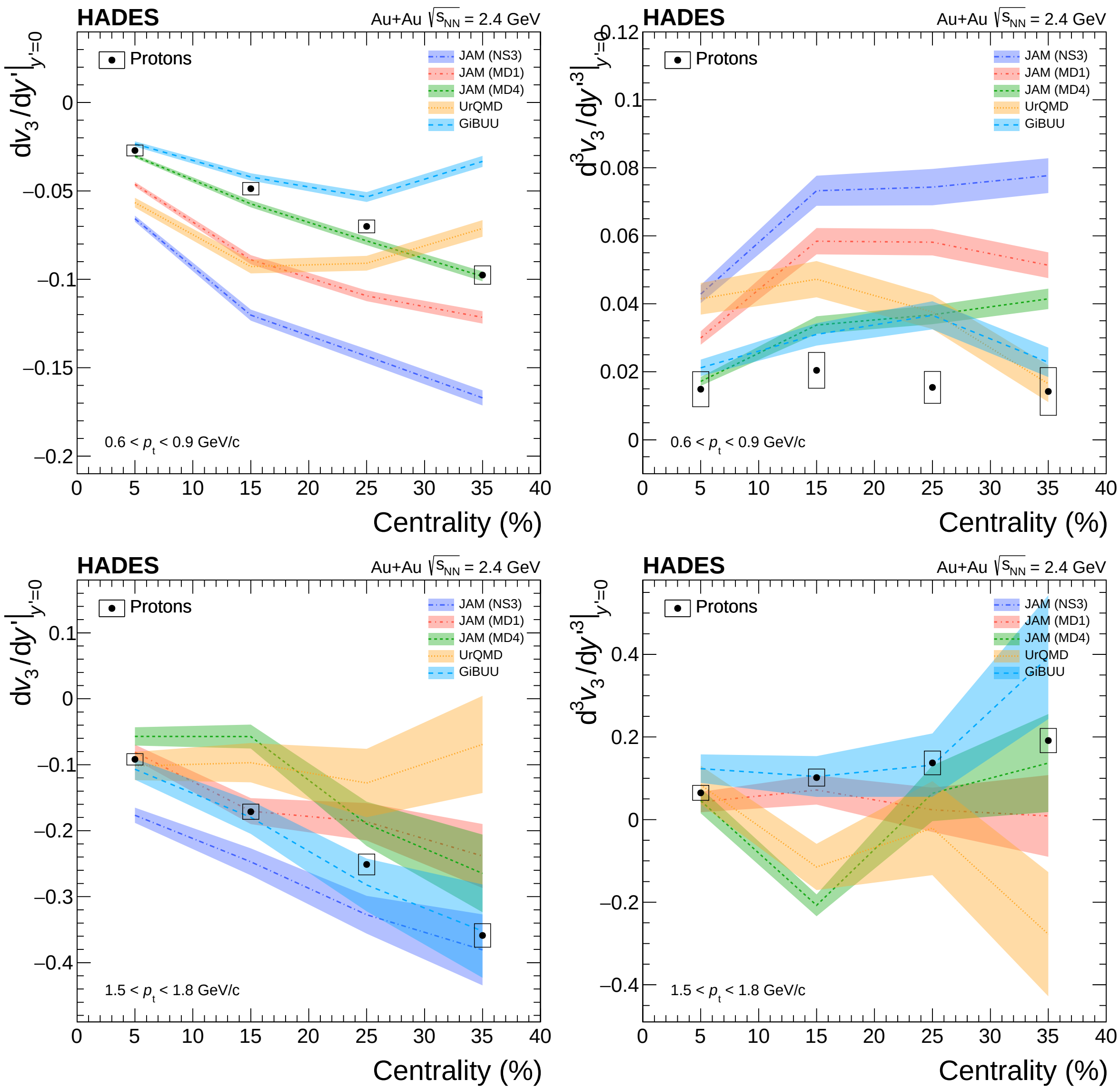

Figure 138: The slope $dv_3/dy'|_{y'=0}$ (left) and the aberrancy $d^3v_3/dy'^3|_{y'=0}$ (right) of the triangular flow of protons in the two transverse momentum intervals $0.6 < p_t < 0.6$ GeV/c (upper panels) and $1.5 < p_t < 1.8$ GeV/c (lower panels) at mid-rapidity. Systematic uncertainties are displayed as boxes. The data are compared to several model predictions (see text for details).

transport of clusters are used in the simulations of flow observables of light nuclei [384, 420, 421]. Further, a consistent treatment of spectator nucleons is important because their interaction with the expanding matter is essential in the description of flow observables.

In the following figures, the model predictions are compared with proton flow coefficients of different orders: v_1 Fig. 137, v_2 Fig. 139, v_3 Fig. 138, and v_4 Fig. 140. The data are measured at mid-rapidity and are presented as a function of centrality in two transverse momentum intervals $0.6 < p_t < 0.6$ GeV/c (upper panels) and $1.5 < p_t < 1.8$ GeV/c (lower panels). In general, all models capture approximately the overall

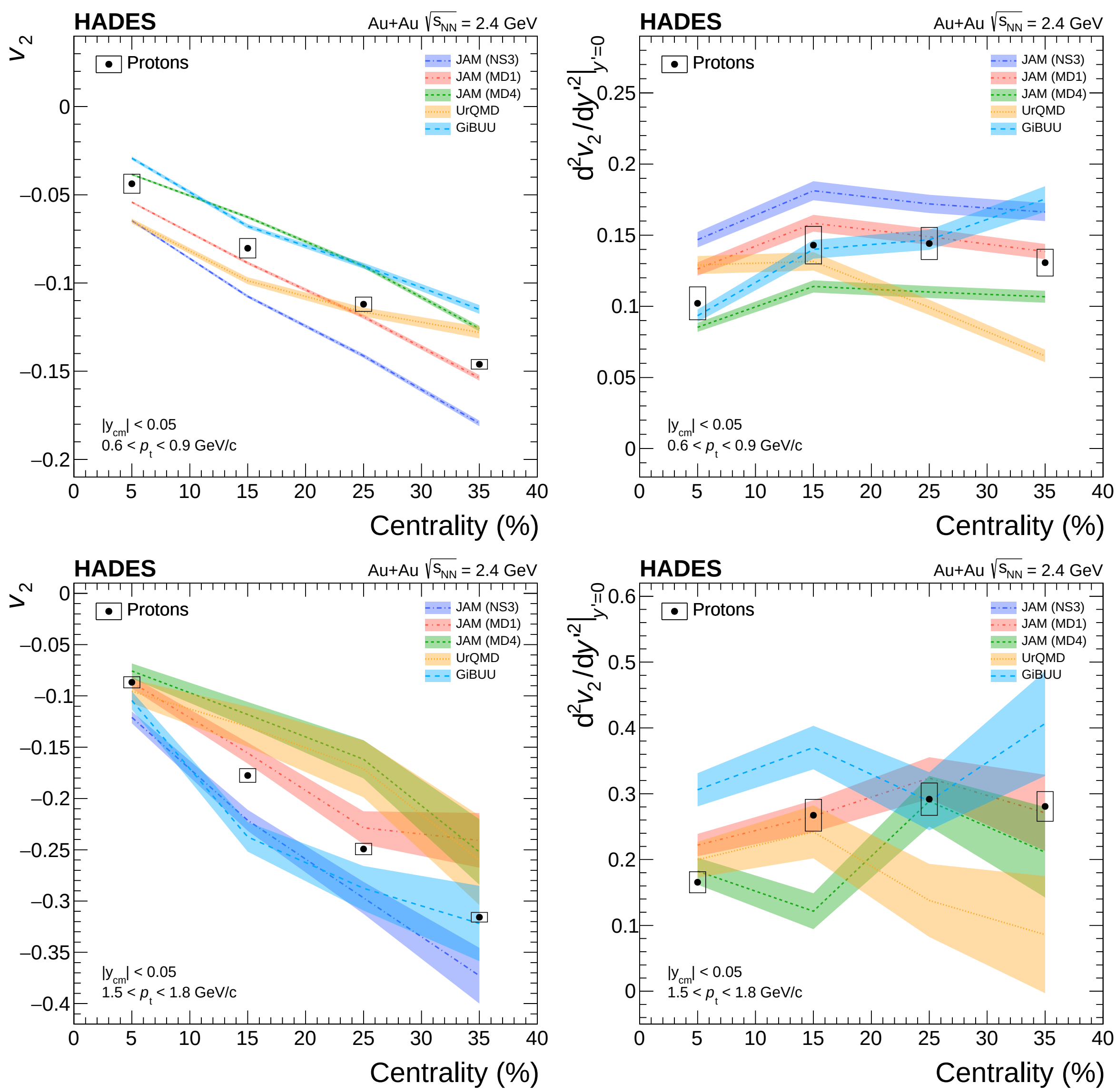

Figure 139: The values of the elliptic flow v_2 (left) and the curvatures $d^2v_4/dy'^2|_{y'=0}$ (right) of protons in the two transverse momentum intervals $0.6 < p_t < 0.6$ GeV/c (upper panels) and $1.5 < p_t < 1.8$ GeV/c (lower panels) at mid-rapidity. Systematic uncertainties are displayed as boxes. The data are compared to several model predictions (see text for details).

magnitude and trend of the measured data. For v_1 and v_3 the slope (left) and the aberrancy (right) are shown, where in the lower p_t region `JAM(MD4)` and `GiBUU` match the data for v_1 and v_2 very well.

For v_2 and v_4 the values at mid-rapidity and the curvatures are presented. All models qualitatively describe the centrality dependence of v_2, but `JAM(MD1)` is closest to the data points. `JAM(MD4)` provides overall best reproduction of all data points (v_1- v_4) and, in particular, results in the best agreement with the v_4 values at mid-rapidity in both p_t intervals. However, `JAM(MD1)` is following much better the trend of the the curvatures $d^2v_4/dy'^2|_{y'=0}$. `UrQMD` is close to the values of v_2 at mid-

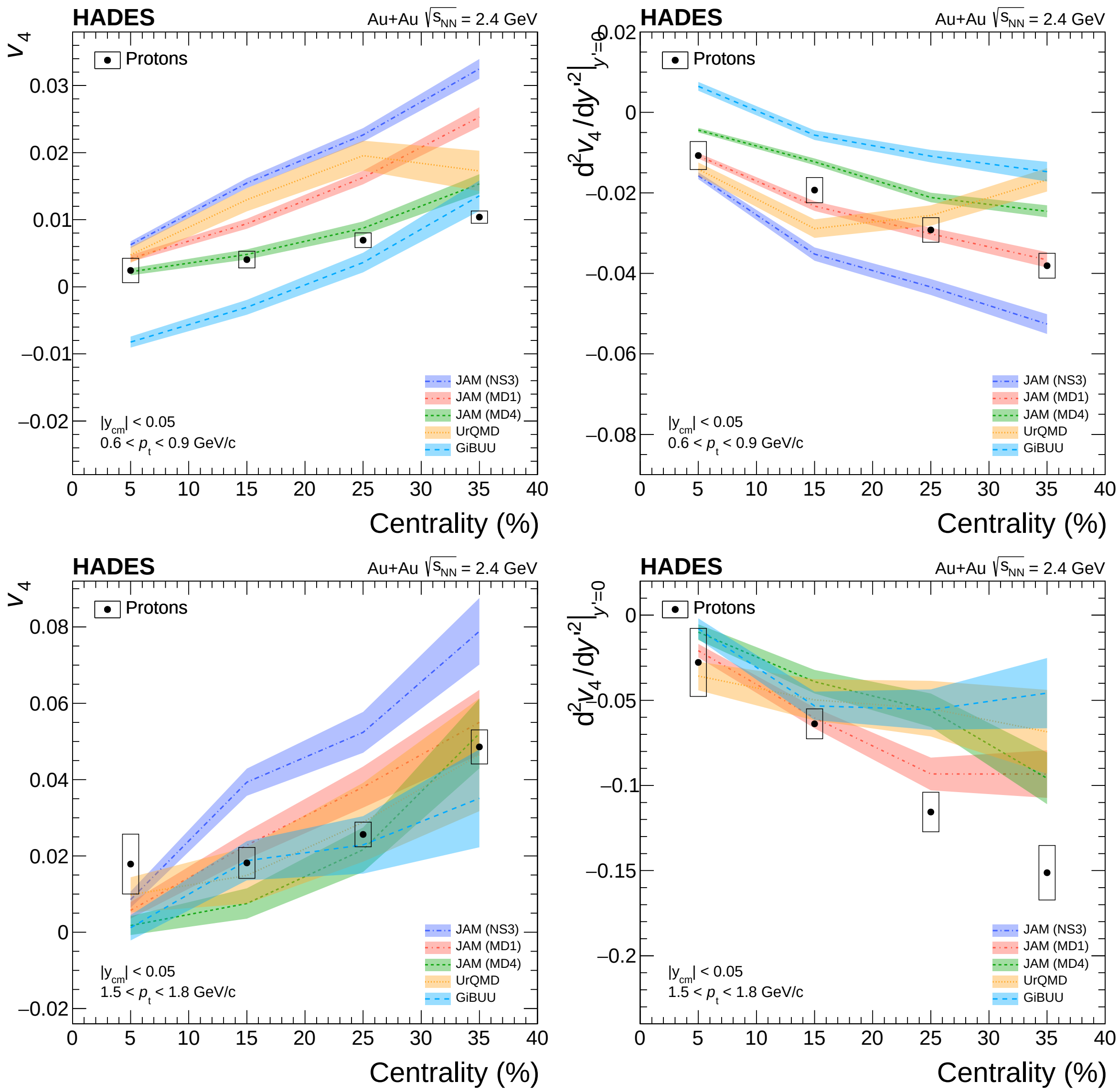

rapidity, but deviates for v_1, v_3 and v_4 at several centralities, mainly in the last centrality class $30-40\%$. `GiBUU` generally reproduces the slope and aberrancy of v_1 and v_3, but can not describe the centrality dependence of v_4. In the higher p_t interval `JAM(MD1)` yields the best match to the data, while `JAM(MD4)` and `JAM(NS3)` do not provide a consistent description of the measurements. Also, for `UrQMD` and `GiBUU`, systematic deviations are observed for some orders of the flow coefficients.

For a consistent determination of the EOS, it is important to establish that the various model approaches do not significantly differ in their predictions. The discrepancies between the data and the model

Figure 140: The values of the quadrangular flow v_4 (left) and the curvatures $d^2v_4/dy'^2|_{y'=0}$ (right) of protons in the two transverse momentum intervals $0.6 < p_t < 0.6$ GeV/c (upper panels) and $1.5 < p_t < 1.8$ GeV/c (lower panels) at mid-rapidity. Systematic uncertainties are displayed as boxes. The data are compared to several model predictions (see text for details).

calculations highlight the difficulties that arise in extracting the EOS of compressed nuclear matter. Transport models should be able to reproduce all features of the flow observables simultaneously, including their centrality, transverse momentum, and rapidity dependence. Further validations and benchmarks of transport models through systematic comparisons with experimental data should test the robustness of the model predictions and reach consistent conclusions regarding the dynamics of heavy-ion collisions. As a prerequisite for the accurate determination of the nuclear equation of state at large baryon and energy densities, our *a priori knowledge* of elementary particle physics and low-density nuclear experiments should be fully incorporated into state-of-the-art models.

Summary

In summary, this thesis presents the results of a multi-differential measurement of collective flow coefficients in Au+Au collisions at $E_{\text{beam}} = 1.23\ A\text{GeV}$, equivalent to a center-of-mass energy in the nucleon-nucleon system of $\sqrt{s_{\text{NN}}} = 2.4$ GeV, performed with the HADES

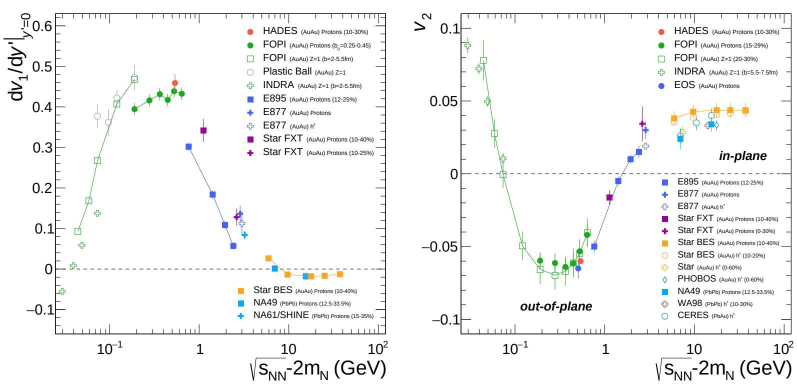

Figure 141: Compilation of directed and elliptic flow measurements as a function of the subtracted centre-of-mass energy $\sqrt{s_{\text{NN}}} - 2\,m_N$. Shown as red points are the slope of v_1 at mid-rapidity (left panel), $dv_1/dy'|_{y'=0}$, and the p_t integrated v_2 at mid-rapidity (right panel) for protons in Au+Au collisions at $\sqrt{s_{\text{NN}}} = 2.4$ GeV ($10-30$ % centrality). These results are compared with data in the same or similar centrality ranges in Au+Au or Pb+Pb collisions. Figure from [332].

experiment at SIS18/GSI. The flow coefficients v_n of the orders $n = 1-6$ are studied for protons, and light nuclei (deuterons and tritons). Preliminary values for the three first flow harmonics v_1 to v_3 were already shown in [333–336] and final results on the flow coefficients v_1 to v_6 in selected regions of phase space in the centrality range $20-30\%$ were published in [337]. The full set of experimental results for the individual Fourier coefficients are now also submitted for publication [332]. The comparison of the p_t-integrated values $dv_1/dy'|_{y'=0}$ and v_2 at mid-rapidity with previously measured experimental world data at different center-of-mass energies is shown in Fig. 141.

The properties of strongly interacting matter are one of the most important and still open topics in nuclear and particle physics. A detailed investigation over a wide range of temperatures and densities is not only important for understanding the low-energy, non-perturbative behaviour of *Quantum Chromodynamics (QCD)*, the underlying theory of the strong interaction. It has also a direct impact on fundamental questions at both, microscopic and cosmic scales, such as the accurate formulation of the *Equation-of-State (EoS)* of dense matter, the features of core-collapse supernovae explosions, the structure and stability of neutron stars, and the process of their merger. Heavy-ion collisions allow the investigation of these properties under extreme conditions in laboratory experiments, because they can compress matter to densities comparable to dense stellar objects. The unique advantage of laboratory-controlled conditions is that, depending on the beam energy, choice of target, bombarding nuclei, and *centrality of each collision*, very different conditions can be explored. In the collision process of two nuclei, the individual nucleons are decelerated owing to nuclear stopping, and their longitudinal kinetic energy is converted into thermal and compressional energy. The gradient of the pressure provides the accelerating forces for the rapidly expanding matter, which exists only for a very short time. In perfectly central collisions, the expansion should be isotropic, leading to symmetrical radial and longitudinal flow. In more peripheral collisions, characterized by a reaction region which is largely nonuniformly distributed, the initially deposited energy and baryon densities decrease from the central core of the reaction to the outer perimeter and form an elliptical shape in the transverse plane. In the longitudinal direction two elongated bands form under these conditions up to the residual fragments, called spectators, which pass by unstopped with the initial velocity. If the expansion is faster than the movement of the spectator residuals, the spectator matter can effectively block particle emission from the central fireball in their direction. The properties of the hot expanding matter, the details of its geometrical initial source, its dynamical interaction with the cold spectator matter, and the intensities due to thermal and collective motion result in complicated emission patterns and should be encoded in various flow moments. It is common to quantify the azimuthal anisotropy in the particle emission via Fourier decomposition, yielding flow coefficients v_n of several orders. It is expected that including specific flow coefficients improves the sensitivity required for a detailed theoretical description of the flow phenomena.

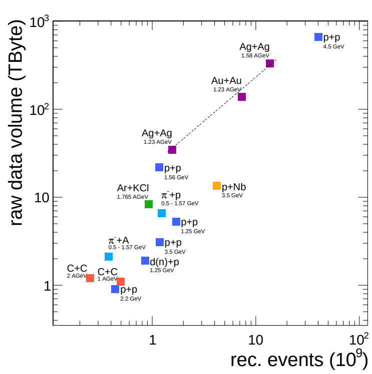

Figure 142: Compilation of the recorded number of events and their total data volume (TByte) of the HADES production beam times. See Fig. 16.

CURRENTLY, the HADES experiment is the only detector setup with the unique ability to measure rare and penetrating probes in elementary and heavy-ion reactions and as well their combination with proton- or pion-introduced reactions at the low-energy frontier. In the compilation in Fig. 142 various experiments with different collision systems and beam energies between $0.5 - 4.5$ GeV, provided by the `UNILAC` and `SIS18`, are shown. The main objective of this high-acceptance and high-statistics experiment is to investigate the *emissivity of resonance matter* [188, 189] formed in heavy-ion collisions in the $1 - 2$ AGeV energy regime, the role of baryonic resonances in these reactions, and the mechanism of strangeness production. Specific constraints on the apparatus design were driven by the precise measurement of the light vector mesons ρ, ω and ϕ via their rare leptonic decay channel. The possibility of performing a variety of measurements with the same apparatus provides a broad and complementary way to explore the properties of strongly interacting matter in elementary exclusive channels, in cold nuclear matter, and in its dense and excited states. In Fig. 143 a cross

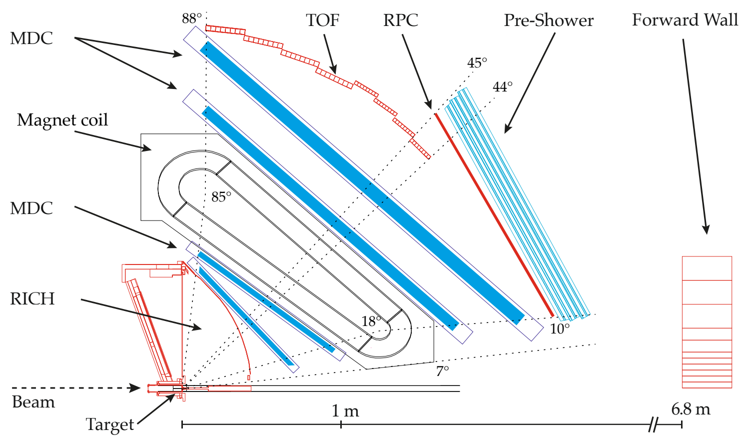

Figure 143: Cross section of one HADES sector. The segmented target is fully surrounded by the RICH detector. The magnet spectrometer consists of four layers of drift chambers (MDC), each two in front of and behind the toroidal magnetic field. At the end of the apparatus the *time-of-flight wall* TOF and the *Resistive Plate Chambers* RPC, followed by the electromagnetic pre-shower detector, are placed. The TOF detector covers the geometrical polar angel between 44° and 88°, the RPC 10° and 45°, with an overlap of 1°. The maximal acceptance coverage in polar angle for charged particle corresponds to the coverage of magnetic field between 18° − 85°. See Fig. 18.

section through the mid-plane of one sector is shown. Two *diamond counters* are mounted as beam detectors directly in front of (`START`) and behind (`VETO`) the segmented target. The magnet spectrometer consists of four *Mini-Drift Chambers* `MDC` per sector, with two in front and two behind the toroidal magnetic field of the *superconducting magnet coils* `ILSE`. Particle trajectories are derived from the hit positions in the `MDCs` and timing detectors `TOF` and `RPC`. The particles are identified using the time-of-flight method in combination with energy loss measurements. For the electron-hadron separation the hadron-blind gas detector `RICH`, and the `PreShower`, replaced by the *Electromagnetic Calorimeter* `ECAL`, are used. The *Forward Wall* `FW` is placed at a distance of 6.8 m behind the target at the small forward angle between 0.3° and 7° and is used to measure the emission angles and charge of the projectile spectators.

The characterisation of the experimental data starts with the properties of beam and target, the trigger conditions used during data taking and the estimated trigger cross section, needed to evaluate the fraction of recorded most central reactions. In the offline analysis several event properties are determined and used for selection methods: the global event vertex, which is the interaction point to which all emitted primary particles are traced back, and the event time T_0, needed for the accurate determination of the particle velocity.

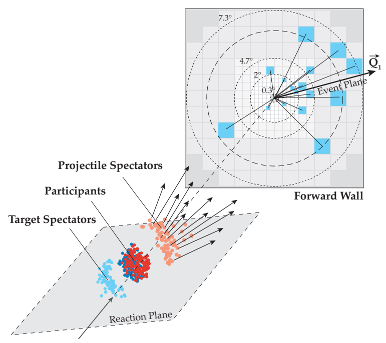

Figure 144: Sketch illustrating the event plane reconstruction using the projectile spectator hits recorded in the Forward Wall. Shown is the *reaction plane* defined by the beam axis $\vec{z}$ and the direction of the impact parameter $\vec{b}$. Oriented to this plane the *participant nucleons* (dark red and blue), as well the *target* (light blue) and *projectile spectators* (light red) are shown. The unstopped forward-going projectile spectators are detected in the cells (blue squares) of the Forward Wall and their emission angles determine the *event flow vector* $\vec{Q}_1$ and the corresponding *event plane*.

THE PROCEDURE of the flow analysis is based on the event plane method [137, 138, 248], where the anisotropies in the azimuthal distribution are quantified by the n^{th} cosine harmonic coefficients of the Fourier series:

$$v_n(p_t, y) = \langle \cos(n\phi) \rangle ,$$

where $\langle \cdots \rangle$ denotes the average over all particles in a given p_t and y interval and all events of the same centrality class. The relative azimuthal angle is given with respect to the orientation of the measured first-order event plane $\phi = \phi_{lab} - \Psi_{\mathrm{EP},1}$. As shown in Fig. 144, from the emission angles ϕ_i of FW hits the *event flow vector* $\vec{Q}_1$ with its corresponding event plane angle $\Psi_{\mathrm{EP},1}$ is determined. Owing to fluctuations and finite multiplicity, the estimated *event plane* has a dispersion and must be corrected. To enable meaningful comparisons between experimental observations and predictions of theoretical models, the classification of events should be well defined, *i.e.* corrected for the *event plane resolution* and within sufficiently narrow intervals of the impact parameter. Part of this work included the implementation of the procedure to determine the reaction centrality and the orientation of the event plane and its resolution.

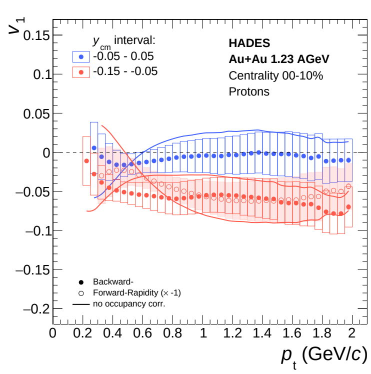

Figure 145: Results for v_1, including their total systematic uncertainties, are shown for protons in the centrality class, $0-10\%$. To illustrate the effect of the occupancy correction the version without correction is overlaid as solid lines.

THE EVALUATION of systematical biases in the flow measurements is an essential part of this thesis. Several sources of uncertainties are identified, which mainly arise from the track selection, the correction for reconstruction inefficiencies, the particle identification, and the effects of azimuthally non-uniform detector acceptance. The systematic point-to-point uncertainties are determined separately for each particle type (proton, deuteron, and triton), order of the flow harmonics v_n, and centrality class. They are derived by independently analyzing all the different variations and then evaluating the overall distributions of the resulting flow coefficients. A dedicated correction method for the flow measurement had to be developed to cope with the reconstruction inefficiencies owing to the occupancies of the detector system. The effect is illustrated in Fig. 145 for directed proton flow v_1.

THE VALIDATION of the results within the range of their systematic uncertainties is done with several consistency checks. Owing to the symmetric longitudinal expansion of the collision system in the centre-of-mass frame, the values of all odd or even flow coefficients should be either *point-* or *reflection-symmetric* around mid-rapidity. This is checked via point-by-point comparisons between backward and forward rapidities, or via a fit with a polynomial function describing this symmetry. One consequence of the symmetry condition is that all odd flow coefficients v_1, v_3, and v_5 should have a *zero crossing* at mid-rapidity. Therefore, the p_t-differentiated odd flow values are checked to be compatible within errors with $v_1 = 0$ and $v_3 = 0$ at mid-rapidity.

Owing to the reflection symmetry in the transverse plane and the assumption that the angular distribution is symmetrical around the reaction plane *any sine term disappears*. The analyses for all variational runs are also performed for each day of data collection separately to study *time-dependent systematic effects*. Another systematic check is performed by analyzing the data recorded with a *reversed magnetic field setting*. The bending directions of positively and negatively charged particles are switched in this configuration, so that they are measured by different areas in the outer two `MDC` layers, as well as `TOF` and `RPC`. No significant differences are observed between the two settings, as shown in Fig. 146. The p_t dependence of v_2 at mid-rapidity measured by HADES compared with results of other experiments in the same energy region (KaoS [357] and FOPI [352]) is shown in Fig. 147. Within uncertainties and considering the slight differences of beam energies, good agreement with the other data sets is found.

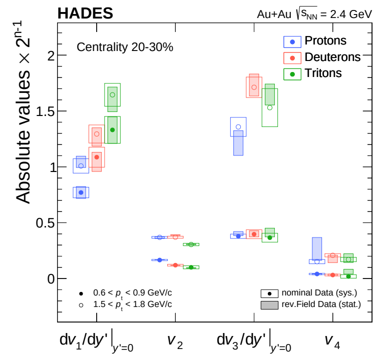

Figure 146: Comparison of the flow coefficients extracted from the total dataset and from data taken with reversed field polarity. Shown are the absolute values $|dv_1/dy'|_{y'=0}|$, $|v_2|$, $|dv_3/dy'|_{y'=0}|$ and $|v_4|$ measured at mid-rapidity for two exemplary p_t intervals and the $10-20$ % centrality class. The data points are scaled for visibility. Only the statistical uncertainties are shown for the data with reversed field polarity and the systematic uncertainties for the nominal values.

Due to the significant extension of the phase space coverage in comparison to previous measurements and due to clearly improved accuracy, several observations can be made. One is that any anisotropy vanishes for $p_t \to 0$, which results in zero values for all flow coefficients. The other is that v_1 shows in general an almost linear and v_2 an approximately quadratic growth with p_t in the region of low transverse momenta, which is supported by analytic considerations [113] and is also observed by other experiments [131, 133, 153, 352, 373]. The same arguments lead to the conclusion that the higher order flow coefficients are proportional to $v_n(p_t) \propto p_t^n$, which is verified here. The next is that a saturation of v_1 and v_2 at large momenta can be observed for the first time in this energy regime. However, for the higher flow coefficients v_3, v_4 and v_5 a saturation behaviour can not be concluded yet from the measured data.

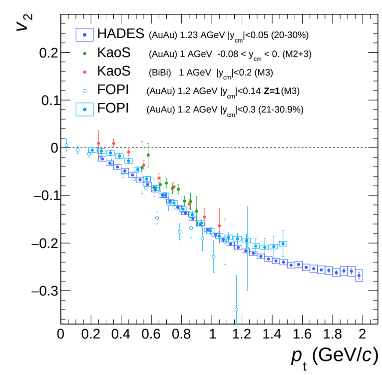

Figure 147: The elliptic flow (v_2) at mid-rapidity of protons in semi-central ($20-30$%) Au+Au collisions at 1.23 AGeV as a function of p_t, in comparison with data in the same energy region and similar centrality selection. Figure form [332].

Considering the large amount of measured data points a phenomenological parametrization allows to organize the data and systematically extract general properties as a function of transverse momentum, rapidity or centrality, and to investigate any mass-ordering between the hydrogen-isotopes. The rapidity- and p_t-dependent parameterization of the odd and even flow coefficients are shown in Fig. 148. The rapidity dependence is well described by a polynomial of the cubic or quadratic form (Eq. 63) or by using trigonometric functions (Eq. 70), and the p_t-dependence with a trigonometric function (Eq. 76) or with Bessel functions (Eq. 75), both motivated by solutions from the *Blast Wave model*. The combination of both trigonometric functions (Eqs. 70 and 76) provides a generalised two-dimensional fit (Eqs. 25) with only four free parameters, which can

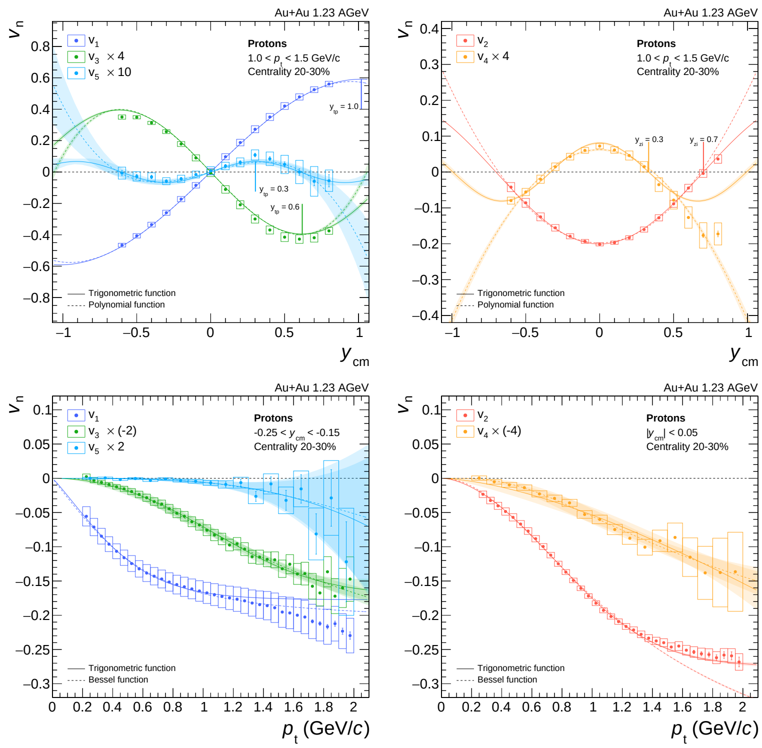

Figure 148: The rapidity (upper) and p_t-dependences (lower) of the odd (left) and even (right panel) flow coefficients are presented for protons in the semi-central $(20-30\%)$ event class. The y_{cm} dependent data, averaged over the p_t interval $1.0 < p_t < 1.5$ GeV/c, is fitted with the trigonometric function in Eq. 70 (solid line) and with the polynomial function in Eq. 63 (dotted line). At forward-rapidities the turning points y_{tp} for the odd harmonics and the zero intercept y_{zi} for the even harmonics are indicated by vertical lines. The p_t dependences of the odd flow coefficients for the rapidity interval $-0.25 < y_{cm} < -0.15$ and of the even flow coefficients v_2 and v_4 at mid-rapidity $|y_{cm}| < 0.05$ are fitted with the trigonometric function in Eq. 76 (solid line) and with the Bessel function in Eq. 75 (dotted line). For visibility the value of the higher order flow coefficients are multiplied by a factor. The coloured bands depict the uncertainties of the individual fits.

be used as a tool to simplify the comparison to model predictions.

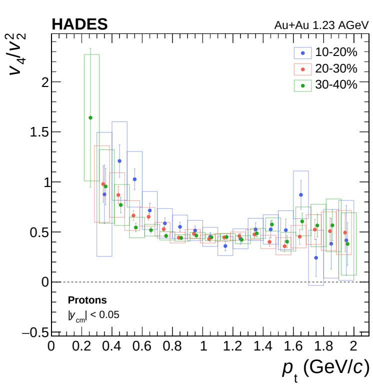

Figure 149: The ratio v_4/v_2^2 as a function of p_t at mid-rapidity $|y_{cm}| < 0.05$ for protons in Au+Au collisions at 1.23 AGeV for three different centralities. Systematic errors are represented by open boxes. See Figure 122.

THE FEATURES of the experimental results can be further investigated with respect to their various scaling properties. The prediction of ideal hydrodynamical simulations [377], confirmed by transport models calculations [338, 383, 384], suggested a scaling between various flow coefficients. It is found that the ratio v_4/v_2^2 for protons and light nuclei (deuterons and tritons) at mid-rapidity approaches values close to 0.5 at high transverse momenta for all centrality classes, as shown for the protons in Figure 149. Similar scaling properties are observed in the ratios $v_3/(v_1 v_2)$ and $v_5/(v_3 v_2)$. Early hydrodynamic calculations [371, 374] investigated anisotropic flow in terms of v_2 and v_4 and their relationship to the initial geometrical anisotropy and the equation-of-state. The conclusion was that both, the hydrodynamic evolution and the geometric configuration [375], can contribute to finite values of v_2 and v_4, and hence a general relation between them should exist. To investigate to what extent the initial geometrical properties of the collision system determine the observed flow pattern, the flow coefficients v_2 and v_4 are scaled with the eccentricities calculated with Glauber MC simulations. In Fig. 150 the values for $\langle \varepsilon_2 \rangle$ and $\langle \varepsilon_4 \rangle$ (left panel), the elliptic flow divided by the second-order eccentricity $v_2/\langle \varepsilon_2 \rangle$ (middle), and the

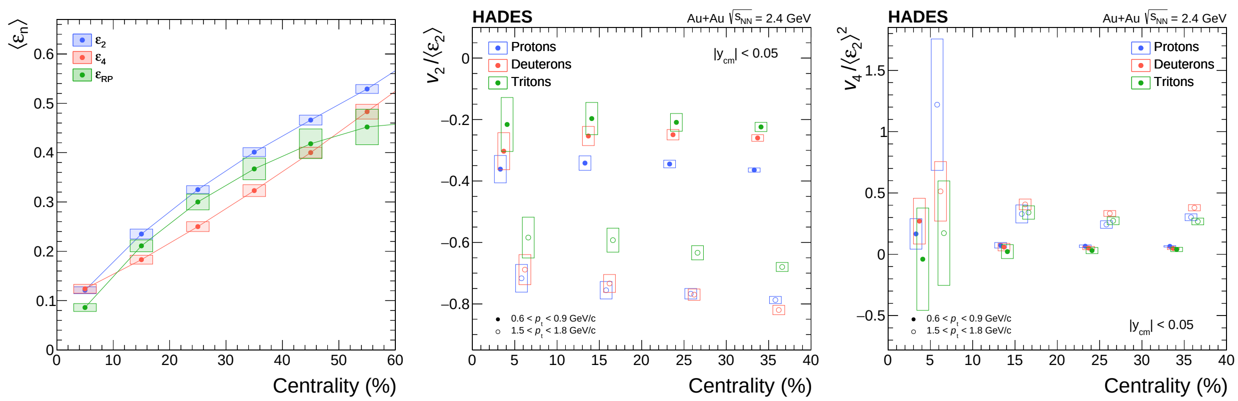

Figure 150: The average participant eccentricities $\langle \varepsilon_2 \rangle$ and $\langle \varepsilon_4 \rangle$ and the reaction plane eccentricity ε_{RP} in the fixed reference frame are shown with their systematic model uncertainties for the different centrality classes, as calculated within the Glauber-MC approach (left). The elliptic v_2 (middle) and quadrangular flow (right) of protons, deuterons, and tritons in two transverse momentum intervals at mid-rapidity in Au+Au collisions at 1.23 *A*GeV for four centrality classes are shown, where the values are divided by the second-order eccentricity $v_2/\langle \varepsilon_2 \rangle$ and square of the second-order eccentricity $v_4/\langle \varepsilon_2 \rangle^2$.

quadrangular flow divided by the square of the second-order eccentricity $v_4/\langle \varepsilon_2 \rangle^2$ (right) are shown for four centrality classes. Remarkably, the scaling results in almost identical values for all centrality classes at high transverse momenta, indicating that the centrality dependence of the elliptic and quadrangular flow of particles emitted at early times is to a large degree already determined by the initial nucleon distribution. It is, however, not immediately clear how the total flow pattern can be related to the initial participant distribution, since the elliptic flow at these beam energies is mainly the result of the so-called squeeze-out effect, caused by the passing spectators.

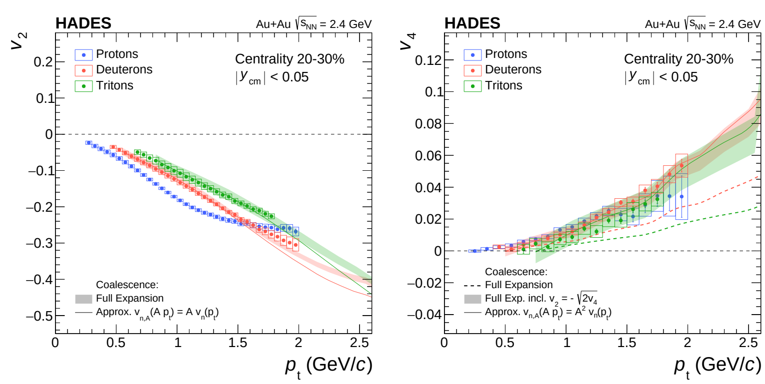

Figure 151: Elliptic flow v_2 (left) and quadrangular flow v_4 (right) of protons, deuterons and tritons in the centrality class $20-30\%$ as a function of p_t at mid-rapidity ($|y_{cm}| < 0.05$). The solid lines represent the proton distribution after scaling according to the approximation $v_{n,A}(A\,p_t) = A\,v_n(p_t)$ in the case of v_2, and to $v_{n,A}(A\,p_t) = A^2\,v_n(p_t)$ in the case of v_4. The coloured bands depict the calculation based on proton spectrum, including its systematic uncertainties, for the nucleon coalescence scenario with higher order terms as given in Eq. (87). In the case of v_4, the additional contribution of v_2 assuming the relation $v_2 = -\sqrt{2\,v_4}$ is included as well. The dashed lines represent the result without the v_2 contribution.

Furthermore, a scaling of the flow coefficients v_2 and v_4 for the three hydrogen isotopes according to their nuclear mass number A is observed and discussed within the picture of nucleon coalescence. The general expressions for $v_{n,A}(Ap_t)$ for nuclei of mass number A including correction terms are given and it is shown that in the case of v_2 they reduce to the simple scaling relation $v_{2,A}(Ap_t) = A\,v_2(p_t)$. An expression for the case of v_4 is also outlined, which includes the additional contribution of v_2, and results in the simple approximation $v_{n,A}(Ap_t) = A^2\,v_n(p_t)$. The v_2 (left) and v_4 (right) values for protons, deuterons and tritons at mid-rapidity ($|y_{cm}| < 0.05$) are shown in Fig. 151 in comparisons with the calculation based on the proton spectrum according the nucleon coalescence scenario, including higher order terms, and in the case of v_4, with the contribution of v_2.

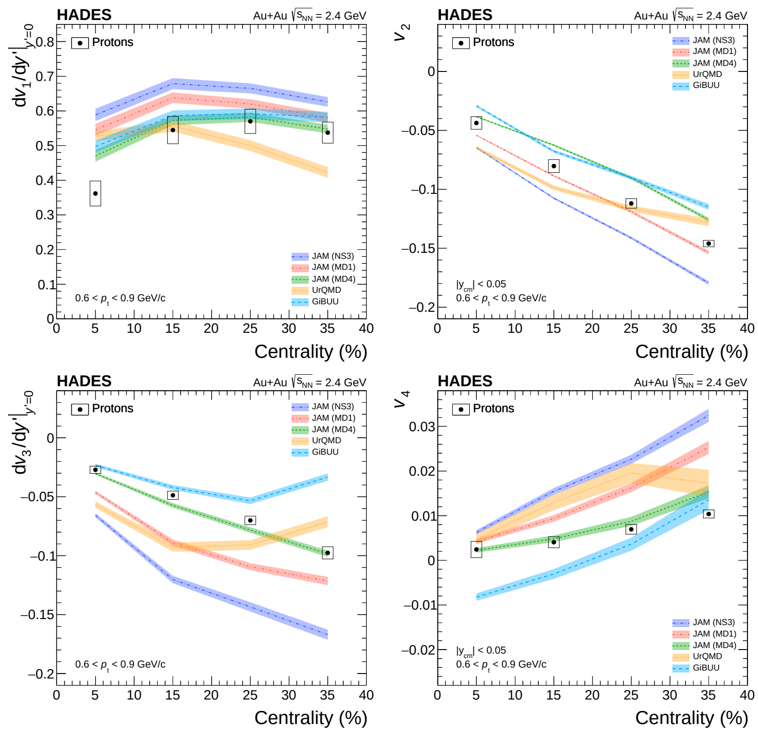

Figure 152: Directed ($dv_1/dy'|_{y'=0}$, upper left panel), elliptic (v_2, upper right panel), triangular ($dv_3/dy'|_{y'=0}$, lower left panel) and quadrangular (v_4, lower right panel) flow of protons in the transverse momentum interval $0.6 < p_t < 0.6$ GeV/c at mid-rapidity in Au+Au collisions at 1.23 AGeV for four centrality classes. The data are compared with several model predictions (see text for details).

State-of-the-art transport model calculations should be able to reproduce all features of the measured flow observables simultaneously, including their centrality, transverse momentum, and rapidity dependence. As a prerequisite for the accurate determination of the nuclear equation of state at large baryon and energy densities, our *a priori knowledge* of elementary particle physics and low-density nuclear experiments should be fully incorporated into the models. To reach consistent conclusions regarding the EOS, it is important to establish that through systematic comparisons with experimental data the various model approaches do not significantly differ in their predictions. As representative examples a selected sample of the measured flow data are compared with the predictions of several transport models using different approaches to formulate the mean-field potentials. The measured values of v_1 to v_4 of protons in the transverse momentum interval $0.6 < p_t < 0.6$ GeV/c at mid-rapidity are shown in Fig. 152 with predictions of `JAM~1.9`, `UrQMD~3.4` and `GiBUU~2019`. The discrepancies between the data and the model calculations highlight the difficulties that arise when extracting the EOS of compressed nuclear matter using this approach.

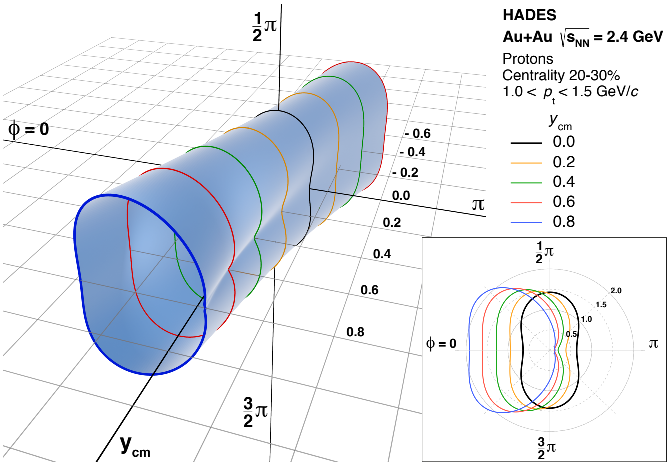

Figure 153: Angular emission pattern of protons with respect to the reaction plane $1/\langle N\rangle\,(dN/d\phi)$ for semi-central $(20-30\%)$ events, integrated over the p_t interval $1.0-1.5$ GeV$/c$. The flow coefficients of the orders $n=1-6$ as listed in Tab. 24 are used. The insert panel shows slices corresponding to different forward rapidities. The figure is published in [337].

THE PRECISE DATA presented here, including higher flow coefficients, allows a three-dimensional characterisation of heavy-ion collisions [337] as shown in Fig. 153. The first suggestion of Fourier decomposition was made in 1979 by Wong [122] as a selection criterion for most central events with perfect azimuthal symmetry, where all Fourier coefficients vanish, and further developed as a general approach to obtain the full event shape by combining the Fourier coefficients [104, 126, 127]. The next goal is to resolve the triple differential invariant cross section, not through Fourier decomposition, but fully corrected by unfolding and deblurring methods [128]. This may enable the extraction of novel information associated with the orientation of the reaction plane, which is generally averaged over the azimuthal angle. This can be the detailed measurement of the coalescence parameter B_A or the apparent temperature and velocity profile of the final particle emission beyond the existing measurements at mid-rapidity [129, 130]. As part of the FAIR Phase-0 physics program at `SIS18`, the HADES collaboration proposed several measurement campaigns, namely pion-induced reactions on CH_2 and C, Ag targets, p+Ag collisions at beam energies of 4.5 GeV, and d+p collisions at 1.0, 1.13, 1.25 and 1.75 AGeV. The measurement of p+p collisions at 4.5 GeV was conducted in 2022, and silver-silver collisions at two beam energies of 1.23 and 1.58 AGeV in 2019. A beam energy scan of Au+Au collisions at lower energies of 0.8, 0.6, 0.4 and 0.2 AGeV is planned, with the aim of extending the multi-differential analyses of various observables with high statistics in the vicinity, where a first-order nuclear liquid-gas phase transition and critical point is expected. The systematic comparison of the flow results, including higher flow coefficients, over different-sized collision systems and their energy dependence, enables the improvement of measurements far beyond previous experiments. The proposed FAIR Phase-0 experiments are acting as a precursor of the future experiments at `SIS100`.

Zusammenfassung

Zusammenfassend ist das Ziel dieser Arbeit die Darstellung der Ergebnisse der multidifferentiellen Messung von kollektiven Flusskoeffizienten in Au+Au-Kollisionen bei $E_{\mathrm{beam}} = 1.23$ AGeV, entsprechend einer

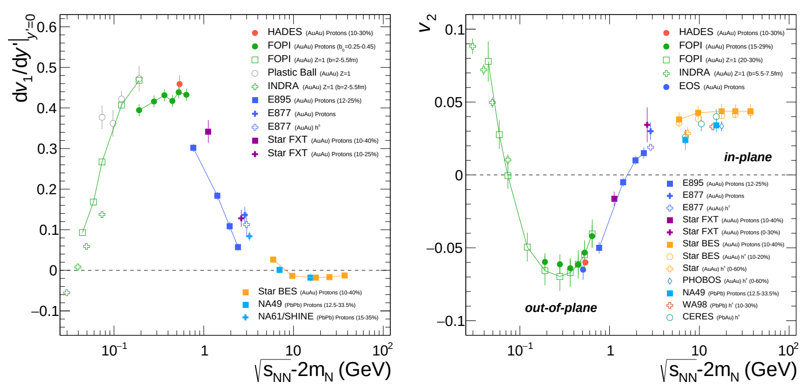

Abbildung 154: Zusammenstellung von gerichteten und elliptischen Flusskoeffizenten als Funktion der abgezogenen Schwerpunktsenergie $\sqrt{s_{\mathrm{NN}}} - 2\,m_N$. Die roten Punkte zeigen die Steigung von v_1, $dv_1/dy'|_{y'=0}$ (linke Abbildung), und v_2 in der Schwerpunkts-Rapidität (rechte Abbildung) für Protonen in Au+Au-Kollisionen bei $\sqrt{s_{\mathrm{NN}}} = 2.4$ GeV ($10-30$ % Zentralität). Diese Ergebnisse werden mit Daten im selben oder ähnlichen Zentralitätsbereich in Au+Au oder Pb+Pb Kollisionen verglichen. Abbildung aus [332].

Nukleon-Nukleon-Schwerpunktenergie von $\sqrt{s_{\mathrm{NN}}} = 2.4$ GeV, durchgeführt mit dem HADES-Experiment am SIS18/GSI. Die Flusskoeffizienten v_n der Ordnungen $n = 1 - 6$ sind für Protonen und leichte Kerne (Deuteronen und Tritonen) bestimmt worden. Vorläufige Werte für die drei ersten Flusskoeffizienten v_1 bis v_3 wurden bereits in [333–336] gezeigt und endgültige Ergebnisse zu den Flusskoeffizienten v_1 bis v_6 in ausgewählten Regionen des Phasenraums im Zentralitätsbereich $20-30$% wurden in [337] veröffentlicht. Der vollständige Satz der experimentellen Ergebnisse wird in [332] beschrieben. Der Vergleich der p_{t}-integrierten Werte $dv_1/dy'|_{y'=0}$ und v_2 an der Schwerpunkts-Rapidität mit zuvor gemessenen experimentellen Daten bei verschiedenen Energien ist in Abb. 154 dargestellt.

Die Eigenschaften der stark wechselwirkenden Materie sind eines der wichtigsten und noch immer offenen Themen in der Kern- und Teilchenphysik. Ihre detaillierte Untersuchung über einen weiten Bereich von Temperaturen und Dichten ist nicht nur wichtig für das Verständnis des nicht-perturbativen Verhaltens der *Quantenchromodyna-*

mik (QCD) bei niedriger Energie. Sie wirkt sich auch unmittelbar auf grundlegende Fragen aus, sowohl auf mikroskopischer als auch auf kosmischer Ebene, z. B. die genaue Formulierung der Zustandsgleichung von dichter Materie, die für unser Verständnis der Merkmale von Supernova-Explosionen mit Kernkollaps, der Struktur und Stabilität von Neutronensternen und des Prozesses ihrer Verschmelzung wesentlich ist. Schwerionenkollisionen ermöglichen die Untersuchung dieser Eigenschaften unter extremen Bedingungen in Laborexperimenten, da sie Materie auf Dichten komprimieren können, die mit dichten stellaren Objekten vergleichbar sind. Der einzigartige Vorteil der im Labor kontrollierten Bedingungen besteht darin, dass je nach Energie des Strahls, der Wahl des Kollisionsystems sowie der unterschiedlichen *Zentralität jeder Kollision* sehr unterschiedliche Bedingungen erforscht werden können. Beim Zusammenstoß zweier Kerne werden die einzelnen Nukleonen abgebremst und ihre longitudinale kinetische Energie wird in Wärme- und Kompressionsenergie umgewandelt. Der Gradient des sich aufbauenden Drucks liefert die Beschleunigungskräfte für die sich schnell ausdehnende Materie, die nur für eine sehr kurze Zeit existiert. Bei perfekt zentralen Kollisionen sollte die Expansion isotrop sein, was zu einem symmetrischen radialen und longitudinalen Fluss führt. Bei peripheren Kollisionen, die durch einen weitgehend ungleichmäßig verteilten Reaktionsbereich gekennzeichnet sind, nehmen die anfängliche deponierte Energie- und Baryonendichte vom zentralen Kern der Reaktion zum äußeren Umfang hin ab und bilden in der Transversalebene eine elliptische Form und in der Längsebene zwei längliche Bänder bis hin zu den verbleibenden Fragmenten, den sogenannten Spektatoren, die ungebremst mit der Ursprungsgeschwindigkeit die Reaktionszone passieren. Wenn die Expansion schneller ist als die Bewegung der Spektatoren, kann die Spektatorenmaterie die Teilchenemission des zentralen Feuerballs in ihre Richtung blockieren. Die Eigenschaften der heißen expandierenden Materie, die Details ihrer geometrischen Quelle, ihre dynamische Wechselwirkung mit der kalten Spektatorenmaterie und die Intensitäten aufgrund der thermischen und kollektiven Bewegung führen zu komplizierten Emissionsmustern und sollten in verschiedenen Flussmomenten kodiert sein. Es ist üblich, die azimutale Anisotropie in der Teilchenemission durch Fourier-Zerlegung zu quantifizieren, was Flusskoeffizienten v_n von mehreren Ordnungen ergibt. Es wird erwartet, dass die Einbeziehung höherer Flusskoeffizienten die Genauigkeit erhöht, die für ein detailliertes theoretisches Verständnis der Strömungsphänomene erforderlich ist.

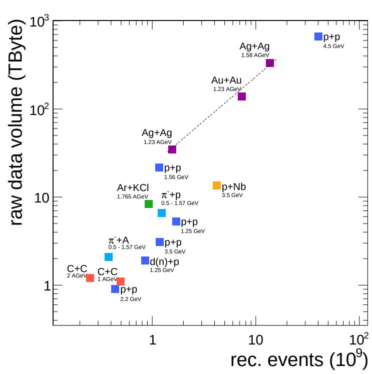

Abbildung 155: Zusammenstellung der Anzahl der aufgezeichneten Ereignisse und deren Gesamtvolumen (TByte) während der HADES-Produktionsstrahlzeiten. Siehe Abb. 16.

ZURZEIT ist das HADES-Experiment das einzige mit der einmaligen Fähigkeit seltene und und durchdringenden Sonden bei niedrigen Energien in Elementar- und Schwerionenreaktionen, sowie deren Kombination mit Protonen- oder Pionen-induzierten Reaktionen zu messen. In der Zusammenstellung in Abb. 155 sind die verschiedenen Experimente mit verschiedenen Kollisionssystemen und Strahlenergien zwischen 0.5 − 4.5 GeV, die vom UNILAC und SIS18 zur Verfügung gestellt wurden, dargestellt. Das Hauptziel des Experiments ist, die Untersuchung des *Emissionsgrades von Resonanzmaterie* [188, 189] mit hoher Akzeptanz und Statistik, die in Schwerionenkollisionen im Energiebereich von 1 − 2 AGeV erzeugt wird, der baryonischen Resonanzen in diesen Reaktionen und der Mechanismen der Strangeness-Produktion. Spezifische Bedingungen für den Detektoraufbau sind durch die präzise Messung der leichten Vektormesonen ρ, ω und ϕ in ihrem seltenen leptonischen Zerfallskanal bestimmt. Die Möglichkeit, eine Vielzahl von Messungen mit demselben Detektor durchzuführen, bietet eine breite und komplementäre Möglichkeit zur Erforschung der Eigenschaften von stark wechselwirkender Materie in elementaren exklusiven Kanälen, in kalter Kernmaterie sowie in ihren dichten und angeregten Zuständen zu untersuchen. In Abb. 156 ist ein Querschnitt durch die Mittelebene eines

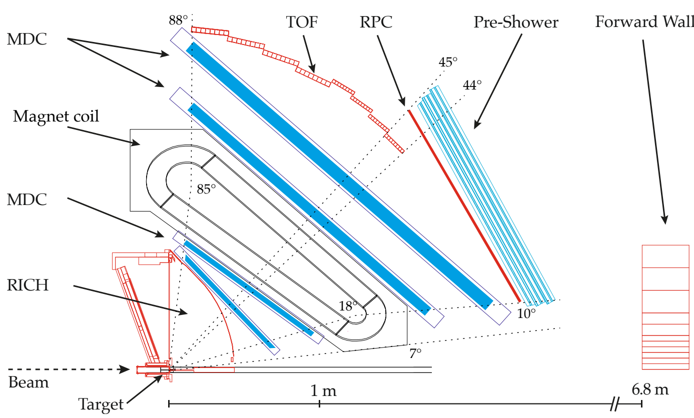

Abbildung 156: Querschnitt durch einen HADES-Sektor. Das segmentierte Target ist vollständig vom RICH-Detektor umgeben. Das Magnetspektrometer besteht aus vier Lagen von Driftkammern (MDC), jeweils zwei vor und hinter dem toroidalen Magnetfeld. Am Ende der Apparatur befinden sich die *Flugzeitwand* TOF und die *Resistive Plate Chambers* RPC, gefolgt von dem elektromagnetischen Pre-Shower-Detektor. Der TOF-Detektor deckt den geometrischen Polarwinkel zwischen 44° und 88° ab, die RPC 10° und 45°, mit einer Überlappung von 1°. Die maximale Akzeptanzabdeckung im Polarwinkel für geladene Teilchen entspricht der Abdeckung des Magnetfeldes zwischen 18° − 85°. Siehe Abb. 18.

Sektors gezeigt. Zwei *Diamantzähler* sind als Strahldetektoren direkt vor (START) und hinter (VETO) dem segmentierten Target angebracht. Das Magnetspektrometer besteht je Sektor aus vier *Mini-Drift Chambers* MDC, wobei sich zwei vor und zwei hinter dem toroidalen Magnetfeld der *supraleitenden Magnetspulen* ILSE befinden. Die Flugbahnen der Teilchen werden aus den Trefferpositionen in den MDCs und den Flugzeitdetektoren TOF und RPC ermittelt. Die Teilchen werden werde mit der Flugzeitmethode in Kombination mit Energieverlustmessungen identifiziert. Für die Elektron-Hadron-Trennung wird der Hadronenblinde Gasdetector RICH, und der PreShower Detektor, der später durch das *Elektromagnetische Kalorimeter* ECAL ersetzt wurde, verwendet. Die *Forward Wall* FW, zur Messung der Ladung und Emissionswinkel der Projektilspektatoren, befindet sich in einem kleinen Vorwärtswinkel zwischen 0,3 − 7° und in einem Abstand von 6,8 m hinter dem Target.

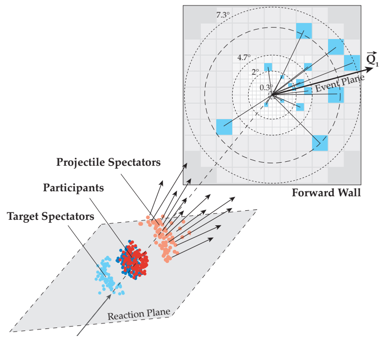

Abbildung 157: Skizze zur Darstellung der Rekonstruktion der Ereignisebene anhand der Treffer der Spektatoren, die in der Forward Wall aufgezeichnet werden. Dargestellt ist die *Reaktionsebene*, die durch die Strahlachse $\vec{z}$ und die Richtung des Stoßparameters $\vec{b}$ definiert ist. Weiter sind die *Participantnukleonen* (dunkelrot und blau), sowie die *Target* (hellblau) und *Projektilspektatoren* (hellrot) dargestellt. Die ungebremsten vorwärtsgerichteten Projektilspektatoren werden in den Zellen (blaue Quadrate) der Forward Wall erfasst und deren Emissionswinkel bestimmt den *Event Flussvektor* $\vec{Q}_1$ und die entsprechende *Event Ebene*.

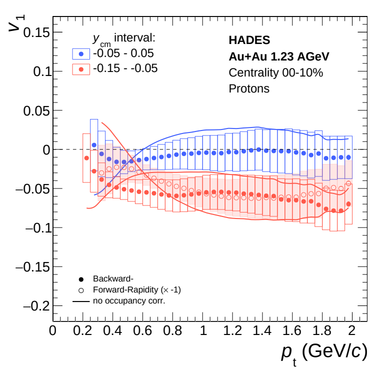

Abbildung 158: Die Ergebnisse für v_1, einschließlich der systematischen Unsicherheiten, sind für Protonen in den Zentralitätsklassen $0-10\%$ dargestellt. Zur Veranschaulichung der Auswirkung der Mehrfachtrefferkorrektur ist die Version ohne diese Korrektur als durchgezogene Linien eingezeichnet.

DIE CHARAKTERISIERUNG der experimentellen Daten beginnt mit der Beschreibung der Strahl- und Target-Eigenschaften, den bei der Datenaufnahme verwendeten Triggerbedingungen und der Abschätzung des getriggerten Anteils des Wirkungsquerschnitts, der zur Bestimmung des Anteils der aufgezeichneten zentralsten Reaktionen benötigt wird. In der Offline-Analyse werden mehrere Ereigniseigenschaften bestimmt und für Auswahlmethoden benutzt: der globale Ereignisvertex, d.h. der Interaktionspunkt zu dem alle emittierten Primärteilchen zurückverfolgt werden, und die Ereigniszeit T_0, die für die genaue Bestimmung der Teilchengeschwindigkeit verwendet wird.

DAS VERFAHREN der Flow Analyse basiert auf der Ereignisebenen-Methode [137, 138, 248] in der die Anisotropien in der azimutalen Verteilung durch die Kosinuskoeffizienten der Fourier-Reihe der n-Ordnung quantifiziert werden:

$$v_n(p_t, y) = \langle \cos(n\phi) \rangle \ , \tag{92}$$

wobei $\langle \cdots \rangle$ den Mittelwert über alle bestimmten Teilchen in einem gegebenen p_t- und y-Intervall und über alle Ereignisse der gleichen Zentralitätsklasse bezeichnet. Der relative azimutale Winkel eines Teilchens wird in Bezug auf die Orientierung der gemessenen Ereignisebene erster Ordnung $\phi = \phi_{lab} - \Psi_{\mathrm{EP},1}$ angegeben. Wie in Abb. 157 gezeigt, wird aus den Emissionswinkeln ϕ_i von Treffern im FW-Detektor der *Ereignisflussvektor* $\vec{Q}_1$ mit dem entsprechenden Winkel der Ereignisebene $\Psi_{\mathrm{EP},1}$ bestimmt. Aufgrund von Fluktuationen und endlicher Multiplizitäten weist die geschätzte *Ereignisebene* eine Dispersion auf und muss anhand der *Auflösung der Ereignisebene* korrigiert werden. Um aussagekräftige Vergleiche zwischen experimentellen Beobachtungen und Vorhersagen theoretischer Modelle zu ermöglichen, sollte die Klassifizierung von Ereignissen gut definiert sein und innerhalb ausreichend enger Intervalle des Stoßparameters liegen. Ein Teil dieser Arbeit umfasste die Implementierung des Verfahrens zur Bestimmung der Zentralität der Reaktion und der Ausrichtung der Ereignisebene und ihrer Auflösung.

DIE BESTIMMUNG von systematischen Fehlern in der Flussmessung ist ein wesentliche Teil dieser Arbeit. Mehrere Quellen von Unsicherheiten sind ermittelt worden, die sich hauptsächlich aus den Qualitätsauswahlkriterien für die analysierten Spuren, dem Korrekturverfahren für Rekonstruktionsineffizienzen, den Verfahren zur Teilchenidentifikation und den Auswirkungen einer uneinheitlichen azimutalen Detektorakzeptanz ergeben. Die systematischen Punkt-zu-Punkt-Unsicherheiten werden für jeden Teilchentyp (Proton, Deuteron und Triton), Ordnung der Flusskoeffizienten v_n und Zentralitätsklasse getrennt bestimmt. Sie werden durch unabhängige Analysen von allen verschiedenen Variationen und anschließende Auswertung der Gesamtverteilungen der resultierenden Werte der Koeffizienten ermittelt. Es musste ein spezielles Korrekturverfahren für die Messung der Flusskoeffizienten entwickelt werden, um die durch die Mehrfachtreffer von Detektorteilsystemen bedingten Ineffizienzen zu korrigieren. Die Auswirkung ist in Abb. 158 anhand der v_1 Werte für Protonen dargestellt.

Die Validierung der Ergebnisse im Bereich ihrer abgeschätzten systematischen Unsicherheiten erfolgt durch mehrere Konsistenzprüfungen. Aufgrund der symmetrischen longitudinalen Ausdehnung des Kollisionssystems im Schwerpunktssystem sollten die Werte aller ungeraden oder geraden Strömungskoeffizienten um die Schwerpunktsrapidität entweder *punkt-* oder *reflexionssymmetrisch* sein. Dies wird durch Punkt-für-Punkt-Vergleiche zwischen Rückwärts- und Vorwärtsrapiditäten oder durch eine Anpassung mit einer Polynomfunktion, die diese Symmetrie beschreibt, überprüft. Eine Folge der Symmetriebedingung ist, dass alle ungeraden Flusskoeffizienten v_1, v_3 und v_5 bei der Schwerpunktsrapidität einen *Nulldurchgang* haben müssen. Daher wird überprüft, ob die p_t-differenzierten ungeraden Flusswerte innerhalb der Unsicherheiten mit $v_1 = 0$ und $v_3 = 0$ bei der Schwerpunktsrapidität kompatibel sind. Aufgrund der Reflexionssymmetrie in der Transversalebene und der Annahme, dass die Winkelverteilung symmetrisch um die Reaktionsebene ist, *verschwinden alle Sinusterme*. Die Analysen aller Variationen erfolgen auch für jeden Tag der Datenerfassung um *zeitabhängige systematische Effekte* zu untersuchen. Eine weitere systematische Prüfung erfolgt durch Analyse der Daten, die mit dem *entgegengesetzten Magnetfeld* aufgezeichnet wurden. Die Ablenkungsrichtungen von positiv und negativ geladenen Teilchen werden in dieser Konfiguration vertauscht, so dass sie von verschiedenen Bereichen in den beiden äußeren `MDC`-Ebenen, sowie `TOF` und `RPC`, gemessen werden. Wie in Abb. 159 zu sehen ist gibt es keine signifikanten Unterschiede zwischen den beiden Einstellungen. Die von HADES gemessene p_t-Abhängigkeit von v_2 bei mittlerer Geschwindigkeit im Vergleich zu Ergebnissen anderer Experimente im gleichen Energiebereich (KaoS [357] und FOPI [352]) ist in Abb. 160 dargestellt. Innerhalb der Unsicherheiten und unter Berücksichtigung der leichten Unterschiede bei den Strahlenergien wird eine gute Übereinstimmung mit den anderen Datensätzen festgestellt.

In Anbetracht der großen Menge an gemessenen Datenpunkten ermöglicht eine phänomenologische Parametrisierung die Organisation der Daten und die systematische Auswertung allgemeiner Eigenschaften als Funktion des transversalen Impulses, der Rapidität oder der Zentralität, sowie einer Massenordnung der Wasserstoffisotopen. Die rapiditäts- und p_t-abhängige Parametrisierung der ungeraden und gera-

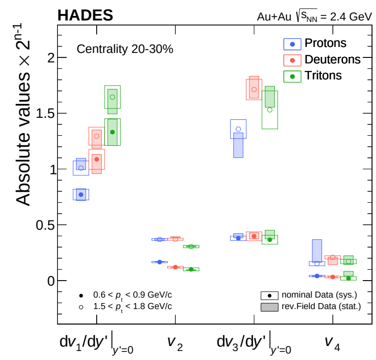

Abbildung 159: Vergleich der Flusskoeffizienten berechnet aus dem gesamten Datensatz und aus Daten, die mit umgekehrter Feldpolarität aufgenommen wurden. Dargestellt sind die absoluten Werte $|dv_1/dy'|_{y'=0}|$, $|v_2|$, $|dv_3/dy'|_{y'=0}|$ und $|v_4|$ gemessen bei der Schwerpunktsrapidität für zwei p_t Intervalle und der $10-20\%$ Zentralitätsklasse. Die Datenpunkte sind zur besseren Sichtbarkeit skaliert. Für die Daten mit umgekehrter Feldpolarität sind nur die statistischen Unsicherheiten und für die Nominalwerte auch die systematischen Unsicherheiten angegeben.

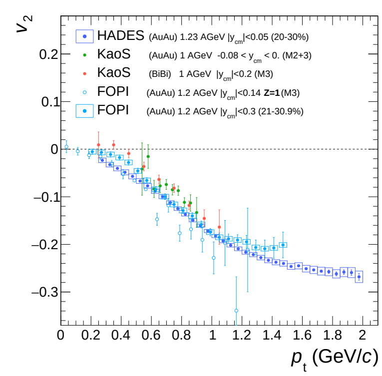

Abbildung 160: Der elliptische Fluss (v_2) bei der Schwerpunktsrapidität von Protonen in semizentralen $(20-30\%)$ Au+Au-Kollisionen bei 1,23 AGeV als Funktion von p_t, im Vergleich mit Daten im gleichen Energiebereich und ähnlicher Zentralitätsauswahl. Abbildung von [332].

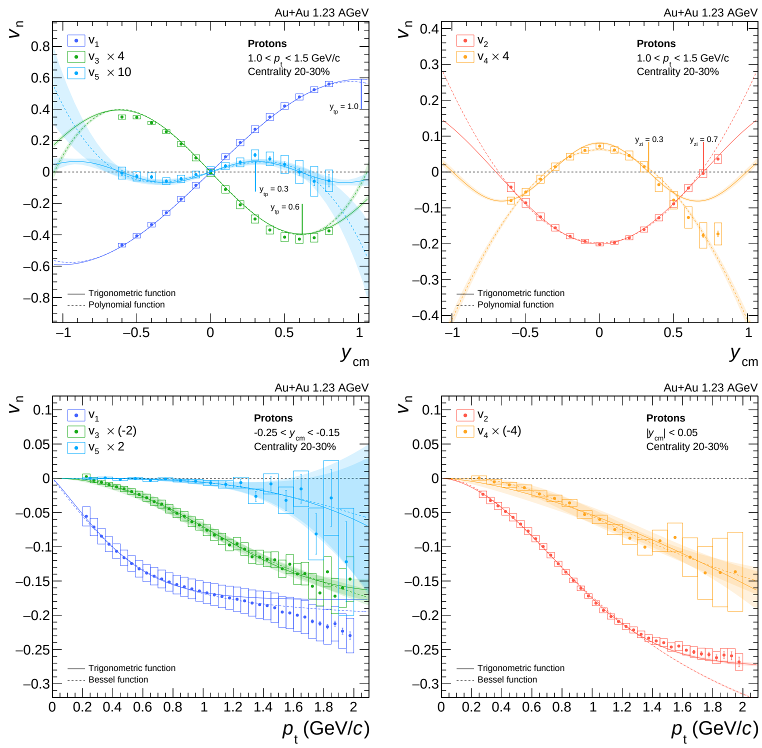

Abbildung 161: Die Rapiditäts- (obere) und p_t-Abhängigkeiten (untere) der ungeraden (linke) und geraden (rechte Bildtafel) Flusskoeffizienten sind für Protonen in der semizentralen ($20-30\%$) Ereignisklasse dargestellt. Die y_{cm}-abhängigen Daten, gemittelt über das p_t-Intervall $1.0 < p_t < 1.5$ GeV/c, werden mit den trigonometrischen Funktionen in Gl. 70 (durchgezogene Linie) und den Polynomfunktionen in Gl. 63 (gepunktete Linie) angepasst. Bei Vorwärtsrapiditäten sind die Wendepunkte y_{tp} für die ungeraden Koeffizienten und der Nulldurchgang y_{zi} für die geraden Koeffizienten durch vertikale Linien gekennzeichnet. Die p_t-Abhängigkeiten der ungeraden Koeffizienten für das Rapiditätsintervall $-0.25 < y_{cm} < -0.15$ und der geraden Koeffizienten v_2 und v_4 bei der Schwerpunktsrapidität $|y_{cm}| < 0.05$ wird mit der trigonometrischen Funktion in Gl. 76 (durchgezogene Linie) und der Bessel-Funktion in Gl. 75 (gepunktete Linie) angepasst. Für die Sichtbarkeit werden die Werte der Flusskoeffizienten höherer Ordnung mit einem Faktor multipliziert. Die farbigen Bänder zeigen die Unsicherheiten der einzelnen Anpassungen.

den Flusskoeffizienten ist in Abb. 161 dargestellt. Die Rapiditätsabhängigkeit wird gut durch ein Polynom der kubischen oder quadratischen Form (Gl. 63) oder durch die Verwendung trigonometrischer Funktionen (Gl. 70), und die p_t-Abhängigkeit mit einer trigonometrischen Funktion (Gl. 76) oder mit Bessel-Funktionen (Gl. 75), beide motiviert durch Lösungen aus dem *Blast Wave model*, beschrieben. Die Kombination der beiden trigonometrischen Funktionen (Gls. 70 und 76) liefert eine verallgemeinerte zweidimensionale Anpassung (Gls. 25) mit nur vier freien Parametern, die als Hilfsmittel zur Vereinfachung von Vergleichen mit Modellvorhersagen verwendet werden kann.

AUFGRUND der im Vergleich zu früheren Messungen deutlich erweiterten Phasenraumabdeckung bei deutlich verbesserter Genauigkeit können mehrere Beobachtungen in den Messdaten gemacht werden. Eine davon ist, dass jegliche Anisotropie für $p_t \to 0$ verschwindet und dass v_1 allgemein ein fast lineares und v_2 ein annähernd quadratisches Wachstum im Bereich niedriger Transversalimpulse zeigt, was durch analytische Überlegungen [113] und auch durch andere Experimente bestätigt wurde [131, 133, 153, 352, 373]. Die gleichen Argumente führen zu der Schlussfolgerung, dass die Flusskoeffizienten höherer Ordnung proportional zu $v_n(p_t) \propto p_t^n$ sind, was hier auch bestätigt wird. Als Nächstes kann zum ersten Mal in diesem Energiebereich eine

Saturation der Werte von v_1 und v_2 bei großen Impulsen beobachtet werden. Ein Saturationsverhalten für die höheren Flusskoeffizienten v_3, v_4 und v_5 kann aus den Messdaten jedoch nicht eindeutig abgeleitet werden.

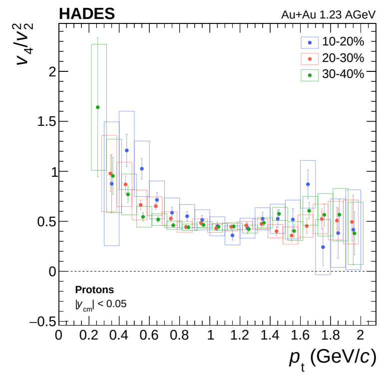

Abbildung 162: Das Verhältnis v_4/v_2^2 als Funktion von p_t bei der Schwerpunktsrapidität $|y_{cm}| < 0{,}05$ für Protonen in Au+Au-Kollisionen bei 1,23 AGeV für drei verschiedene Zentralitäten. Systematische Fehler sind durch offene Kästen dargestellt. Siehe Abbildung 122.

Die Merkmale der experimentellen Ergebnisse können mit Hilfe ihrer unterschiedlichen Skalierungseigenschaften untersucht werden. Die Vorhersage von idealen hydrodynamischen Simulationen [377], bestätigt durch Berechnungen von Transport Modellen [338, 383, 384], deuten auf ein Skalierverhalten zwischen verschiedenen Flusskoeffizienten an. Es konnte festgestellt werden, dass das Verhältnis v_4/v_2^2 für Protonen und leichte Kerne (Deuteronen und Tritonen) bei der Schwerpunktsrapidität bei hohen Transversalimpulsen für alle Zentralitätsklassen Werte nahe 0.5 erreicht, wie für die Protonen in Abbildung 149 gezeigt wird. Ähnliche Skalierungseigenschaften zeigen sich bei den Verhältnissen $v_3/(v_1 v_2)$ und $v_5/(v_3 v_2)$. Frühe hydrodynamische Berechnungen [371, 374] untersuchten die Flussanisotropie in Bezug auf v_2 und v_4 und ihre Beziehung zur anfänglichen geometrischen Anisotropie und der Zustandsgleichung. Die Schlussfolgerung war, dass sowohl die hydrodynamische Entwicklung, als auch die geometrische Konfiguration zu bestimmten Werten von v_2 und v_4 beitragen kann [375] und daher eine allgemeine Beziehung zwischen ihnen bestehen sollte. Um zu untersuchen, inwieweit die anfänglichen geometrischen Eigenschaften des Kollisionssystems das beobachtete Flussmuster bestimmen, werden die Flusskoeffizienten v_2 und v_4 mit den aus Glauber-MC-Simulationen berechneten Exzentrizitäten skaliert. In Abb. 150 sind die Werte für $\langle \varepsilon_2 \rangle$ und $\langle \varepsilon_4 \rangle$ (linkes Bild), der elliptische Fluss geteilt durch die Exzentrizität zweiter Ordnung $v_2/\langle \varepsilon_2 \rangle$ (mitte) und der quadratische Fluss geteilt durch das Quadrat der Exzentrizität zweiter Ordnung $v_4/\langle \varepsilon_2 \rangle^2$ (rechts) für vier Zentralitätsklassen dargestellt. Bemerkenswerterweise ergibt die Skalierung bei hohen Transversalimpulsen fast identische Werte

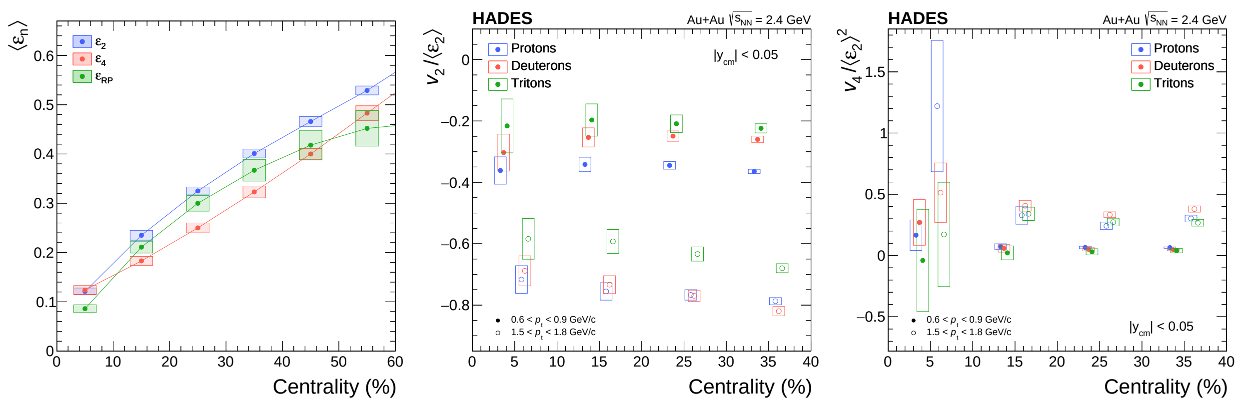

Abbildung 163: Die gemittelten Participant-Exzentrizitäten $\langle \varepsilon_2 \rangle$ und $\langle \varepsilon_4 \rangle$, sowie die Reaktionsebenen-Exzentrizität ε_{RP} aus Glauber-MC Berechnungen, sind mit ihren systematischen Modellunsicherheiten für verschiedene Zentralitätsklassen dargestellt (links). Die elliptische v_2 (Mitte) und quadratische Fluss v_4 (rechts) von Protonen, Deuteronen und Tritonen in zwei Transversalimpulsintervallen bei der Schwerpunktsrapidität in Au+Au-Kollisionen bei 1,23 AGeV für vier Zentralitätsklassen ist gezeigt, wobei die Werte durch die Exzentrizität zweiter Ordnung $v_2/\langle \varepsilon_2 \rangle$ und das Quadrat der Exzentrizität zweiter Ordnung $v_4/\langle \varepsilon_2 \rangle^2$ geteilt sind.

für alle Zentralitätsklassen, was darauf hindeutet, dass die Zentralitätsabhängigkeit des elliptischen und quadratischen Flusses von Teilchen, die zu frühen Zeiten emittiert werden, bereits zu einem großen Teil durch die anfängliche Nukleonenverteilung bestimmt wird. Es ist nicht sofort klar, wie das Flussmuster direkt mit der anfänglichen Participant-Verteilung in Verbindung gebracht werden kann, da der elliptische Fluss bei diesen Strahlenergien hauptsächlich das Ergebnis des so genannten Squeeze-out-Effekts ist, der durch die vorbeiziehenden Spektatoren verursacht wird.

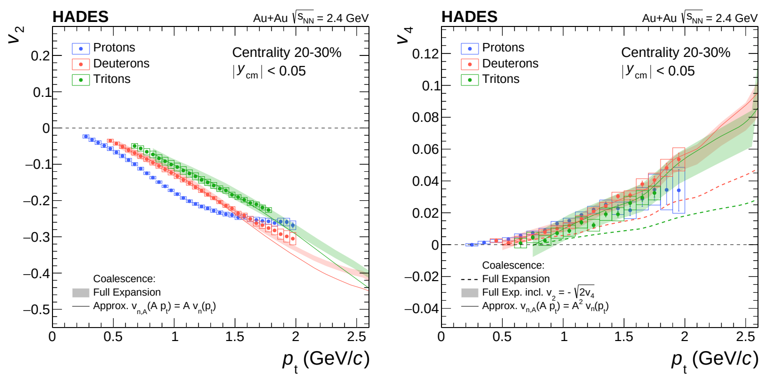

Abbildung 164: Der elliptische Fluss v_2 (links) und der quadratische Fluss v_4 (rechts) von Protonen, Deuteronen und Tritonen in den Zentralitätsklassen $20-30\%$ als Funktion von p_t bei Schwerpunktsrapidität ($|y_{cm}| < 0,05$). Die durchgezogenen Linien stellen die Protonenverteilung dar nach Skalierung gemäß der Näherung $v_{n,A}(A\,p_t) = A\,v_n(p_t)$ im Fall von v_2 und entsprechend $v_{n,A}(A\,p_t) = A^2\,v_n(p_t)$ im Fall von v_4. Die farbigen Bänder zeigen die aus dem Protonenspektrum berechneten Ergebnisse, einschließlich der systematischen Unsicherheiten, für das Szenario der Nukleonenkoaleszenz, wie in Gl. 87 angegeben. Im Fall von v_4 ist der zusätzliche Beitrag von v_2 unter Annahme der Beziehung $v_2 = -\sqrt{2\,v_4}$ berücksichtigt. Die gestrichelten Linien stellen das Ergebnis ohne den zusätzlichen Beitrag von v_2 dar.

Weiterhin wird eine Skalierung der Flusskoeffizienten v_2 und v_4 für die drei Wasserstoffisotope in Abhängigkeit von ihrer Kernmassenzahl A beobachtet und im Rahmen des Konzepts der Nukleon Koaleszenz diskutiert. Die allgemeinen Formulierungen für $v_{n,A}(Ap_t)$ für Kerne der Massenzahl A einschließlich der Korrekturterme werden angegeben und es wird gezeigt, dass sie sich im Fall von v_2 auf die einfache Skalierungsrelation $v_{2,A}(Ap_t) = A\,v_2(p_t)$ reduzieren. Es wird auch ein Verfahren für den Fall von v_4 skizziert, das den zusätzlichen Beitrag von v_2 einbezieht und zu der einfachen Näherung $v_{n,A}(Ap_t) = A^2\,v_n(p_t)$ gelangt. Die Werte für v_2 (links) und v_4 (rechts) von Protonen, Deuteronen und Tritonen bei der Schwerpunktsrapidität ($|y_{cm}| < 0.05$) sind in Abb. 164 im Vergleich zu den berechneten Ergebnissen aus dem Protonenspektrum gemäß dem Szenario der Nukleonenkoaleszenz dargestellt, im Fall von v_4 mit dem zusätzlichen Beitrag von v_2.

Transportmodellrechnungen sollten in der Lage sein alle Merkmale der gemessenen Fluss-Observablen gleichzeitig zu reproduzieren, einschließlich ihrer Abhängigkeit von der Zentralität, dem transversalen Impulses und ihrer Rapidität. Als Voraussetzung für die genaue Bestimmung der nuklearen Zustandsgleichung bei großen Baryon- und Energiedichten sollte unser *apriorisches Wissen* der Elementarteilchen- und der Nuklearphysik vollständig in die Modelle einfließen. Für konsistente Schlussfolgerungen bezüglich der Zustandsgleichung ist es

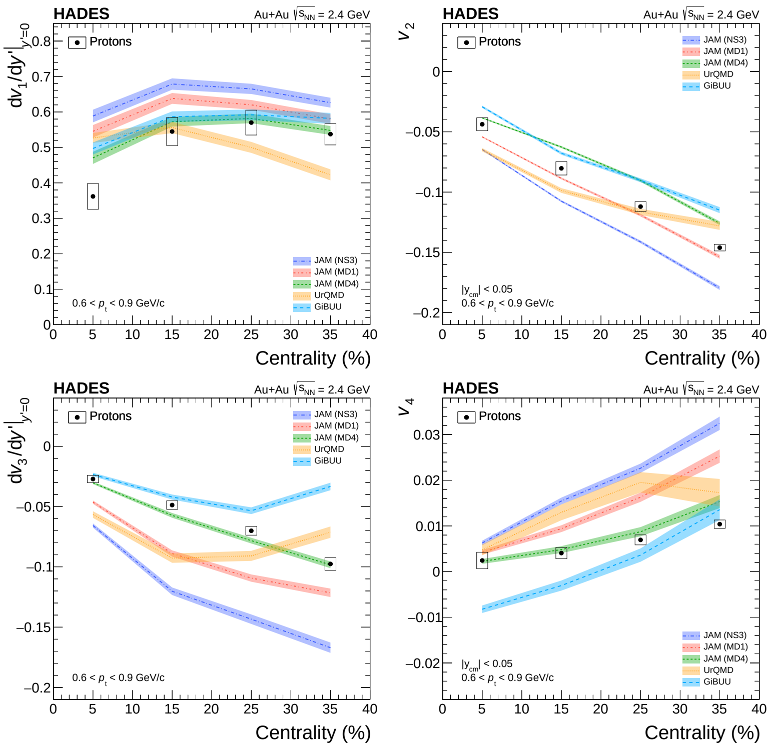

Abbildung 165: Gerichteter ($dv_1/dy'|_{y'=0}$, oberes linkes Bild), elliptischer (v_2, oberes rechtes Bild), triangulärer ($dv_3/dy'|_{y'=0}$, unteres linkes Bild) und quadratischer (v_4, unteres rechtes Bild) Fluss von Protonen in dem Transversalimpulsintervall $0.6 < p_t < 0.6$ GeV$/c$ an der Schwerpunkts-Rapidität in Au+Au-Kollisionen bei 1.23 *A*GeV für vier Zentralitätsklassen. Die Daten werden mit verschiedenen Modellvorhersagen verglichen (siehe Text für Details).

wichtig, durch systematische Vergleiche mit experimentellen Daten festzustellen, dass sich die verschiedenen Modellansätze in ihren Vorhersagen nicht wesentlich unterscheiden. Als repräsentative Beispiele wird ein ausgewählter Satz von gemessenen Flussdaten mit den Vorhersagen mehrerer Transportmodelle mit unterschiedlichen Ansätzen zur Formulierung der *Mean Field* Potentiale verglichen. Die gemessenen Werte von v_1 bis v_4 von Protonen im Transversalimpulsintervall $0.6 < p_t < 0.6$ GeV$/c$ bei der Schwerpunktsrapidität sind in Abb. 152 mit Vorhersagen von JAM 1.9, UrQMD 3.4 und GiBUU 2019 dargestellt. Die Diskrepanzen zwischen den Daten und den Modellrechnungen verdeutlichen die Schwierigkeiten, die bei der Extraktion der Zustandsgleichung von komprimierter Kernmaterie mit diesem Ansatz auftreten.

Die vorgestellten präzisen Daten, einschließlich höherer Flusskoeffizienten, erlauben eine dreidimensionale Charakterisierung von Schwerionenkollisionen, wie in Abb. 153 gezeigt. Der erste Vorschlag zur Fourier-Zerlegung wurde 1979 von Wong [122] als Auswahlkriterium für die zentralsten Ereignisse mit perfekter azimutaler Symmetrie gemacht, bei denen alle Fourier-Koeffizienten verschwinden, und es wurde ein allgemeiner Ansatz entwickelt, um die vollständige Ereignisform durch Kombination der Fourier-Koeffizienten zu erhalten [104, 126, 127]. Das nächste Ziel ist es, den dreifach-differentiellen inva-

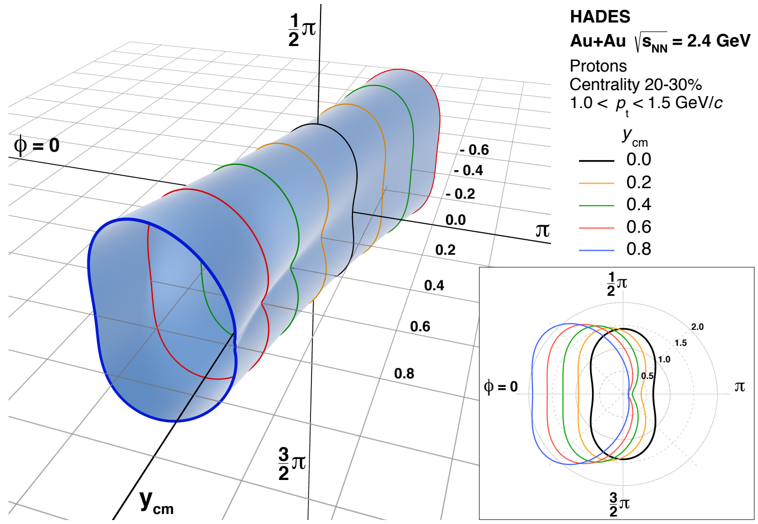

Abbildung 166: Winkelverteilung der Protonenemission in Bezug auf die Reaktionsebene $1/\langle N\rangle\,(dN/d\phi)$ für semizentrale $(20-30\%)$ Ereignisse, integriert über das p_t-Intervall $1{,}0-1{,}5$ GeV$/c$. Die Flusskoeffizienten der Ordnungen $n=1-6$ werden verwendet. Die eingefügte Abbildung zeigt Schnitte die verschiedenen Vorwärtsrapiditäten entsprechen. Die Abbildung ist veröffentlicht in [337].

rianten Wirkungsquerschnitt zu bestimmen, und zwar nicht durch Fourier-Zerlegung, sondern vollständig korrigiert durch Entfaltungs- und *Deblurring* [128]. Dies kann die Ermittlung neuer Merkmale im Zusammenhang mit der Ausrichtung der Reaktionsebene ermöglichen, die im Allgemeinen über den Azimutwinkel ausgemittelt werden. Dabei kann es sich um die detaillierte Messung des Koaleszensparameters B_A oder um das Temperatur- und Geschwindigkeitsprofil der finalen Teilchenemission handeln, die über die bestehenden Messungen an der Schwerpunkts-Rapidität hinausgehen [129, 130].

Als Teil des FAIR-Phase-0 Physikprogramms am `SIS18` plant die HADES-Kollaboration mehrere Messkampagnen: pion-induzierte Reaktionen an CH_2- und C, Ag-Targets, p+Ag-Kollisionen bei Strahlenergien von 4.5 GeV und d+p-Kollisionen bei 1.0, 1.13, 1.25 und 1.75 *A*GeV. Die Messung von p+p-Kollisionen bei 4.5 GeV wurde im Jahr 2022 durchgeführt, und die von Silber-Silber-Kollisionen bei zwei Strahlenergien von 1.23 und 1.58 AGeV im Jahr 2019. Ein Beam Energy Scan von Au+Au-Kollisionen bei niedrigeren Energien von 0.8, 0.6, 0.4 und 0.2 *A*GeV ist geplant, um die multidifferenziellen Analysen verschiedener Observablen mit hoher Statistik in der Nähe, wo ein nuklearer Flüssig-Gas-Phasenübergang erster Ordnung und ein kritischer Punkt erwartet wird, zu erweitern. Der systematische Vergleich der Flussergebnisse, einschließlich höherer Flusskoeffizienten, über unterschiedlich große Kollisionssysteme und deren Energieabhängigkeit, ermöglicht eine Verbesserung der Messungen weit über bisherige Experimente hinaus. Die vorgeschlagenen FAIR-Phase-0 Experimente dienen als Vorläufer für die zukünftigen Experimente am `SIS100`.

Bibliography

[1] Frank Wilczek. “Prelude to Compressed Baryonic Matter”. In: *Lect. Notes Phys.* 814 (2011), pp. 1–10. DOI: 10.1007/978-3-642-13293-3_1. arXiv: 1001.2729 [hep-ph] (page 15).

[2] Bengt Friman et al., eds. *The CBM physics book: Compressed baryonic matter in laboratory experiments*. Vol. 814. 2011. DOI: 10.1007/978-3-642-13293-3 (page 15).

[3] “The NuPECC Long Range Plan 2017: Perspectives in Nuclear Physics”. In: (2017). URL: https://www.nupecc.org/pub/lrp17/lrp2017.pdf (page 15).

[4] Wit Busza, Krishna Rajagopal, and Wilke van der Schee. “Heavy Ion Collisions: The Big Picture, and the Big Questions”. In: *Ann. Rev. Nucl. Part. Sci.* 68 (2018), pp. 339–376. DOI: 10.1146/annurev-nucl-101917-020852. arXiv: 1802.04801 [hep-ph] (page 15).

[5] Slavko Bogdanov et al. “Snowmass 2021 Cosmic Frontier White Paper: The Dense Matter Equation of State and QCD Phase Transitions”. In: *2022 Snowmass Summer Study*. Sept. 2022. arXiv: 2209.07412 [astro-ph.HE] (page 15).

[6] Burkhard Kampfer. “Cosmic phase transitions”. In: *Annalen Phys.* 9 (2000), pp. 605–635. DOI: 10.1002/1521-3889(200009)9:8<605::AID-ANDP605>3.0.CO;2-6. arXiv: astro-ph/0004403 (page 16).

[7] M. Oertel et al. “Equations of state for supernovae and compact stars”. In: *Rev. Mod. Phys.* 89.1 (2017), p. 015007. DOI: 10.1103/RevModPhys.89.015007. arXiv: 1610.03361 [astro-ph.HE] (page 16).

[8] Luciano Rezzolla et al., eds. *The Physics and Astrophysics of Neutron Stars*. Vol. 457. Springer, 2018. DOI: 10.1007/978-3-319-97616-7 (page 16).

[9] Jürgen Schaffner-Bielich. *Compact Star Physics*. Cambridge University Press, Aug. 2020. ISBN: 978-1-316-84835-7, 978-1-107-18089-5. DOI: 10.1017/9781316848357 (page 16).

[10] P. W. Anderson. “More Is Different”. In: *Science* 177.4047 (1972), pp. 393–396. DOI: 10.1126/science.177.4047.393 (page 16).

[11] Steven Weinberg. *The First Three Minutes. A Modern View of the Origin of the Universe*. 1977. ISBN: 978-0-465-02437-7 (page 16).

[12] Sergio Chibbaro, Lamberto Rondoni, and Angelo Vulpiani. “Reductionism, emergence and levels of reality”. In: *Springer, Berlin. by ETH* 3.20 (2014), p. 17 (page 16).

[13] Sophia Kivelson and Steven A. Kivelson. “Defining emergence in physics”. In: *npj Quantum Materials* 1 (2016), pp. 2397–4648. DOI: 10.1038/npjquantmats.2016.24 (page 16).

[14] B. Russell. *History of Western Philosophy*. Routledge classics. Routledge, 2004. ISBN: 9780415325059. URL: http://books.google.de/books?id=Ey94E3sOMA0C (page 16).

[15] Frank Wilczek. "Origins of Mass". In: *Central Eur. J. Phys.* 10 (2012), pp. 1021–1037. DOI: 10.2478/s11534-012-0121-0. arXiv: 1206.7114 [hep-ph] (page 16).

[16] Andrew R. Liddle. *An introduction to modern cosmology*. 1998 (page 16).

[17] Max Tegmark et al. "Dimensionless constants, cosmology and other dark matters". In: *Phys. Rev. D* 73 (2006), p. 023505. DOI: 10.1103/PhysRevD.73.023505. arXiv: astro-ph/0511774 (pages 16, 18).

[18] Herwig Schopper, ed. *Particle Physics Reference Library: Volume 1: Theory and Experiments*. Cham: Springer Nature, 2020. ISBN: 978-3-030-38206-3, 978-3-030-38207-0. DOI: 10.1007/978-3-030-38207-0 (page 17).

[19] Murray Gell-Mann. "The Eightfold Way: A Theory of strong interaction symmetry". In: (Mar. 1961). DOI: 10.2172/4008239 (page 17).

[20] Yuval Ne'eman. "Derivation of strong interactions from a gauge invariance". In: *Nucl. Phys.* 26 (1961). Ed. by R. Ruffini and Y. Verbin, pp. 222–229. DOI: 10.1016/0029-5582(61)90134-1 (page 17).

[21] Murray Gell-Mann. "A Schematic Model of Baryons and Mesons". In: *Phys. Lett.* 8 (1964), pp. 214–215. DOI: 10.1016/S0031-9163(64)92001-3 (page 17).

[22] E. D. Bloom et al. "High-Energy Inelastic $e - p$ Scattering at 6° and 10°". In: *Phys. Rev. Lett.* 23 (16 Oct. 1969), pp. 930–934. DOI: 10.1103/PhysRevLett.23.930 (page 17).

[23] M. Breidenbach et al. "Observed Behavior of Highly Inelastic Electron-Proton Scattering". In: *Phys. Rev. Lett.* 23 (16 Oct. 1969), pp. 935–939. DOI: 10.1103/PhysRevLett.23.935 (page 17).

[24] R. L. Workman et al. "Review of Particle Physics". In: *PTEP* 2022 (2022), p. 083C01. DOI: 10.1093/ptep/ptac097 (page 17).

[25] David J. Gross and Frank Wilczek. "Ultraviolet Behavior of Non-Abelian Gauge Theories". In: *Phys. Rev. Lett.* 30 (26 June 1973), pp. 1343–1346. DOI: 10.1103/PhysRevLett.30.1343 (page 17).

[26] H. David Politzer. "Reliable Perturbative Results for Strong Interactions?" In: *Phys. Rev. Lett.* 30 (26 June 1973), pp. 1346–1349. DOI: 10.1103/PhysRevLett.30.1346 (page 17).

[27] Siegfried Bethke. "Pre-2019 summaries of α_s". In: (2019), pp. 7–12. DOI: 10.22323/1.365.0001 (page 17).

[28] Guido Altarelli. "Experimental Tests of Perturbative QCD". In: *Ann. Rev. Nucl. Part. Sci.* 39 (1989), pp. 357–406. DOI: 10.1146/annurev.ns.39.120189.002041 (page 17).

[29] "A detailed map of Higgs boson interactions by the ATLAS experiment ten years after the discovery". In: *Nature* 607.7917 (2022), pp. 52–59. DOI: 10.1038/s41586-022-04893-w. arXiv: 2207.00092 [hep-ex] (page 18).

[30] K. Schweda et al. "D anti-D correlations as a sensitive probe for thermalization high-energy nuclear collisions". In: *36th International Symposium on Multiparticle Dynamics*. Oct. 2006. arXiv: nucl-ex/0610043 (page 18).

[31] N. Cabibbo and G. Parisi. "Exponential hadronic spectrum and quark liberation". In: *Physics Letters B* 59.1 (1975), pp. 67–69. ISSN: 0370-2693. DOI: 10.1016/0370-2693(75)90158-6 (page 18).

[32] R. Hagedorn. "Statistical thermodynamics of strong interactions at high-energies". In: *Nuovo Cim.Suppl.* 3 (1965), pp. 147–186 (page 18).

[33] Edward V. Shuryak. "Quark-Gluon Plasma and Hadronic Production of Leptons, Photons and Psions". In: *Phys. Lett. B* 78 (1978), p. 150. DOI: 10.1016/0370-2693(78)90370-2 (page 18).

[34] J. Adamczewski-Musch et al. "Probing dense baryon-rich matter with virtual photons". In: *Nature Phys.* 15.10 (2019), pp. 1040–1045. DOI: 10.1038/s41567-019-0583-8 (pages 19, 20).

[35] O. Kaczmarek et al. "Phase boundary for the chiral transition in (2+1) -flavor QCD at small values of the chemical potential". In: *Phys. Rev. D* 83 (2011), p. 014504. DOI: 10.1103/PhysRevD.83.014504. arXiv: 1011.3130 [hep-lat] (page 19).

[36] C. R. Allton et al. "Equation of state for two flavor QCD at nonzero chemical potential". In: *Phys. Rev. D* 68 (1 July 2003), p. 014507. DOI: 10.1103/PhysRevD.68.014507 (page 19).

[37] G. Endrődi et al. "The QCD phase diagram at nonzero quark density". English. In: *Journal of High Energy Physics* 2011.4, 1 (2011). DOI: 10.1007/JHEP04(2011)001 (page 19).

[38] Y. Aoki et al. "The Order of the quantum chromodynamics transition predicted by the standard model of particle physics". In: *Nature* 443 (2006), pp. 675–678. DOI: 10.1038/nature05120. arXiv: hep-lat/0611014 (page 19).

[39] Szabolcs Borsányi et al. "The QCD equation of state with dynamical quarks". English. In: *Journal of High Energy Physics* 2010.11, 77 (2010). DOI: 10.1007/JHEP11(2010)077 (page 19).

[40] A. Bazavov et al. "Chiral crossover in QCD at zero and non-zero chemical potentials". In: *Phys. Lett. B* 795 (2019), pp. 15–21. DOI: 10.1016/j.physletb.2019.05.013. arXiv: 1812.08235 [hep-lat] (page 19).

[41] Szabolcs Borsanyi et al. "Is there still any T_c mystery in lattice QCD? Results with physical masses in the continuum limit III". In: *JHEP* 09 (2010), p. 073. DOI: 10.1007/JHEP09(2010)073. arXiv: 1005.3508 [hep-lat] (page 19).

[42] Hans J. Specht. "Thermal Dileptons from Hot and Dense Strongly Interacting Matter". In: *AIP Conf. Proc.* 1322.1 (2010). Ed. by Juan M. Nieves, Eulogio Oset, and Manuel J. Vicente Vacas, pp. 1–10. DOI: 10.1063/1.3541982. arXiv: 1011.0615 [nucl-ex] (pages 19, 20).

[43] Stefan Floerchinger and Christof Wetterich. "Chemical freeze-out in heavy ion collisions at large baryon densities". In: *Nucl. Phys. A* 890-891 (2012), pp. 11–24. DOI: 10.1016/j.nuclphysa.2012.07.009. arXiv: 1202.1671 [nucl-th] (pages 19, 20).

[44] J. Pochodzalla et al. "Probing the nuclear liquid - gas phase transition". In: *Phys. Rev. Lett.* 75 (1995), pp. 1040–1043. DOI: 10.1103/PhysRevLett.75.1040 (pages 19, 20).

[45] Christian S. Fischer. "QCD at finite temperature and chemical potential from Dyson–Schwinger equations". In: *Prog. Part. Nucl. Phys.* 105 (2019), pp. 1–60. DOI: 10.1016/j.ppnp.2019.01.002. arXiv: 1810.12938 [hep-ph] (page 19).

[46] J. Cleymans et al. “Comparison of chemical freeze-out criteria in heavy-ion collisions”. In: *Phys. Rev. C* 73 (2006), p. 034905. DOI: 10.1103/PhysRevC.73.034905. arXiv: hep-ph/0511094 (page 19).

[47] F. Becattini, J. Manninen, and M. Gazdzicki. “Energy and system size dependence of chemical freeze-out in relativistic nuclear collisions”. In: *Phys. Rev. C* 73 (2006), p. 044905. DOI: 10.1103/PhysRevC.73.044905. arXiv: hep-ph/0511092 (page 19).

[48] A. Andronic, P. Braun-Munzinger, and J. Stachel. “Thermal hadron production in relativistic nuclear collisions: The hadron mass spectrum, the horn, and the {QCD} phase transition”. In: *Physics Letters B* 673.2 (2009), pp. 142–145. ISSN: 0370-2693. DOI: 10.1016/j.physletb.2009.02.014 (page 19).

[49] Anton Andronic et al. “Decoding the phase structure of QCD via particle production at high energy”. In: *Nature* 561.7723 (2018), pp. 321–330. DOI: 10.1038/s41586-018-0491-6. arXiv: 1710.09425 [nucl-th] (page 19).

[50] Szabolcs Borsanyi et al. “QCD thermodynamics on the lattice and in the Hadron Resonance Gas model”. In: *Journal of Physics: Conference Series* 336.1 (2011), p. 012019. URL: http://stacks.iop.org/1742-6596/336/i=1/a=012019 (page 19).

[51] F. Karsch and K. Redlich. “Probing freeze-out conditions in heavy ion collisions with moments of charge fluctuations”. In: *Physics Letters B* 695.1–4 (2011), pp. 136–142. ISSN: 0370-2693. DOI: 10.1016/j.physletb.2010.10.046 (page 19).

[52] Volodymyr Vovchenko, Mark I. Gorenstein, and Horst Stoecker. “van der Waals Interactions in Hadron Resonance Gas: From Nuclear Matter to Lattice QCD”. In: *Phys. Rev. Lett.* 118.18 (2017), p. 182301. DOI: 10.1103/PhysRevLett.118.182301. arXiv: 1609.03975 [hep-ph] (page 19).

[53] Kenji Fukushima. “Hadron resonance gas and mean-field nuclear matter for baryon number fluctuations”. In: *Phys. Rev. C* 91 (4 Apr. 2015), p. 044910. DOI: 10.1103/PhysRevC.91.044910 (page 19).

[54] H. Schulz et al. “On the time-development of the liquid-vapor phase transition in an expanding nuclear system”. In: *Phys. Lett. B* 147 (1984), pp. 17–22. DOI: 10.1016/0370-2693(84)90583-5 (page 20).

[55] V. Serfling et al. “Temperatures of exploding nuclei”. In: *Phys. Rev. Lett.* 80 (1998), pp. 3928–3931. DOI: 10.1103/PhysRevLett.80.3928. arXiv: nucl-ex/9801006 (page 20).

[56] Vicky Kalogera et al. “The Next Generation Global Gravitational Wave Observatory: The Science Book”. In: (Nov. 2021). arXiv: 2111.06990 [gr-qc] (page 20).

[57] Dmitrii G Yakovlev et al. “Lev Landau and the concept of neutron stars”. In: *Physics-Uspekhi* 56.3 (Mar. 2013), pp. 289–295. DOI: 10.3367/ufne.0183.201303f.0307 (page 20).

[58] J. Chadwick. “Possible Existence of a Neutron”. In: *Nature* 129 (1932), p. 312. DOI: 10.1038/129312a0. URL: http://dx.doi.org/10.1038/129312a0 (page 20).

[59] J. R. Oppenheimer and G. M. Volkoff. “On massive neutron cores”. In: *Phys. Rev.* 55 (1939), pp. 374–381. DOI: 10.1103/PhysRev.55.374 (page 20).

[60] B. P. Abbott et al. "GW170817: Measurements of neutron star radii and equation of state". In: *Phys. Rev. Lett.* 121.16 (2018), p. 161101. DOI: 10.1103/PhysRevLett.121.161101. arXiv: 1805.11581 [gr-qc] (page 20).

[61] Luciano Rezzolla, Elias R. Most, and Lukas R. Weih. "Using gravitational-wave observations and quasi-universal relations to constrain the maximum mass of neutron stars". In: *Astrophys. J. Lett.* 852.2 (2018), p. L25. DOI: 10.3847/2041-8213/aaa401. arXiv: 1711.00314 [astro-ph.HE] (page 20).

[62] Ben Margalit and Brian D. Metzger. "Constraining the Maximum Mass of Neutron Stars From Multi-Messenger Observations of GW170817". In: *Astrophys. J. Lett.* 850.2 (2017), p. L19. DOI: 10.3847/2041-8213/aa991c. arXiv: 1710.05938 [astro-ph.HE] (page 20).

[63] Gordon Baym et al. "From hadrons to quarks in neutron stars: a review". In: *Rept. Prog. Phys.* 81.5 (2018), p. 056902. DOI: 10.1088/1361-6633/aaae14. arXiv: 1707.04966 [astro-ph.HE] (page 20).

[64] Elias R. Most et al. "Probing neutron-star matter in the lab: connecting binary mergers to heavy-ion collisions". In: (Jan. 2022). arXiv: 2201.13150 [nucl-th] (page 20).

[65] E. Rutherford. "The scattering of alpha and beta particles by matter and the structure of the atom". In: *Phil. Mag. Ser. 6* 21 (1911), pp. 669–688. DOI: 10.1080/14786440508637080 (page 22).

[66] H. A. Bethe and R. F. Bacher. "Nuclear Physics A. Stationary States of Nuclei". In: *Rev. Mod. Phys.* 8 (1936), pp. 82–229. DOI: 10.1103/RevModPhys.8.82 (page 22).

[67] Niels Bohr and John Archibald Wheeler. "The Mechanism of nuclear fission". In: *Phys. Rev.* 56 (1939), pp. 426–450. DOI: 10.1103/PhysRev.56.426 (page 22).

[68] H. A. Bethe. "Theory of nuclear matter". In: *Ann. Rev. Nucl. Part. Sci.* 21 (1971), pp. 93–244. DOI: 10.1146/annurev.ns.21.120171.000521 (page 22).

[69] A. Bohr and B. R. Mottelson. "The many facets of nuclear structure". In: *Ann. Rev. Nucl. Part. Sci.* 23 (1973), pp. 363–393. DOI: 10.1146/annurev.ns.23.120173.002051 (page 22).

[70] N. Herrmann, J. P. Wessels, and T. Wienold. "Collective flow in heavy ion collisions". In: *Ann. Rev. Nucl. Part. Sci.* 49 (1999), pp. 581–632. DOI: 10.1146/annurev.nucl.49.1.581 (pages 22, 24).

[71] P. Danielewicz. "Flow and the equation of state of nuclear matter". In: *Nucl. Phys. A* 685 (2001). Ed. by W. Norenberg, D. Guerreau, and V. Metag, pp. 368–383. DOI: 10.1016/S0375-9474(01)00554-1. arXiv: nucl-th/0009091 (page 22).

[72] Eugene Gardner and C. M. G. Lattes. "Production of Mesons by the 184-Inch Berkeley Cyclotron". In: *Science* 107.2776 (1948), pp. 270–271. DOI: 10.1126/science.107.2776.270. URL: http://www.sciencemag.org/content/107/2776/270.short (page 22).

[73] Heinz Koppe. In: *Zeitschrift für Naturforschung A* 3.4 (1948), pp. 251–252. DOI: doi:10.1515/zna-1948-0411. URL: http://www.znaturforsch.com/aa/v03a/3a0251.pdf (page 22).

[74] H. Koppe. "On the Production of Mesons". In: *Phys. Rev.* 76 (1949), pp. 688–688. DOI: 10.1103/PhysRev.76.688 (page 22).

[75] Enrico Fermi. “High-energy nuclear events”. In: *Prog. Theor. Phys.* 5 (1950), pp. 570–583. DOI: 10.1143/PTP.5.570 (page 22).

[76] L. D. Landau. “On the multiparticle production in high-energy collisions”. In: *Izv. Akad. Nauk Ser. Fiz.* 17 (1953). [English translation: Collected Papers of L. D. Landau, edited by D. ter Haar (Elsevier, 2013)]., pp. 51–64 (page 22).

[77] S. Z. Belenkij and L. D. Landau. “Hydrodynamic theory of multiple production of particles”. In: *Usp. Fiz. Nauk* 56 (1955), p. 309. DOI: 10.1007/BF02745507 (pages 22, 24, 25).

[78] AE Glassgold, Warren Heckrotte, and Kenneth M Watson. “Collective excitations of nuclear matter”. In: *Annals of Physics* 6.1 (1959), pp. 1–36. DOI: https://doi.org/10.1016/0003-4916(59)90037-5 (page 22).

[79] T. D. Lee. “Abnormal Nuclear States and Vacuum Excitations”. In: *Rev. Mod. Phys.* 47 (1975). Ed. by G. Feinberg, pp. 267–275. DOI: 10.1103/RevModPhys.47.267 (page 23).

[80] R. Stock and Arthur M. Poskanzer. “Heavy Ion Reactions at Relativistic Energies”. In: *Comments Nucl. Part. Phys.* 7.2 (1977), pp. 41–47 (page 23).

[81] R. Hagedorn. “How to Deal with Relativistic Heavy Ion Collisions”. In: *Workshop on Future Relativistic Heavy Ion Experiments.* Jan. 1981, pp. 236–281. DOI: 10.1007/978-3-319-17545-4_26 (pages 23–25).

[82] Erwin M. Friedlander and Harry H. Heckman. “Relativistic Heavy-Ion Collisions: Experiment”. In: *Treatise on Heavy-Ion Science: Volume 4 Extreme Nuclear States*. Ed. by D.Allan Bromley. Springer US, 1985, pp. 401–562. ISBN: 978-1-4615-8099-7. DOI: 10.1007/978-1-4615-8097-3_4 (page 23).

[83] J. A. Maruhn and W. Greiner. “Relativistic Heavy-Ion Reactions: Theoretical Models”. In: *Treatise on Heavy-Ion Science*. Ed. by D.Allan Bromley. Springer US, 1985, pp. 563–680. ISBN: 978-1-4615-8097-3. DOI: 10.1007/978-1-4615-8097-3_5 (page 23).

[84] Gordon Baym. “RHIC: From dreams to beams in two decades”. In: *Nucl. Phys. A* 698 (2002). Ed. by T. J. Hallman et al., pp. XXIII–XXXII. DOI: 10.1016/S0375-9474(01)01342-2. arXiv: hep-ph/0104138 (page 23).

[85] Werner Scheid, Rainer Ligensa, and Walter Greiner. “Ion-Ion Potentials and the Compressibility of Nuclear Matter”. In: *Phys. Rev. Lett.* 21.21 (1968), p. 1479. DOI: 10.1103/PhysRevLett.21.1479 (page 23).

[86] G. F. Chapline et al. “Highly excited nuclear matter”. In: *Phys. Rev. D* 8 (1973), pp. 4302–4308. DOI: 10.1103/PhysRevD.8.4302 (page 23).

[87] C. Y. Wong and T. A. Welton. “Supersonic heavy-ion collisions”. In: *Phys. Lett. B* 49 (1974), pp. 243–245. DOI: 10.1016/0370-2693(74)90423-7 (page 23).

[88] Werner Scheid, Hans Muller, and Walter Greiner. “Nuclear Shock Waves in Heavy-Ion Collisions”. In: *Phys. Rev. Lett.* 32 (1974), pp. 741–745. DOI: 10.1103/PhysRevLett.32.741 (page 23).

[89] A. A Amsden et al. “Relativistic Hydrodynamic Theory of Heavy Ion Collisions”. In: *Phys. Rev. Lett.* 35 (1975), pp. 905–908. DOI: 10.1103/PhysRevLett.35.905 (page 23).

[90] A. Y. Abul-Magd. "Nuclear Shock Waves in Relativistic Heavy Ion Collisions". In: *Phys. Rev. C* 12 (1975), pp. 343–345. DOI: 10.1103/PhysRevC.12.343 (page 23).

[91] M. I. Sobel et al. "Shock Waves in Colliding Nuclei". In: *Nucl. Phys. A* 251 (1975), pp. 502–529. DOI: 10.1016/0375-9474(75)90545-X (page 23).

[92] Francis H. Harlow. "Fluid dynamics in Group T-3 Los Alamos National Laboratory. (LA-UR-03-3852)". In: *Journal of Computational Physics* 195.2 (2004), pp. 414–433. DOI: 10.1016/j.jcp.2003.09.031 (page 23).

[93] George F. Bertsch. "Comment on nuclear shock waves in heavy-ion collisions". In: *Phys. Rev. Lett.* 34 (1975), pp. 697–698. DOI: 10.1103/PhysRevLett.34.697 (page 23).

[94] Dirk H. Rischke, Stefan Bernard, and Joachim A. Maruhn. "Relativistic hydrodynamics for heavy ion collisions. 1. General aspects and expansion into vacuum". In: *Nucl. Phys. A* 595 (1995), pp. 346–382. DOI: 10.1016/0375-9474(95)00355-1. arXiv: nucl-th/9504018 (page 23).

[95] Peter F. Kolb and Ulrich W. Heinz. "Hydrodynamic description of ultrarelativistic heavy ion collisions". In: (May 2003). Ed. by Rudolph C. Hwa and Xin-Nian Wang, pp. 634–714. arXiv: nucl-th/0305084 (page 23).

[96] Horst Stoecker and W. Greiner. "High-Energy Heavy Ion Collisions: Probing the Equation of State of Highly Excited Hadronic Matter". In: *Phys. Rept.* 137 (1986), pp. 277–392. DOI: 10.1016/0370-1573(86)90131-6 (pages 23, 146).

[97] R. B. Clare and D. Strottman. "Relativistic Hydrodynamics and heavy ion reactions". In: *Phys. Rept.* 141 (1986), pp. 177–280. DOI: 10.1016/0370-1573(86)90090-6 (pages 23, 31).

[98] Horst Stoecker, J. A. Maruhn, and W. Greiner. "Collective sideward flow of nuclear matter in violent high-energy heavy ion collisions". In: *Phys. Rev. Lett.* 44 (1980), p. 725. DOI: 10.1103/PhysRevLett.44.725 (page 23).

[99] Horst Stoecker et al. "Jets of Nuclear Matter From High-energy Heavy Ion Collisions". In: *Phys. Rev. C* 25 (1982), pp. 1873–1876. DOI: 10.1103/PhysRevC.25.1873 (page 23).

[100] H. A. Gustafsson et al. "Collective Flow Observed in Relativistic Nuclear Collisions". In: *Phys. Rev. Lett.* 52 (1984), pp. 1590–1593. DOI: 10.1103/PhysRevLett.52.1590 (pages 24, 27).

[101] Hans H. Gutbrod, Arthur M. Poskanzer, and Hans Georg Ritter. "PLASTIC BALL EXPERIMENTS". In: *Rept. Prog. Phys.* 52 (1989), p. 1267. DOI: 10.1088/0034-4885/52/10/003 (pages 24, 145).

[102] Hans H. Gutbrod. "The Path to Heavy Ions at LHC and Beyond". In: *Melting Hadrons, Boiling Quarks - From Hagedorn Temperature to Ultra-Relativistic Heavy-Ion Collisions at CERN: With a Tribute to Rolf Hagedorn*. Ed. by Johann Rafelski. 2016, pp. 97–106. DOI: 10.1007/978-3-319-17545-4_13 (page 24).

[103] R. E. Renfordt et al. "Stopping Power and Collective Flow of Nuclear Matter in the Reaction Ar+Pb at 0.8 GeV/u". In: *Phys. Rev. Lett.* 53 (1984), pp. 763–766. DOI: 10.1103/PhysRevLett.53.763 (pages 24, 27).

[104] P. Danielewicz and G. Odyniec. "Transverse Momentum Analysis of Collective Motion in Relativistic Nuclear Collisions". In: *Phys. Lett. B* 157 (1985), pp. 146–150. DOI: 10.1016/0370-2693(85)91535-7 (pages 24, 25, 27, 69, 181, 191).

[105] J. Gosset et al. "Nuclear collective flow from Gaussian fits to triple differential distributions". In: *Phys. Lett. B* 247 (1990), pp. 233–237. DOI: 10.1016/0370-2693(90)90888-D (page 24).

[106] M. Demoulins et al. "Measurement of a baryon azimuthal emission pattern in Ne + (NaF, Nb, Pb) collisions at 800-MeV per nucleon". In: *Phys. Lett. B* 241 (1990), pp. 476–480. DOI: 10.1016/0370-2693(90)91855-6 (page 24).

[107] W. Reisdorf and H. G. Ritter. "Collective flow in heavy-ion collisions". In: *Ann. Rev. Nucl. Part. Sci.* 47 (1997), pp. 663–709. DOI: 10.1146/annurev.nucl.47.1.663 (pages 24, 146).

[108] A. Andronic et al. "Systematics of Stopping and Flow in Au+Au Collisions". In: *Eur. Phys. J.* A30 (2006), pp. 31–46. DOI: 10.1140/epja/i2006-10101-2. arXiv: nucl-ex/0608015 [nucl-ex] (pages 24, 69, 72, 145, 146).

[109] Sergei A. Voloshin, Arthur M. Poskanzer, and Raimond Snellings. "Collective phenomena in non-central nuclear collisions". In: *Landolt-Bornstein* 23 (2010). Ed. by R. Stock, pp. 293–333. DOI: 10.1007/978-3-642-01539-7_10. arXiv: 0809.2949 [nucl-ex] (page 24).

[110] Ulrich Heinz and Raimond Snellings. "Collective flow and viscosity in relativistic heavy-ion collisions". In: *Ann. Rev. Nucl. Part. Sci.* 63 (2013), pp. 123–151. DOI: 10.1146/annurev-nucl-102212-170540. arXiv: 1301.2826 [nucl-th] (page 24).

[111] Hans Georg Ritter and Reinhard Stock. "Collective Flow of QCD Matter: a Historical Introduction". In: *J. Phys. G* 41 (2014), p. 124002. DOI: 10.1088/0954-3899/41/12/124002. arXiv: 1408.4296 [nucl-ex] (pages 24, 27).

[112] Jerzy Bartke. *Introduction to relativistic heavy ion physics*. World Scientific, 2009. ISBN: 9789810212315. URL: http://books.google.de/books?id=WMGZngEACAAJ (pages 24, 27).

[113] P. Danielewicz. "Effects of compression and collective expansion on particle emission from central heavy ion reactions". In: *Phys. Rev. C* 51 (1995), pp. 716–750. DOI: 10.1103/PhysRevC.51.716. arXiv: nucl-th/9408018 (pages 24, 151, 177, 188).

[114] W. Reisdorf et al. "Nuclear stopping from 0.09-A-GeV to 1.93-A-GeV and its correlation to flow". In: *Phys. Rev. Lett.* 92 (2004), p. 232301. DOI: 10.1103/PhysRevLett.92.232301. arXiv: nucl-ex/0404037 (page 24).

[115] Brent Barker and Pawel Danielewicz. "Shear viscosity from nuclear stopping". In: *Phys. Rev.* C99.3 (2019), p. 034607. DOI: 10.1103/PhysRevC.99.034607. arXiv: 1612.04874 [nucl-th] (pages 24, 32, 33).

[116] J. D. Bjorken. "Highly Relativistic Nucleus-Nucleus Collisions: The Central Rapidity Region". In: *Phys. Rev. D* 27 (1983), pp. 140–151. DOI: 10.1103/PhysRevD.27.140 (pages 24, 25).

[117] W.D. Myers. "A Model for High-Energy Heavy Ion Collisions". In: *Nucl. Phys. A* 296 (1978), pp. 177–188. DOI: 10.1016/0375-9474(78)90420-7 (pages 24, 25).

[118] J. Gosset, Joseph I. Kapusta, and G.D. Westfall. "Calculations With the Nuclear Firestreak Model". In: *Phys. Rev. C* 18 (1978), pp. 844–855. DOI: 10.1103/PhysRevC.18.844 (page 24).

[119] Philip J. Siemens and John O. Rasmussen. "Evidence for a blast wave from compress nuclear matter". In: *Phys. Rev. Lett.* 42 (1979), pp. 880–887. DOI: 10.1103/PhysRevLett.42.880 (pages 25, 149).

[120] Ekkard Schnedermann, Josef Sollfrank, and Ulrich W. Heinz. "Thermal phenomenology of hadrons from 200-A/GeV S+S collisions". In: *Phys. Rev. C* 48 (1993), pp. 2462–2475. DOI: 10.1103/PhysRevC.48.2462. arXiv: nucl-th/9307020 (pages 25, 149).

[121] M. A. Lisa et al. "Radial flow in Au + Au collisions at E = 0.25-A/GeV - 1.15-A/Gev". In: *Phys. Rev. Lett.* 75 (1995), pp. 2662–2665. DOI: 10.1103/PhysRevLett.75.2662. arXiv: nucl-ex/9502001 (page 25).

[122] Cheuk-Yin Wong. "Selection of central events in intermediate energy heavy-ion collisions". In: *Phys. Lett. B* 88 (1979), pp. 39–42. DOI: 10.1016/0370-2693(79)90108-4 (pages 25, 50, 181, 191).

[123] G. Bertsch and A. A. Amsden. "Heavy ion collisions at intermediate energy". In: *Phys. Rev. C* 18 (1978), pp. 1293–1297. DOI: 10.1103/PhysRevC.18.1293 (pages 25, 149).

[124] A. Andronic et al. "Excitation function of elliptic flow in Au+Au collisions and the nuclear matter equation of state". In: *Phys. Lett. B* 612 (2005), pp. 173–180. DOI: 10.1016/j.physletb.2005.02.060. arXiv: nucl-ex/0411024 (page 25).

[125] A. Le Fèvre et al. "Origin of elliptic flow and its dependence on the equation of state in heavy ion reactions at intermediate energies". In: *Phys. Rev. C* 98.3 (2018), p. 034901. DOI: 10.1103/PhysRevC.98.034901. arXiv: 1611.07500 [nucl-th] (pages 25, 31, 165).

[126] Jean-Yves Ollitrault. "Determination of the reaction plane in ultrarelativistic nuclear collisions". In: *Phys. Rev.* D48 (1993), pp. 1132–1139. DOI: 10.1103/PhysRevD.48.1132. arXiv: hep-ph/9303247 [hep-ph] (pages 25, 26, 50, 70, 71, 181, 191).

[127] S. Voloshin and Y. Zhang. "Flow study in relativistic nuclear collisions by Fourier expansion of Azimuthal particle distributions". In: *Z. Phys.* C70 (1996), pp. 665–672. DOI: 10.1007/s002880050141. arXiv: hep-ph/9407282 [hep-ph] (pages 25, 50, 70, 141, 181, 191).

[128] Pawel Danielewicz and Mizuki Kurata-Nishimura. "Deblurring 3D Characteristics of Heavy-Ion Collisions". In: (Sept. 2021). arXiv: 2109.02626 [nucl-th] (pages 26, 141, 181, 192).

[129] S. Wang et al. "In-Plane Retardation of Collective Expansion in Au+Au Collisions". In: *Phys. Rev. Lett.* 76 (1996), pp. 3911–3914. DOI: 10.1103/PhysRevLett.76.3911 (pages 26, 181, 192).

[130] G. Stoicea et al. "Azimuthal dependence of collective expansion for symmetric heavy ion collisions". In: *Phys. Rev. Lett.* 92 (2004), p. 072303. DOI: 10.1103/PhysRevLett.92.072303. arXiv: nucl-ex/0401041 (pages 26, 181, 192).

[131] W. Reisdorf et al. "Systematics of azimuthal asymmetries in heavy ion collisions in the 1 A GeV regime". In: *Nucl. Phys.* A876 (2012), pp. 1–60. DOI: 10.1016/j.nuclphysa.2011.12.006. arXiv: 1112.3180 [nucl-ex] (pages 26, 83, 142, 145–147, 151, 177, 188).

[132] J. Barrette et al. "Observation of anisotropic event shapes and transverse flow in Au + Au collisions at AGS energy". In: *Phys. Rev. Lett.* 73 (1994), pp. 2532–2535. DOI: 10.1103/PhysRevLett.73.2532. arXiv: hep-ex/9405003 (pages 26, 145, 146).

[133] J. Barrette et al. "Proton and pion production relative to the reaction plane in Au + Au collisions at AGS energies". In: *Phys. Rev.* C56 (1997), pp. 3254–3264. DOI: 10.1103/PhysRevC.56.3254. arXiv: nucl-ex/9707002 [nucl-ex] (pages 26, 75, 76, 145, 149–151, 177, 188).

[134] J. Barrette et al. “Energy and charged particle flow in a 10.8-A/GeV/c Au + Au collisions”. In: *Phys. Rev.* C55 (1997). [Erratum: Phys. Rev.C56,2336(1997)], pp. 1420–1430. DOI: 10.1103/PhysRevC.55.1420,10.1103/PhysRevC.56.2336. arXiv: nucl-ex/9610006 [nucl-ex] (pages 26, 145).

[135] Michael L. Miller et al. “Glauber modeling in high energy nuclear collisions”. In: *Ann.Rev.Nucl.Part.Sci.* 57 (2007), pp. 205–243. DOI: 10.1146/annurev.nucl.57.090506.123020. arXiv: nucl-ex/0701025 [nucl-ex] (pages 26, 28).

[136] Jean-Yves Ollitrault. “Flow systematics from SIS to SPS energies”. In: *Nucl. Phys. A* 638 (1998). Ed. by T. Hatsuda et al., pp. 195–206. DOI: 10.1016/S0375-9474(98)00413-8. arXiv: nucl-ex/9802005 (pages 26, 50, 71).

[137] Jean-Yves Ollitrault. “On the measurement of azimuthal anisotropies in nucleus-nucleus collisions”. In: (Nov. 1997). arXiv: nucl-ex/9711003 (pages 26, 50, 51, 70, 71, 176, 186).

[138] Arthur M. Poskanzer and S. A. Voloshin. “Methods for analyzing anisotropic flow in relativistic nuclear collisions”. In: *Phys. Rev.* C58 (1998), pp. 1671–1678. DOI: 10.1103/PhysRevC.58.1671. arXiv: nucl-ex/9805001 [nucl-ex] (pages 26, 50, 51, 69, 70, 73, 102, 176, 186).

[139] K.G.R. Doss et al. “Nuclear Collective Flow as a Function of Projectile Energy and Mass”. In: *Phys. Rev. Lett.* 57 (1986), pp. 302–305. DOI: 10.1103/PhysRevLett.57.302 (pages 27, 142).

[140] J.D. Bowman, W.J. Swiatecki, and C.F. Tsang. “Abrasion and Ablation of Heavy Ions”. In: (1973). URL: http://escholarship.org/uc/item/8nm3b276 (page 28).

[141] J. Hufner, K. Schafer, and B. Schurmann. “Abrasion-ablation in reactions between relativistic heavy ions”. In: *Phys. Rev. C* 12 (1975), pp. 1888–1898. DOI: 10.1103/PhysRevC.12.1888 (page 28).

[142] J. Adamczewski-Musch et al. “Centrality determination of Au + Au collisions at 1.23A GeV with HADES”. In: *Eur. Phys. J.* A54.5 (2018), p. 85. DOI: 10.1140/epja/i2018-12513-7. arXiv: 1712.07993 [nucl-ex] (pages 28, 55, 67, 155, 156).

[143] Constantin Loizides, Jason Kamin, and David d’Enterria. “Improved Monte Carlo Glauber predictions at present and future nuclear colliders”. In: *Phys. Rev. C* 97.5 (2018). [Erratum: Phys.Rev.C 99, 019901 (2019)], p. 054910. DOI: 10.1103/PhysRevC.97.054910. arXiv: 1710.07098 [nucl-ex] (pages 28, 155).

[144] Behruz Kardan. “Centrality Determination at 1.23 AGeV Gold-Gold collision and readout-electronics for the HADES electromagnetic calorimeter”. Diploma thesis. Goethe-Universität, Frankfurt am Main, 2015 (pages 28, 39, 55, 67).

[145] A. Bialas, M. Bleszynski, and W. Czyz. “Multiplicity Distributions in Nucleus-Nucleus Collisions at High-Energies”. In: *Nucl. Phys. B* 111 (1976), pp. 461–476. DOI: 10.1016/0550-3213(76)90329-1 (pages 29, 65).

[146] B. Alver and G. Roland. “Collision geometry fluctuations and triangular flow in heavy-ion collisions”. In: *Phys. Rev.* C81 (2010). [Erratum: Phys. Rev.C82,039903(2010)], p. 054905. DOI: 10.1103/PhysRevC.82.039903,10.1103/PhysRevC.81.054905. arXiv: 1003.0194 [nucl-th] (page 29).

[147] Hermann Wolter et al. “Transport model comparison studies of intermediate-energy heavy-ion collisions”. In: *Prog. Part. Nucl. Phys.* 125 (2022), p. 103962. DOI: 10.1016/j.ppnp.2022.103962. arXiv: 2202.06672 [nucl-th] (pages 30, 165).

[148] Jun Xu. “Transport approaches for the description of intermediate-energy heavy-ion collisions”. In: *Prog. Part. Nucl. Phys.* 106 (2019), pp. 312–359. DOI: 10.1016/j.ppnp.2019.02.009. arXiv: 1904.00131 [nucl-th] (pages 30, 165).

[149] Maria Colonna et al. “Comparison of heavy-ion transport simulations: Mean-field dynamics in a box”. In: *Phys. Rev. C* 104.2 (2021), p. 024603. DOI: 10.1103/PhysRevC.104.024603. arXiv: 2106.12287 [nucl-th] (pages 30, 165).

[150] Jun Xu et al. “Understanding transport simulations of heavy-ion collisions at 100A and 400A MeV: Comparison of heavy-ion transport codes under controlled conditions”. In: *Phys. Rev. C* 93.4 (2016), p. 044609. DOI: 10.1103/PhysRevC.93.044609. arXiv: 1603.08149 [nucl-th] (pages 30, 165).

[151] Joseph I. Kapusta. “DEUTERON AND ENTROPY PRODUCTION AND THE NUCLEAR LIQUID - GAS PHASE TRANSITION”. In: *Phys. Rev. C* 29 (1984), pp. 1735–1743. DOI: 10.1103/PhysRevC.29.1735 (page 31).

[152] Pawel Danielewicz, Roy Lacey, and William G. Lynch. “Determination of the equation of state of dense matter”. In: *Science* 298 (2002), pp. 1592–1596. DOI: 10.1126/science.1078070. arXiv: nucl-th/0208016 [nucl-th] (pages 31, 165).

[153] C. Pinkenburg et al. “Elliptic flow: Transition from out-of-plane to in-plane emission in Au + Au collisions”. In: *Phys. Rev. Lett.* 83 (1999), pp. 1295–1298. DOI: 10.1103/PhysRevLett.83.1295. arXiv: nucl-ex/9903010 [nucl-ex] (pages 31, 146, 147, 151, 177, 188).

[154] A. Le Fèvre et al. “Constraining the nuclear matter equation of state around twice saturation density”. In: *Nucl. Phys. A* 945 (2016), pp. 112–133. DOI: 10.1016/j.nuclphysa.2015.09.015. arXiv: 1501.05246 [nucl-ex] (page 31).

[155] C. Fuchs et al. “Probing the nuclear equation of state by K+ production in heavy ion collisions”. In: *Phys. Rev. Lett.* 86 (2001), pp. 1974–1977. DOI: 10.1103/PhysRevLett.86.1974. arXiv: nucl-th/0011102 (page 31).

[156] Christian Thomas Sturm et al. “Evidence for a soft nuclear equation of state from kaon production in heavy ion collisions”. In: *Phys. Rev. Lett.* 86 (2001), pp. 39–42. DOI: 10.1103/PhysRevLett.86.39. arXiv: nucl-ex/0011001 (page 31).

[157] G. A. Lalazissis, J. Konig, and P. Ring. “A New parametrization for the Lagrangian density of relativistic mean field theory”. In: *Phys. Rev. C* 55 (1997), pp. 540–543. DOI: 10.1103/PhysRevC.55.540. arXiv: nucl-th/9607039 (page 31).

[158] Qiu-bao Pan and Pawel Danielewicz. “From sideward flow to nuclear compressibility”. In: *Phys. Rev. Lett.* 70 (1993). [Erratum: Phys.Rev.Lett. 70, 3523 (1993)], pp. 2062–2065. DOI: 10.1103/PhysRevLett.70.2062 (page 31).

[159] A. B. Larionov et al. “Squeezeout of nuclear matter in peripheral heavy ion collisions and momentum dependent effective interactions”. In: *Phys. Rev.* C62 (2000), p. 064611. DOI: 10.1103/PhysRevC.62.064611. arXiv: nucl-th/0006009 [nucl-th] (pages 31, 165).

[160] P. K. Sahu and W. Cassing. "Differential flow of protons in Au+Au collisions at AGS energies". In: *Nucl. Phys. A* 712 (2002), pp. 357–369. DOI: 10.1016/S0375-9474(02)01287-3. arXiv: nucl-th/0208002 (pages 31, 165).

[161] W. G. Lynch et al. "Probing the Symmetry Energy with Heavy Ions". In: *Prog. Part. Nucl. Phys.* 62 (2009), p. 427. DOI: 10.1016/j.ppnp.2009.01.001. arXiv: 0901.0412 [nucl-ex] (page 31).

[162] Yongjia Wang et al. "Determination of the nuclear incompressibility from the rapidity-dependent elliptic flow in heavy-ion collisions at beam energies 0.4 A –1.0 A GeV". In: *Phys. Lett. B* 778 (2018), pp. 207–212. DOI: 10.1016/j.physletb.2018.01.035. arXiv: 1804.04293 [nucl-th] (pages 31, 165).

[163] J. Aichelin et al. "Importance of Momentum Dependent Interactions for the Extraction of the Nuclear Equation of State From High-energy Heavy Ion Collisions". In: *Phys. Rev. Lett.* 58 (1987), pp. 1926–1929. DOI: 10.1103/PhysRevLett.58.1926 (page 31).

[164] G. M. Welke et al. "Azimuthal distributions in heavy ion collisions and the nuclear equation of state". In: *Phys. Rev. C* 38 (1988), pp. 2101–2107. DOI: 10.1103/PhysRevC.38.2101 (page 31).

[165] Charles Gale et al. "Transverse momenta, nuclear equation of state, and momentum-dependent interactions in heavy-ion collisions". In: *Phys. Rev. C* 41 (1990), pp. 1545–1552. DOI: 10.1103/PhysRevC.41.1545 (page 31).

[166] K. Weber et al. "A Relativistic effective interaction for heavy ion collisions". In: *Nucl. Phys. A* 539 (1992), pp. 713–751. DOI: 10.1016/0375-9474(92)90134-6 (page 31).

[167] T. Maruyama et al. "Relativistic BUU approach with momentum dependent mean fields". In: *Phys. Lett. B* 297 (1992), pp. 228–232. DOI: 10.1016/0370-2693(92)91253-6 (page 31).

[168] P. K. Sahu et al. "Baryon flow at SIS energies and beyond". In: *Nucl. Phys. A* 640 (1998), pp. 493–504. DOI: 10.1016/S0375-9474(98)00464-3. arXiv: nucl-th/9801043 (page 31).

[169] P. K. Sahu et al. "Baryon flow from SIS to AGS energies". In: *Nucl. Phys. A* 672 (2000), pp. 376–386. DOI: 10.1016/S0375-9474(99)00854-4. arXiv: nucl-th/9907002 (pages 31, 165).

[170] Pawel Danielewicz. "Determination of the mean field momentum dependence using elliptic flow". In: *Nucl. Phys.* A673 (2000), pp. 375–410. DOI: 10.1016/S0375-9474(00)00083-X. arXiv: nucl-th/9912027 [nucl-th] (pages 31, 165).

[171] L. Shi and P. Danielewicz. "Nuclear isospin diffusivity". In: *Phys. Rev. C* 68 (2003), p. 064604. DOI: 10.1103/PhysRevC.68.064604. arXiv: nucl-th/0304030 (page 32).

[172] T. Gaitanos, C. Fuchs, and H.H. Wolter. "Nuclear stopping and flow in heavy ion collisions and the in-medium NN cross section". In: *Phys. Lett. B* 609 (2005), pp. 241–246. DOI: 10.1016/j.physletb.2005.01.069. arXiv: nucl-th/0412055 (page 32).

[173] J.-B. Rose et al. "Shear viscosity of a hadron gas and influence of resonance lifetimes on relaxation time". In: *Phys. Rev.* C97.5 (2018), p. 055204. DOI: 10.1103/PhysRevC.97.055204. arXiv: 1709.03826 [nucl-th] (page 32).

[174] Jan Rais, Kai Gallmeister, and Carsten Greiner. "The Shear Viscosity to Entropy Density Ratio of Hagedorn States". In: (2019). arXiv: 1909.04522 [hep-ph] (page 32).

[175] Nasser Demir and Steffen A. Bass. "Shear-Viscosity to Entropy-Density Ratio of a Relativistic Hadron Gas". In: *Phys. Rev. Lett.* 102 (2009), p. 172302. DOI: 10.1103/PhysRevLett.102.172302. arXiv: 0812.2422 [nucl-th] (page 32).

[176] Jonah E. Bernhard et al. "Quantifying properties of hot and dense QCD matter through systematic model-to-data comparison". In: *Phys. Rev. C* 91.5 (2015), p. 054910. DOI: 10.1103/PhysRevC.91.054910. arXiv: 1502.00339 [nucl-th] (page 32).

[177] P. Kovtun, Dan T. Son, and Andrei O. Starinets. "Viscosity in strongly interacting quantum field theories from black hole physics". In: *Phys. Rev. Lett.* 94 (2005), p. 111601. DOI: 10.1103/PhysRevLett.94.111601. arXiv: hep-th/0405231 (page 32).

[178] Nicolai Christiansen et al. "Transport Coefficients in Yang–Mills Theory and QCD". In: *Phys. Rev. Lett.* 115.11 (2015), p. 112002. DOI: 10.1103/PhysRevLett.115.112002. arXiv: 1411.7986 [hep-ph] (page 32).

[179] A. S. Khvorostukhin, V. D. Toneev, and D. N. Voskresensky. "Viscosity Coefficients for Hadron and Quark-Gluon Phases". In: *Nucl. Phys.* A845 (2010), pp. 106–146. DOI: 10.1016/j.nuclphysa.2010.05.058. arXiv: 1003.3531 [nucl-th] (page 32).

[180] Yu. B. Ivanov and A. A. Soldatov. "Entropy Production and Effective Viscosity in Heavy-Ion Collisions". In: *Eur. Phys. J.* A52.12 (2016), p. 367. DOI: 10.1140/epja/i2016-16367-7. arXiv: 1605.02476 [nucl-th] (page 32).

[181] Yu. B. Ivanov and A. A. Soldatov. "Estimation of the shear viscosity from 3FD simulations of Au + Au collisions at $\sqrt{s_{NN}}$ = 3.3-39 GeV". In: *Eur. Phys. J.* A52.5 (2016), p. 117. DOI: 10.1140/epja/i2016-16117-y. arXiv: 1604.03261 [nucl-th] (page 32).

[182] Fred Cooper and Graham Frye. "Comment on the Single Particle Distribution in the Hydrodynamic and Statistical Thermodynamic Models of Multiparticle Production". In: *Phys. Rev. D* 10 (1974), p. 186. DOI: 10.1103/PhysRevD.10.186 (pages 33, 149).

[183] V.N. Russkikh et al. "Analysis of intermediate-energy heavy ion collisions within relativistic mean field two fluid model". In: *Nucl. Phys. A* 572 (1994), pp. 749–790. DOI: 10.1016/0375-9474(94)90409-X (page 33).

[184] Dirk H. Rischke et al. "The Phase transition to the quark - gluon plasma and its effects on hydrodynamic flow". In: *Acta Phys. Hung. A* 1 (1995), pp. 309–322 (page 33).

[185] Yu.B. Ivanov, V. N. Russkikh, and V. D. Toneev. "Relativistic heavy-ion collisions within 3-fluid hydrodynamics: Hadronic scenario". In: *Phys. Rev.* C73 (2006), p. 044904. DOI: 10.1103/PhysRevC.73.044904 (page 33).

[186] Iu.A. Karpenko et al. "Estimation of the shear viscosity at finite net-baryon density from $A + A$ collision data at $\sqrt{s_{\mathrm{NN}}} = 7.7 - 200$ GeV". In: *Phys. Rev. C* 91.6 (2015), p. 064901. DOI: 10.1103/PhysRevC.91.064901. arXiv: 1502.01978 [nucl-th] (page 33).

[187] P. Batyuk et al. "Event simulation based on three-fluid hydrodynamics for collisions at energies available at the Dubna Nuclotron-based Ion Collider Facility and at the Facility for Antiproton and Ion Research in Darmstadt". In: *Phys. Rev.* C94 (2016), p. 044917. DOI: 10.1103/PhysRevC.94.044917 (page 33).

[188] U. Mosel and V. Metag. “Evidence for resonance matter at SIS”. In: *Nucl. Phys. News* 3.4 (1993), pp. 25–27. DOI: 10.1080/10506899308221163 (pages 35, 174, 185).

[189] Piotr Salabura and Joachim Stroth. “Dilepton radiation from strongly interacting systems”. In: *Prog. Part. Nucl. Phys.* 120 (2021), p. 103869. DOI: 10.1016/j.ppnp.2021.103869. arXiv: 2005.14589 [nucl-ex] (pages 35, 174, 185).

[190] G. Agakichiev et al. “Dielectron Production in C12+C12 Collisions at 2A GeV with the HADES Spectrometer”. In: *Phys. Rev. Lett.* 98 (5 Feb. 2007), p. 052302. DOI: 10.1103/PhysRevLett.98.052302 (page 36).

[191] G. Agakishiev et al. “Study of dielectron production in collisions at”. In: *Physics Letters B* 663.1–2 (2008), pp. 43–48. ISSN: 0370-2693. DOI: 10.1016/j.physletb.2008.03.062 (page 36).

[192] G Agakishiev et al. “Dielectron production in Ar + KCl collisions at 1.76A GeV”. In: *Phys. Rev. C* 84 (1 July 2011), p. 014902. DOI: 10.1103/PhysRevC.84.014902 (page 36).

[193] G. Agakishiev et al. “Inclusive dielectron spectra in p+p collisions at 3.5 GeV kinetic beam energy”. In: *Eur. Phys. J. A* 48 (2012), p. 64. DOI: 10.1140/epja/i2012-12064-y. arXiv: 1112.3607 [nucl-ex] (page 36).

[194] G. Agakishiev et al. “First measurement of proton-induced low-momentum dielectron radiation off cold nuclear matter”. In: *Physics Letters B* 715.4–5 (2012), pp. 304–309. ISSN: 0370-2693. DOI: 10.1016/j.physletb.2012.08.004 (page 36).

[195] Tetyana Galatyuk. “HADES overview”. In: *Nuclear Physics A* 0 (2014), pp. -. ISSN: 0375-9474. DOI: 10.1016/j.nuclphysa.2014.10.044 (page 36).

[196] J. Biernat et al. “a secondary pion beam for the hades experiment”. In: (2013). URL: http://www.e12.ph.tum.de/~rlalik/HADES_Cerberos_TDR.pdf (page 36).

[197] Simon Spies. “HADES Overview - Recent results from Ag+Ag collisions at $\sqrt{s_{NN}} = 2.55$ GeV measured by HADES”. In: *EPJ Web Conf.* 259 (2022), p. 01007. DOI: 10.1051/epjconf/202225901007 (page 36).

[198] G. Agakichiev et al. “Origin of the low-mass electron pair excess in light nucleus–nucleus collisions”. In: *Physics Letters B* 690.2 (2010), pp. 118–122. ISSN: 0370-2693. DOI: http://dx.doi.org/10.1016/j.physletb.2010.05.010 (page 36).

[199] R. J. Porter et al. “Dielectron Cross Section Measurements in Nucleus-Nucleus Reactions at 1.0*A* GeV”. In: *Phys. Rev. Lett.* 79 (7 Aug. 1997), pp. 1229–1232. DOI: 10.1103/PhysRevLett.79.1229 (page 36).

[200] D. Schüll W. Koenig U. Kopf. “Specification of the HADES Superconducting Torus System”. In: (1995). URL: http://web-docs.gsi.de/~webhades/docs/magnet/magspec.ps.gz (page 37).

[201] P. Salabura et al. “HADES: A High Acceptance DiElectron Spectrometer”. In: *Nucl. Phys. Proc. Suppl.* 44 (1995), pp. 701–707. DOI: 10.1016/0920-5632(95)00605-2 (page 38).

[202] R. Schicker et al. “Acceptance and resolution simulation studies for the dielectron spectrometer HADES at GSI”. In: *Nucl. Instrum. Meth. A* 380 (1996), pp. 586–596. DOI: 10.1016/0168-9002(96)00732-2. arXiv: nucl-ex/9605004 (page 38).

[203] J. Friese. “Studying in-medium hadron properties with HADES”. In: *Prog. Part. Nucl. Phys.* 42 (1999), pp. 235–245. DOI: 10.1016/S0146-6410(99)00079-4 (page 38).

[204] Jan Michel. “Development and Implementation of a New Trigger and Data Acquisition System for the HADES Detector”. Dissertation. Goethe-Universität, Frankfurt am Main, 2012 (pages 39, 42, 43, 55).

[205] Adrian Rost. “Design, installation and commissioning of new read-out electronics for HADES ECAL and diamond detectors for T0-reconstruction and beam diagnostics”. Dissertation. Technische Universität Darmstadt, 2020 (pages 39, 40).

[206] W. Czyzycki et al. “Electromagnetic Calorimeter for HADES”. In: (2011). arXiv: 1109.5550 [nucl-ex] (page 39).

[207] M. Akrawy et al. “Development studies for the OPAL end cap electromagnetic calorimeter using vacuum photo triode instrumented leadglass”. In: *Nuclear Instruments and Methods in Physics Research Section A: Accelerators, Spectrometers, Detectors and Associated Equipment* 290.1 (1990), pp. 76–94. ISSN: 0168-9002. DOI: 10.1016/0168-9002(90)90346-8 (page 39).

[208] Adrian Amatus Weber. “Development of readout electronics for the RICH detector in the HADES and CBM experiments - HADES RICH upgrade, mRICH detector construction and analysis -”. PhD thesis. Giessen University, 2021. URL: http://dx.doi.org/10.22029/jlupub-288 (page 39).

[209] M. Wiebusch et al. “Towards new Front-End Electronics for the HADES Drift Chamber System”. In: *Nucl. Instrum. Meth.* A936 (2019), pp. 386–388. DOI: 10.1016/j.nima.2018.11.057. arXiv: 1810.12695 [physics.ins-det] (page 40).

[210] Michael Wiebusch. “Towards new front-end electronics for the HADES drift chamber system”. PhD thesis. Goethe-Universität, Frankfurt am Main, 2019 (pages 40, 78).

[211] J. Pietraszko et al. “Low Gain Avalanche Detectors for the HADES reaction time (T_0) detector upgrade”. In: *Eur. Phys. J.* A56.7 (2020), p. 183. DOI: 10.1140/epja/s10050-020-00186-w. arXiv: 2005.12965 [physics.ins-det] (page 40).

[212] J. Glatz et al. “Operational aspects of the high current upgrade at the UNILAC”. In: *eConf* C000821 (2000), MOD12. arXiv: physics/0008110 [physics.acc-ph] (page 40).

[213] R. Hollinger, K. Tinschert, Pfister, et al. “Ion Source Operation at the GSI Accelerator Facility”. In: vol. 2013-1. Darmstadt: GSI Helmholtzzentrum für Schwerionenforschung, 2013, 257–p. URL: http://repository.gsi.de/record/52153 (page 40).

[214] A. Adonin and R. Hollinger. “*R&D* Projects with High Current Ion Sources”. In: vol. 2013-1. Darmstadt: GSI Helmholtzzentrum für Schwerionenforschung, 2013, 265 p. URL: http://repository.gsi.de/record/52160 (page 40).

[215] G. Otto / GSI. “Foto: HADES Gold Targets”. In: (). URL: https://www.gsi.de/forschungbeschleuniger/forschung_ein_ueberblick/hades_experiment/aufbau_des_hades_experiments.htm (page 41).

[216] Birgit Kindler et al. "Targets for the electron–positron pair spectrometer HADES". In: *Nuclear Instruments and Methods in Physics Research Section A: Accelerators, Spectrometers, Detectors and Associated Equipment* 655.1 (2011), pp. 95–99. ISSN: 0168-9002. DOI: 10.1016/j.nima.2011.06.029 (page 41).

[217] T. Bretz. "Magnetfeldeigenschaften des Spektrometers HADES". Master thesis. Technische Universität München, 1999 (page 42).

[218] C. Müntz et al. "The HADES tracking system". In: *Nuclear Instruments and Methods in Physics Research Section A: Accelerators, Spectrometers, Detectors and Associated Equipment* 535.1–2 (2004). Proceedings of the 10th International Vienna Conference on Instrumentation, pp. 242–246. ISSN: 0168-9002. DOI: 10.1016/j.nima.2004.07.232 (page 42).

[219] G. Agakishiev et al. "The High-Acceptance Dielectron Spectrometer HADES". In: *Eur. Phys. J.* A41 (2009), pp. 243–277. DOI: 10.1140/epja/i2009-10807-5. arXiv: 0902.3478 [nucl-ex] (pages 42, 77, 78, 93).

[220] J. Pietraszko. "Beam detectors in Au+Au run and future developments". In: (2013). URL: https://indico.gsi.de/materialDisplay.py?contribId=9&sessionId=4&materialId=slides&confId=2142 (page 43).

[221] J. Pietraszko et al. "Radiation damage in single crystal CVD diamond material investigated with a high current relativistic 197Au beam". In: *Nuclear Instruments and Methods in Physics Research Section A: Accelerators, Spectrometers, Detectors and Associated Equipment* 763.0 (2014), pp. 1–5. ISSN: 0168-9002. DOI: 10.1016/j.nima.2014.06.006 (page 43).

[222] J. Pietraszko et al. "Diamonds as timing detectors for minimum-ionizing particles: The HADES proton-beam monitor and START signal detectors for time of flight measurements". In: *Nuclear Instruments and Methods in Physics Research Section A: Accelerators, Spectrometers, Detectors and Associated Equipment* 618.1–3 (2010), pp. 121–123. ISSN: 0168-9002. DOI: 10.1016/j.nima.2010.02.113 (page 43).

[223] Birgit Kindler et al. "Coating of diamonds for detector application". In: *Journal of radioanalytical and nuclear chemistry* 305.3 (2015), pp. 963–969. ISSN: 0022-4081. DOI: 10.1007/s10967-014-3912-5. URL: http://repository.gsi.de/record/183632 (page 43).

[224] C. Agodi et al. "The HADES time-of-flight wall". In: *Nuclear Instruments and Methods in Physics Research Section A: Accelerators, Spectrometers, Detectors and Associated Equipment* 492.1–2 (2002), pp. 14–25. ISSN: 0168-9002. DOI: 10.1016/S0168-9002(02)01004-5 (page 44).

[225] G. Kornakov et al. "Performance study and calibration strategy of the HADES scintillator TOF Wall with fast digital readout". In: (Mar. 2021). arXiv: 2103.07416 [physics.ins-det] (page 44).

[226] D. Belver et al. "The HADES RPC inner TOF wall". In: *Nuclear Instruments and Methods in Physics Research Section A: Accelerators, Spectrometers, Detectors and Associated Equipment* 602.3 (2009). Proceedings of the 9th International Workshop on Resistive Plate Chambers and Related Detectors RPC08, pp. 687–690. ISSN: 0168-9002. DOI: 10.1016/j.nima.2008.12.090 (page 44).

[227] A. Blanco et al. "In-beam measurements of the HADES-TOF RPC wall". In: *Nuclear Instruments and Methods in Physics Research Section A: Accelerators, Spectrometers, Detectors and Associated Equipment* 602.3 (2009). Proceedings of the 9th International Workshop on Resistive Plate Chambers and Related Detectors RPC08, pp. 691–695. ISSN: 0168-9002. DOI: 10.1016/j.nima.2008.12.091 (page 44).

[228] P. Cabanelas et al. "Performances of multi-gap timing RPCs for relativistic ions in the range Z=1-6". In: *JINST* 4 (2009), P11007. DOI: 10.1088/1748-0221/4/11/P11007. arXiv: 0905.0682 [nucl-ex] (page 44).

[229] O.V. Andreeva et al. "Forward scintillation hodoscope for nuclear fragment detection at the high acceptance dielectron spectrometer (HADES) setup". In: *Instruments and Experimental Techniques* 57.2 (2014), pp. 103–119. ISSN: 0020-4412. DOI: 10.1134/S0020441214020146 (page 45).

[230] J. W. Harris et al. "Pion production in high-energy nucleus-nucleus collisions". In: *Phys. Rev. Lett.* 58 (5 Feb. 1987), pp. 463–466. DOI: 10.1103/PhysRevLett.58.463 (page 45).

[231] R. Brockmann et al. *GSI Scientific Report 1983 [GSI Report 1984-1]*. Darmstadt: GSI, 1984, p. 241. URL: http://repository.gsi.de/record/53548 (page 45).

[232] A. R. Wolf et al. "Multistep Production of η and Hard π^0 Mesons in Subthreshold Au-Au Collisions". In: *Phys. Rev. Lett.* 80 (24 June 1998), pp. 5281–5284. DOI: 10.1103/PhysRevLett.80.5281 (page 45).

[233] P. Senger et al. "The kaon spectrometer at SIS". In: *Nuclear Instruments and Methods in Physics Research Section A: Accelerators, Spectrometers, Detectors and Associated Equipment* 327.2–3 (1993), pp. 393–411. ISSN: 0168-9002. DOI: 10.1016/0168-9002(93)90706-N (page 45).

[234] K.O. Lapidus. "Investigation of the production of electron-positron pairs in nucleon-nucleon interactions with the HADES detector". In: *Physics of Atomic Nuclei* 73.6 (2010), pp. 985–987. ISSN: 1063-7788. DOI: 10.1134/S1063778810060128 (page 45).

[235] Christian Lippmann. "Particle identification". In: *Nuclear Instruments and Methods in Physics Research Section A: Accelerators, Spectrometers, Detectors and Associated Equipment* 666.0 (2012). Advanced Instrumentation, pp. 148–172. ISSN: 0168-9002. DOI: 10.1016/j.nima.2011.03.009 (pages 45, 88).

[236] E. Albrecht et al. "VUV absorbing vapours in n-perfluorocarbons". In: *Nuclear Instruments and Methods in Physics Research Section A: Accelerators, Spectrometers, Detectors and Associated Equipment* 510.3 (2003), pp. 262–272. ISSN: 0168-9002. DOI: 10.1016/S0168-9002(03)01867-9 (page 46).

[237] T.A Filippas et al. "Precision measurements of gas refractivity by means of a Fabry–Perot interferometer illustrated by the monitoring of radiator refractivity in the DELPHI RICH detectors". In: *Nuclear Instruments and Methods in Physics Research Section B: Beam Interactions with Materials and Atoms* 196.3–4 (2002), pp. 340–348. ISSN: 0168-583X. DOI: 10.1016/S0168-583X(02)01291-0 (page 46).

[238] K. Zeitelhack et al. "The HADES RICH detector". In: *Nuclear Instruments and Methods in Physics Research Section A: Accelerators, Spectrometers, Detectors and Associated Equipment* 433.1–2 (1999), pp. 201–206. ISSN: 0168-9002. DOI: 10.1016/S0168-9002(99)00371-X (page 46).

[239] J. Friese et al. "A new carbon based VUV mirror of high radiation length for the HADES RICH". In: *Nuclear Instruments and Methods in Physics Research Section A: Accelerators, Spectrometers, Detectors and Associated Equipment* 502.1 (2003), pp. 241–245. ISSN: 0168-9002. DOI: 10.1016/S0168-9002(03)00281-X (page 46).

[240] A. Bałanda et al. "The HADES Pre-Shower detector". In: *Nuclear Instruments and Methods in Physics Research Section A: Accelerators, Spectrometers, Detectors and Associated Equipment* 531.3 (2004), pp. 445–458. ISSN: 0168-9002. DOI: 10.1016/j.nima.2004.05.082 (page 46).

[241] G.D. Alekseev et al. "Investigation of self-quenching streamer discharge in a wire chamber". In: *Nuclear Instruments and Methods* 177.2–3 (1980), pp. 385–397. ISSN: 0029-554X. DOI: 10.1016/0029-554X(80)90049-X (page 46).

[242] M. Atac, A.V. Tollestrup, and D. Potter. "Self-quenching streamers". In: *Nuclear Instruments and Methods in Physics Research* 200.2–3 (1982), pp. 345–354. ISSN: 0167-5087. DOI: 10.1016/0167-5087(82)90453-7 (page 46).

[243] R. Brun and F. Rademakers. "ROOT: An object oriented data analysis framework". In: *Nucl. Instrum. Meth. A* 389 (1997). Ed. by M. Werlen and D. Perret-Gallix, pp. 81–86. DOI: 10.1016/S0168-9002(97)00048-X (page 47).

[244] I. Fröhlich et al. "Pluto: A Monte Carlo Simulation Tool for Hadronic Physics". In: *PoS* ACAT (2007), p. 076. DOI: 10.22323/1.050.0076. arXiv: 0708.2382 [nucl-ex] (page 47).

[245] René Brun et al. "GEANT Detector Description and Simulation Tool". In: (Oct. 1994). DOI: 10.17181/CERN.MUHF.DMJ1 (pages 47, 64, 66, 83, 84).

[246] Rolf Hagedorn. *Relativistic kinematics: a guide to the kinematic problems of high-energy physics*. New York, NY: Benjamin, 1963. ISBN: 978-1-258-26194-8 (page 49).

[247] Cheuk-Yin Wong. *Introduction to high-energy heavy ion collisions*. World Scientific, 1995. ISBN: 978-981-02-0263-7 (page 49).

[248] N. Borghini et al. "Effects of momentum conservation on the analysis of anisotropic flow". In: *Phys. Rev. C* 66 (2002), p. 014901. DOI: 10.1103/PhysRevC.66.014901. arXiv: nucl-th/0202013 (pages 50, 51, 70, 176, 186).

[249] Claude A. Pruneau. *Data Analysis Techniques for Physical Scientists*. Oct. 2017. DOI: 10.1017/9781108241922 (page 50).

[250] W. Bayer, U. Scheeler, and Petra Schütt. "Accelerator Operation Report". In: vol. 2013-1. Darmstadt: GSI Helmholtzzentrum für Schwerionenforschung, 2013, 255–p. URL: http://repository.gsi.de/record/52152 (page 52).

[251] Heidi Schuldes. "Charged kaon and ϕ reconstruction in Au+Au collisions at 1.23 AGeV". PhD thesis. Goethe U., Frankfurt (main), 2016. URL: http://publikationen.ub.uni-frankfurt.de/frontdoor/index/index/docId/42489 (pages 52, 61, 77, 80, 93, 109).

[252] Claudia Behnke. "Reconstruction of π^0 and η mesons via conversion in ^{197}Au+^{197}Au at 1.23 GeV/u with the HADES Spectrometer". PhD thesis. Goethe U., Frankfurt (main), 2016. URL: https://publikationen.ub.uni-frankfurt.de/frontdoor/index/index/docId/44136 (pages 52, 97).

[253] Timo Scheib. “Λ and K_s^0 production in Au+Au collisions at 1.23A GeV”. PhD thesis. Goethe U., Frankfurt (main), 2017. URL: https://d-nb.info/1138276731/34 (pages 52, 58, 61, 80, 105, 109).

[254] Patrick Sellheim. “Reconstruction of the low-mass dielectron signal in 1.23A GeV Au+Au collisions”. PhD thesis. Goethe U., Frankfurt (main), 2017. URL: http://publikationen.ub.uni-frankfurt.de/frontdoor/index/index/docId/44417 (pages 52, 97, 109).

[255] Szymon Harabasz. “Reconstruction of virtual photons from Au+Au collisions at 1.23 GeV/u”. PhD thesis. Jagiellonian University, 2017. URL: http://www.fais.uj.edu.pl/documents/41628/136724573/HarabaszSzymon_thesis_toSubmit.compressed.pdf (pages 52, 61).

[256] Robert André Heinrich Greifenhagen. “Two-Pion Intensity-Interferometry in Collisions of Au+Au at $\sqrt{s_{NN}}$ = 2.41 GeV measured with HADES”. PhD thesis. Dresden, Tech. U., 2020. URL: https://nbn-resolving.org/urn:nbn:de:bsz:14-qucosa2-737159 (pages 52, 86).

[257] Frédéric Julian Kornas. “Global polarization of Λ hyperons as a probe for vortical effects in A+A collisions at HADES”. PhD thesis. Technische Universität Darmstadt, 2021. DOI: 10.26083/tuprints-00019763 (pages 52, 88).

[258] Lukáš Chlad. “Study of transverse flow of kaons in Au+Au collisions at 1.23A GeV”. PhD thesis. Charles University of Prague, 2021. URL: http://hdl.handle.net/20.500.11956/170699 (pages 52, 88).

[259] Jan Michel. Private Communication (page 54).

[260] J. Jaros et al. “Nucleus-Nucleus Total Cross-Sections for Light Nuclei at 1.55-GeV/c/Nucleon and 2.89-GeV/c/Nucleon”. In: *Phys. Rev. C* 18 (1978), pp. 2273–2292. DOI: 10.1103/PhysRevC.18.2273 (page 55).

[261] H.H Heckman et al. “Fragmentation of He-4, C-12, N-14, and O-16 Nuclei in Nuclear Emulsion at 2.1-GeV/Nucleon”. In: *Phys. Rev. C* 17 (1978), pp. 1735–1747. DOI: 10.1103/PhysRevC.17.1735 (page 55).

[262] C.J. Benesh, B.C. Cook, and J.P. Vary. “Single Nucleon Removal in Relativistic Nuclear Collisions”. In: *Phys. Rev. C* 40 (1989), pp. 1198–1206. DOI: 10.1103/PhysRevC.40.1198 (page 55).

[263] E.O. Abdrahmanov et al. “Interaction cross sections and negative pion multiplicities in nucleus-nucleus collisions at 4.2 GeV/c per nucleon”. In: *Zeitschrift für Physik C Particles and Fields* 5.1 (1980), pp. 1–8. ISSN: 0170-9739. DOI: 10.1007/BF01546951. URL: http://dx.doi.org/10.1007/BF01546951 (page 55).

[264] T. Aumann et al. “Inclusive measurements of electromagnetic dissociation of Au-197 targets”. In: *Phys. Rev. C* 47 (1993), pp. 1728–1737. DOI: 10.1103/PhysRevC.47.1728 (page 55).

[265] Claudia Höhne. *System-Size Dependence of Strangeness Production in Heavy-Ion Collisions at 158 AGeV*. 2003. URL: http://archiv.ub.uni-marburg.de/diss/z2003/0627 (page 55).

[266] C. Alt et al. “Inclusive production of charged pions in p+p collisions at 158-GeV/c beam momentum”. In: *Eur. Phys. J. C* 45 (2006), pp. 343–381. DOI: 10.1140/epjc/s2005-02391-9. arXiv: hep-ex/0510009 (page 55).

[267] R. Schicker and Haralabos Tsertos. “Simulation studies of the HADES first level trigger. Part 1: Performance in heavy ion induced reactions”. In: *Nucl. Instrum. Meth. A* (1996). arXiv: nucl-ex/9610002 [nucl-ex] (page 56).

[268] Georgy Kornakov. “Collision time reconstruction and particle identification in AuAu collisions at 1.23A GeV with HADES”. In: *GSI Scientific Report 2016* GSI Report 2017-1 (2017). DOI: 10.15120/GR-2017-1. URL: https://repository.gsi.de/record/201280 (page 60).

[269] A. Akindinov and other. “Performance of the ALICE Time-Of-Flight detector at the LHC”. English. In: *The European Physical Journal Plus* 128.4, 44 (2013). DOI: 10.1140/epjp/i2013-13044-x. URL: http://dx.doi.org/10.1140/epjp/i2013-13044-x (page 61).

[270] S. A. Bass et al. “Microscopic models for ultrarelativistic heavy ion collisions”. In: *Prog. Part. Nucl. Phys.* 41 (1998), pp. 255–369. DOI: 10.1016/S0146-6410(98)00058-1. arXiv: nucl-th/9803035 (pages 64, 66, 84).

[271] T. Abbott et al. “Measurement of Energy Emission from O+A and p+A Collisions at 14.5 GeV/c per Nucleon with a Lead-Glass Array”. In: *Phys. Lett. B* 197 (1987), pp. 285–290. DOI: 10.1016/0370-2693(87)90385-6 (page 65).

[272] E. A. De Wolf, I. M. Dremin, and W. Kittel. “Scaling laws for density correlations and fluctuations in multiparticle dynamics”. In: *Phys. Rept.* 270 (1996), pp. 1–141. DOI: 10.1016/0370-1573(95)00069-0. arXiv: hep-ph/9508325 (page 65).

[273] Y. Akiba et al. “Two-particle rapidity correlations from the Bose-Einstein effect in central Si-28 + Au collisions at 14.6-A-GeV/c and intermittency”. In: *Phys. Rev. C* 56 (1997), pp. 1544–1552. DOI: 10.1103/PhysRevC.56.1544 (page 65).

[274] S. S. Adler et al. “Measurement of density correlations in pseudorapidity via charged particle multiplicity fluctuations in Au+Au collisions at s(NN)**(1/2) = 200-GeV”. In: *Phys. Rev. C* 76 (2007), p. 034903. DOI: 10.1103/PhysRevC.76.034903. arXiv: 0704.2894 [nucl-ex] (page 65).

[275] Jan Fiete Grosse-Oetringhaus and Klaus Reygers. “Charged-Particle Multiplicity in Proton-Proton Collisions”. In: *J. Phys. G* 37 (2010), p. 083001. DOI: 10.1088/0954-3899/37/8/083001. arXiv: 0912.0023 [hep-ex] (page 65).

[276] Rudolph Rogly, Giuliano Giacalone, and Jean-Yves Ollitrault. “Reconstructing the impact parameter of proton-nucleus and nucleus-nucleus collisions”. In: *Phys. Rev. C* 98.2 (2018), p. 024902. DOI: 10.1103/PhysRevC.98.024902. arXiv: 1804.03031 [nucl-th] (page 67).

[277] J.D. Frankland et al. “Reconstructing the impact parameter dependence of experimental observables from intermediate energy heavy-ion collision data”. In: (Nov. 2020). arXiv: 2011.04496 [nucl-ex] (page 68).

[278] A. S. Goldhaber. “Statistical models of fragmentation processes”. In: *Phys. Lett. B* 53 (1974), pp. 306–308. DOI: 10.1016/0370-2693(74)90388-8 (page 68).

[279] D. E. Greiner et al. “Momentum Distributions of Isotopes Produced by Fragmentation of Relativistic C-12 and O-16 Projectiles”. In: *Phys. Rev. Lett.* 35 (1975), p. 152. DOI: 10.1103/PhysRevLett.35.152 (page 68).

[280] L. Shi, P. Danielewicz, and R. Lacey. “Spectator response to the participant blast”. In: *Phys. Rev.* C64 (2001), p. 034601. DOI: 10.1103/PhysRevC.64.034601. arXiv: nucl-th/0104074 [nucl-th] (page 68).

[281] V. Fohr et al. “Experimental study of fragmentation products in the reactions 112Sn + 112Sn and 124Sn + 124Sn at 1 AGeV”. In: *Phys. Rev.* C84 (2011), p. 054605. DOI: 10.1103/PhysRevC.84.054605. arXiv: 1106.5368 [nucl-ex] (page 68).

[282] J. P. Bondorf et al. “Spectator Recoil in Intermediate-Energy Heavy Ion Collisions”. In: *Nucl. Phys. A* 43 (1984), pp. 445–453. DOI: 10.1016/0375-9474(84)90048-4 (page 69).

[283] George I. Fai, Wei-ming Zhang, and M. Gyulassy. “Optimizing Heavy Ion Experiments to Probe Dense Nuclear Matter”. In: *Phys. Rev. C* 36 (1987), pp. 597–601. DOI: 10.1103/PhysRevC.36.597 (page 69).

[284] C. A. Ogilvie et al. “Transverse collective motion in intermediate-energy heavy-ion collisions”. In: *Phys. Rev. C* 40 (1989), pp. 2592–2599. DOI: 10.1103/PhysRevC.40.2592 (page 69).

[285] C. A. Ogilvie et al. “Determination of the impact vector in intermediate energy heavy ion collisions”. In: *Phys. Rev. C* 40 (1989), pp. 654–663. DOI: 10.1103/PhysRevC.40.654 (page 69).

[286] D. Krofcheck et al. “Disappearance of Flow in Heavy-Ion Collisions”. In: *Phys. Rev. Lett.* 63 (1989), pp. 2028–2031. DOI: 10.1103/PhysRevLett.63.2028 (page 69).

[287] W. M. Zhang et al. “Onset of flow of charged fragments in Au - Au collisions”. In: *Phys. Rev. C* 42 (1990), pp. 491–494. DOI: 10.1103/PhysRevC.42.R491 (page 69).

[288] M. B. Tsang et al. “Reaction plane determination for Ar-36 + Au-197 collisions at E/A=35 MeV”. In: *Phys. Rev. C* 44 (1991), pp. 2065–2081. DOI: 10.1103/PhysRevC.44.2065 (page 69).

[289] D. Krofcheck et al. “Disappearance of flow as a probe of the nuclear equation of state”. In: *Phys. Rev. C* 46 (1992), pp. 1416–1424. DOI: 10.1103/PhysRevC.46.1416 (page 69).

[290] Nicolas Borghini, Phuong Mai Dinh, and Jean-Yves Ollitrault. “A New method for measuring azimuthal distributions in nucleus-nucleus collisions”. In: *Phys. Rev. C* 63 (2001), p. 054906. DOI: 10.1103/PhysRevC.63.054906. arXiv: nucl-th/0007063 (page 69).

[291] J. Lukasik and W. Trautmann. “Reaction plane dispersion at intermediate energies”. In: *International Workshop on Multifragmentation and Related Topics (IWM 2005)*. Mar. 2006. arXiv: nucl-ex/0603028 (pages 69, 72).

[292] K. G. R. Doss et al. “Fragment Flow in Nuclear Collisions”. In: *Phys. Rev. Lett.* 59 (1987), pp. 2720–2723. DOI: 10.1103/PhysRevLett.59.2720 (pages 69, 145).

[293] D. Brill. “Azimutal anisotrope Teilchenemission in relativistischen Schwerionenstössen”. Dissertation. Goethe-Universitaet Frankfurt, 1993 (page 73).

[294] Ilya Selyuzhenkov and Sergei Voloshin. “Effects of non-uniform acceptance in anisotropic flow measurement”. In: *Phys. Rev.* C77 (2008), p. 034904. DOI: 10.1103/PhysRevC.77.034904. arXiv: 0707.4672 [nucl-th] (pages 76, 102, 103).

[295] Vladimir Pechenov. Private Communication (page 77).

[296] Jochen Markert. “Untersuchung zum Ansprechverhalten der Vieldraht-Driftkammern niedriger Massenbelegung des HADES-Experimentes”. PhD thesis. Goethe U., Frankfurt (main), 2005 (pages 77, 78, 92).

[297] Anar Rustamov. “Exclusive eta Meson Reconstruction in Proton-Proton Collisions at 2.2 GeV with the HADES Spectrometer and High Resolution Tracking”. Dissertation. Technische Universität Darmstadt, 2006. URL: http://tuprints.ulb.tu-darmstadt.de/724/ (page 78).

[298] N. Bastid et al. “First analysis of anisotropic flow with Lee-Yang zeroes”. In: *Phys. Rev.* C72 (2005), p. 011901. DOI: 10.1103/PhysRevC.72.011901. arXiv: nucl-ex/0504002 [nucl-ex] (pages 83, 155).

[299] W. Reisdorf et al. “Systematics of pion emission in heavy ion collisions in the 1A- GeV regime”. In: *Nucl. Phys.* A781 (2007), pp. 459–508. DOI: 10.1016/j.nuclphysa.2006.10.085. arXiv: nucl-ex/0610025 [nucl-ex] (page 83).

[300] J. Barrette et al. “Proton and pion production in Au + Au collisions at 10.8A-GeV/c”. In: *Phys. Rev.* C62 (2000), p. 024901. DOI: 10.1103/PhysRevC.62.024901. arXiv: nucl-ex/9910004 [nucl-ex] (page 83).

[301] R. Lacasse. “Hadron production in 10.8 A GeV/c Au+Au collisions”. PhD thesis. McGill University, 1998. URL: http://web-docs.gsi.de/~misko/e877/theses/theses.html (page 83).

[302] T. W. Piazza. “Proton and Pion Distributions from Au+Au Collisions at 10.8 A GeV/c”. PhD thesis. SUNY at Stony Brook, 1997. URL: http://web-docs.gsi.de/~misko/e877/theses/theses.html (page 84).

[303] S. Voloshin. “Occupancy correction. Method n + 1.” In: *E877 Note HD-96/08/15* (1996). URL: http://web-docs.gsi.de/~misko/e877/notes/HD-96-08-15.ps.gz (page 84).

[304] S. Voloshin. “Occupancy correction. Method n + 1. Version 2.” In: *E877 Note HD-96/08/27* (1996). URL: http://web-docs.gsi.de/~misko/e877/notes/HD-96-08-27.ps.gz (page 84).

[305] B. B. Back et al. “Pseudorapidity and centrality dependence of the collective flow of charged particles in Au+Au collisions at $\sqrt{s}_{NN} = 130$ GeV”. In: *Phys. Rev. Lett.* 89 (2002), p. 222301. DOI: 10.1103/PhysRevLett.89.222301. arXiv: nucl-ex/0205021 (page 84).

[306] B. B. Back et al. “Energy dependence of elliptic flow over a large pseudorapidity range in Au+Au collisions at RHIC”. In: *Phys. Rev. Lett.* 94 (2005), p. 122303. DOI: 10.1103/PhysRevLett.94.122303. arXiv: nucl-ex/0406021 [nucl-ex] (pages 84, 146).

[307] M. M. Aggarwal et al. “Azimuthal anisotropy of photon and charged particle emission in Pb-208 + Pb-208 collisions at 158-A-GeV/c”. In: *Eur. Phys. J.* C41 (2005), pp. 287–296. DOI: 10.1140/epjc/s2005-02249-2. arXiv: nucl-ex/0406022 [nucl-ex] (pages 84, 146).

[308] Rashmi Raniwala, Sudhir Raniwala, and Yogendra P. Viyogi. “Effect of finite granularity of detectors on anisotropy coefficients”. In: *Eur. Phys. J.* C48 (2006), pp. 677–682. DOI: 10.1140/epjc/s10052-006-0083-8. arXiv: nucl-ex/0502023 [nucl-ex] (page 84).

[309] M. Bleicher et al. “Relativistic hadron hadron collisions in the ultrarelativistic quantum molecular dynamics model”. In: *J. Phys. G* 25 (1999), pp. 1859–1896. DOI: 10.1088/0954-3899/25/9/308. arXiv: hep-ph/9909407 (page 84).

[310] J. Adamczewski-Musch et al. “Identical pion intensity interferometry in central Au + Au collisions at 1.23 A GeV”. In: *Phys. Lett.* B795 (2019), pp. 446–451. DOI: 10.1016/j.physletb.2019.06.047. arXiv: 1811.06213 [nucl-ex] (page 86).

[311] J. Adamczewski-Musch et al. “Identical pion intensity interferometry at $\sqrt{s_{\mathrm{NN}}} = 2.4$ GeV: HADES collaboration”. In: *Eur. Phys. J. A* 56.5 (2020), p. 140. DOI: 10.1140/epja/s10050-020-00116-w. arXiv: 1910.07885 [nucl-ex] (page 86).

[312] Pavel Tlusty. Private Communication (pages 86, 87).

[313] A. Prozorov. “Simulation study of effects induced by final granularity of detector in particle flow”. In: *J. Phys. Conf. Ser.* 1667.1 (2020). Ed. by Marco Destefanis et al., p. 012034. DOI: 10.1088/1742-6596/1667/1/012034 (page 88).

[314] Mateusz Grunwald. “Flow correction for 1.23A GeV au+au collisions at the HADES experiment”. In: *Proc. SPIE Int. Soc. Opt. Eng.* 11581 (2020). Ed. by Ryszard S. Romaniuk and Maciej Linczuk, 115810R. DOI: 10.1117/12.2580447 (page 88).

[315] D. Durand, E. Suraud, and B. Tamain. *Nuclear dynamics in the nucleonic regime*. 2001 (page 88).

[316] Fabio Sauli. *Gaseous Radiation Detectors: Fundamentals and Applications*. Vol. 36. Cambridge University Press, Aug. 2014. DOI: 10.1017/CBO9781107337701 (page 91).

[317] P. A. Zyla et al. “Review of Particle Physics”. In: *PTEP* 2020.8 (2020), p. 083C01. DOI: 10.1093/ptep/ptaa104 (page 91).

[318] F. Sauli. “Principles of Operation of Multiwire Proportional and Drift Chambers”. In: (May 1977). DOI: 10.5170/CERN-1977-009 (page 92).

[319] M. Aguilar-Benitez et al. “Inclusive particle production in 400-GeV/c p p interactions”. In: *Z. Phys.* C50 (1991), pp. 405–426. DOI: 10.1007/BF01551452 (page 92).

[320] Jaroslav Adam et al. “Bulk properties of the system formed in $Au + Au$ collisions at $\sqrt{s_{\mathrm{NN}}}$ =14.5 GeV at the BNL STAR detector”. In: *Phys. Rev. C* 101.2 (2020), p. 024905. DOI: 10.1103/PhysRevC.101.024905. arXiv: 1908.03585 [nucl-ex] (page 92).

[321] A. Schmah. “Produktion von Seltsamkeit in Ar+KCl Reaktionen bei 1.756 AGeV”. Dissertation. Technische Universität Darmstadt, Darmstadt, 2008 (page 93).

[322] Joana Katharina Wirth. “(Strange) Meson Production in Pion-Nucleus Collisions at 1.7 GeV/c”. PhD thesis. Technische Universität München, 2019 (page 93).

[323] Alexander Sadovsky. “Internal Note”. In: (2015) (pages 101, 109).

[324] Mikhail Mamaev, Oleg Golosov, and Ilya Selyuzhenkov. “Estimating Non-Flow Effects in Measurements of Anisotropic Flow of Protons with the HADES Experiment at GSI”. In: *Phys. Part. Nucl.* 53.2 (2022), pp. 277–281. DOI: 10.1134/S1063779622020514. arXiv: 2012.04433 [nucl-ex] (page 102).

[325] M. Mamaev, O. Golosov, and I. Selyuzhenkov. “Directed flow of protons with the event plane and scalar product methods in the HADES experiment at SIS18”. In: *J. Phys. Conf. Ser.* 1690.1 (2020). Ed. by Petr Teterin, p. 012122. DOI: 10.1088/1742-6596/1690/1/012122 (page 102).

[326] Nicolas Borghini, Phuong Mai Dinh, and Jean-Yves Ollitrault. "Flow analysis from multiparticle azimuthal correlations". In: *Phys. Rev. C* 64 (2001), p. 054901. DOI: 10.1103/PhysRevC.64.054901. arXiv: nucl-th/0105040 (page 103).

[327] Ante Bilandzic et al. "Generic framework for anisotropic flow analyses with multiparticle azimuthal correlations". In: *Phys. Rev.* C89.6 (2014), p. 064904. DOI: 10.1103/PhysRevC.89.064904. arXiv: 1312.3572 [nucl-ex] (page 103).

[328] Roger Barlow. "Systematic errors: Facts and fictions". In: *Advanced Statistical Techniques in Particle Physics. Proceedings, Conference, Durham, UK, March 18-22, 2002*. 2002, pp. 134–144. arXiv: hep-ex/0207026 [hep-ex]. URL: http://www.ippp.dur.ac.uk/Workshops/02/statistics/proceedings//barlow.pdf (pages 104, 110).

[329] Joel Heinrich and L. Lyons. "Systematic errors". In: *Ann. Rev. Nucl. Part. Sci.* 57 (2007), pp. 145–169. DOI: 10.1146/annurev.nucl.57.090506.123052 (page 104).

[330] K. Piasecki et al. "Centrality dependence of subthreshold ϕ meson production in Ni + Ni collisions at 1.9A GeV". In: *Phys. Rev.* C94.1 (2016), p. 014901. DOI: 10.1103/PhysRevC.94.014901. arXiv: 1602.04378 [nucl-ex] (page 104).

[331] S. Spies. "Rekonstruktion schwacher Zerfälle in Au+Au Kollisionen bei 1,23A GeV". Master thesis. Goethe-Universität,Frankfurt am Main, 2018 (page 105).

[332] J. Adamczewski-Musch et al. "Proton, deuteron and triton flow measurements in Au+Au collisions at $\sqrt{s_{NN}} = 2.4$ GeV". In: *Eur. Phys. J.* A (Aug. 2022). arXiv: 2208.02740 [nucl-ex] (pages 113, 173, 177, 183, 187).

[333] Behruz Kardan. "Flow harmonics of Au+Au collisions at 1.23 AGeV with HADES". In: *J. Phys. Conf. Ser.* 742.1 (2016), p. 012008. DOI: 10.1088/1742-6596/742/1/012008 (pages 113, 173, 183).

[334] Behruz Kardan. "Collective flow measurements with HADES in Au+Au collisions at 1.23A GeV". In: *Nucl. Phys.* A967 (2017), pp. 812–815. DOI: 10.1016/j.nuclphysa.2017.05.026 (pages 113, 173, 183).

[335] Behruz Kardan. "Collective flow measurements with HADES in Au+Au collisions at 1.23A GeV". In: *PoS* CPOD2017 (2018), p. 049. DOI: 10.22323/1.311.0049 (pages 113, 173, 183).

[336] Behruz Kardan. "Collective flow and correlations measurements with HADES in Au+Au collisions at 1.23 AGeV". In: *Nucl. Phys.* A982 (2019), pp. 431–434. DOI: 10.1016/j.nuclphysa.2018.09.061. arXiv: 1809.07821 [nucl-ex] (pages 113, 173, 183).

[337] J. Adamczewski-Musch et al. "Directed, Elliptic, and Higher Order Flow Harmonics of Protons, Deuterons, and Tritons in Au + Au Collisions at $\sqrt{s_{NN}} = 2.4$ GeV". In: *Phys. Rev. Lett.* 125 (2020), p. 262301. DOI: 10.1103/PhysRevLett.125.262301. arXiv: 2005.12217 [nucl-ex] (pages 113, 114, 118, 140, 141, 153, 173, 181, 183, 192).

[338] Paula Hillmann et al. "First, second, third and fourth flow harmonics of deuterons and protons in Au+Au reactions at 1.23 A GeV". In: *J. Phys. G* 47.5 (2020), p. 055101. DOI: 10.1088/1361-6471/ab6fcf. arXiv: 1907.04571 [nucl-th] (pages 114, 115, 118, 119, 153–155, 178, 189).

[339] Tom Reichert, Jan Steinheimer, and Marcus Bleicher. "3-dimensional flow analysis: A novel tool to study the collision geometry and the Equation-of-State". In: (July 2022). arXiv: 2207.02594 [nucl-th] (page 141).

[340] Steven H. Schot. “Aberrancy: Geometry of the Third Derivative”. In: *Mathematics Magazine* 51.5 (1978), pp. 259–275. DOI: 10.1080/0025570X.1978.11976728 (page 142).

[341] A. Andronic et al. “Differential directed flow in Au+Au collisions”. In: *Phys. Rev.* C64 (2001), p. 041604. DOI: 10.1103/PhysRevC.64.041604. arXiv: nucl-ex/0108014 [nucl-ex] (pages 142, 145).

[342] A. Andronic et al. “Directed flow in Au + Au, Xe + CsI and Ni + Ni collisions and the nuclear equation of state”. In: *Phys. Rev.* C67 (2003), p. 034907. DOI: 10.1103/PhysRevC.67.034907. arXiv: nucl-ex/0301009 [nucl-ex] (page 142).

[343] M. D. Partlan et al. “Fragment flow in Au + Au collisions”. In: *Phys. Rev. Lett.* 75 (1995), pp. 2100–2103. DOI: 10.1103/PhysRevLett.75.2100 (page 142).

[344] H. Liu et al. “Sideward flow in Au + Au collisions between 2-A-GeV and 8-A-GeV”. In: *Phys. Rev. Lett.* 84 (2000), pp. 5488–5492. DOI: 10.1103/PhysRevLett.84.5488. arXiv: nucl-ex/0005005 [nucl-ex] (pages 145, 146).

[345] E. Kashirin et al. “Directed flow measurement in Pb+Pb collisions at P_{lab} = 13A GeV/c collected with NA61/SHINE at SPS”. In: *J. Phys. Conf. Ser.* 1690.1 (2020). Ed. by Petr Teterin, p. 012127. DOI: 10.1088/1742-6596/1690/1/012127 (page 145).

[346] C. Alt et al. “Directed and elliptic flow of charged pions and protons in Pb + Pb collisions at 40-A-GeV and 158-A-GeV”. In: *Phys. Rev. C* 68 (2003), p. 034903. DOI: 10.1103/PhysRevC.68.034903. arXiv: nucl-ex/0303001 (pages 145, 146, 149).

[347] L. Adamczyk et al. “Beam-Energy Dependence of the Directed Flow of Protons, Antiprotons, and Pions in Au+Au Collisions”. In: *Phys. Rev. Lett.* 112.16 (2014), p. 162301. DOI: 10.1103/PhysRevLett.112.162301(2014),10.1103/PhysRevLett.112.162301. arXiv: 1401.3043 [nucl-ex] (page 145).

[348] Jaroslav Adam et al. “Flow and interferometry results from Au+Au collisions at $\sqrt{s_{NN}} = 4.5$ GeV”. In: *Phys. Rev. C* 103.3 (2021), p. 034908. DOI: 10.1103/PhysRevC.103.034908. arXiv: 2007.14005 [nucl-ex] (page 145).

[349] Mohamed Abdallah et al. “Light nuclei collectivity from sNN=3 GeV Au+Au collisions at RHIC”. In: *Phys. Lett. B* 827 (2022), p. 136941. DOI: 10.1016/j.physletb.2022.136941. arXiv: 2112.04066 [nucl-ex] (page 145).

[350] J. Barrette et al. “Energy and charged particle flow in a 10.8-A/GeV/c Au + Au collisions”. In: *Phys. Rev. C* 55 (1997). [Erratum: Phys.Rev.C 56, 2336–2336 (1997)], pp. 1420–1430. DOI: 10.1103/PhysRevC.55.1420. arXiv: nucl-ex/9610006 (page 145).

[351] Heng Liu. “Collective motion in fully reconstructed gold on gold collisions between 2 and 8 GeV per nucleon”. PhD thesis. 1998. URL: https://www.proquest.com/docview/304422481 (page 146).

[352] A. Andronic et al. “Excitation function of elliptic flow in Au+Au collisions and the nuclear matter equation of state”. In: *Phys. Lett.* B612 (2005), pp. 173–180. DOI: 10.1016/j.physletb.2005.02.060. arXiv: nucl-ex/0411024 [nucl-ex] (pages 146, 147, 151, 177, 187, 188).

[353] D. Adamova et al. “New results from CERES”. In: *Nucl. Phys.* A698 (2002), pp. 253–260. DOI: 10.1016/S0375-9474(01)01371-9 (page 146).

[354] B. I. Abelev et al. "Identified particle production, azimuthal anisotropy, and interferometry measurements in Au+Au collisions at s(NN)**(1/2) = 9.2- GeV". In: *Phys. Rev.* C81 (2010), p. 024911. DOI: 10.1103/PhysRevC.81.024911. arXiv: 0909.4131 [nucl-ex] (page 146).

[355] L. Adamczyk et al. "Inclusive charged hadron elliptic flow in Au + Au collisions at $\sqrt{s_{NN}}$ = 7.7 - 39 GeV". In: *Phys. Rev.* C86 (2012), p. 054908. DOI: 10.1103/PhysRevC.86.054908. arXiv: 1206.5528 [nucl-ex] (page 146).

[356] Jessica Kintner. "Squeeze-Out and Flow of Pions from 1.5 GeV/Nucleon Au+Au". Dissertation. University of California Davis, 1993 (page 147).

[357] D. Brill et al. "Study of the out-of-plane emission of protons and light fragments in symmetric heavy-ion collisions". In: *Z. Phys.* A355 (1996), pp. 61–68. DOI: 10.1007/s002180050078 (pages 147, 177, 187).

[358] Dieter Brill. "Azimutal anisotrope Teilchenemission in relativistischen Schwerionenstössen". Dissertation, Frankfurt (Main), Goethe-University, 1993. Dissertation. Darmstadt: Frankfurt (Main), Goethe-University, 1993 (page 147).

[359] L. B. Venema et al. "Azimuthal asymmetry of neutral pion emission in Au+Au reactions at 1 GeV/nucleon". In: *Phys. Rev. Lett.* 71 (1993), pp. 835–838. DOI: 10.1103/PhysRevLett.71.835 (page 147).

[360] Jiangyong Jia, Sooraj Radhakrishnan, and Mingliang Zhou. "Forward-backward multiplicity fluctuation and longitudinal harmonics in high-energy nuclear collisions". In: *Phys. Rev. C* 93.4 (2016), p. 044905. DOI: 10.1103/PhysRevC.93.044905. arXiv: 1506.03496 [nucl-th] (page 149).

[361] Adam Bzdak and Derek Teaney. "Longitudinal fluctuations of the fireball density in heavy-ion collisions". In: *Phys. Rev. C* 87.2 (2013), p. 024906. DOI: 10.1103/PhysRevC.87.024906. arXiv: 1210.1965 [nucl-th] (page 149).

[362] D.A. Brown et al. "Imaging three dimensional two-particle correlations for heavy-ion reaction studies". In: *Phys. Rev. C* 72 (2005), p. 054902. DOI: 10.1103/PhysRevC.72.054902. arXiv: nucl-th/0507015 (page 149).

[363] Sergei A. Voloshin. "Transverse radial expansion and directed flow". In: *Phys. Rev. C* 55 (1997), R1630–R1632. DOI: 10.1103/PhysRevC.55.R1630. arXiv: nucl-th/9611038 (pages 149, 150).

[364] P. Huovinen et al. "Radial and elliptic flow at RHIC: Further predictions". In: *Phys. Lett.* B503 (2001), pp. 58–64. DOI: 10.1016/S0370-2693(01)00219-2. arXiv: hep-ph/0101136 [hep-ph] (pages 149, 150).

[365] Fabrice Retiere and Michael Annan Lisa. "Observable implications of geometrical and dynamical aspects of freeze out in heavy ion collisions". In: *Phys. Rev. C* 70 (2004), p. 044907. DOI: 10.1103/PhysRevC.70.044907. arXiv: nucl-th/0312024 (page 149).

[366] Boris Tomasik. "Disentangling spatial and flow anisotropy". In: *Acta Phys. Polon. B* 36 (2005), pp. 2087–2104. arXiv: nucl-th/0409074 (page 149).

[367] Clement Gombeaud and Jean-Yves Ollitrault. "Effects of flow fluctuations and partial thermalization on v(4)". In: *Phys. Rev. C* 81 (2010), p. 014901. DOI: 10.1103/PhysRevC.81.014901. arXiv: 0907.4664 [nucl-th] (pages 149, 150, 153).

[368] M. Csanad, T. Csorgo, and B. Lorstad. “Buda-Lund hydro model for ellipsoidally symmetric fireballs and the elliptic flow at RHIC”. In: *Nucl. Phys. A* 742 (2004), pp. 80–94. DOI: 10.1016/j.nuclphysa.2004.06.023. arXiv: nucl-th/0310040 (pages 149, 150).

[369] T. Csorgo et al. “Observables and initial conditions for selfsimilar ellipsoidal flows”. In: *Phys. Rev. C* 67 (2003), p. 034904. DOI: 10.1103/PhysRevC.67.034904. arXiv: hep-ph/0108067 (page 150).

[370] Denes Molnar and Sergei A. Voloshin. “Elliptic flow at large transverse momenta from quark coalescence”. In: *Phys. Rev. Lett.* 91 (2003), p. 092301. DOI: 10.1103/PhysRevLett.91.092301. arXiv: nucl-th/0302014 (pages 150, 159, 160).

[371] Peter F. Kolb, Josef Sollfrank, and Ulrich W. Heinz. “Anisotropic flow from AGS to LHC energies”. In: *Phys. Lett. B* 459 (1999), pp. 667–673. DOI: 10.1016/S0370-2693(99)00720-0. arXiv: nucl-th/9906003 (pages 150, 153, 178, 189).

[372] Jean-Yves Ollitrault. “Anisotropy as a signature of transverse collective flow”. In: *Phys. Rev. D* 46 (1992), pp. 229–245. DOI: 10.1103/PhysRevD.46.229 (page 150).

[373] J. Barrette et al. “Directed flow of light nuclei in Au + Au collisions at AGS energies”. In: *Phys. Rev. C* 59 (1999), pp. 884–888. DOI: 10.1103/PhysRevC.59.884. arXiv: nucl-ex/9805006 (pages 151, 177, 188).

[374] D. Teaney and Edward V. Shuryak. “An Unusual space-time evolution for heavy ion collisions at high-energies due to the QCD phase transition”. In: *Phys. Rev. Lett.* 83 (1999), pp. 4951–4954. DOI: 10.1103/PhysRevLett.83.4951. arXiv: nucl-th/9904006 (pages 153, 178, 189).

[375] Peter F. Kolb. “v(4): A Small, but sensitive observable for heavy ion collisions”. In: *Phys. Rev. C* 68 (2003), p. 031902. DOI: 10.1103/PhysRevC.68.031902. arXiv: nucl-th/0306081 (pages 153, 178, 189).

[376] Arthur M. Poskanzer. “Azimuthal anisotropy: The Higher harmonics”. In: *J. Phys. G* 30 (2004). Ed. by Hans Georg Ritter and Xin-Nian Wang, S1225–S1228. DOI: 10.1088/0954-3899/30/8/095. arXiv: nucl-ex/0403019 (page 153).

[377] Nicolas Borghini and Jean-Yves Ollitrault. “Momentum spectra, anisotropic flow, and ideal fluids”. In: *Phys. Lett. B* 642 (2006), pp. 227–231. DOI: 10.1016/j.physletb.2006.09.062. arXiv: nucl-th/0506045 (pages 153, 178, 189).

[378] J. Adams et al. “Azimuthal anisotropy at RHIC: The First and fourth harmonics”. In: *Phys. Rev. Lett.* 92 (2004), p. 062301. DOI: 10.1103/PhysRevLett.92.062301. arXiv: nucl-ex/0310029 [nucl-ex] (page 153).

[379] A. Adare et al. “Elliptic and hexadecapole flow of charged hadrons in Au+Au collisions at $\sqrt{s_{NN}} = 200$ GeV”. In: *Phys. Rev. Lett.* 105 (2010), p. 062301. DOI: 10.1103/PhysRevLett.105.062301. arXiv: 1003.5586 [nucl-ex] (page 153).

[380] Georges Aad et al. “Measurement of the azimuthal anisotropy for charged particle production in $\sqrt{s_{NN}} = 2.76$ TeV lead-lead collisions with the ATLAS detector”. In: *Phys. Rev.* C86 (2012), p. 014907. DOI: 10.1103/PhysRevC.86.014907. arXiv: 1203.3087 [hep-ex] (page 153).

[381] Serguei Chatrchyan et al. "Studies of Azimuthal Dihadron Correlations in Ultra-Central PbPb Collisions at $\sqrt{s_{NN}} = 2.76$ TeV". In: *JHEP* 02 (2014), p. 088. DOI: 10.1007/JHEP02(2014)088. arXiv: 1312.1845 [nucl-ex] (page 153).

[382] S. Acharya et al. "Energy dependence and fluctuations of anisotropic flow in Pb-Pb collisions at $\sqrt{s_{\mathrm{NN}}} = 5.02$ and 2.76 TeV". In: *JHEP* 07 (2018), p. 103. DOI: 10.1007/JHEP07(2018)103. arXiv: 1804.02944 [nucl-ex] (page 153).

[383] J. Wang et al. "Effect of initial fluctuations on the collective flow in intermediate-energy heavy ion collisions". In: *Phys. Rev. C* 90.5 (2014), p. 054601. DOI: 10.1103/PhysRevC.90.054601. arXiv: 1411.1812 [nucl-th] (pages 154, 155, 178, 189).

[384] Justin Mohs et al. "Collective flow at SIS energies within a hadronic transport approach: Influence of light nuclei formation and equation of state". In: *Phys. Rev. C* 105.3 (2022), p. 034906. DOI: 10.1103/PhysRevC.105.034906. arXiv: 2012.11454 [nucl-th] (pages 154, 155, 169, 178, 189).

[385] S. Manly et al. "System size, energy and pseudorapidity dependence of directed and elliptic flow at RHIC". In: *Nucl. Phys. A* 774 (2006). Ed. by T. Csorgo et al., pp. 523–526. DOI: 10.1016/j.nuclphysa.2006.06.079. arXiv: nucl-ex/0510031 (page 156).

[386] Rajeev S. Bhalerao and Jean-Yves Ollitrault. "Eccentricity fluctuations and elliptic flow at RHIC". In: *Phys. Lett. B* 641 (2006), pp. 260–264. DOI: 10.1016/j.physletb.2006.08.055. arXiv: nucl-th/0607009 (page 156).

[387] B. Alver et al. "Importance of correlations and fluctuations on the initial source eccentricity in high-energy nucleus-nucleus collisions". In: *Phys. Rev. C* 77 (2008), p. 014906. DOI: 10.1103/PhysRevC.77.014906. arXiv: 0711.3724 [nucl-ex] (page 156).

[388] S. A. Voloshin. "Anisotropic flow". In: *Nucl. Phys. A* 715 (2003). Ed. by H. Gutbrod, J. Aichelin, and K. Werner, pp. 379–388. DOI: 10.1016/S0375-9474(02)01450-1. arXiv: nucl-ex/0210014 (page 158).

[389] E. V. Shuryak. "The Azimuthal asymmetry at large p(t) seem to be too large for a 'jet quenching'". In: *Phys. Rev. C* 66 (2002), p. 027902. DOI: 10.1103/PhysRevC.66.027902. arXiv: nucl-th/0112042 (page 158).

[390] S. T. Butler and C. A. Pearson. "Deuterons from High-Energy Proton Bombardment of Matter". In: *Phys. Rev.* 129 (1963), pp. 836–842. DOI: 10.1103/PhysRev.129.836 (page 159).

[391] A. Schwarzschild and C. Zupancic. "Production of Tritons, Deuterons, Nucleons, and Mesons by 30-GeV Protons on A-1, Be, and Fe Targets". In: *Phys. Rev.* 129 (1963), pp. 854–862. DOI: 10.1103/PhysRev.129.854 (page 159).

[392] H. H. Gutbrod et al. "Final State Interactions in the Production of Hydrogen and Helium Isotopes by Relativistic Heavy Ions on Uranium". In: *Phys. Rev. Lett.* 37 (1976), pp. 667–670. DOI: 10.1103/PhysRevLett.37.667 (page 159).

[393] H. Sato and K. Yazaki. "On the coalescence model for high-energy nuclear reactions". In: *Phys. Lett. B* 98 (1981), pp. 153–157. DOI: 10.1016/0370-2693(81)90976-X (page 159).

[394] Denes Molnar. "Elliptic flow form quark coalescence: Mass ordering or quark number scaling?" In: (Aug. 2004). arXiv: nucl-th/0408044 (page 159).

[395] Zi-wei Lin and Denes Molnar. "Quark coalescence and elliptic flow of charm hadrons". In: *Phys. Rev. C* 68 (2003), p. 044901. DOI: 10.1103/PhysRevC.68.044901. arXiv: nucl-th/0304045 (page 159).

[396] Peter F. Kolb et al. "Momentum anisotropies in the quark coalescence model". In: *Phys. Rev. C* 69 (2004), p. 051901. DOI: 10.1103/PhysRevC.69.051901. arXiv: nucl-th/0402049 (pages 159, 160).

[397] Carl B. Dover et al. "Relativistic coalescence model for high-energy nuclear collisions". In: *Phys. Rev.* C44 (1991), pp. 1636–1654. DOI: 10.1103/PhysRevC.44.1636 (page 160).

[398] J. L. Nagle et al. "Coalescence of deuterons in relativistic heavy ion collisions". In: *Phys. Rev. C* 53 (1996), pp. 367–376. DOI: 10.1103/PhysRevC.53.367 (pages 160, 167).

[399] Rudiger Scheibl and Ulrich W. Heinz. "Coalescence and flow in ultrarelativistic heavy ion collisions". In: *Phys. Rev. C* 59 (1999), pp. 1585–1602. DOI: 10.1103/PhysRevC.59.1585. arXiv: nucl-th/9809092 (page 160).

[400] Yasushi Nara, Tomoyuki Maruyama, and Horst Stoecker. "Momentum-dependent potential and collective flows within the relativistic quantum molecular dynamics approach based on relativistic mean-field theory". In: *Phys. Rev. C* 102.2 (2020), p. 024913. DOI: 10.1103/PhysRevC.102.024913. arXiv: 2004.05550 [nucl-th] (page 165).

[401] Paula Hillmann, Jan Steinheimer, and Marcus Bleicher. "Directed, elliptic and triangular flow of protons in Au+Au reactions at 1.23 A GeV: a theoretical analysis of the recent HADES data". In: *J. Phys.* G45.8 (2018), p. 085101. DOI: 10.1088/1361-6471/aac96f. arXiv: 1802.01951 [nucl-th] (page 165).

[402] O. Buss et al. "Transport-theoretical Description of Nuclear Reactions". In: *Phys. Rept.* 512 (2012), pp. 1–124. DOI: 10.1016/j.physrep.2011.12.001. arXiv: 1106.1344 [hep-ph] (page 165).

[403] T. Gaitanos et al. "Breathing mode in an improved transport approach". In: *Phys. Rev. C* 81 (2010), p. 054316. DOI: 10.1103/PhysRevC.81.054316. arXiv: 1003.4863 [nucl-th] (page 165).

[404] Tom Reichert et al. "Comparison of heavy ion transport simulations: Ag + Ag collisions at E_{lab} = 1.58A GeV". In: *J. Phys. G* 49.5 (2022), p. 055108. DOI: 10.1088/1361-6471/ac5dfe. arXiv: 2111.07652 [nucl-th] (page 166).

[405] Tom Reichert et al. "Harmonic flow correlations in Au+Au reactions at 1.23 AGeV: a new testing ground for the equation-of-state and expansion geometry". In: *Eur. Phys. J. C* 82.6 (2022), p. 510. DOI: 10.1140/epjc/s10052-022-10480-0. arXiv: 2203.15550 [nucl-th] (page 166).

[406] Tom Reichert et al. "A Systematic Comparison of Ag+Ag and Au+Au Reactions at 1.23 AGeV". In: (Aug. 2022). arXiv: 2208.10871 [nucl-th] (page 166).

[407] Yasushi Nara and Akira Ohnishi. "Mean-field update in the JAM microscopic transport model: Mean-field effects on collective flow in high-energy heavy-ion collisions at sNN=2–20 GeV energies". In: *Phys. Rev. C* 105.1 (2022), p. 014911. DOI: 10.1103/PhysRevC.105.014911. arXiv: 2109.07594 [nucl-th] (page 166).

[408] Yasushi Nara et al. "Directed flow of Λ in high-energy heavy-ion collisions and Λ potential in dense nuclear matter". In: (Aug. 2022). arXiv: 2208.01297 [nucl-th] (page 166).

[409] "United Generators version 2.0". In: (). URL: https://github.com/FairRootGroup/UniGen (page 167).

[410] Sukanya Sombun et al. "Deuteron production from phase-space coalescence in the UrQMD approach". In: *Phys. Rev. C* 99.1 (2019), p. 014901. DOI: 10.1103/PhysRevC.99.014901. arXiv: 1805.11509 [nucl-th] (page 167).

[411] Paula Hillmann et al. "Coalescence, the thermal model and multi-fragmentation: The energy and volume dependence of light nuclei production in heavy ion collisions". In: (Sept. 2021). arXiv: 2109.05972 [hep-ph] (page 167).

[412] A. J. Baltz et al. "Strange cluster formation in relativistic heavy ion collisions". In: *Phys. Lett. B* 325 (1994), pp. 7–12. DOI: 10.1016/0370-2693(94)90063-9 (page 167).

[413] D. E. Kahana et al. "Modeling cluster production at the AGS". In: *Phys. Rev. C* 54 (1996), pp. 338–352. DOI: 10.1103/PhysRevC.54.338. arXiv: nucl-th/9601019 (page 167).

[414] R. Mattiello et al. "Nuclear clusters as a probe for expansion flow in heavy ion reactions at 10-A/GeV - 15-A/GeV". In: *Phys. Rev. C* 55 (1997), pp. 1443–1454. DOI: 10.1103/PhysRevC.55.1443. arXiv: nucl-th/9607003 (page 167).

[415] V. D. Toneev and K. K. Gudima. "PARTICLE EMISSION IN LIGHT AND HEAVY ION REACTIONS." In: *Nucl. Phys. A* 400 (1983). Ed. by G. F. Bertsch, C. K. Gelbke, and D. K. Scott, pp. 173C–190C. DOI: 10.1016/0375-9474(83)90433-5 (page 167).

[416] J. Steinheimer et al. "Hypernuclei, dibaryon and antinuclei production in high energy heavy ion collisions: Thermal production versus Coalescence". In: *Phys. Lett. B* 714 (2012), pp. 85–91. DOI: 10.1016/j.physletb.2012.06.069. arXiv: 1203.2547 [nucl-th] (page 167).

[417] M. Baznat et al. "Monte-Carlo Generator of Heavy Ion Collisions DCM-SMM". In: *Phys. Part. Nucl. Lett.* 17.3 (2020), pp. 303–324. DOI: 10.1134/S1547477120030024. arXiv: 1912.09277 [nucl-th] (page 167).

[418] Stepan G. Mashnik et al. "Production of energetic light fragments in extensions of the CEM and LAQGSM event generators of the Monte Carlo transport code MCNP6". In: *Phys. Rev. C* 95.3 (2017), p. 034613. DOI: 10.1103/PhysRevC.95.034613. arXiv: 1607.02506 [nucl-th] (page 167).

[419] S. Agostinelli et al. "GEANT4–a simulation toolkit". In: *Nucl. Instrum. Meth. A* 506 (2003), pp. 250–303. DOI: 10.1016/S0168-9002(03)01368-8 (page 167).

[420] P. Danielewicz and G. F. Bertsch. "Production of deuterons and pions in a transport model of energetic heavy ion reactions". In: *Nucl. Phys. A* 533 (1991), pp. 712–748. DOI: 10.1016/0375-9474(91)90541-D (page 169).

[421] Susanne Gläßel et al. "Cluster and hypercluster production in relativistic heavy-ion collisions within the parton-hadron-quantum-molecular-dynamics approach". In: *Phys. Rev. C* 105.1 (2022), p. 014908. DOI: 10.1103/PhysRevC.105.014908. arXiv: 2106.14839 [nucl-th] (page 169).

Danksagung

Mein größter Dank geht an meinen Doktorvater Christoph Blume für die Möglichkeit sowohl meine Diplomarbeit als auch meine Doktorarbeit mit diesem spannenden Thema durchführen zu können. Zudem möchte ich ihm für seine ausnahmslosen Unterstützung bei allen Herausforderungen danken, sowie für seine stetigen Mühen mir immer all meine Fragen aus seinem nahezu unerschöpfliche Erfahrungsschatz zu beantworten.

Meinem Doktorgroßvater Reinhard Stock möchte ich herzlich danken, für die unermüdliche Unterstützung und die immer faszinierenden Fragestellungen und Antworten, und von dessen Wissen ich bei jedem unserer Gespräche im höchsten Maße profitierte.

Ich bedanke mich bei Joachim Stroth für die vielen hilfreichen Anregungen und die Begutachtung meiner Arbeit, sowie dafür immer die richtige Antwort parat zu haben auf die kleinen Geheimnisse die sich in einen so komplexen Detektorsystem wie HADES verstecken.

Auch bei meinem externen Supervisor Markus Bleicher möchte ich mich bedanken, für die immer sehr hilfreich Diskussionen, insbesondere aus der Perspektive eines außenstehenden Theoretikers.

Ich möchte der gesamten HADES Kollaboration, für Ihre warmherzige Aufnahme, der sehr angenehmen Atmosphäre und den lehrreichen Diskussionen danken, u.a. Piotr Salabura, Tetyana Galatyuk, Gosia Gumberidze, Romain Holzmann, Jochen Markert und Jürgen Friese. Insbesondere an Herbert Ströbele und Pavel Tlusty geht mein Dank, für die hilfreichen Ratschäge und Anleitungen bei den Analysen rund um Centrality und Flow.

Auch an Volodya Vovchenko, Manuel Lorenz und Benjamin Dönigus geht ein *Excited-Nuclei* Dankeschön.

Meinen Zimmerkollegen Julian Book, Heidi Schuldes, Benjamin Brudnyi und Murad Esen möchte ich besonders herzlich danken für die spannenden Diskussionen und die regelmäßigen Kaffeepausen, auch meinen HADES Mitstreitern Timo, Patrick, Katharina, Claudia und den CBM Mitstreitern Florian und Susanne für die schöne Zeit abseits der Physik bei einem Bierchen. Weiter gilt mein Dank auch an Maja, Max, Mathilde, Benedict, Naomi, Kim und Laura, die ich mitbetreuen durfte.

Ich möchte auch an dieser Stelle an Robert Greifenhagen erinnern, mit dem ich bei unterschiedlichen Problemstellungen in unser beider verschieden Analysen gemeinsame Lösungen gefunden haben.

Ein riesiges Dankeschön geht an Marianne Frey für ihre herzliche Art und ihr Organisationstalent, sowie allen Mitgliedern des IKF, die einem immer spontan bei jeglichen Problemen oder Fragen immer zur Seite stehen.

Meinem Vater und meiner Schwester gebührt ein besonderer Danke ich für ihre Kraft und ihren Rückhalt.

Für Jana und Carlo, die *meine Welt im innersten zusammenhalten*, die wichtigen Dingen im Leben im Blick haben, sowie mir jeden Tag versüßen. Ohne die Unterstützung und den Rückhalt von Jana wäre diese Arbeit unmögliche gewesen.